Coulomb Drag in Multiwall Carbon Nanotubes

Master Thesis in Physics

Anders Mathias Lunde

Niels Bohr Institute,
University of Copenhagen
and
MIC – Department of Micro and Nanotechnology,
Technical University of Denmark

Supervisors: Antti-Pekka Jauho and Karsten Flensberg

22nd January 2004

Preface

The present master thesis is submitted to the candidacy to the cand. scient. title at the Copenhagen University. The work was carried out at the Department of Micro and Nanotechnology (MIC) at the Technical University of Denmark in the Theoretical Nanotechnology group under the supervision of Antti-Pekka Jauho and Karsten Flensberg (at the Niels Bohr int., Copenhagen University).

I will like to thank my supervisors for their enormous work and patience. I will also like to thank Mads Brandbyge for constructive discussions about the band structure of carbon nanotubes. For discussions about the experimental possibilities I will like to thank Peter Bøglid and Jesper Nygård. Furthermore, I will like to thank Laurits Højgaard Olesen for teaching me MATLAB and helping me do numerical integration. I will also like to thank Morten Høgsbro larsen for proof reading the manuscript. For discussions in general, I will like to thank the Theoretical Nanotechnology group at MIC, T. Vuković and S. Roche. During the work on the present thesis, I got the possibility to give a oral contribution at the "International Conference on Nonequilibrium Carrier Dynamics in Semiconductors" (HCIS13), Modena, Italy. This was only possible due to funding from MIC and the Ørsted laboratory at the Copenhagen University. This opportunity was strongly appreciated. Further funding from the Danish Physical society was given to present a poster at the annual meeting, which is also acknowledged. Furthermore the hospitality of MIC is acknowledged. At last I want to thank family and friends for understanding and patience during the last hectic months.

Contents

List of symbols

General notation

Symbol	Description
T	Temperature
ε_{F}	Fermi level (Fermi energy)
$e > 0$	Elementary charge (defined as positive)
(x, y, z)	Cartesian coordinates
(r, θ, z)	Cylindrical coordinates
μ	Chemical potential
$\theta(x)$	The step function (zero for $x < 0$, one for $x > 0$)
FBZ	The First Brillouin Zone
$V_{12}(\lvert\mathbf{r}_1 - \mathbf{r}_2\rvert)$	The inter subsystem Coulomb interaction
$\ln(x)$	The natural logarithm of x
ϵ_0	The vacuum permittivity

Coulomb drag notation

Symbol	Description	Reference
ρ_{21}	The transresistivity	sec. 1.2
$F^{(i)}_{\nu\nu'}(q, \omega)$	The F function (the available (q, ω) phase space)	eq.(3.36,3.44)
E_i	Electric field in subsystem i along the cylinder	
J_i	Current density in subsystem i along the cylinder	eq.(3.10)
I_i	Current in subsystem i along the cylinder	eq.(3.5)
ν	The band index representing a collection of indices	sec. 3.1
$\tilde{e}_i$	The carrier charge for subsystem i	
n_i	Carrier density in subsystem i	
μ_{Tr}	Transport mobility (single subsystem property)	eq.(3.13)
L	Length of the nanotubes (i.e. $L \equiv L_1 = L_2$)	
a_i	Lattice constant for subsystem i (tubes: $a_i = \lvert\mathbf{T}_i\rvert$)	
r_i^c	Radius of cylinder i	
$\hbar\omega$	Transferred energy in the interaction process	
q	Transferred crystal wave vector	
κ	Permittivity constant $\kappa = \epsilon_r\epsilon_0$	eq.(F.1)
$\mathcal{J}(\nu_1\nu_1', \nu_2\nu_2')$	Selection rules for the band indices	eq.(3.21)

Carbon nanotube notation

Symbol	Description	Reference
$\mathbf{C}$	Chiral vector	eq.(2.3)
(n, m)	Nanotube index from $\mathbf{C}$	eq.(2.3)
$\mathbf{a}_1$,$\mathbf{a}_2$	Primitive vectors of graphene	eq.(2.1)
$\mathbf{b}_1$,$\mathbf{b}_2$	Basis vectors in reciprocal space of graphene	eq.(2.2)
$\mathbf{d}$	Vector connecting the two atoms in the unit cell	fig.2.1
D	Diameter	eq.(2.4)
$\mathbf{R}_{i=A,B}$	Lattice vector of graphene	sec.2.1.1
$\mathbf{G}$	Reciprocal lattice vector of graphene	sec.2.1.1
$a_{\text{C-C}}$	Interatomic distance ($a_{\text{C-C}} = \lvert\mathbf{d}\rvert$)	sec.2.1.1
a	$a = \sqrt{3}a_{\text{C-C}}$	sec.2.1.1
$\gcd(a, b)$	Greatest common divisor of a and b for $a, b \in \mathbb{Z}$	
$\mathcal{S}(h, \varphi)$	The helical symmetry operation	p. 15
$\mathbf{H}$	Vector generating the helical symmetry	eq.(2.6)
p_1,p_2	Defined from $\mathbf{H} = p_1\mathbf{a}_1 + p_2\mathbf{a}_2$	eq.(2.6)
$\mathcal{C}_\mathfrak{n}$	The discrete rotational symmetry operation	p. 16
$\mathbf{C}_\mathfrak{n}$	Vector generating the rotational symmetry	eq.(2.7)
$\mathfrak{n}$	Defined as $\gcd(n, m)$	eq.(2.6)
$\mathbf{T}$	Translational vector	eq.(2.8)
$\mathbf{G_C}$,$\mathbf{G_T}$	Reciprocal lattice vectors of a nanotube structure	eq.(2.9)
$\mathcal{N}$	Number of graphene unit cells in a tube unit cell	eq.(2.10)
$\psi_\mathbf{k}(\mathbf{r})$	Wave function of graphene	eq.(2.12)
α, β	Coefficients of the tight binding wave function	eq.(2.12,2.33)
$\Psi(\mathbf{r})$	The atomic $2p_z$ orbitals	eq.(2.12)
$\Upsilon(\mathbf{k})$	Sum over three nearest neighbours	eq.(2.21)
$\gamma_0 > 0$	Nearest neighbour hopping matrix element ($\sim$3eV)	eq.(2.18)
s_0	Nearest neighbour overlap (of order 0.1)	eq.(2.19)
k	Wave vector (in 1D) along the tube	eq.(2.30)
n_c	Quantum number from quantization around tube	eq.(2.29,2.31)
κ	Helical quantum number (from $\mathcal{S}(h, \varphi)$)	eq.(2.33)
$\mathfrak{m}$	Crystal angular momentum (from $\mathcal{C}_\mathfrak{n}$)	eq.(2.33)
$\xi = \pm 1$	Direction of velocity in metallic nanotubes	eq.(2.58)
$\mathbf{K}_\varsigma$	Zeros in graphene band structure	sec.2.2.4
$\varsigma = \pm 1$	Index of the zero in graphene band structure	sec.2.2.4
$\mathfrak{K}$	The deviation from $\mathbf{K}_\varsigma$	sec.2.2.4
v_0	Velocity in metallic nanotubes ($v_0 = \frac{\sqrt{3}\gamma_0 a}{2\hbar}$)	eq.(5.1)
ψ^ξ_{k,n^ξ_c}	Bloch wave function of metallic nanotubes	p.39
$g(\mathbf{k}, \mathbf{k}')$	Information from Bloch states in matrix element	eq.(2.66)

Chapter 1

Introduction

In this chapter we introduce the two central concepts of this thesis: Coulomb drag and carbon nanotubes. Before we begin, a comment of personal nature is stated.

1.1 Why is condensed matter physics interesting?

Basically all condensed matter systems consist of a lot of particles such as electrons and atoms. Both atoms and electrons are fairly well understood, but in a condensed matter system in principle all the inter-particle interactions need to be included to find the properties of the system, i.e. a many particle problem needs to be solved[1]. This is in general a very difficult task and approximations are needed. In a first approach all the interactions between particles are neglected. This drastic approximation called the independent particle picture [1] (e.g. Bloch theory) has been very successful to explain many properties of metals, semiconductors and other systems. When interactions between the particles are taken into account, new exciting phenomena arise such as superconductivity, phase transitions, collective excitations (e.g. plasmons and spin waves) and so on. As we shall see, Coulomb drag is one such phenomenon. So when more particles are together one can have properties *not* stemming from the single particles, but from the inter particle interactions! Furthermore it is by no means trivial to find good approximations and somehow it is here good physical intuition and physical arguments are needed. So even though condensed matter systems consist of fairly well understood particles it is not straight forward to make a good description of such a system; or as Anderson puts it [2]: reductionism is not constructionism.

This makes condensed matter physics one of the most exciting areas in science and of fundamental interest in my opinion.

[1] To be precise, an atom does have a lot of inter-particle interactions between the core and the electrons and among the electrons, but here we have the atom-atom interaction in mind.

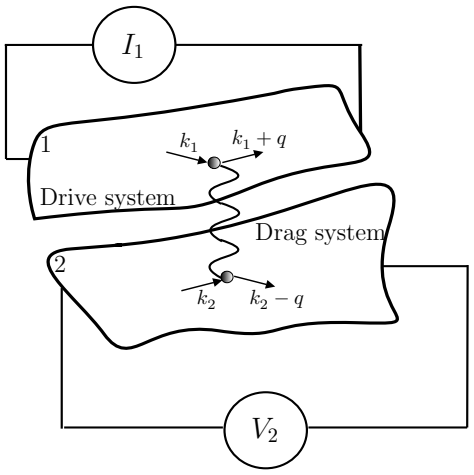

Figure 1.1: The general idea behind Coulomb drag in any system is depicted. Here the drive system (labelled 1) transfers momentum to the drag system (labelled 2) via an effective interaction such as the screened Coulomb interaction.

1.2 What is Coulomb drag and how is it studied?

When two spatially separated systems (e.g. two conductors) are brought together the particles of the two systems begin to interact. If there are free carriers in the two systems and they are close enough together, tunnelling between the two systems takes place. If they are a bit further apart the charged carriers can interact via other mechanisms such as the long-range Coulomb interaction. This is the regime, where the phenomenon of *drag* can take place.

The idea of drag, as seen on figure 1.1, is that by a current I_1 through one system (the drive system) a current in another system (the drag system) can be induced. This happens by momentum transfer from the carriers of the drive system to the carriers in the drag system via carrier-carrier interaction. This interaction can be a phonon mediated interaction or a (screened) Coulomb interaction and thereby the name *Coulomb drag*. This effect was first suggested by Pogrebinskiĭ [3] in 1977 and independently by Price [4] in 1983. As we shall briefly describe in section 1.5 this has been intensively investigated both experimentally and theoretically for two parallel electron gases in two dimensions.

To study Coulomb drag experimentally, a voltmeter can be placed on the drag system as in figure 1.1. Since the voltmeter has a large resistance the current in the drag system is (close to) zero and therefore the momentum transfer from the drive current I_1 builds up a voltage drop V_2 in the drag system. For isotropic systems this leads to the introduction of the *transresistance*, $R_{21} = \frac{V_2}{I_1}$, or in terms of the magnitude of the current density J_1 and the magnitude of the induced electric field E_2 the *transresistivity* $\rho_{21} = \frac{E_2}{J_1}$. One of the most difficult experimental task is to make independent contacts to the two subsystems to be able to measure the transresistance (without having short circuits), since the typical distance between e.g. coupled quantum wells are of order 40nm.

To see that the transresistivity ρ_{21} is the relevant quantity to study to obtain

information about the Coulomb drag effect, we make a simple semiclassical calculation (in one dimension for simplicity). The average force F_2 on the carriers of charge $\tilde{e}_2$ in systems 2 (figure 1.1) from the induced electric field E_2 is $F_2 = \tilde{e}_2 E_2$, but the force is also the average rate of momentum transfer to each carrier in system 2, i.e. the magnitudes of the two are equal: $F_2 = \langle \frac{\partial p_2}{\partial t} \rangle$. Note that the drag current is induced in the same direction as the drive current J_1, so the drive current and the induced voltage drop are in opposite directions, however, here only the magnitudes are considered. The current density J_1 in system 1 can be written in terms of a drift velocity $\langle v_1 \rangle$ as $J_1 = \tilde{e}_1 n_1 \langle v_1 \rangle$, where n_1 and $\tilde{e}_1$ are the carrier density and charge in system 1, respectively. Therefore the transresistivity is

$$\rho_{21} = \frac{E_2}{J_1} = \frac{F_2}{\tilde{e}_2 \tilde{e}_1 n_1 \langle v_1 \rangle} = \frac{1}{\tilde{e}_2 \tilde{e}_1 n_1} \frac{\langle \frac{\partial p_2}{\partial t} \rangle}{\langle v_1 \rangle}, \tag{1.1}$$

i.e. it is proportional to the average momentum transfer to each carrier in the drag system per unit drift velocity in the drive system. It is thereby the relevant quantity to study to understand the Coulomb drag effect. If there is a well defined effective mass[2] m_1 the drift velocity is $\langle v_1 \rangle = \frac{\langle p_1 \rangle}{m_1}$ and the rate of momentum transfer τ_{21}^{-1} can be defined through $\tau_{21}^{-1} = \langle \frac{\partial p_2}{\partial t} \rangle / \langle p_1 \rangle$ as done in [6].

In general, a 2×2 resistance matrix can be defined in the linear response regime (i.e. small electric fields) between the voltages V_i and the currents I_i in the two subsystems:

$$\begin{pmatrix} V_1 \\ V_2 \end{pmatrix} = \begin{pmatrix} R_{11} & R_{12} \\ R_{21} & R_{22} \end{pmatrix} \begin{pmatrix} I_1 \\ I_2 \end{pmatrix}. \tag{1.2}$$

Here $R_{21} = R_{12}$ due to the Onsager relations, which are symmetry relations for coupled transport phenomena [7, p. 60]. Equivalently one can define a resistivity matrix coupling the systems through:

$$\begin{pmatrix} \boldsymbol{E}_1 \\ \boldsymbol{E}_2 \end{pmatrix} = \begin{pmatrix} \boldsymbol{\rho}_{11} & \boldsymbol{\rho}_{12} \\ \boldsymbol{\rho}_{21} & \boldsymbol{\rho}_{22} \end{pmatrix} \begin{pmatrix} \boldsymbol{J}_1 \\ \boldsymbol{J}_2 \end{pmatrix}, \tag{1.3}$$

where in general the electric fields $\mathbf{E}_i$ and current densities $\boldsymbol{J}_i$ are vectors and the resistivities $\boldsymbol{\rho}_{ij}$ are tensors (with e.g. cartesian components). In this thesis the current densities and electric fields are one dimensional so the resistivities are numbers.

An expression for the transresistivity ρ_{21} is derived in chapter 3 and it of course depends on the inter particle interaction explicitly, since the phenomenon is due to this interaction. This makes Coulomb drag especially interesting since the resistance (in a two-probe measurement) for many other systems such as

[2] If the second derivative of the energy with respect to the wave vector is non zero, then the effective mass m is well defined, since $\frac{1}{m} = \frac{1}{\hbar^2} \frac{\mathrm{d}^2 \varepsilon}{\mathrm{d}k^2}$ in one dimension [5, p. 210]. This is the case for e.g. quadratic bands.

a metal do not strongly depend on the particle-particle interaction. Physically this is due to momentum conservation in the carrier-carrier collisions, so the total momentum of the current is not affected by the interactions[3]. So Coulomb drag is a unique transport measurement of the carrier-carrier interactions, which depends crucially on many-body effects such as screening.

Coulomb drag might even be technologically important in the future as electrical components and circuits on chips become closer packed in the never ending desire to make smaller devices.

1.3 What is a Carbon nanotube?

In 1985 Smalley's group [9] discovered[4] the so called C_{60} molecule or Bucky-ball, which is a hollow spherical molecule with carbon atoms on the surface packed in a structure like a football, i.e. with 12 pentagons and 20 hexagons. They thereby added a third kind of crystal structure for carbon besides the two already known forms: Graphite and diamond[5].

In 1991 Iijima [10] found jet another but analogous kind of crystal structure for carbon: *The carbon nanotube*. A carbon nanotube is basically a sheet of graphite folded into a tube of diameter from about 1nm and length normally[6] ranging to a few μm. Depending on how the graphite sheet is folded the carbon nanotube can be either metallic or semiconducting[7]. Experimentally, carbon nanotubes are often produced wriggled into each other like a rope (called nanotube ropes) or are coaxial inside each other, called a *multiwall carbon nanotube*. A multiwall carbon nanotube can contain several coaxial (single wall) carbon nanotubes and to our best knowledge there is no correlation between weather the different layers (tubes) are semiconducting or metallic. On figure 1.2(a) a multiwall carbon nanotube with only two walls is shown. Electronic transport in nanotubes has been observed experimentally both in the ballistic and diffusive regime (see section 2.3). More details of carbon nanotubes will be given later in chapter 2.

[3]This can be made explicit see e.g. [8, p.131]. Note further that Umklapp processes can give some small resistance from the inter particle interaction, since these are not momentum conserving (in the strict sense).

[4]For this discovery R. E. Crul Jr., H. W. Kroto and R. E. Smalley were awarded the Nobel price in chemistry in 1996.

[5]It is interesting to note that these have very different properties stemming only from there crystal structure. Graphite is soft, black and a semimetal [1, p. 304] whereas diamond is a very hard, transparent and an insulator.

[6]There has been reports on extremely long carbon nanotube yarns up to 30cm [11], i.e. not single molecules.

[7]Recently it has been possible experimentally to separate metallic and semiconducting single wall nanotube [12].

1.3.1 Luttinger liquid contra Fermi liquid for a carbon nanotube

The conduction electrons on a metallic single wall carbon nanotube are confined to move in one dimension along the tube and as we shall see in chapter 2 the energy bands near the Fermi level are very close to being linear. This and the one dimensional nature of nanotubes have led people to consider carbon nanotubes as so-called Luttinger liquids (see e.g. [13, 14, 15, 16]). A Luttinger liquid is a strictly one dimensional interacting electron gas, where there are only collective low energy excitations (plasmons) instead of single particle excitations as in a Fermi liquid (such as an interacting electron gas in two and three dimensions)[8]. The stability of Luttinger liquid behavior crucially depends on the one dimensional nature of the theory and there is still much debate if carbon nanotubes are really Luttinger Liquids or Fermi Liquids (see e.g. [21] and ref. therein). In multiwall carbon nanotubes the case is even more uncertain since inter wall coupling and Coulomb screening between the walls tend to break down the Luttinger Liquid effects. Some experiments show Luttinger Liquid effects in multiwall nanotubes (such as power laws) and some can be understood by Fermi liquid theory [22]. A recent experiment indicates that doped multiwall nanotubes are not Luttinger Liquids [23]. So it is an important question to answer if multiwall carbon nanotubes and nanotubes in general are Luttinger Liquids or Fermi Liquids or a crossover as some studies suggest [24].

We work within the Fermi Liquid picture throughout this thesis. It could of course be very interesting to develop a theory for the Coulomb drag in multiwall carbon nanotubes for a Luttinger Liquid and then compare the two fundamentally different theories with experiments. This would be a step on the way to understanding if multiwall carbon nanotubes are really Luttinger liquids or not. Therefore we provide a benchmark for experiments.

1.4 The merging of the Coulomb drag and multiwall carbon nanotubes

In this thesis, we will merge the concepts of multiwall carbon nanotubes and Coulomb drag by letting the two subsystems in the drag setup be an inner and an outer nanotube in a multiwall nanotube as sketched on figure 1.2(b). So we imagine sending a current through an outer (inner) tube and find the voltage drop this induces on an inner (outer) tube by the Coulomb drag. In other words

[8] For a short qualitative overview of the break down of Fermi Liquid theory in one dimension and the emerge of Luttinger Liquid theory, see [17] or the new edition of [18, chap.19]. For a longer more detailed review see [19]. A self contained review of some of the Luttinger liquid effects in single wall metallic nanotubes is found in [20].

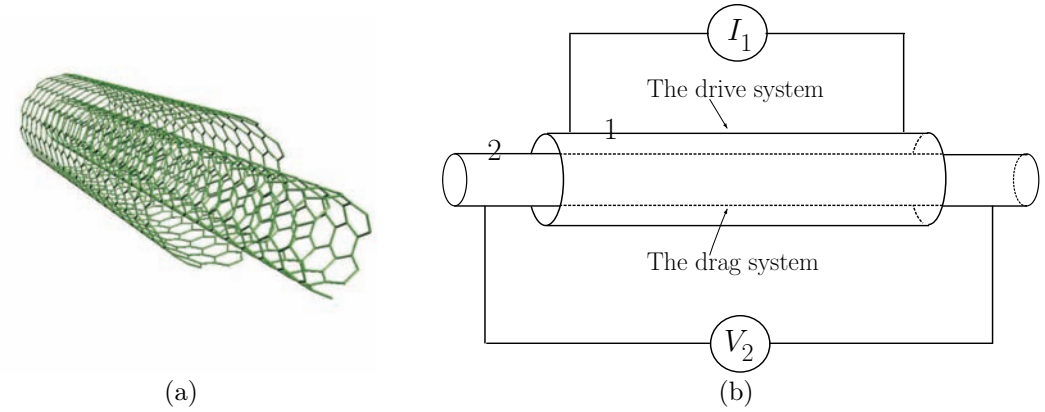

Figure 1.2: (a) Two coaxial single wall carbon nanotubes forming a double wall carbon nanotube, i.e. an example of a multiwall carbon nanotube. Both of these nanotubes are so-called armchair nanotubes (as will be explained in chapter 2) and are metallic. (b) The experimental setup to measure Coulomb drag in multiwall carbon nanotubes. For this to be possible experimentally independent contacts are needed on an inner and an outer nanotube after the removal of one or more of the outer shells in a multiwall carbon nanotube.

we want to calculate the intershell resistance originating from the Coulomb interaction of the carriers in the two shells.

To do this experimentally one needs to remove parts of the outer shell(s) in a controlled way in order to make independent contacts on an inner and an outer nanotube. The shell removal has already been done several times experimentally [25, 26, 27], but to our knowledge no one has yet made the independent contacts needed to perform the experiment. Experiments are currently being done at the Copenhagen University by Birte Rasmussen and Jesper Nygård.

Furthermore, since we work in the Coulomb drag regime, we neglect tunnelling between neighboring tubes in the multiwall nanotube. There is indirect experimental evidence that this is a good approximation. Firstly studies on graphite (which also has a layered structure) show that there is a difference of two orders of magnitude between the resistance across and along the layers of graphite sheets [28]. Another experiment on Aharonov-Bohm oscillations [18, p. 270] in multiwall carbon nanotubes suggests that only the outermost tube carries the current, i.e. the current is not distributed across the shells in a multiwall nanotube[29][9]. Furthermore Cumings and Zettl performed an experiment, where they pulled some inner shells out of a multiwall nanotube after opening the end of the multiwall tube [31]. So there is some evidence that the shells are weakly bound only by van der Waals forces and that it is reasonable to neglect the intershell tunnelling. Nevertheless it could be interesting to include weak tunnelling

[9]The same conclusion was found in [30].

and to see the effect of it on the transresistivity.

1.4.1 Other work on the intershell resistance and Coulomb drag in nanotubes

Previous works on carbon nanotubes and Coulomb drag have been done. As an example crossed single wall carbon nanotubes junctions has been studied both experimentally [32][33, chap.3] and theoretically using Luttinger liquid theory [34, 35][10]. Here the single wall nanotubes interact only at a single point.

Coulomb drag between parallel single wall nanotubes has also been considered in [37] and between one dimensional quantum wires (not with an emphasis on nanotubes) has also been investigated in the ballistic regime, using both Luttinger and Fermi liquid theory [38, 39]. Also, the diffusive one dimensional regime has been considered [40].

There has also been some effort to calculate the intershell resistance in multiwall tubes as we will now describe. In both [41] and [42] density functional theory in the ballistic regime were used.

In [42], a multiwall nanotube gently being pulled out of a liquid metal is modelled to find an explanation of the experimental results [30], where ballistic transport in multiwall nanotubes with unexpected prefactors of the conductance quantum $\frac{e^2}{h}$ were observed. The possible explanation of this effect is a blocking of conductance channels due to inter wall interaction and a redistribution of the current in the other layers (i.e. other than the outer one) [42]. Another explanation of this experiment is an effect of the contacts [43], since the nanotube in the liquid metal will be doped and thereby has a shifted Fermi level, which affects the transmission across the contact-tube interface.

In [41], a double wall nanotube of two concentric metallic (so called armchair) nanotubes are modelled. Here the conductance steps are found not to change dramatically if the inter tube interaction is included (see figure 3 in [41]). The method used to model the inter wall interaction is a tight binding approximation (i.e. Hückel theory), which is very different from our way of modelling, since it includes tunnelling as the only mechanism. Also [42] uses tunnelling as the only mechanism.

Another theoretical study of the conductance of a multiwall nanotube is done by S. Roche et. al. in [44, 45]. Here, the time evolution of a wave packet initially on the outer shell is considered. The wave packet redistribute itself across the multiwall structure in the presence of tunnelling between the layers, which is modelled be solving the time dependent Schrödinger equation numerically. The result of the simulations are that defect-free incommensurate nanotubes (i.e. aperiodic) can be diffusive in the sense of having finite localization length. Furthermore, the

[10] Another study of crossed Luttinger liquids is found in [36], but it is not focussed on nanotubes.

conductance is found to be a power law of the temperature below 1K. The tunnelling between the layers used in this work is 1/8 of the tunnelling between the atoms in the same layer and is furthermore suppressed by an exponential factor with the intershell distance in the exponent. Tunnelling of this magnitude is inspired by density functional calculations [46].

In the present work we find the intershell resistance (transresistivity) in the diffusive limit from the Coulomb interaction between the carriers in the different shells and neglect the tunnelling between different shells completely.

1.5 Coulomb drag in coupled two dimensional electron gases

Coulomb drag has previously been investigated intensively both experimentally and theoretically for two parallel two dimensional electron systems. Here we will give a very short introduction, for a further review see [47].

1.5.1 The low temperature regime: Coulomb and phonon mediated drag

The first experiments done by T. J. Gramila et. al. [48] for semiconductor hetero structures began the intense activity in the field of Coulomb drag between parallel planar systems. They fabricated two separated GaAs/AlGaAs quantum wells and made independent contacts to them. The measurements of the transresistivity were done in a temperature interval from about 0.5K to 7K compared to a Fermi temperature at $T_{\mathrm{F}} = 62\mathrm{K}$ and a separation[11] d between (the center of) the quantum wells of 37.5nm and 42.5nm. They found theoretically a temperature dependence of the transresistivity at low temperatures, $\rho_{21} \propto T^2$, by coupling two Boltzmann equations – one for each layer. Their experiment was only in qualitative agreement with this result. The measurements as seen on figure 1.3(a) shows a small peak instead of a straight line in the transresistivity over temperature squared, $\frac{\rho_{21}}{T^2}$, as a function of temperature. In figure 1.3 the rate of momentum transfer τ_{21}^{-1} is used instead of ρ_{21}, remembering eq.(1.1) in the case of quadratic bands: $\rho_{21} = \frac{m_1}{n_1 \tilde{e}_1 \tilde{e}_2 \tau_{21}}$.

To explain the results better Jauho and Smith [6] calculated the transresistivity in great detail also by coupled Boltzmann equations. This was done in the case of a Thomas-Fermi screened Coulomb interaction and one quadratic band in each of the two quantum wells. This gave them a transresistivity for two identical

[11] This separation is about an order of magnitude larger than in multiwall nanotubes. So for the assumption of no tunnelling between the shells in a multiwall nanotube to be acceptable, the tunnelling barrier has to be significantly higher than in semiconductor structures.

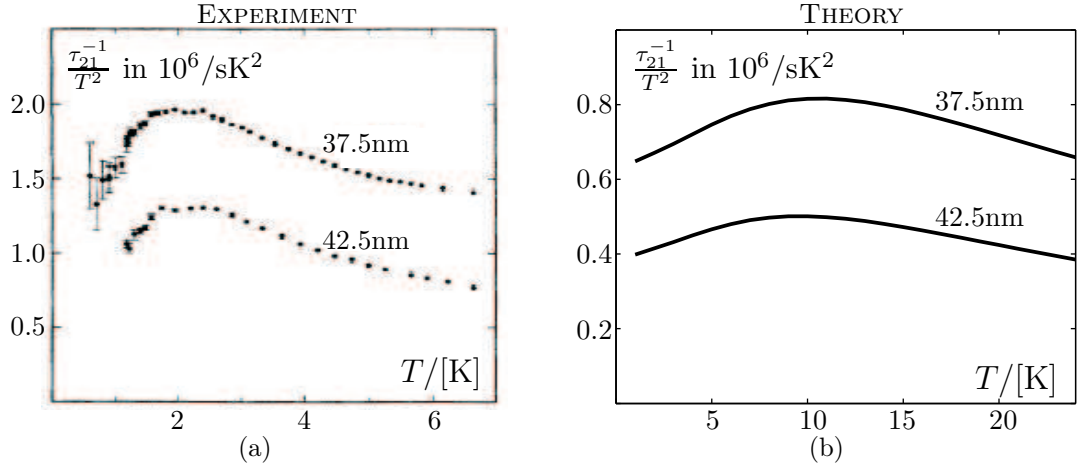

Figure 1.3: (a) The first measurements done by Gramila et. al. [48] on the momentum transfer rate between two parallel quantum wells in a semiconductor heterostructure. The peak at about 2K is explained by a combination of Coulomb and phonon mediated drag. (b) A reproduction of the numerical integration of eq.(1.4) first done by Jauho and Smith in [6]. Both figures shows the momentum transfer rate τ_{21}^{-1}, which has the connection to the transresistivity as $\rho_{21} = \frac{m}{ne^2\tau_{21}}$ in the case of quadratic bands and identical wells.

two dimensional electron gasses as [6]:

$$\rho_{21} = \frac{\hbar^2}{2\pi^2 n^2 e^2 k_{\mathrm{B}} T} \int_0^\infty \mathrm{d}q \int_0^\infty \mathrm{d}\omega \; q^3 \frac{|e\phi(q)|^2 \big(\mathrm{Im}\chi(q,\omega)\big)^2}{\sinh^2\left(\frac{\hbar\omega}{2k_{\mathrm{B}}T}\right)}, \tag{1.4}$$

where n is the carrier density in each of the layers, $\mathrm{Im}\chi(q,\omega)$ is the imaginary part of the polarizability[12], $e\phi(q)$ is the screened (Fourier transformed) Coulomb interaction in the Thomas-Fermi approximation and $\hbar q$ and $\hbar\omega$ are the transferred momentum and energy in the interaction process, respectively. We will later in chapter 3 generalize this formula to the case of more bands of some general form and cylindrical geometry. At low temperatures $\mathrm{Im}\chi$ can be approximated by the small q and ω limit as $\mathrm{Im}\chi(q,\omega) \simeq \frac{m^2\omega}{2\pi\hbar^3 q k_{\mathrm{F}}}$ and the transresistivity in eq.(1.4) can be calculated analytically to be [6]:

$$\rho_{21} = \frac{\hbar\pi^2\zeta(3)}{16e^2\varepsilon_{\mathrm{F}}^2} \frac{(k_{\mathrm{B}}T)^2}{(k_{\mathrm{F}}d)^2(q_{\mathrm{TF}}d)^2} \propto \frac{T^2}{d^4}, \tag{1.5}$$

where q_{TF} is the Thomas-Fermi screening vector, k_{F} the Fermi wave vector, ε_{F} the Fermi energy and $\zeta(3)$ the Riemann Zeta function of three[13]. This was the

[12]The general linear response function between some induced charge ρ_{ind} and an external field ϕ_{ext}: $\rho_{\mathrm{ind}} = \chi\phi_{\mathrm{ext}}$ in Fourier space [18, p. 105].

[13]Generally it is: $\zeta(x) = \sum_{n=1}^{\infty} \frac{1}{n^x}$. For $x \leq 1$ one has to use the analytical continued version of the Riemann zeta function in order not to have a divergence.

result previously obtained by Gramila et.al. [48] (apart from a factor of two).

Instead of using this low temperature limit Jauho and Smith made a numerical integration of the double integral in eq.(1.4). We have reproduced their result and obtained the same result by a numerical integration (in Matlab), which is seen on figure 1.3(b). In calculating these curves, the zero temperature imaginary part of the polarizability is used, since we are still well below the Fermi temperature $T_{\mathrm{F}} = 62\mathrm{K}$. The Thomas-Fermi screened potential is calculated self-consistently by the Poisson equation for finite width quantum wells (see [6] for further details). The interaction $e\phi(q)$ decreases with increasing q and $\sinh^{-2}\left(\frac{\hbar\omega}{2k_{\mathrm{B}}T}\right)$ decreases with increasing ω which makes the integrand most important for small q and ω. Therefore the dominating process is the single particle electron-hole excitation around the Fermi surface. Note that we have no parameters to fit the curves.

By comparing the theoretical and the experimental curves on figure 1.3, a notable difference is observed. Firstly the peak in the measurements at about 2K is not as broad as the theoretical peaks at about 10K, i.e. from zero to 6K the theory just gives a straight increasing line where there should be a peak. Secondly, the measured transresistivity is about a factor of two higher than the calculated one. Therefore the direct Coulomb interaction is not sufficient to explain the measurements alone. By taking both the Coulomb and phonon mediated interaction into account the curves can be understood also quantitatively [49]. It turns out that for large inter layer separation the phonon contribution becomes more important, which both theory [49] and experiment [50] shows. The theory has only one free parameter, which is the phonon mean free path, but it can account for both the temperature, density and inter layer separation dependence of the transresistivity.

1.5.2 The high temperature regime: Plasmon enhanced drag

At higher temperatures, a better model for the interaction has to be considered to capture the essential physics of the Coulomb drag. This is the random phase approximation (RPA) instead of the Thomas-Fermi approximation and in the RPA the interaction becomes dependent on the transferred energy $\hbar\omega$ and the temperature. So in the transresistivity formula (1.4) the interchange

$$e\phi(q) \to \frac{V_{12}(q)}{\epsilon(q,\omega)} \tag{1.6}$$

is made, where $V_{12}(q)$ is the (Fourier transform of the) bare Coulomb interaction between the layers and $\epsilon(q,\omega)$ is the dielectric function:

$$\begin{aligned}\epsilon(q,\omega) =& \big(1 - V_{11}(q)\chi_1(q,\omega)\big)\big(1 - V_{22}(q)\chi_2(q,\omega)\big) \\ &- \big(V_{12}(q)\big)^2\chi_1(q,\omega)\chi_2(q,\omega).\end{aligned} \tag{1.7}$$

Here $V_{ii}(q)$ is the intralayer Coulomb interaction (i.e. a two dimensional Coulomb interaction) and $\chi_i(q,\omega)$ is the polarizability for layer i.

For zero temperature the plasmon dispersion relations $\omega(q)$ are found by setting the dielectric function equal to zero, $\epsilon(q,\omega(q)) = 0$ [18, p. 210]. At such plasmon frequencies the screened RPA potential (1.6) would diverge and hence give a large (in principle infinite) contribution to the transresistivity in eq.(1.4) and this is the idea of the plasmon enhanced Coulomb drag as first discovered theoretically by Flensberg and Hu in [51, 52]. Of course a zero temperature plasmon does not give an enhancement as a function of temperature. For finite temperature the plasmon modes are obtained by solving $\mathrm{Re}\big[\epsilon(q,\omega(q))\big] = 0$ and thereby one can have an enhanced electron interaction, but still finite –and a finite drag– due to the imaginary part of the dielectric function. Calculating the temperature dependent polarizability cannot be done analytically and a numerical evaluation of

$$\chi(q,\omega) = -\int \frac{\mathrm{d}\mathbf{k}}{(2\pi)^2} \frac{f^0(\varepsilon_{\mathbf{k}}) - f^0(\varepsilon_{\mathbf{k}+\mathbf{q}})}{\varepsilon_{\mathbf{k}} - \varepsilon_{\mathbf{k}+\mathbf{q}} - \hbar\omega + i\delta} \tag{1.8}$$

is needed [52]. Here $f^0(\varepsilon)$ is the Fermi function of the quadratic energy band $\varepsilon_{\mathbf{k}} = \frac{\hbar^2\mathbf{k}^2}{2m}$ and δ is a positive infinitesimal.

A numerical calculation shows that a large enhancement of ρ_{21}/T^2 appears at about $T \simeq 0.2T_\mathrm{F}$ and peaks at $T \simeq 0.5T_\mathrm{F}$ [52]. This is large compared to the small peak seen at low temperatures (in figure 1.3(a)). Furthermore for large temperatures, the plasmon enhancement gives $\rho_{21} \propto d^{-3}$ instead of the low temperature result (1.5). The theoretical prediction (with no free parameters) was later confirmed experimentally by Hill et. al. [53].

So Coulomb drag probes both single particle excitations at low temperatures ($T \ll T_\mathrm{F}$) and collective excitations, plasmons, at higher temperature ($T \sim 0.5T_\mathrm{F}$). This is rare and exciting for a transport measurement, which normally do not capture interparticle interactions as discussed above.

1.5.3 Other extensions

Much more can be said about the field of Coulomb drag and inter layer interaction for two parallel two dimensional electron gases (see e.g. [39, chapter 1]).

One of the exciting new phenomena is the Bose-Einstein condensation of electron-hole pairs (excitons) in double quantum wells (see e.g. [54] and reference therein). One of the tricks here is to have a hole in one quantum well and an electron in the other well, so that they are spatially separated and thereby cannot recombine with each other. This is considered both experimentally and theoretically [55].

Another exciting area is the Coulomb drag in mesoscopic systems, i.e. on the borderline between the macroscopic and the atomic scale, where the translational symmetry is broken and the dimensions can be smaller than the phase-breaking

length. One of the theoretical predictions is that there should be a large sample to sample variation in the mesoscopic fluctuations which can even exceed the mean value of the transresistivity [56, 57, 39].

Chapter 2

Elements of carbon nanotube physics

In this chapter, we introduce carbon nanotube properties relevant for the electronic transport in nanotubes such as the lattice structure, energy band structure, Bloch states and impurity scattering, needed to understand the Coulomb drag in multiwall nanotubes.

2.1 Crystal structure

A carbon nanotube can be viewed as a sheet of graphite folded into a cylinder. In order to understand carbon nanotubes, we therefore begin by describing the crystal structure of a graphite sheet (often called graphene).

2.1.1 A graphite sheet

Graphite is built up by weakly coupled layers separated by 0.335 nm [58]. Each layer consists of a hexagonal (honeycomb) lattice as seen on figure 2.1(a), where the distance between two neighboring carbon atoms is $a_{\text{C-C}} = 0.142$ nm. Due to the geometry of the hexagonal lattice it is necessary to have at least two atoms in each unit cell [1, p.75]. One choice of the Bravais lattice is spanned by the two non-orthogonal primitive vectors

$$\mathbf{a}_1 = \frac{a}{2}\begin{pmatrix}\sqrt{3}\\ -1\end{pmatrix} \quad \text{and} \quad \mathbf{a}_2 = \frac{a}{2}\begin{pmatrix}\sqrt{3}\\ 1\end{pmatrix}, \tag{2.1}$$

where $a \equiv |\mathbf{a}_1| = |\mathbf{a}_2| = \sqrt{3}a_{\text{C-C}}$ was introduced. Other conventions are also used in the literature [59, 60][1]. The two atoms in each unit cell are labelled by A

[1]Here $\mathbf{a}_1 = a(1,0)$ and $\mathbf{a}_2 = \frac{a}{2}(-1,\sqrt{3})$ given in a coordinate system rotated $\pi/4$ with respect to the system seen on figure 2.1(a) is used. This system has some advantages such as

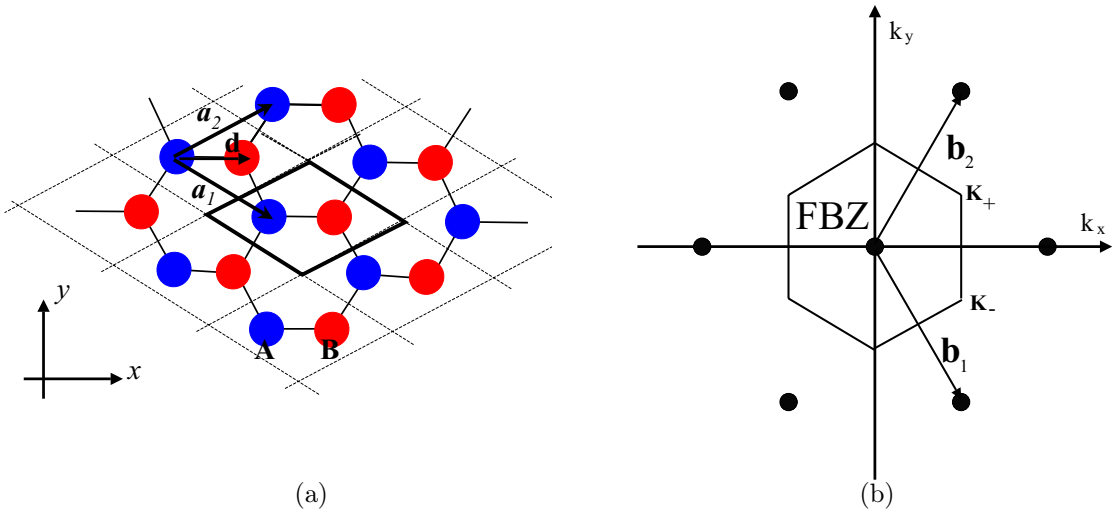

Figure 2.1: (a) The lattice of a graphite sheet, graphene, is seen to be spanned by the lattice vectors $\mathbf{a}_1$ and $\mathbf{a}_2$. The unit cell is marked by the thick parallelogram and it contains two atoms A and B connected by $\mathbf{d} = \frac{1}{3}(\mathbf{a}_1 + \mathbf{a}_2)$. (b) The first Brillouin zone (FBZ) of graphene and the reciprocal lattice vectors $\mathbf{b}_1$ and $\mathbf{b}_2$ are seen. The $\mathbf{K}_\pm = \frac{2\pi}{a}(\frac{1}{\sqrt{3}}, \pm\frac{1}{3})$ are also shown for later reference.(Note that the other corners of the FBZ are equivalent to $\mathbf{K}_\pm$, since they are connected by reciprocal lattice vectors.)

and B, respectively, and graphene can therefore be described by two equivalent sublattices with A and B atoms at $\mathbf{R}_A = n_1\mathbf{a}_1 + n_2\mathbf{a}_2$ and $\mathbf{R}_B = n_1\mathbf{a}_1 + n_2\mathbf{a}_2 + \mathbf{d}$ $(n_1, n_2 \in \mathbb{Z})$, respectively, where $\mathbf{d} = \frac{1}{3}(\mathbf{a}_1 + \mathbf{a}_2) = (a_{\text{C-C}}, 0)$ connects the two atoms in the unit cell (see figure 2.1(a)).

The reciprocal space is spanned by

$$\mathbf{b}_1 = \frac{2\pi}{a}\begin{pmatrix} \frac{1}{\sqrt{3}} \\ -1 \end{pmatrix} \quad \text{and} \quad \mathbf{b}_2 = \frac{2\pi}{a}\begin{pmatrix} \frac{1}{\sqrt{3}} \\ 1 \end{pmatrix}, \tag{2.2}$$

which are found from the definition of the reciprocal lattice: $\mathbf{a}_i \cdot \mathbf{b}_j = 2\pi\delta_{i,j}$ [1, p.87]. The First Brillouin Zone (FBZ) is the Wigner-Seitz unit cell in the reciprocal lattice, i.e. its boundaries are found by making perpendicular cuts halfway between each neighboring lattice point as seen on figure 2.1(b).

2.1.2 A carbon nanotube

To construct the lattice of a single wall carbon nanotube a sheet of graphite is folded into a cylinder. Or to put it mathematically: a conformal mapping (i.e.

a simpler way to describe the electronic structure even though it is less symmetric and not as widely used as the one stated in the text.

an angle conserving mapping) from a plane of graphene to a cylinder is made. This can be done in many ways and the particular way determines the properties of the nanotube, e.g. if it is metallic or semiconducting, as we shall see below. To distinguish differently folded carbon nanotubes the *Chiral vector* $\mathbf{C}$ is defined as

$$\mathbf{C} = n\mathbf{a}_1 + m\mathbf{a}_2, \tag{2.3}$$

where $n, m \in \mathbb{Z}$ and $0 \leq |n| \leq m$ is chosen to avoid degeneracy [61]. The Chiral vector connects the two sides which are folded together and it thereby becomes the circumference of the nanotube as seen on figure 2.2. Therefore the crystal structure of a single wall carbon nanotube is specified by indices (n, m) from eq.(2.3). Nanotubes are conventionally divided into three categories: The armchair (n, n) tubes, the zigzag $(n, 0)$ tubes[2] and the rest are called chiral nanotubes. Geometrical properties of a nanotube can found in terms of the indices (n, m) such as the diameter:

$$D = \frac{|\mathbf{C}|}{\pi} = \frac{a\sqrt{n^2 + m^2 + mn}}{\pi}, \tag{2.4}$$

where the relations $\mathbf{a}_2 \cdot \mathbf{a}_1 = \frac{a^2}{2}$ and $|\mathbf{a}_2|^2 = |\mathbf{a}_1|^2 = a^2$ were used.

The primitive unit cell

We now consider the primitive (i.e. the minimum) unit cell of a carbon nanotube. The nanotube crystal lattice can be seen as built up by two discrete symmetries: A helical and a rotational symmetry. A helical symmetry operation $\mathcal{S}(h, \varphi)$ consists of a screw operation around the nanotube axis, i.e. combining a rotation of angle φ around the tube axis with a translation of length h along the tube. This makes a spiral of atoms. The rotational symmetry operation $\mathcal{C}_\mathfrak{n}$ rotates the lattice around the nanotube axis by an angle of $\frac{2\pi}{\mathfrak{n}}$. By combining these two symmetries the nanotube lattice structure can be constructed from a unit cell of only two atoms as in the case of graphene [62, 61].

To specify the helical symmetry operation $\mathcal{S}(h, \varphi)$ as in [62] we introduce the lattice vector $\mathbf{H} = p_1\mathbf{a}_1 + p_2\mathbf{a}_2$, which (after the conformal mapping) will generate the helical symmetry. To find $p_1, p_2 \in \mathbb{Z}$ we give the helical variables in terms of the generating vector $\mathbf{H}$:

$$h = \frac{|\mathbf{H} \times \mathbf{C}|}{|\mathbf{C}|} \qquad \text{and} \qquad \varphi = \frac{2\pi}{|\mathbf{C}|}\mathbf{H} \cdot \frac{\mathbf{C}}{|\mathbf{C}|}, \tag{2.5}$$

which can be seen by geometrical considerations[3]. To chose $\mathbf{H}$ we want h and $|\mathbf{H}|$ to be as small as possible (or equivalently h and φ), so that the helical symmetry

[2]Zigzag tubes have a zigzag pattern around the circumferential and some see an "armchair" pattern around an armchair nanotube [63].

[3]When doing the cross products one has to enlarge the vectors to three dimensions e.g. by adding a zero third component (i.e. $\mathbf{a}_1 = \frac{a}{2}(\sqrt{3}, -1) \to \mathbf{a}_1 = \frac{a}{2}(\sqrt{3}, -1, 0)$), since cross products strictly only makes sense for three dimensional vectors.

operation can generate as much of the tube as possible (i.e. making spirals with the shortest possible translation and rotation). So $|\mathbf{H}\times\mathbf{C}| = |p_1 m - p_2 n||\mathbf{a}_2\times\mathbf{a}_1|$ should be as small as possible but nonzero. Therefore the integers p_1 and p_2 should be chosen as the smallest pair of integers (in the sense of minimizing $|\mathbf{H}| = a\sqrt{p_1^2+p_2^2+p_1p_2}$), fulfilling[4]

$$p_1 m - p_2 n = \gcd(n,m) \equiv \mathfrak{n}, \tag{2.6}$$

where $\gcd(\cdot,\cdot)$ is the greatest common divisor of the two integers. We can now identify the helical symmetry for a given nanotube (n,m). An example of $\mathbf{H}$ is seen on figure 2.2.

The rotational symmetry operation $\mathcal{C}_\mathfrak{n}$ is generated (after the conformal mapping) by the smallest lattice vector proportional to $\mathbf{C}$, which leaves the lattice invariant [61]. This is seen to be

$$\mathbf{C}_\mathfrak{n} = \frac{\mathbf{C}}{\mathfrak{n}} = \frac{n}{\mathfrak{n}}\mathbf{a}_1 + \frac{m}{\mathfrak{n}}\mathbf{a}_2, \tag{2.7}$$

where $\mathfrak{n} = \gcd(n,m)$. There is no smaller lattice vector proportional to $\mathbf{C}$, since $\gcd(\frac{n}{\mathfrak{n}},\frac{m}{\mathfrak{n}}) = 1$. The smallest rotation leaving a (n,m) nanotube invariant is therefore $\frac{2\pi}{\mathfrak{n}}$.

So by combining these two symmetries any tube can be generated from a two atomic unit cell and a conformal mapping (see figure 2.2 for an example). Alternatively one can chose a unit cell consisting of all the $2\mathfrak{n}$ atoms generated by the rotation and only use the helical symmetry to generated the tube from a unit cell of $2\mathfrak{n}$ atoms [62, 61].

The translational unit cell

Any nanotube also has translational symmetry along the tube and therefore it is also possible to introduce a larger unit cell, which we will refer to as the translational unit cell. This is often the unit cell used [58], even though it contains a much larger number of atoms than two, i.e. it is *not* the primitive unit cell. The translational symmetry can be generated by a lattice vector along the tube (commonly called the translational vector [58]) $\mathbf{T} = t_1\mathbf{a}_1 + t_2\mathbf{a}_2$, which is defined as the smallest possible lattice vector (of graphene) perpendicular to $\mathbf{C}$. By using $\mathbf{a}_i\cdot\mathbf{a}_j = a^2\delta_{i,j} + \frac{a^2}{2}(1-\delta_{i,j})$ one has $0 = \mathbf{C}\cdot\mathbf{T} = \frac{a^2}{2}\big(t_1(2n+m) + t_2(2m+n)\big)$ and since $t_1, t_2 \in \mathbb{Z}$ should be as small (in absolute value) as possible, the translation vector is:

$$\mathbf{T} = \frac{2m+n}{\gcd(2m+n,2n+m)}\mathbf{a}_1 - \frac{2n+m}{\gcd(2m+n,2n+m)}\mathbf{a}_2, \tag{2.8}$$

[4]This can be proven by number theoretical arguments and we chose the positive solution ($p_1 m - p_2 n = \pm\gcd(n,m)$) corresponding to right-handed helixes, see [62] for details.

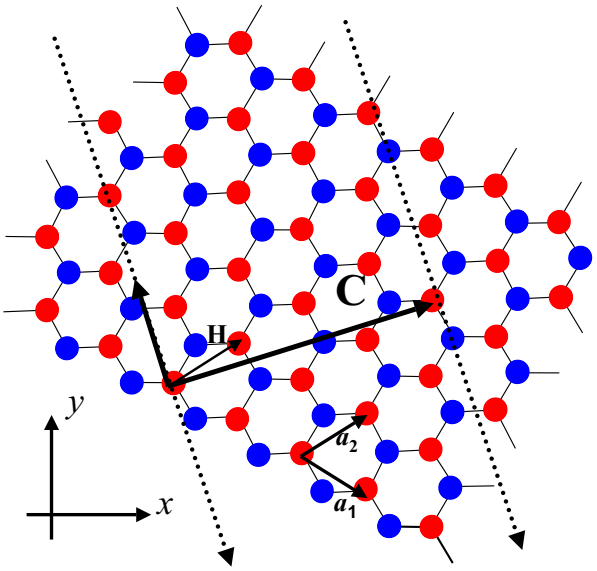

Figure 2.2: A carbon nanotube is made by folding the graphite sheet into a tube by connecting the two dotted lines. The specific example shown is a $(1,3)$ tube, i.e. $\mathbf{C} = \mathbf{a}_1 + 3\mathbf{a}_2$ becomes the circumferential. The translation vector is $\mathbf{T} = 7\mathbf{a}_1 - 5\mathbf{a}_2$ along the tube (the direction, *not* the length, is shown by the vector perpendicular to $\mathbf{C}$). The vector generating the helical symmetry is $\mathbf{H} = \mathbf{a}_2$, which is seen to generate the entire nanotube, since $\mathfrak{n} = 1$ so only a 2π rotation leaves the lattice invariant. Note that the length of $\mathbf{T}$ compared to e.g. $\mathbf{a}_i$ makes the translational unit cell of the tube contain a large number of atoms ($2\mathcal{N} = 52$) compared to the graphene unit cell of two atoms.

where t_1 and t_2 can be read off.

The basis of the reciprocal space from the translational unit cell of the nanotube can be found as for graphene through the relation $\mathbf{G_A} \cdot \mathbf{B} = 2\pi\delta_{\mathbf{A},\mathbf{B}}$, where $\mathbf{A}$ and $\mathbf{B}$ are either $\mathbf{C}$ or $\mathbf{T}$. This gives:

$$\mathbf{G_C} = \frac{1}{\mathcal{N}}(-t_2\mathbf{b}_1 + t_1\mathbf{b}_2) \quad \text{and} \quad \mathbf{G_T} = \frac{1}{\mathcal{N}}(m\mathbf{b}_1 - n\mathbf{b}_2), \tag{2.9}$$

where $\mathcal{N}$ turns out to be the number of graphene unit cells in the translational unit cell [58, chap.3], given by[5]

$$\mathcal{N} = \frac{|\mathbf{C} \times \mathbf{T}|}{|\mathbf{a}_1 \times \mathbf{a}_2|} = \frac{2(m^2 + n^2 + nm)}{\gcd(2m + n, 2n + m)}. \tag{2.10}$$

So the translational unit cell contains $2\mathcal{N}$ atoms, which is much larger than the two (or $2\mathfrak{n}$) atoms in the unit cell for the combined helical and rotational symmetry (or the helical symmetry only). We shall see in section 2.2.2 that the direction $\mathbf{G_C}$ is quantized (into a few values), giving rise to a one dimensional band structure.

2.2 Energy band structure

We obtain the band structure, i.e. the eigenenergies and energy eigenfunctions of a single wall carbon nanotube, in two ways: By using periodic boundary

[5]The size of the cross product gives the area spanned by the two vectors.

conditions for the band structure of graphene as in [60, 64] and directly from the helical and rotational symmetries as in [62]. The two ways of obtaining the band structure are compared and shown to give the same energy bands, but with a different numbering scheme.

2.2.1 Band structure of a graphite sheet

A free carbon atom has six electrons: two very strongly bound in the lower energy $1s$ orbital[6] and four in the energy degenerate $2s$, $2p_x$, $2p_y$ and $2p_z$ orbitals. In graphene the orbitals $2s$, $2p_x$ and $2p_y$ are combined in three new linear combinations to form the so-called sp^2 orbitals. These orbitals are in the same plane and make the strong chemical bonds to the three other carbon atoms in graphene (pictured as "black sticks" in figure 2.1(a)). These bonds take up three electrons, which are localized and bound. The last electron in the half filled $2p_z$ orbital can "hop" (i.e. tunnel) to the other $2p_z$ orbitals and thereby it is the only orbital contributing to electron transport in graphene. Furthermore the $2p_z$ orbital is orthogonal to the plane and has a node in the plane, so it does not have an overlap with the sp^2 orbitals [58]. Therefore we now make a tight binding model [1, chap.10] of graphene to find the band structure. This was first done by Wallace [65].

The model for the single electron Hamiltonian includes a kinetic part and the lattice potential from each atom in the unit cell of graphene,

$$H(\mathbf{r}) = H_{\text{kin}} + \sum_{\mathbf{R}_A} \big(\underbrace{V(\mathbf{r}-\mathbf{R}_A) + V(\mathbf{r}-\mathbf{R}_A-\mathbf{d})}_{\text{Atomic potentials}} \big), \tag{2.11}$$

which as usual leads to a Bloch function $\psi_{\mathbf{k}}(\mathbf{r})$, ($\mathbf{r} = (x, y)$ and $\mathbf{k} = (k_x, k_y)$) [1, chap.8]. Any Bloch function in a general monatomic Bravais lattice can be written as a sum of Wannier functions $f(\mathbf{r}-\mathbf{R})$ as $\psi_{\mathbf{k}}(\mathbf{r}) = \sum_{\mathbf{R}} e^{i\mathbf{R}\cdot\mathbf{k}} f(\mathbf{r}-\mathbf{R})$, which can be seen as a (non conventional) Fourier transformation for fixed $\mathbf{r}$. Here the Wannier functions (or Fourier coefficients) can be shown to have very similar properties to the atomic orbitals such as localization on the lattice points [1, p.187] and therefore $f(\mathbf{r}-\mathbf{R})$ is often replaced by the atomic orbital [58, 65, 66, 67]. Note that the Wannier form fulfills the Bloch theorem $\psi_{\mathbf{k}}(\mathbf{r}+\mathbf{R}) = e^{i\mathbf{k}\cdot\mathbf{R}}\psi_{\mathbf{k}}(\mathbf{r})$, shown by translating the lattice vectors in the sum.

As the Bloch state for the case with a two atomic unit cell as for graphene a

[6] Here an atomic state with unspecified spin is called an orbital, so there can be a maximum of two electrons in one orbital.

superposition of Wannier functions at sublattices A and B is made [1, p.185]:

$$\psi_{\mathbf{k}}(\mathbf{r}) = \frac{1}{\sqrt{N}} \sum_{\mathbf{R}_A} e^{i\mathbf{k}\cdot\mathbf{R}_A} \Big(\alpha\Psi(\mathbf{r}-\mathbf{R}_A) + \beta\Psi(\mathbf{r}-\mathbf{R}_A-\mathbf{d}) \Big) \tag{2.12}$$

$$= \alpha\frac{1}{\sqrt{N}} \sum_{\mathbf{R}_A} e^{i\mathbf{k}\cdot\mathbf{R}_A}\Psi(\mathbf{r}-\mathbf{R}_A) + \beta\frac{1}{\sqrt{N}} \sum_{\mathbf{R}_A} e^{i\mathbf{k}\cdot\mathbf{R}_A}\Psi(\mathbf{r}-\mathbf{R}_A-\mathbf{d})$$

$$\equiv \alpha\phi_{A,\mathbf{k}}(\mathbf{r}) + \beta\phi_{B,\mathbf{k}}(\mathbf{r}), \tag{2.13}$$

where $N \equiv \sum_{\mathbf{R}_A}$ is the number of unit cells in graphene, $\phi_{A/B,\mathbf{k}}$ are Wannier decompositions on each sublattice and α,β are to be determined by the following calculation. A priori the $\Psi(\mathbf{r})$ are Wannier functions, but we will approximate them by the $2p_z$ orbitals[7], which makes it possible for them to have an overlap[8] [1, p.188]. Here Ψ is normalized on each lattice point, $|\langle\Psi(\mathbf{r}-\mathbf{R}_i)|\Psi(\mathbf{r}-\mathbf{R}_i)\rangle|^2 = 1$, $(i = A, B)$, so $\phi_{A/B,\mathbf{k}}$ are normalized if the overlap between different sublattice points (on the same sublattice) is neglected. $\psi_{\mathbf{k}}(\mathbf{r})$ is only normalized if the overlap between the two sublattices are also zero, i.e. $\langle\Psi(\mathbf{r}-\mathbf{R}_A)|\Psi(\mathbf{r}-\mathbf{R}_B)\rangle = 0$ for all $\mathbf{R}_A, \mathbf{R}_B$, and $|\alpha|^2 + |\beta|^2 = 1$. Since the overlap is small $\psi_{\mathbf{k}}(\mathbf{r})$ is almost normalized, i.e. $|\langle\psi_{\mathbf{k}}|\psi_{\mathbf{k}}\rangle|^2 \simeq 1$.

The energy eigenvalues and eigenstates are found from the Schrödinger equation

$$H\psi_{\mathbf{k}}(\mathbf{r}) = \varepsilon_{\mathbf{k}}\psi_{\mathbf{k}}(\mathbf{r}), \tag{2.14}$$

by multiplying from the left with $\phi^*_{A,\mathbf{k}}$ and $\phi^*_{B,\mathbf{k}}$, respectively, and integrating over $\mathbf{r}$. Written in matrix form this is[9]:

$$\begin{pmatrix} H_{AA} & H_{AB} \\ H_{BA} & H_{BB} \end{pmatrix} \begin{pmatrix} \alpha \\ \beta \end{pmatrix} = \varepsilon_{\mathbf{k}} \begin{pmatrix} S_{AA} & S_{AB} \\ S_{BA} & S_{BB} \end{pmatrix} \begin{pmatrix} \alpha \\ \beta \end{pmatrix}, \tag{2.15}$$

where the matrix elements are $(i, j = A, B)$:

$$H_{ij} \equiv \int \mathrm{d}\mathbf{r}\phi^*_{i,\mathbf{k}}(\mathbf{r})H\phi_{j,\mathbf{k}}(\mathbf{r}), \tag{2.16}$$

$$S_{ij} \equiv \int \mathrm{d}\mathbf{r}\phi^*_{i,\mathbf{k}}(\mathbf{r})\phi_{j,\mathbf{k}}(\mathbf{r}). \tag{2.17}$$

To calculate these matrix elements, we assume that only the nearest neighbour

[7] In eq.(2.12) we see the reason why the tight binding method is often called the method of linear combination of atomic orbitals (LCAO), which is indeed what eq.(2.12) is.

[8] In the end of the calculation only matrix elements of H and inner products between these states are needed and these numbers are often found by fitting density functional theory calculation to tight binding calculations [68, 66], so the precise form of the Wannier functions (or $2p_z$ orbitals) are not used.

[9] Note that this is diagonal in $\mathbf{k}$ as can be seen in the element evaluation.

atoms contribute to the integrals[10], i.e.:

$$\int \mathrm{d}\mathbf{r}\Psi^*(\mathbf{r}-\mathbf{R}_i)H\Psi(\mathbf{r}-\mathbf{R}_j) = \begin{cases} \varepsilon_0 & \text{for} \quad |\mathbf{R}_i-\mathbf{R}_j| = 0 \\ -\gamma_0 & \text{for} \quad |\mathbf{R}_i-\mathbf{R}_j| = a_{\text{C-C}} \\ 0 & \text{for} \quad |\mathbf{R}_i-\mathbf{R}_j| > a_{\text{C-C}} \end{cases}, \tag{2.18}$$

$$\int \mathrm{d}\mathbf{r}\Psi^*(\mathbf{r}-\mathbf{R}_i)\Psi(\mathbf{r}-\mathbf{R}_j) = \begin{cases} 1 & \text{for} \quad |\mathbf{R}_i-\mathbf{R}_j| = 0 \\ s_0 & \text{for} \quad |\mathbf{R}_i-\mathbf{R}_j| = a_{\text{C-C}} \\ 0 & \text{for} \quad |\mathbf{R}_i-\mathbf{R}_j| > a_{\text{C-C}} \end{cases}, \tag{2.19}$$

where i and j are either A or B. Note that the nearest neighbour is always on the other sublattice. Here ε_0 is the energy of the atomic orbital $2p_z$, $\gamma_0 > 0$ is of order 3eV and $s_0 \sim 0.1$ [66, 69, 68, 58] found by fitting to density functional theory results. Similar numbers are found from experiments [70, 71][11]. Note that these parameters are chosen real. By using the nearest neighbour approximation we have $S_{AA} = S_{BB} = 1$ as required by the normalization condition and

$$H_{AA} = \frac{1}{N}\sum_{\mathbf{R}'_A,\mathbf{R}_A} e^{i\mathbf{k}\cdot(\mathbf{R}_A-\mathbf{R}'_A)} \int \mathrm{d}\mathbf{r}\Psi^*(\mathbf{r}-\mathbf{R}'_A)H\Psi(\mathbf{r}-\mathbf{R}_A) = \varepsilon_0 \tag{2.20}$$

equal to H_{BB}, since the two sublattices are equal (apart from a translation in space). Furthermore $H_{AB} = H^*_{BA}$ and by using eq.(2.18)

$$\begin{aligned} H_{AB} &= \frac{1}{N}\sum_{\mathbf{R}'_A}\sum_{\mathbf{R}_A} e^{i\mathbf{k}\cdot(\mathbf{R}'_A-\mathbf{R}_A)} \int \mathrm{d}\mathbf{r}\Psi^*(\mathbf{r}-\mathbf{R}_A)H\Psi(\mathbf{r}-\mathbf{R}'_A-\mathbf{d}) \\ &= \frac{1}{N}\sum_{\mathbf{R}'_A}\left(1+e^{-i\mathbf{k}\cdot\mathbf{a}_1}+e^{-i\mathbf{k}\cdot\mathbf{a}_2}\right)(-\gamma_0) \\ &= -\gamma_0\big(1+e^{-i\mathbf{k}\cdot\mathbf{a}_1}+e^{-i\mathbf{k}\cdot\mathbf{a}_2}\big) \\ &\equiv -\gamma_0\Upsilon(\mathbf{k}), \end{aligned} \tag{2.21}$$

where the $\mathbf{R}_A$ sum was done over the three nearest neighbours in the B sublattice, giving three terms all with the same matrix element $-\gamma_0$ due to symmetry. In the same way $S_{AB} = S^*_{BA}$ and $S_{AB} = s_0\Upsilon(\mathbf{k})$ by using eq.(2.19). Therefore the Schrödinger eq.(2.15) is,

$$\begin{pmatrix} \varepsilon_0-\varepsilon_{\mathbf{k}} & -(\gamma_0+s_0\varepsilon_{\mathbf{k}})\Upsilon(\mathbf{k}) \\ -(\gamma_0+s_0\varepsilon_{\mathbf{k}})\Upsilon^*(\mathbf{k}) & \varepsilon_0-\varepsilon_{\mathbf{k}} \end{pmatrix}\begin{pmatrix} \alpha \\ \beta \end{pmatrix} = \begin{pmatrix} 0 \\ 0 \end{pmatrix}, \tag{2.22}$$

which only has non-trivial solutions if the determinant is zero. This gives the two eigenenergies $\varepsilon_{\mathbf{k}}$:

$$\varepsilon^+_{\mathbf{k}} = \frac{\varepsilon_0+\gamma_0|\Upsilon(\mathbf{k})|}{1-s_0|\Upsilon(\mathbf{k})|} \quad \text{and} \quad \varepsilon^-_{\mathbf{k}} = \frac{\varepsilon_0-\gamma_0|\Upsilon(\mathbf{k})|}{1+s_0|\Upsilon(\mathbf{k})|}. \tag{2.23}$$

[10] One could get better band structure by including more than the nearest neighbour as in [66].

[11] In [70] $\gamma_0 = 2.7\pm0.1$eV is obtained. In [71] $\gamma_0 = 2.45$eV is found. None of these experiments states values of s_0.

Note that we obtained two eigenvalues as a direct consequence of the two atoms in the unit cell. If $\Upsilon(\mathbf{k}) = 0$ the only eigenenergy is ε_0 and the two corresponding degenerate eigenvectors are $\binom{1}{0}$ and $\binom{0}{1}$. If on the other hand $\Upsilon(\mathbf{k}) \neq 0$ the eigenvectors corresponding to each of the eigenvalues $\varepsilon_{\mathbf{k}}^{\pm}$ in eq.(2.23) are:

$$\begin{pmatrix} \alpha \\ \beta \end{pmatrix}_{\pm} = \frac{1}{\sqrt{2}} \begin{pmatrix} \frac{(\gamma_0 + s_0 \varepsilon_{\mathbf{k}}^{\pm})\Upsilon(\mathbf{k})}{\varepsilon_0 - \varepsilon_{\mathbf{k}}^{\pm}} \\ 1 \end{pmatrix} = \frac{1}{\sqrt{2}} \begin{pmatrix} \mp \frac{\Upsilon(\mathbf{k})}{|\Upsilon(\mathbf{k})|} \\ 1 \end{pmatrix}, \tag{2.24}$$

independent of the constants ε_0,s_0 and γ_0. Note that $\frac{\Upsilon(\mathbf{k})}{|\Upsilon(\mathbf{k})|}$ is just a complex phase factor $e^{i \arg(\Upsilon(\mathbf{k}))}$. This can be inserted into the Wannier decomposition (2.12) to obtain the two Block states in terms of localized functions on the lattice points. So we have now found the possible energies and eigenstates *for a given point in* $\mathbf{k}$*-space*.

Each atomic $2p_z$ orbital contributes one electron to the energy band structure (two per unit cell) and thereby $2N$ of the $4N$ states are filled, i.e. half filling without doping and/or a gate voltage. Since $\varepsilon_{\mathbf{k}}^{+} \geq \varepsilon_{\mathbf{k}}^{-}$ for all $\mathbf{k} \in$ FBZ and $\varepsilon_{\mathbf{k}}^{\pm}$ contains the same number of states ($2N$), $\varepsilon_{\mathbf{k}}^{-}$ is completely occupied and $\varepsilon_{\mathbf{k}}^{+}$ empty at zero temperature. So the Fermi level is at $\varepsilon_{\mathrm{F}} = \varepsilon_0$ and the Fermi points in $\mathbf{k}$-space fulfills $\Upsilon(\mathbf{k}) = 0$ as seen by eq.(2.23). There are six such points in the corners of the FBZ and they are degenerate by symmetry in pairs of two, called $\mathbf{K}_{\pm}$, since the other four points can be obtained by a reciprocal lattice vector. They are found to be[12]: $\mathbf{K}_{\pm} = \frac{2\pi}{a}(\frac{1}{\sqrt{3}}, \pm\frac{1}{3})$ as seen on figure 2.1(b). Since the Fermi points are single points (not lines in the $\mathbf{k}$ plane) graphene (and thereby also graphite) is a semimetal also called a zero-gap semiconductor [1, 65, 58].

We are only interested in the transport properties of graphene, which are mainly given by the band structure around the Fermi level where $|\Upsilon(\mathbf{k})|$ is small and since $s_0 \sim 0.1$ we have $s_0|\Upsilon(\mathbf{k})| \ll 1$ near ε_{F}. Therefore the denominator in the energies (2.23) can be neglected and doing so the Fermi energy $\varepsilon_{\mathrm{F}} = \varepsilon_0$ only moves the bands up or down and we can choose our zero of energy to be $\varepsilon_{\mathrm{F}} = \varepsilon_0 = 0$. This gives the energies and (unchanged) eigenstates:

$$\boxed{\varepsilon_{\mathbf{k}}^{\pm} = \pm\gamma_0|\Upsilon(\mathbf{k})|, \qquad \begin{pmatrix} \alpha \\ \beta \end{pmatrix}_{\pm} = \frac{1}{\sqrt{2}} \begin{pmatrix} \mp \frac{\Upsilon(\mathbf{k})}{|\Upsilon(\mathbf{k})|} \\ 1 \end{pmatrix}}, \tag{2.25}$$

where $\Upsilon(\mathbf{k}) = 1 + e^{-i\mathbf{k}\cdot\mathbf{a}_1} + e^{-i\mathbf{k}\cdot\mathbf{a}_2}$ and

$$|\Upsilon(\mathbf{k})| = \sqrt{3 + 2\cos(\mathbf{k}\cdot\mathbf{a}_1) + 2\cos(\mathbf{k}\cdot\mathbf{a}_2) + 2\cos(\mathbf{k}\cdot(\mathbf{a}_1 - \mathbf{a}_2))} \tag{2.26}$$

$$= \sqrt{1 + 4\cos\left(\frac{\sqrt{3}k_x a}{2}\right)\cos\left(\frac{k_y a}{2}\right) + 4\cos^2\left(\frac{k_y a}{2}\right)}. \tag{2.27}$$

[12]Note that $\Upsilon(\mathbf{k}) = 0$ is a complex equation in two variables and can be solved by identifying the imaginary and real part, respectively.

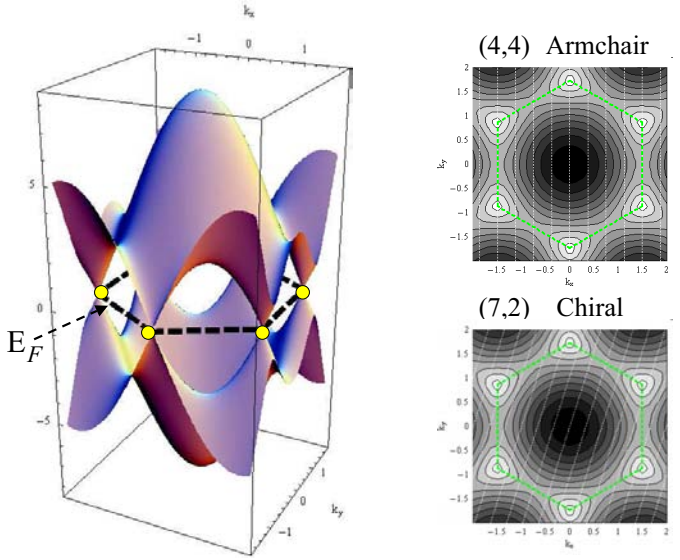

Figure 2.3: Left: The energy band structure of graphene from eq.(2.25). The (undoped) Fermi level is seen and the (yellow) dots represent the $\mathbf{K}_\pm$ points. Right: The possible $\mathbf{k}$ (white lines) of a semiconducting $(7,2)$ and a metallic $(4,4)$ nanotube shown in the FBZ (green dashed lines) of graphene, i.e. the two dimensional band structure is sliced into one dimensional bands by the periodic boundary condition. A contour plot of $\varepsilon^-_{\mathbf{k}}$ (eq.(2.25)) is also seen.

$\varepsilon^\pm_{\mathbf{k}}$ are seen on figure 2.3. Often the simplified band structure (2.25) is found directly by assuming that $s_0 = 0$ from the beginning [65, 58], but since the value of $s_0 \neq 0$ is shown later to be of great importance for the Coulomb drag in multiwall nanotube, this was not done here.

2.2.2 Carbon nanotube band structure

To model the band structure of a multiwall carbon nanotube we assume that the band structure of the individual singlewall tubes are as if they were isolated singlewall nanotubes. This is a good approximation but of course not completely true [72]. Therefore we now find the band structure of an isolated singlewall carbon nanotube.

Band structure by using periodic boundary conditions of graphene

In appendix A we show how the energy and wave function for a cylinder in the free electron model is obtained by making periodic boundary conditions for a two dimensional electron gas. Here we will do the same thing, i.e. apply periodic boundary conditions around the tube (in the $\mathbf{C}$ direction) for the graphene band structure to get the bands of a nanotube. It is not obvious that this will work for carbon nanotubes, since the folding brings the $2p_z$ atomic orbitals closer together (further apart) on the inside (outside) of the tube. Such effects of the curvature [73] have been shown to open energy gaps near the Fermi level of metallic nanotubes for very small radius nanotubes $r \lesssim 0.2$ nm but for larger radii the zone folding works remarkably well [60, 64, 62].

To apply the periodic boundary condition the wave function for graphene should satisfy $\psi_{\mathbf{k}}(\mathbf{r}+\mathbf{C}) = \psi_{\mathbf{k}}(\mathbf{r})$, to fit the tube. By using the Bloch theorem for the graphene lattice we have

$$\psi_{\mathbf{k}}(\mathbf{r}+\mathbf{C}) = e^{i\mathbf{k}\cdot\mathbf{C}}\psi_{\mathbf{k}}(\mathbf{r}) = \psi_{\mathbf{k}}(\mathbf{r}), \tag{2.28}$$

so the periodic boundary condition in the last equality gives the restriction on $\mathbf{k}$:

$$\mathbf{k}\cdot\mathbf{C} = 2\pi n_c, \tag{2.29}$$

where n_c is an integer. Decomposing the wave vector along the tube and around the circumference as

$$\mathbf{k} = k\frac{\mathbf{T}}{|\mathbf{T}|} + k_c\frac{\mathbf{C}}{|\mathbf{C}|} \tag{2.30}$$

and inserting this form in eq.(2.29) we obtain $k_c = \frac{2\pi}{|\mathbf{C}|}n_c$. Here $|\mathbf{C}|$ is short (compared to the tube length) and thereby k_c splits up the two dimensional band structure (2.25) into one dimensional subbands labelled by n_c and a continuous[13] k along the tube. This is completely analogue to the free electron model mapped onto a cylinder as seen in appendix A. The slicing of the 2D band structure can be seen for different nanotubes on figure 2.3.

To avoid degeneracy we have to restrict n_c. This is done by choosing n_c in an interval so that no other n_c value in the interval gives the same wave vector $\mathbf{k}$ plus some reciprocal lattice vector of *graphene*[14]. Explicitly we have

$$\begin{aligned}\mathbf{k} &= k\frac{\mathbf{T}}{|\mathbf{T}|} + k_c\frac{\mathbf{C}}{|\mathbf{C}|} = k\frac{\mathbf{T}}{|\mathbf{T}|} + k_c\frac{\mathbf{G_C}}{|\mathbf{G_C}|} = k\frac{\mathbf{T}}{|\mathbf{T}|} + n_c\mathbf{G_C} \\ &= k\frac{\mathbf{T}}{|\mathbf{T}|} + n_c\frac{1}{\mathcal{N}}\underbrace{(-t_2\mathbf{b}_1 + t_1\mathbf{b}_2)}_{(\star)},\end{aligned} \tag{2.31}$$

where $\frac{\mathbf{C}}{|\mathbf{C}|} = \frac{\mathbf{G_C}}{|\mathbf{G_C}|}$, $|\mathbf{G_C}| = \frac{2\pi}{|\mathbf{C}|}$ and the definition of $\mathbf{G_C}$ in eq.(2.9) were used. Here $(\star)$ is a reciprocal lattice vector of graphene and by construction of t_1 and t_2 (see above eq.(2.8)) no integer can be taken outside the parenthesis to make a shorter reciprocal lattice vector times an integer. Therefore n_c is restricted to $n_c \in \{0, 1, 2, \ldots, \mathcal{N}-1\}$, since all other n_c values would give some $\mathbf{k}$ in this set plus a reciprocal lattice vector of graphene, so the same wave function would be obtained.

The energies and energy eigenstates are now obtained for a particular carbon nanotube (n, m) by inserting the restricted wave vector (2.31) into the band structure for graphene $\varepsilon^{\pm}_{\mathbf{k}}$ and $\binom{\alpha}{\beta}_{\pm}$ in eq.(2.25), where k is in the one dimensional

[13] As always, only continuous in the long tube limit otherwise quantized in units of $\frac{2\pi}{L}$.

[14] It should *not* be a reciprocal lattice vector for the nanotube, since the Bloch theorem in the form $\psi_{\mathbf{k}+\mathbf{G}}(\mathbf{r}) = \psi_{\mathbf{k}}(\mathbf{r})$ is only valid for all graphene reciprocal lattice vectors $\mathbf{G}$ and not for all nanotube reciprocal lattice vectors, when $\psi_{\mathbf{k}}(\mathbf{r})$ is given by (2.12).

FBZ, $-\frac{\pi}{|\mathbf{T}|} \leq k < \frac{\pi}{|\mathbf{T}|}$ and $n_c \in \{0, 1, 2, \ldots, \mathcal{N}-1\}$. Note that this is the band structure for the (large) translational unit cell where k is along the tube.

This gives all the possible energy values as a function of k, but does not tell us a priori how to connect the energy bands (at points of doubt such as crossings). This is done in general by considering the symmetries of the points and connecting points belonging to the same symmetry. This can be done by group theoretical arguments such as in [67, 75, 76], but also by examining the wavefunction directly in the specific case as done later (see page 29, figure 2.4 and section 2.2.4). The group theoretical approach has the advantage of labelling the bands by quantum numbers arising from the symmetry properties such as a crystal angular momentum stemming from the discrete rotational symmetry. We shall see that n_c is closely related to the crystal angular momentum. This labelling has great importance in the calculation of matrix elements since some elements can be zero due to the symmetries. Furthermore one can use a (generalized) Wigner-Eckart theorem [67, 77, 78].

If a $\mathbf{K}_+$ or $\mathbf{K}_-$ point is among the points in the one dimensional band structure, then the nanotube becomes metallic by having states at the Fermi surface, if the nanotube does not have a band gap and is semiconducting. As we shall see (in section 2.2.4) one third of the nanotubes are metallic and two thirds are semiconducting. Experimentally one finds both semiconducting and metallic tubes [58, 74].

Band structure by using the helical and rotational symmetries

The helical $\mathcal{S}(h, \varphi)$ and rotational $\mathcal{C}_\mathfrak{n}$ symmetries are now used to find the band structure for a nanotube using the primitive unit cell (see p.15). The Hamiltonian is invariant under the lattice symmetries and therefore[15] $[H, \mathcal{C}_\mathfrak{n}] = 0$ and $[H, \mathcal{S}(h, \varphi)] = 0$. Furthermore the two lattice symmetries commute $[\mathcal{C}_\mathfrak{n}, \mathcal{S}(h, \varphi)] = 0$, so it is possible to find common eigenstates $|\psi\rangle$ of the three operators[16]:

$$H|\psi\rangle = \varepsilon|\psi\rangle, \quad \mathcal{C}_\mathfrak{n}|\psi\rangle = c|\psi\rangle \quad \text{and} \quad \mathcal{S}(h, \varphi)|\psi\rangle = s|\psi\rangle, \tag{2.32}$$

where the eigenvalues c and s are complex numbers. To find the eigenvalue c we note that $(\mathcal{C}_\mathfrak{n})^\mathfrak{n}$ is the identity operator (rotation of the lattice by 2π), so $c^\mathfrak{n} = 1$, which has the rots $c = e^{-i\frac{2\pi\mathfrak{m}}{\mathfrak{n}}}$ for $\mathfrak{m} \in \{0, 1, \ldots, \mathfrak{n}-1\}$, where the minus sign in the exponent is introduced for later convenience.

The eigenvalue s is found in the following way: Let $\mathfrak{L} \gg 1$ be the number of times the helical operation is used to get from one end of the tube to the other, i.e. it is proportional to the length of the tube L. We now apply periodic

[15] The same symbol for the symmetry groups and the symmetry operators are used, since the meaning is clear from the contents.

[16] The same method can be used to prove Bloch's theorem using translational symmetry, i.e. to find an eigenstate of both the translational operator and the Hamiltonian, see [1, p.134]

boundary conditions to the nanotube, so the two ends are equivalent, which is completely analogue to the Born-von Karman boundary conditions often used in solids [1, p.135]. Therefore $(\mathcal{S}(h,\varphi))^{\mathfrak{L}}$ is the identity operator and $s = e^{-i\frac{2\pi n}{\mathfrak{L}}}$ with[17] $n \in \{-\mathfrak{L}/2, \ldots, \mathfrak{L}/2\}$, but since $\mathfrak{L} \gg 1$ we introduce $\kappa = \frac{2\pi n}{\mathfrak{L}} \in]-\pi, \pi]$, i.e. an (almost) continuous dimensionless index. We can now label the eigenstate by use of the symmetry eigenvalues: $|\psi\rangle = |\kappa, \mathfrak{m}\rangle$, where $-\pi < \kappa \leq \pi$ is analogue to k (but *not* the same) and $\mathfrak{m} \in \{0, 1, \ldots, \mathfrak{n}-1\}$ is the crystal angular momentum along the nanotube, since it stems from the discrete rotational symmetry[18].

To find the $|\kappa, \mathfrak{m}\rangle$ state explicitly as in [62] we use a Wannier decomposition for a two atomic unit cell as for the graphene layer eq.(2.12) (section 2.2.1):

$$|\kappa, \mathfrak{m}\rangle = \frac{1}{\sqrt{\mathfrak{n}\mathfrak{L}}} \sum_{l=-\frac{\mathfrak{L}}{2}}^{\frac{\mathfrak{L}}{2}} \sum_{p=0}^{\mathfrak{n}-1} e^{i\kappa l} e^{i\frac{2\pi\mathfrak{m}}{\mathfrak{n}}p} \big(\alpha \Psi_A(l,p) + \beta \Psi_B(l,p)\big), \tag{2.33}$$

where $\Psi_I(l,p)$ $(I = A, B)$ is a Wannier function approximated by an $2p_z$ orbital at each atom in the two atomic unit cell, i.e. a tight binding approximation. The unit cell at l, p is obtained by l applications of $\mathcal{S}(h,\varphi)$ and p applications of $\mathcal{C}_{\mathfrak{n}}$ from some chosen origin, i.e. at the lattice vector $\mathbf{R} = l\mathbf{H} + p\mathbf{C}_{\mathfrak{n}}$ (before the conformal mapping). Note that $|\kappa, \mathfrak{m}\rangle$ in eq.(2.33) is an eigenstate of $\mathcal{S}(h,\varphi)$ and $\mathcal{C}_{\mathfrak{n}}$.

Just as in the calculation of the graphene band structure this is an eigenstate of the Hamiltonian, $H|\kappa, \mathfrak{m}\rangle = \varepsilon_{\kappa\mathfrak{m}}|\kappa, \mathfrak{m}\rangle$, and by diagonalization (of a 2×2 matrix) we obtain the eigenenergies and the coefficients α and β as a function of κ and $\mathfrak{m}$. The solution is formally the same as for the band structure of graphene in eq.(2.25) (in section 2.2.1), but when calculating H_{AB} we express the nearest neighbours in terms of l and p and thereby get $\Upsilon(\kappa, \mathfrak{m})$ as[19]

$$\Upsilon(\kappa, \mathfrak{m}) = 1 + e^{-i\frac{\kappa n}{\mathfrak{n}} + i\frac{2\pi\mathfrak{m}p_1}{\mathfrak{n}}} + e^{i\frac{\kappa m}{\mathfrak{n}} - i\frac{2\pi\mathfrak{m}p_2}{\mathfrak{n}}}. \tag{2.34}$$

The eigenenergies for a specific $-\pi < \kappa \leq \pi$ and $\mathfrak{m} \in \{0, 1, \ldots, \mathfrak{n}-1\}$ are $\varepsilon^{\pm}_{\kappa\mathfrak{m}} = \pm\gamma_0 |\Upsilon(\kappa, \mathfrak{m})|$ from eq.(2.25), i.e.

$$\varepsilon^{\pm}_{\kappa\mathfrak{m}} = \pm\gamma_0 \Bigg[3 + 2\cos\left(\frac{\kappa n - 2\pi\mathfrak{m}p_1}{\mathfrak{n}}\right) + 2\cos\left(\frac{\kappa m - 2\pi\mathfrak{m}p_2}{\mathfrak{n}}\right) + 2\cos\left(\frac{\kappa(n+m) - 2\pi\mathfrak{m}(p_1+p_2)}{\mathfrak{n}}\right) \Bigg]^{\frac{1}{2}}, \tag{2.35}$$

[17] We assume $\mathfrak{L}$ to be an even integer, which has no practical importance, since $\mathfrak{L} \gg 1$.

[18] Just as angular momentum quantum number m stems from a continuous rotational symmetry of a system around an axis (conventionally called the z-axis).

[19] To identify the nearest neighbours in the l, p coordinates we observe that any lattice vector $\mathbf{R} = q_1\mathbf{a}_1 + q_2\mathbf{a}_2$ can be written as $\mathbf{R} = q_1\mathbf{a}_1 + q_2\mathbf{a}_2 = l\mathbf{H} + p\mathbf{C}_{\mathfrak{n}}$, which gives $l = \frac{q_2 n - q_1 m}{\mathfrak{n}}$ and $p = q_1 p_2 - q_2 p_1$ (modulo $\mathfrak{n}$) for an (n, m) tube and $\mathbf{H} = p_1\mathbf{a}_1 + p_2\mathbf{a}_2$.

where p_1 and p_2 are found from eq.(2.6). Note that we still have the (non-doped) Fermi level at $\varepsilon_{\mathrm{F}} = 0$. We still have to connect the energy bands by considering the symmetries of the wave functions of the bands near crossing of the bands (i.e. at $\Upsilon(\kappa, \mathfrak{m}) = 0$ where the calculation of the band structure is not valid) as we shall see shortly.

Comparison of the band structure for the two different unit cells

We now compare the band structure obtained from the primitive unit cell and the (larger) translational unit cell. An analogue situation for a simple tight binding chain is considered in appendix B, where we see that by choosing a unit cell larger than the primitive unit cell we get a smaller FBZ with more bands in it. These extra bands are obtained from folding the bands from the FBZ of the primitive unit cell into the smaller FBZ of the larger unit cell. The same thing essentially happens in the case of carbon nanotubes, but the bands in the translational and the primitive unit cell are described by a priori different indices: The bands from the primitive unit cell are labelled by a continuous (dimensionless) $\kappa \in]-\pi, \pi]$ (from $\mathcal{S}(h, \varphi)$) and a crystal angular momentum $\mathfrak{m} \in \{0, 1, \ldots, \mathfrak{n}-1\}$ whereas the bands from the translational unit cell have a continuous wave vector $k \in]-\frac{\pi}{|\mathbf{T}|}, \frac{\pi}{|\mathbf{T}|}]$ along the tube and a discrete label $n_c \in \{0, 1, \ldots, \mathcal{N}-1\}$. To connect these two descriptions we have

$$\kappa = \mathbf{k} \cdot \mathbf{H} \qquad \text{and} \qquad \frac{2\pi\mathfrak{m}}{\mathfrak{n}} = \mathbf{k} \cdot \mathbf{C}_{\mathfrak{n}}, \tag{2.36}$$

where $\mathbf{k}$ is the restricted (2D) wave vector of graphene eq.(2.31) with periodic boundary conditions, i.e. $\mathbf{k}$ contains both k and n_c. Therefore κ depends on both k and n_c, whereas $\mathfrak{m} = n_c$ (modulo $\mathfrak{n}$)[20] from eq.(2.29) [61]. So the bands from the primitive unit cell (as a function of κ) is pushed into the smaller FBZ (as a function of e.g. ka) for the translational unit cell and the crystal angular momentum $\mathfrak{m}$ is split up into $n_c = \mathfrak{m}, \mathfrak{m}+\mathfrak{n}, \mathfrak{m}+2\mathfrak{n}, \ldots < \mathcal{N}$.

As an example consider a $(6, 7)$ tube: Here $\mathfrak{n} = 1$ and $\mathcal{N} = 254$, so this tube only has two bands for the primitive unit cell with both $\mathfrak{m} = 0$. These two bands are pushed into a much smaller FBZ of the translational unit cell and thereby split up into 2×254 bands, i.e. all bands have zero crystal angular momentum.

For the tight binding chain in appendix B we note the following: Only for the primitive unit cell are the explicit expressions for the energy bands and eigen functions periodic functions of the wave vector with the period of the reciprocal lattice vector. For the larger unit cell this is not the case, so one has to repeat the structure from the FBZ by hand to obtain a periodic band structure for the larger unit cell. For the nanotube the situation is the same: For the primitive

[20] Explicitly: $\underbrace{\{0, 1, \ldots, \mathcal{N}-1\}}_{n_c \text{ value}} = \underbrace{\{0, 1, \ldots, \mathfrak{n}-1, 0, 1, \ldots, \mathfrak{n}-1, \ldots, 0, 1, \ldots, \mathfrak{n}-1\}}_{\text{crystal angular momentum } \mathfrak{m} \text{ of the } n_c \text{ value}}$.

unit cell, the energy eq.(2.35) and eigenfunction eq.(2.33) are periodic functions for $\kappa \to \kappa + 2\pi$ and/or $\mathfrak{m} \to \mathfrak{m} + \mathfrak{n}$, since $\Upsilon(\kappa, \mathfrak{m})$ eq.(2.34) is invariant under these transformations. For the (larger) translational unit cell this is not the case, since $\Upsilon(\mathbf{k})$ eq.(2.21) with the restricted wave vector eq.(2.31) is not periodic for $\mathbf{k} \to \mathbf{k} + \frac{2\pi}{|\mathbf{T}|}$. We therefore make the band structure for the translational unit cell periodic by hand.

The Fermi level and gaps openings in metallic nanotubes

The Fermi level of a nanotube can be shifted by doping up to ± 0.5eV and applying a gate voltage ε_{F} can be changed by about ± 1eV, which should be compared to the band width $\sim \gamma_0 \simeq 3$eV. The lattice structure is often unaffected by doping, since the doping molecules or atoms bind to the surface of the nanotube by Van der Waals forces [79, 80, 81, 82, 83, 84]. So by moving ε_{F}, semiconducting tubes can become conducting. For $\varepsilon_{\mathrm{F}} = 0$ the band structure of graphene is symmetric around the Fermi level, i.e. for each $\mathbf{k} \in \mathrm{FBZ}$ there is (at zero temperature) an occupied state with energy $\varepsilon^-_{\mathbf{k}}$ and an empty state with energy $-\varepsilon^-_{\mathbf{k}} = \varepsilon^+_{\mathbf{k}}$. This is called particle-hole symmetry and is carried over to the nanotube band structure (see also section 5.3.3). If the Fermi level is shifted, the particle hole symmetry is broken.

In the tight-binding calculation we assumed that the overlap integral has the same value $-\gamma_0$ for all the three nearest neighbours. This is true for graphene, but for the nanotube the distance to the three nearest neighbours change a small amount due to the curvature, i.e. one should have three different constants γ_1, γ_2 and γ_3 in front of the three terms in Υ. This will open very small gaps[21] for all metallic nanotubes except for armchair (n, n) nanotubes [61, 85]. However, all metallic tubes have been predicted to open gaps in nanotube ropes due to inter tube interactions [86].

2.2.3 Examples of carbon nanotube band structure

We now consider two examples of metallic nanotubes: Armchair and (metallic) zigzag tubes. These two examples are in a sense a model of all the metallic nanotubes as we shall see in section 2.2.4.

The band structure of an armchair nanotube

The band structure can be constructed for both the translational unit cell and the primitive unit cell. We begin by considering the translational unit cell.

For the armchair nanotube we have (per definition) $\mathbf{C} = n(\mathbf{a}_1 + \mathbf{a}_2)$, i.e. $n = m$, so from eq.(2.8) $t_1 = 1 = -t_2$ and from eq.(2.10) $\mathcal{N} = 2n$, which gives

[21] The size of the gap depends on the values of γ_1, γ_2 and γ_3.

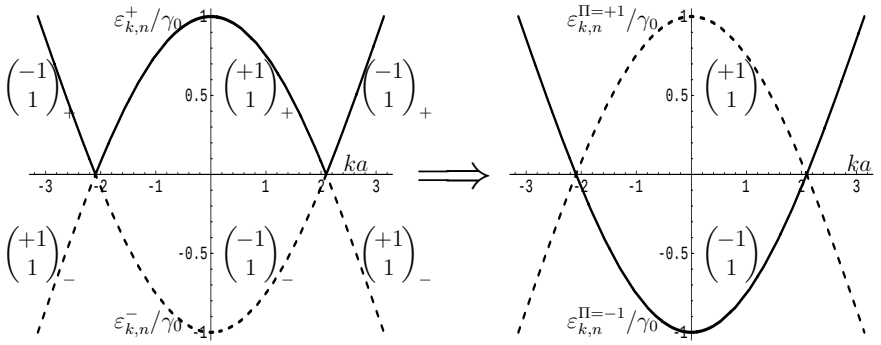

Figure 2.4: An illustration of how to construct the energy bands near ε_{F} for an armchair nanotube. At the left side of the figure the eigenvectors (2.42) are seen in intervals where $\Upsilon(\mathbf{k}) \neq 0$, i.e. $\varepsilon^{\pm}_{k,n} \neq 0$, and by requiring continuity at the points $ka = \pm\frac{2\pi}{3}$, where $\Upsilon(\mathbf{k}) = 0$ we obtain the band structure near the Fermi level. The states and corresponding energies are parity eigenstates and thereby labelled by parity $\Pi = \pm 1$ in the angular coordinate as explained in the text. Energies are in units of γ_0.

$\mathbf{G_C} = \frac{1}{2n}(\mathbf{b}_1 + \mathbf{b}_2)$. The restriction on $\mathbf{k}$ due to the periodic boundary condition eq.(2.31) is therefore (in (k_x, k_y) representation):

$$\mathbf{k} = k \begin{pmatrix} 0 \\ -1 \end{pmatrix} + \frac{2\pi n_c}{\sqrt{3}an} \begin{pmatrix} 1 \\ 0 \end{pmatrix}, \tag{2.37}$$

where[22] $n_c = 0, 1, \ldots, 2n-1$ and $-\frac{\pi}{a} \leq k < \frac{\pi}{a}$ since $|\mathbf{T}| = a$. Note how the k_x and k_y separate nicely in the case of armchair nanotubes. Inserting $\mathbf{k}$ eq.(2.37) in $\Upsilon(\mathbf{k})$ we have

$$\Upsilon(\mathbf{k}) = 1 + e^{-i\pi\frac{n_c}{n}} 2\cos\left(\frac{ka}{2}\right) \tag{2.38}$$

and therefore by use of eq.(2.27), the possible energy values become

$$\varepsilon^{\pm}_{k,n_c} = \pm\gamma_0 \sqrt{1 + 4\cos\left(\frac{n_c\pi}{n}\right)\cos\left(\frac{ka}{2}\right) + 4\cos^2\left(\frac{ka}{2}\right)}. \tag{2.39}$$

Here we see armchair nanotubes to be metallic, since $\varepsilon^{\pm}_{k,n}$ $(n_c = n)$ has states at the Fermi level when $ka = \pm\frac{2\pi}{3}$. The energy bands of a $(5,5)$ tube are shown in figure 2.7(a). The coefficients α and β for the Bloch states (2.12) for the armchair nanotube are (from eq.(2.25))

$$\begin{pmatrix} \alpha \\ \beta \end{pmatrix}_{\pm} = \frac{1}{\sqrt{2}} \begin{pmatrix} \mp\frac{\left(1+e^{-i\pi\frac{n_c}{n}}2\cos\left(\frac{ka}{2}\right)\right)}{\sqrt{1+4\cos\left(\frac{n_c\pi}{n}\right)\cos\left(\frac{ka}{2}\right)+4\cos^2\left(\frac{ka}{2}\right)}} \\ 1 \end{pmatrix}. \tag{2.40}$$

[22]Note that only half of the possible n_c values were used in [64], which was corrected in [58].

The transport properties are due to the energies near ε_{F} and we therefore focus on them for the rest of this section. The energies near the Fermi level are only for $n_c = n$ and in this situation eq.(2.39) and eq.(2.40) simplify *for a specific* k to:

$$\varepsilon_{k,n}^{\pm} = \pm\gamma_0 \left|1 - 2\cos\left(\frac{ka}{2}\right)\right| \qquad \text{and} \tag{2.41}$$

$$\begin{pmatrix} \alpha \\ \beta \end{pmatrix}_{\pm} = \frac{1}{\sqrt{2}} \begin{pmatrix} \mp\mathrm{sign}\big(1 - 2\cos(\frac{ka}{2})\big) \\ 1 \end{pmatrix}. \tag{2.42}$$

We will now construct the energy bands (near ε_{F}) for k in the whole FBZ and not just for specific k values as given in eq.(2.41) and eq.(2.42) and label these bands by their symmetry properties. The eigenmatrix equation (2.22) gives specific eigenvectors to specific eigenvalues in intervals where $\Upsilon(\mathbf{k}) \neq 0$ due to continuity. To connect these intervals, we require the eigenvector as a function of k to be continuous across the points where $\Upsilon(\mathbf{k}) = 0$, even though the eigenvectors (2.24) are not eigenvectors at the point where $\Upsilon(\mathbf{k}) = 0$. This gives us a way to construct the energy bands as a function of k when in doubt, such as at band crossings. In practice one can do this by considering the limit of the inner product of the eigenvectors from each side as a function of k of a point where $\Upsilon(\mathbf{k}) = 0$. In the present case of eq.(2.41) and eq.(2.42) this is easy due to the sign function as seen on figure 2.4 and the right band structure is

$$\varepsilon_{k,n}^{\Pi} = -\Pi\gamma_0 \left(1 - 2\cos\left(\frac{ka}{2}\right)\right) \qquad \text{and} \tag{2.43}$$

$$\begin{pmatrix} \alpha \\ \beta \end{pmatrix}_{\Pi} = \frac{1}{\sqrt{2}} \begin{pmatrix} \Pi \\ 1 \end{pmatrix}, \tag{2.44}$$

where $\Pi = \pm 1$ turns out to be the parity with respect to the angular coordinate in cylindrical coordinates as we shall show now. Explicitly by inserting (2.44) into (2.12) the Bloch states are:

$$\begin{aligned} \psi_{k,n}^{\Pi}(\mathbf{r}) &= \frac{1}{\sqrt{2N}} \sum_{\mathbf{R}_A} e^{i\mathbf{k}\cdot\mathbf{R}_A} \Big(\Pi\Psi(\mathbf{r} - \mathbf{R}_A) + \Psi(\mathbf{r} - \mathbf{R}_A - \mathbf{d})\Big) \qquad (2.45) \\ &= \frac{1}{\sqrt{2N}} \sum_{t,\mathfrak{r}} e^{i\pi\mathfrak{r} + i\frac{ka}{2}t} \left[\Pi\Psi\left(\mathbf{r} - \frac{a}{2}\begin{pmatrix}\sqrt{3}\mathfrak{r} \\ -t\end{pmatrix}\right) + \Psi\left(\mathbf{r} - \frac{a}{2}\begin{pmatrix}\sqrt{3}\mathfrak{r} + \frac{2}{\sqrt{3}} \\ -t\end{pmatrix}\right)\right], \end{aligned}$$

where the sum over the lattice vector written as $\mathbf{R}_A = l_1\mathbf{a}_1 + l_2\mathbf{a}_2$, $l_1, l_2 \in \mathbb{Z}$, is redefined in terms of $t \equiv l_1 - l_2$ and $\mathfrak{r} \equiv l_1 + l_2$, which corresponds to a translation along the tube and a rotation, respectively. To see that $\psi_{k,n}^{\Pi}(\mathbf{r})$ is a parity eigenstate, consider figure 2.5. Here an unfolded armchair nanotube is seen and the directions $\mathbf{C}$ (around the tube) and $\mathbf{T}$ (along the tube) are shown.

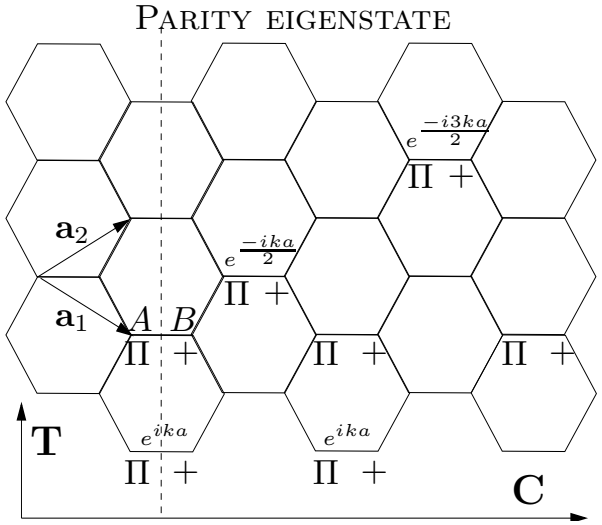

Figure 2.5: The figure shows that the two Bloch states eq.(2.45) in an armchair nanotube with energy near ε_{F} are parity eigenstates with respect to a mirror plane (dashed line) along the tube. The chiral vector $\mathbf{C}$ and translation vector $\mathbf{T}$ are also seen, i.e. the tube is folded in the $\mathbf{C}$ direction.

We choose the phase of the wave function (2.45) to be zero at the points A and B, i.e. all $\mathbf{R}_A$ are with respect to A in this unit cell. The term of the wave function (2.45) from the unit cell at A is $\Big(\Pi\Psi(\mathbf{r}-\mathbf{R}_A)+\Psi(\mathbf{r}-\mathbf{R}_A-\mathbf{d})\Big)$, $(t=\mathfrak{r}=0)$ pictured as Π and $+$ in figure 2.5. The neighboring cell to the right at $\mathbf{R}_A=\mathbf{a}_1+\mathbf{a}_2$, $(t=0,\,\mathfrak{r}=2)$ has the same term, since $e^{i\mathbf{k}\cdot(\mathbf{a}_1+\mathbf{a}_2)}=1$. The terms at the other unit cells are seen equivalently and shown in the figure. The parity is now seen by making a reflection in the dashed line (which is a mirror plane when the tube is folded), since Π and $+$ are interchanged. So by introducing cylindrical coordinates $\mathbf{r}=(\theta,r,z)$ and a parity operator $\mathcal{P}_\theta$ we have[23]:

$$\mathcal{P}_\theta\Big(\psi^{\Pi}_{k,n}(\theta,r,z)\Big)\equiv\psi^{\Pi}_{k,n}(-\theta,r,z)=\Pi\psi^{\Pi}_{k,n}(\theta,r,z), \tag{2.46}$$

where $-\pi\leq\theta<\pi$. These conclusions were also found in [67], but by a completely different method[24].

We now consider the band structure using the primitive unit cell. From eq.(2.6) we have $\mathfrak{n}=n$, $p_1=1$ and $p_2=0$, so $\Upsilon(\kappa,\mathfrak{m})=1+e^{-i\kappa+i\frac{2\pi\mathfrak{m}}{n}}+e^{i\kappa}$ for $\mathfrak{m}\in\{0,1,\ldots,n-1\}$. Inserting this into eq.(2.35) and eq.(2.25) we have energies and eigen states for specific κ and $\mathfrak{m}$. Again the bands has to be reconnected at points where $\Upsilon(\kappa,\mathfrak{m})=0$ to cross the Fermi level ($\varepsilon_{\mathrm{F}}=0$) as on figure 2.4. The connection between the descriptions for the different unit cells is (from eq.(2.36)): $\kappa=\frac{ka}{2}+\frac{n_c\pi}{n}$ and $\mathfrak{m}=n_c$ (modulo n). So the band near ε_{F} ($n_c=n$) has crystal angular momentum $\mathfrak{m}=0$ and of course also has a parity index: $\varepsilon^{\Pi}_{\kappa\mathfrak{m}=0}=-\Pi\gamma_0(1+2\cos(\kappa))$. This bands is pushed into the translational FBZ

[23]Note that originally $\mathbf{r}=(x,y)$ was in the plane of graphene and when it was folded, x became cyclic, so that for a constant radius r we might as well use cylindrical coordinates.

[24]By taking a starting point in the group symmetries of the lattices and thereafter use group theoretical arguments to achieve the band structure.

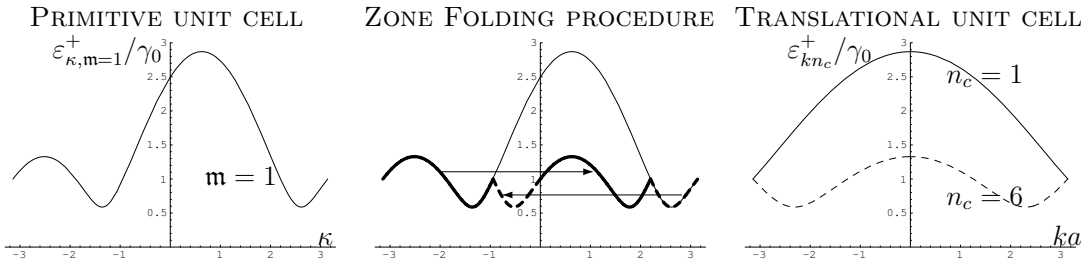

Figure 2.6: (Left): The $\mathfrak{m}=1$ band for a $(5,5)$ tube in the FBZ of the primitive unit cell as a function of $\kappa \in]-\pi,\pi]$ from eq.(2.35). (Center): The $\mathfrak{m}=1$ band is pushed into the smaller FBZ of the translational unit cell by using $\kappa = \frac{ka}{2} + \frac{n_c\pi}{5}$ and that $n_c = 1$ and $n_c = 6$, since $\mathfrak{m}=1$. Note that the band is symmetrical around $\frac{\pi}{5}$, since $\mathfrak{m}=1$. (Right): The band structure for the translational unit cell. Both bands have crystal angular momentum $\mathfrak{m}=1$, but indices $n_c=1$ and $n_c=6$.

to become the two bands with $n_c = 0$ and $n_c = n$. In figure 2.6 we see how the $\mathfrak{m}=1$ band for a $(5,5)$-tube is pushed into the FBZ of the translational unit cell from the primitive unit cell. Further examples can be made by the *Mathematica* program found in [87].

The band structure of a zigzag nanotube

A Zigzag nanotube have a zigzag pattern along $\mathbf{C}$, which is found by using $(n,0)$, $(0,m)$ or $\mathbf{C}$ along y (see figure 2.2) due to lattice symmetry. Again we begin by a description for the translational unit cell and thereafter briefly discus band structure using the primitive unit cell.

For $(n,0)$ we have $t_1 = 1$, $t_2 = -2$, $\mathcal{N} = 2n$ so $\mathbf{G_C} = \frac{1}{2n}(2\mathbf{b}_1 + \mathbf{b}_2)$ and therefore the periodic boundary condition eq.(2.31) gives:

$$\mathbf{k} = -\frac{1}{2}k\begin{pmatrix}1\\ \sqrt{3}\end{pmatrix} + \frac{2\pi n_c}{na^2}\mathbf{a}_1, \tag{2.47}$$

which gives

$$\Upsilon(\mathbf{k}) = e^{\frac{i\pi n_c}{n}}\left(2\cos\left(\frac{n_c\pi}{n}\right) + e^{-\frac{i\sqrt{3}ka}{2}}\right), \tag{2.48}$$

where $n_c = 0, 1, \ldots, 2n-1$ and $-\frac{\pi}{\sqrt{3}a} < k \leq \frac{\pi}{\sqrt{3}a}$ since $|\mathbf{T}| = \sqrt{3}a$. The possible eigenenergies are:

$$\varepsilon^{\pm}_{k,n_c} = \pm\gamma_0\sqrt{1 + 4\cos\left(\frac{n_c\pi}{n}\right)\cos\left(\frac{\sqrt{3}ka}{2}\right) + 4\cos^2\left(\frac{n_c\pi}{n}\right)} \tag{2.49}$$

as seen on figure 2.7(b) for $n = 6$.

For zigzag tubes to be metallic eq.(2.49) (or eq.(2.48)) has to be zero for some k, which is only true when $n_c = \frac{2n}{3}$ or $n_c = \frac{4n}{3}$, i.e. zigzag nanotubes are only

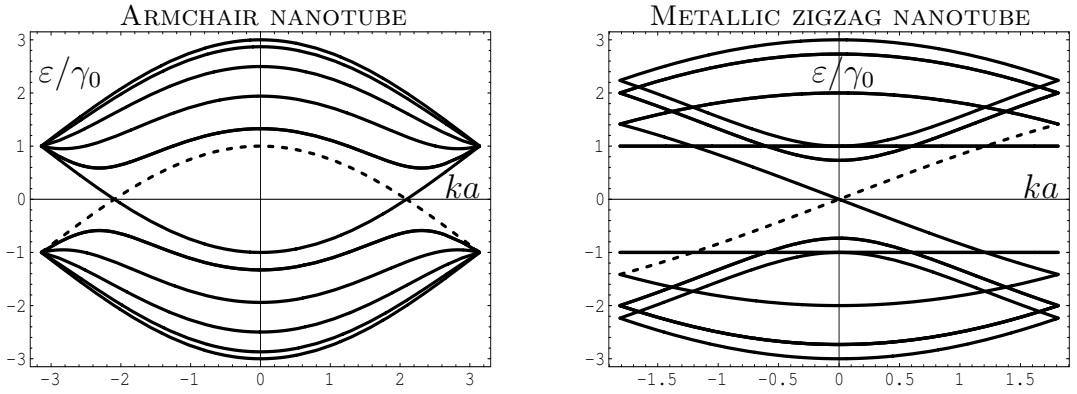

(a) (b)

Figure 2.7: The energy bands for (a) an armchair $(5,5)$ nanotube and (b) a metallic zigzag $(6,0)$ nanotube. In both there are four crossings of the Fermi level ($\varepsilon_{\rm F}=0$), since the zigzag bands are degenerate. These two examples are good representatives of metallic nanotubes, since all metallic nanotubes have four crossings either at $k=0$ or $k=\pm\frac{2\pi}{3|\mathbf{T}|}$ as shown in section 2.2.4.

metallic when n is dividable by 3. Then $n_c=\frac{2n}{3}$ or $n_c=\frac{4n}{3}$ (referred to as $\tilde{n}_c$), we have $\Upsilon(\mathbf{k})=e^{\frac{i\pi\tilde{n}_c}{n}}\left(-1+e^{-\frac{ika\sqrt{3}}{2}}\right)$ and eq.(2.49) is $\varepsilon^{\pm}_{k,\tilde{n}_c}=\pm2\gamma_0|\sin\left(\frac{\sqrt{3}ka}{4}\right)|$, which is only zero at $k=0$ in the FBZ. To connect the energies to a band structure we do as in the case of armchair nanotubes. Near $k=0$, we have, to first order in k:

$$\alpha^{\pm}_{k,\tilde{n}_c}=\pm\frac{\Upsilon(\mathbf{k})}{|\Upsilon(\mathbf{k})|}\simeq\mp ie^{\frac{i\pi\tilde{n}_c}{n}}\mathrm{sign}(k). \tag{2.50}$$

So near the Fermi level the band structure has four[25] crossing bands:

$$\varepsilon^{\xi}_{k,\tilde{n}_c}=\xi\hbar v_0k\quad\text{and}\quad\begin{pmatrix}\alpha\\ \beta\end{pmatrix}_{\xi,\tilde{n}_c}=\frac{1}{\sqrt{2}}\begin{pmatrix}-\xi ie^{\frac{i\pi\tilde{n}_c}{n}}\\ 1\end{pmatrix} \tag{2.51}$$

where $\xi=\pm1$ and the energies were expanded to first order. The symmetry is not as clear in this situation (see [67]).

Using the primitive unit cell we find $p_1=0$, $p_2=-1$ and $\mathfrak{n}=n$ from eq.(2.6), so by eq.(2.34) $\Upsilon(\kappa,\mathfrak{m})=1+e^{-i\kappa}+e^{\frac{i2\pi\mathfrak{m}}{n}}$ for a $(n,0)$ tube. From $\Upsilon(\kappa,\mathfrak{m})=0$ we see that the metallic bands $n_c=\frac{2n}{3}$ and $n_c=\frac{4n}{3}$ have crystal angular momentum $\mathfrak{m}=\frac{2n}{3}$ and $\mathfrak{m}=\frac{n}{3}$, respectively.

[25]Two bands of the same form from $n_c=\frac{2n}{3}$ and $n_c=\frac{4n}{3}$, i.e. degenerate into pairs.

2.2.4 Expanding the band structure at the Fermi level

To find the band structure for a general nanotube around the Fermi level and to show some general properties of these bands, we now expand $\Upsilon(\mathbf{k})$ for graphene around its zeros: $\mathbf{K}_\varsigma = \frac{2\pi}{a}(\frac{1}{\sqrt{3}}, \varsigma\frac{1}{3})$, where $\varsigma = \pm 1$. Writing the wave vector (of graphene) as $\mathbf{k} = \boldsymbol{\mathfrak{K}} + \mathbf{K}_\varsigma$ and assuming the length of $\boldsymbol{\mathfrak{K}}$ small we have

$$\begin{aligned}\Upsilon(\boldsymbol{\mathfrak{K}} + \mathbf{K}_\varsigma) &\simeq \nabla_{\mathbf{k}}\Upsilon(\mathbf{k})|_{\mathbf{K}_\varsigma} \cdot \boldsymbol{\mathfrak{K}} = -\left(i\boldsymbol{\mathfrak{K}}\cdot\mathbf{a}_1 e^{-i\mathbf{K}_\varsigma\cdot\mathbf{a}_1} + i\boldsymbol{\mathfrak{K}}\cdot\mathbf{a}_2 e^{-i\mathbf{K}_\varsigma\cdot\mathbf{a}_2}\right) \\ &= \frac{\sqrt{3}a}{2}(i\mathfrak{K}_x + \varsigma\mathfrak{K}_y), \end{aligned} \tag{2.52}$$

where $\boldsymbol{\mathfrak{K}} = (\mathfrak{K}_x, \mathfrak{K}_y)$ and hence $|\Upsilon(\boldsymbol{\mathfrak{K}} + \mathbf{K}_\varsigma)| = \frac{\sqrt{3}a}{2}\sqrt{\mathfrak{K}_x^2 + \mathfrak{K}_y^2} \equiv \frac{\sqrt{3}a}{2}|\boldsymbol{\mathfrak{K}}|$ independent of ς. Making a rotation of the coordinate system from the x and y axis to the orthonormal basis $(\frac{\mathbf{T}}{|\mathbf{T}|}, \frac{\mathbf{C}}{|\mathbf{C}|})$ (see figure 2.2) we can write $\boldsymbol{\mathfrak{K}} = \mathfrak{K}_T\frac{\mathbf{T}}{|\mathbf{T}|} + \mathfrak{K}_C\frac{\mathbf{C}}{|\mathbf{C}|}$. This form of $\boldsymbol{\mathfrak{K}}$ is inserted into the periodic boundary condition eq.(2.29), $\mathbf{k}\cdot\mathbf{C} = 2\pi n_c$, to get the band structure of a carbon nanotube and we obtain

$$\mathfrak{K}_C = \frac{2n_c}{D} - \frac{(n+m) + \varsigma\frac{1}{3}(m-n)}{D}, \tag{2.53}$$

and since the length of any vector is invariant under a rotation (in particular $|\boldsymbol{\mathfrak{K}}| = \sqrt{\mathfrak{K}_T^2 + \mathfrak{K}_C^2}$) the possible energy values eq.(2.25) are[26]

$$\varepsilon^{\pm}_{\mathfrak{K}_T, n_c} = \pm\frac{2\hbar v_0}{D}\sqrt{\left(\frac{\mathfrak{K}_T D}{2}\right)^2 + \left(n_c - \frac{(n+m) + \varsigma\frac{1}{3}(m-n)}{2}\right)^2}, \tag{2.54}$$

so the energies near $\varepsilon_{\mathrm{F}} = 0$ are for $n_c^{\varsigma=+1} = \frac{2m+n}{3}$ and $n_c^{\varsigma=-1} = \frac{2n+m}{3}$. From this we see the condition for a nanotubes to be metallic[27]:

A (n, m) nanotube is metallic in the nearest neighbour tight binding model if and only if $\frac{2n+m}{3}$ is an integer.

Note that if just one of the integers $2n + m$, $2m + n$ or $n - m$ is divisible by 3 so are the other two other[28]. This rule predicts that in a random sample of nanotubes such as a multiwall or a rope of nanotubes, there will be 1/3 metallic and 2/3 semiconducting tubes. For semiconducting tubes we can find the band gap $\varepsilon_{\mathrm{gap}}$ from eq.(2.54) by setting $\mathfrak{K}_T = 0$ and $n_c - \frac{(n+m)+\varsigma\frac{1}{3}(m-n)}{2} = \pm\frac{1}{3}$ to be

$$\varepsilon_{\mathrm{gap}} = \frac{2a_{\mathrm{C\text{-}C}}\gamma_0}{D}, \tag{2.55}$$

[26] It should be noted, that we use an expansion of the *graphene* dispersion relation, so it is only strictly valid for small $\mathfrak{K}_T$ and $\mathfrak{K}_C$. Therefore it describes the metallic states best (since these have $\mathfrak{K}_C = 0$) and the semiconducting states less precise.

[27] Note that there exists an $n_c \in \{0, 1, \ldots, \mathcal{N}-1\}$ so that e.g. $n_c = \frac{2m+n}{3}$ (assuming $\frac{2m+n}{3} \in \mathbb{Z}$) , since $\mathcal{N} > \frac{2m+n}{3}$ seen by using eq.(2.10) and the fact that $2m + n \geq \gcd(2n + m, 2m + n)$.

[28] $\frac{2n+m}{3} \in \mathbb{Z}$ if and only if $\frac{n-m}{3} \in \mathbb{Z}$. Proof: $2n + m = 3n - (n - m)$ so the statement is true since $\frac{3n}{3} \in \mathbb{Z}$. Similar equations proves the other implications.

so the larger the diameter the smaller the band gap. One often see the larger nanotubes to be conducting because the Fermi level is shifted into the conduction band, which makes more than 1/3 of the tubes conducting in experiments [79].

The Bloch state for metallic nanotubes for $\mathbf{k}$ near $\mathbf{K}_\varsigma$ can also be found by setting $\mathfrak{K}_C = 0$ so $\binom{\mathfrak{K}_x}{\mathfrak{K}_y} = \mathfrak{K}_T \frac{\mathbf{T}}{|\mathbf{T}|}$, which is inserted into eq.(2.52) and it gives

$$\binom{\alpha}{\beta}_{\pm} = \frac{1}{\sqrt{2}} \begin{pmatrix} \mp \frac{i(m-n)-\varsigma\sqrt{3}(n+m)}{2\sqrt{n^2+m^2+mn}} \mathrm{sign}(\mathfrak{K}_T) \\ 1 \end{pmatrix}, \tag{2.56}$$

which depends on which point we expand around, i.e. on ς. The sign function gives that all metallic bands in a nanotube cross the undoped Fermi level ($\varepsilon_{\mathrm{F}} = 0$) and have velocity $v_0 = \pm\frac{\sqrt{3}\gamma_0 a}{2}$ near $\varepsilon_{\mathrm{F}} = 0$ from eq.(2.54). So when connecting the bands in the right way the coefficients α and β become independent of $\mathfrak{K}_T$, i.e. of k, in this first order expansion.

We now find the point, where $k \in$ FBZ crosses the Fermi level ($\varepsilon_{\mathrm{F}} = 0$). From eq.(2.31) we know by definition that $k \equiv \mathbf{k} \cdot \frac{\mathbf{T}}{|\mathbf{T}|} = \boldsymbol{\mathfrak{K}} \cdot \frac{\mathbf{T}}{|\mathbf{T}|} + \mathbf{K}_\varsigma \cdot \frac{\mathbf{T}}{|\mathbf{T}|} = \mathfrak{K}_T + \mathbf{K}_\varsigma \cdot \frac{\mathbf{T}}{|\mathbf{T}|}$. At the crossing we have $\mathfrak{K}_T = 0$, so the crossing point is:

$$\mathbf{K}_\varsigma \cdot \frac{\mathbf{T}}{|\mathbf{T}|} = \frac{\pi(m-n-\varsigma(n+m))}{\gcd(2n+m, 2m+n)|\mathbf{T}|} = \begin{cases} \frac{-2\pi n}{\gcd(2n+m,2m+n)|\mathbf{T}|} & \text{for } \varsigma = +1 \\ \frac{2\pi m}{\gcd(2n+m,2m+n)|\mathbf{T}|} & \text{for } \varsigma = -1 \end{cases}, \tag{2.57}$$

which shows[29] that any metallic nanotube have bands crossing the Fermi level ($\varepsilon_{\mathrm{F}} = 0$) either at $k = 0$ or at $k = \pm\frac{2\pi}{3|\mathbf{T}|}$ for k in FBZ, $-\frac{\pi}{|\mathbf{T}|} \leq k < \frac{\pi}{|\mathbf{T}|}$. So each $\mathbf{K}_\pm$ (and thereby each $n_c = n_c^{\varsigma=\pm1}$) gives rise to one crossing point and the two crossing points are either degenerate at $k = 0$ or separated at $k = \pm\frac{2\pi}{3|\mathbf{T}|}$.

In conclusion, all metallic nanotubes (n, m) have four (two $n_c = n_c^{\varsigma=\pm1}$) linear crossings at the Fermi level ($\varepsilon_{\mathrm{F}} = 0$)

$$\varepsilon^{\xi}_{\mathfrak{K}_T, n_c^\varsigma} = \xi\hbar v_0 \mathfrak{K}_T \quad \text{and} \quad \binom{\alpha}{\beta}_{\xi,\varsigma} = \frac{1}{\sqrt{2}} \begin{pmatrix} -\xi\frac{i(m-n)-\varsigma\sqrt{3}(n+m)}{2\sqrt{n^2+m^2+mn}} \\ 1 \end{pmatrix}, \tag{2.58}$$

[29]Proof: Introduce $g \equiv \gcd(2n+m, 2m+n)$ and since we have metallic tubes we can divide into two cases: $g = 3$ and $g \neq 3$.
If $g = 3$ we have $-\frac{2\pi n}{g|\mathbf{T}|} = -\frac{2\pi n}{3|\mathbf{T}|}$ and $\frac{2\pi m}{g|\mathbf{T}|} = \frac{2\pi m}{3|\mathbf{T}|}$, which are $\pm\frac{2\pi}{3|\mathbf{T}|}$ or 0 when pulled into the FBZ$= [-\frac{\pi}{|\mathbf{T}|}, \frac{\pi}{|\mathbf{T}|}[$ depending on n and m. When $\frac{n}{3} \in \mathbb{Z}$ (and therefore also $\frac{m}{3} \in \mathbb{Z}$ by $\frac{n-m}{3} \in \mathbb{Z}$) both projections are taken into 0 by a reciprocal vector and the bands crossing $k = 0$ becomes double degenerate. If $\frac{n}{3} \notin \mathbb{Z}$ the crossings are at $\pm\frac{2\pi}{3|\mathbf{T}|}$.
If $g \neq 3$ we have $2n + m = gx$ and $2m + n = gy$ for some $x, y \in \mathbb{Z}$ ($\gcd(x, y) = 1$), which gives $n = g(2x - y)/3$ and $m = g(2y - x)/3$. Therefore $-\frac{2\pi n}{g|\mathbf{T}|} = -\frac{2\pi g(2x-y)}{3g|\mathbf{T}|} = -\frac{2\pi(2x-y)}{3|\mathbf{T}|}$ and $\frac{2\pi m}{g|\mathbf{T}|} = \frac{2\pi(2y-x)}{3|\mathbf{T}|}$ are both 0 or $\pm\frac{2\pi}{3|\mathbf{T}|}$ when taken into the FBZ for any $x, y \in \mathbb{Z}$. Again we have double degeneracy, when both are taken into zero.

at either $k = 0$ or at $k = \pm\frac{2\pi}{3|\mathbf{T}|}$, where k is along the tube in the FBZ: $-\frac{\pi}{|\mathbf{T}|} \leq k < \frac{\pi}{|\mathbf{T}|}$ and $\xi = \pm 1$ gives the direction of the velocity. This makes armchair[30] and metallic zigzag nanotubes two good examples of metallic nanotubes as seen on figure 2.7. The same conclusions can be made by expanding $\Upsilon(\kappa, \mathfrak{m})$ for the primitive unit cell eq.(2.34) to first order in κ around the zero(s) of $\Upsilon(\kappa, \mathfrak{m})$.

The $\mathbf{k} \cdot \mathbf{p}$ approximation and the Dirac neutrino picture

Instead of a tight binding model for the band structure of carbon nanotubes one can use the $\mathbf{k} \cdot \mathbf{p}$ approximation and obtain similar results [59].

In general the $\mathbf{k} \cdot \mathbf{p}$ approximation is a local description around the Fermi surface, where the Schrödinger equation is written by decomposing the Bloch function as $\psi_{\mathbf{k}}(\mathbf{r}) = e^{i\mathbf{k}\cdot\mathbf{r}} u_{\mathbf{k}}(\mathbf{r})$. The Schrödinger equation of a periodic potential $U(\mathbf{r})$ is therefore rewritten (in general) to:

$$\left(\frac{\hbar^2 k^2}{2m_e} + \frac{\widehat{\mathbf{p}}^2}{2m_e} + \frac{\hbar \mathbf{k} \cdot \widehat{\mathbf{p}}}{m_e} + U(\mathbf{r}) \right) u_{\mathbf{k}}(\mathbf{r}) = \varepsilon_{\mathbf{k}} u_{\mathbf{k}}(\mathbf{r}), \tag{2.59}$$

where $\widehat{\mathbf{p}}$ is the momentum operator, $\mathbf{k}$ the wave vector (not an operator) and m_e the mass of the electron. The task in the $\mathbf{k} \cdot \mathbf{p}$ approximation is to extract information by expanding $u_{\mathbf{k}}(\mathbf{r})$ around the Fermi level in the same spirit as in the tight binding approximation. The name of the approximation stems from the $\mathbf{k} \cdot \widehat{\mathbf{p}}$ term, when the above rewriting of the Schrödinger equation is used (see e.g. [88] for further details).

The $\mathbf{k} \cdot \mathbf{p}$ approximation for carbon nanotubes gives the same conclusions as found by the expansion around $\mathbf{K}_{\pm}$, since inserting eq.(2.52) in eq.(2.22) one has the Hamiltonian matrix from the $\mathbf{k} \cdot \mathbf{p}$ approximation [59]. If we view the Schrödinger equation in the $\mathbf{k} \cdot \mathbf{p}$ approximation as a (decoupled) two component matrix equation (one component for each sublattice and setting $s_0 = 0$) it is formally equivalent to the Dirac equation[31], where the spinor is not the electrons spin but a pseudo spin representing the sublattice [89, 90]. Since the energy bands of graphene touch ε_{F}, the problem is analogue to a free massless[32] neutrino on a cylinder. This gives plane wave states times a pseudo spin [91, 92], $e^{i\mathbf{k}\cdot\mathbf{r}} \begin{pmatrix} \pm e^{i \arg(\Upsilon(\mathbf{k}))} \\ 1 \end{pmatrix}$, where the notation is well chosen, since the two components do not have an overlap (in this scheme). This scheme takes into account the important fact of two atoms in the unit cell of graphene, which is not captured by a simple plane wave approximation as often used in transport calculations. It has been argued that this might be the reason for the long mean free paths in metallic

[30] Note that armchair tubes have four crossing of $\varepsilon_{\mathrm{F}} = 0$, but only two bands, since $n_c^{\varsigma=+1} = n_c^{\varsigma=-1}$. This is not true in general for tubes with crossings at $k = \pm\frac{2\pi}{3|\mathbf{T}|}$, consider e.g. a $(7, 4)$ tube.

[31] Or rather the Weyl′s equation, since there is no antiparticle part.

[32] Massless since using the relativistic energy $\varepsilon = \pm\sqrt{p^2 + m^2}$, $(c = 1)$ for $m = 0$ one has a gapless energy spectrum with linear dispersion.

nanotubes [93, 91, 92] and we shall see that it also has profound consequences for the Coulomb drag in multiwall nanotubes.

We use the tight binding Wannier decomposition eq.(2.12) (or eq.(2.33)) in our calculations, which also includes the overlap between the sublattices and thereby are more general. However, the remarkable consequences from the two atomic unit cell remains.

2.3 Transport in carbon nanotubes

Transport of electrons through some sample depends on the number of scattering events an electron encounters going through the structure. A scattering event typically happens due to an impurity, a lattice defect or a lattice vibration (phonon), where the importance of the mechanism depends on the temperature. If there are only a few scattering events the conductor is called ballistic and if there are many events it is called diffusive [94]. It is not a sharp transition between the two transport regimes, but merely a crossover as the scattering becomes more frequent. The experimental conditions and internal structure determine which regime we are in. Carbon nanotubes have been observed in both regimes for both singlewall and multiwall nanotubes. Also the contacts to the tube seem to have an important role to play.

If a single wall metallic nanotube is ballistic, it should have a conductance of $\frac{4e^2}{h}$ from the Landauer-Büttiker formula [18] with perfect transmission (i.e. transmission coefficients equal to one), which is predicted theoretically [95]. Recently this has also been found experimentally at low temperatures [96], but ballistic transport has been seen before in single wall nanotubes at lower conductances often explained as contacts effects [97, 98]. Some other experiments show signs of ballistic transport in single wall nanotubes [99].

Multiwall nanotubes have also been observed to be ballistic when contacted by a liquid metal [30], but many other experiments with other types of solid contacts show multiwall nanotubes to be diffusive [97, 80, 99, 29].

We will assume in our calculations of the Coulomb drag resistance, that the transport is diffusive as we shall seen in chapter 3. Furthermore we will use the Boltzmann equation to model the transport in multiwall nanotubes. This has been done successfully before to model other phenomena in nanotubes such as the liquid flow (of e.g. water) above a tube [100], the effect on transport by a magnetic field [101] and high electric field transport [102, 103, 104]. Furthermore the thermal power in nanotube ropes has been explained by phonon drag using the Boltzmann equation [105], which successfully explain the experiments [106].

2.3.1 Backscattering from impurities in metallic nanotubes

The resistance of any material with lattice structure is determined by the phonons at high temperatures and the impurity scattering at low temperatures [18, p.163], i.e. a Bloch wave does not give rise to resistance. We therefore consider an impurity bound to the surface of the tube by Van der Waals forces as is often the case (as previously described on page 27), which makes *the impurity potential* $V(\mathbf{r})$ *slowly varying on a scale of the interatomic distance* $a_{\text{C-C}}$. The impurity potential $V(\mathbf{r})$ is regarded as a perturbation to the Hamiltonian (2.11) and the matrix elements $\langle\psi_{\mathbf{k}'}|V(\mathbf{r})|\psi_{\mathbf{k}}\rangle$ of the potential between the Bloch states (2.12) describe the scattering probability $\mathbf{k} \to \mathbf{k}'$ due to the (single) impurity and is therefore connected to the conductivity as shown in [101]. Such an impurity potential has previously been considered in the Dirac neutrino scheme [91, 92], where the backscattering was shown to be absent to all orders in the impurity potential leading to a large conductivity.

We describe this calculation in detail, since it essentially can be used again, when we do the Coulomb matrix element, needed to find the Coulomb drag between the shells in a multiwall nanotube as we shall see in section 2.3.2.

Graphene

The impurity matrix element for two general Bloch states (2.12) of graphene is:

$$\begin{aligned}\langle\psi_{\mathbf{k}'}|V(\mathbf{r})|\psi_{\mathbf{k}}\rangle = \frac{1}{N}\int \mathrm{d}\mathbf{r}\sum_{\mathbf{R}'_A} e^{-i\mathbf{k}'\cdot\mathbf{R}'_A}\Big(\alpha'^{*}\Psi^{*}(\mathbf{r}-\mathbf{R}'_A)+\beta'^{*}\Psi^{*}(\mathbf{r}-\mathbf{R}'_A-\mathbf{d})\Big)\\ \times V(\mathbf{r})\sum_{\mathbf{R}_A} e^{i\mathbf{k}\cdot\mathbf{R}_A}\Big(\alpha\Psi(\mathbf{r}-\mathbf{R}_A)+\beta\Psi(\mathbf{r}-\mathbf{R}_A-\mathbf{d})\Big) \qquad (2.60)\end{aligned}$$

and reordering the terms we get

$$\begin{aligned}\langle\psi_{\mathbf{k}'}|V(\mathbf{r})|\psi_{\mathbf{k}}\rangle = \frac{1}{N}\sum_{\mathbf{R}'_A,\mathbf{R}_A} e^{-i\mathbf{k}'\cdot\mathbf{R}'_A+i\mathbf{k}\cdot\mathbf{R}_A}\Bigg[\alpha'^{*}\alpha\int \mathrm{d}\mathbf{r}\Psi^{*}(\mathbf{r}-\mathbf{R}'_A)V(\mathbf{r})\Psi(\mathbf{r}-\mathbf{R}_A) \quad (\star)\\ +\alpha'^{*}\beta\int \mathrm{d}\mathbf{r}\Psi^{*}(\mathbf{r}-\mathbf{R}'_A)V(\mathbf{r})\Psi(\mathbf{r}-\mathbf{R}_A-\mathbf{d}) \qquad (\star\star)\\ +\beta'^{*}\alpha\int \mathrm{d}\mathbf{r}\Psi^{*}(\mathbf{r}-\mathbf{R}'_A-\mathbf{d})V(\mathbf{r})\Psi(\mathbf{r}-\mathbf{R}_A) \qquad (\star\star')\\ +\beta'^{*}\beta\int \mathrm{d}\mathbf{r}\Psi^{*}(\mathbf{r}-\mathbf{R}'_A-\mathbf{d})V(\mathbf{r})\Psi(\mathbf{r}-\mathbf{R}_A-\mathbf{d})\Bigg], \qquad (\star')\end{aligned}$$

where the integrals are over the surface of the N unit cells of graphene. The atomic orbitals Ψ are localized at the lattice points and the impurity potential $V(\mathbf{r})$ is slowly varying, which makes the integral in the first term $(\star)$:

$$\int \mathrm{d}\mathbf{r}\Psi^{*}(\mathbf{r}-\mathbf{R}'_A)V(\mathbf{r})\Psi(\mathbf{r}-\mathbf{R}_A) \simeq V(\mathbf{R}_A)\delta_{\mathbf{R}_A,\mathbf{R}'_A} \qquad (2.61)$$

still using only nearest neighbour overlap. The integral in $(\star')$ is found in the same way to be $V(\mathbf{R}_A+\mathbf{d})\delta_{\mathbf{R}_A,\mathbf{R}'_A}$. By using the assumption of $V(\mathbf{r})$ to be slowly varying on a scale of $a_{\text{C-C}}=|\mathbf{d}|$ we see the integrals in $(\star')$ and $(\star)$ are the same: $V(\mathbf{R}_A+\mathbf{d})\simeq V(\mathbf{R}_A)$. Note that in this calculation it is not enough to assume slow variation of $V(\mathbf{r})$ on a scale of the width of Ψ, which is only needed in eq.(2.61), but also on the longer scale of the interatomic distance $a_{\text{C-C}}$. The term $(\star\star)$ including the sum over the lattice in the nearest neighbour approximation is found as in eq.(2.21) and again by using the localization of Ψ and slow variation of $V(\mathbf{r})$:

$$\sum_{\mathbf{R}'_A,\mathbf{R}_A} e^{-i\mathbf{k}'\cdot\mathbf{R}'_A+i\mathbf{k}\cdot\mathbf{R}_A}\int \mathrm{d}\mathbf{r}\Psi^*(\mathbf{r}-\mathbf{R}'_A)V(\mathbf{r})\Psi(\mathbf{r}-\mathbf{R}_A-\mathbf{d})$$

$$\simeq \sum_{\mathbf{R}_A} e^{i\mathbf{k}\cdot\mathbf{R}_A}V(\mathbf{R}_A)\sum_{\mathbf{R}'_A} e^{-i\mathbf{k}'\cdot\mathbf{R}'_A}\int \mathrm{d}\mathbf{r}\Psi^*(\mathbf{r}-\mathbf{R}'_A)\Psi(\mathbf{r}-\mathbf{R}_A-\mathbf{d}) \tag{2.62}$$

$$=\sum_{\mathbf{R}_A} e^{i\mathbf{k}\cdot\mathbf{R}_A}V(\mathbf{R}_A)e^{-i\mathbf{k}'\cdot\mathbf{R}_A}s_0\Upsilon(\mathbf{k}')=s_0\Upsilon(\mathbf{k}')\sum_{\mathbf{R}_A} e^{i(\mathbf{k}-\mathbf{k}')\cdot\mathbf{R}_A}V(\mathbf{R}_A). \tag{2.63}$$

In eq.(2.62) we could equally well have taken $V(\mathbf{R}'_A)$ outside the integral and done the sum over $\mathbf{R}_A$ because of the assumed slow variation of the potential. This procedure would have resulted in $\Upsilon(\mathbf{k})$ instead of $\Upsilon(\mathbf{k}')$. The sum over $\mathbf{R}_A$ in eq.(2.63) is a sum over the Fourier transform at different reciprocal lattice vectors (as we shall see shortly in eq.(2.65)) and due to the slow variation of $V(\mathbf{R}_A)$ the Fourier transform is a peak-like function around $\mathbf{k}-\mathbf{k}'=\mathbf{G}$, i.e. there is no difference in using $\mathbf{k}$ or $\mathbf{k}'$ in Υ, since $\Upsilon(\mathbf{k}+\mathbf{G})=\Upsilon(\mathbf{k})$.

The $(\star\star')$ term is found in the same way to be:

$$\sum_{\mathbf{R}_A,\mathbf{R}'_A} e^{i\mathbf{k}\cdot\mathbf{R}_A-i\mathbf{k}'\cdot\mathbf{R}'_A}\int \mathrm{d}\mathbf{r}\Psi^*(\mathbf{r}-\mathbf{R}'_A-\mathbf{d})V(\mathbf{r})\Psi(\mathbf{r}-\mathbf{R}_A)$$

$$\simeq s_0\Upsilon^*(\mathbf{k})\sum_{\mathbf{R}_A} e^{i(\mathbf{k}-\mathbf{k}')\cdot\mathbf{R}_A}V(\mathbf{R}_A), \tag{2.64}$$

where we could as well have obtained $\Upsilon^*(\mathbf{k}')$ as explained above.

In all the terms we now have the sum over the potential at different lattice sites and by inserting the Fourier transform[33] of the potential we get:

$$\frac{1}{N}\sum_{\mathbf{R}_A} e^{i(\mathbf{k}-\mathbf{k}')\cdot\mathbf{R}_A}V(\mathbf{R}_A)=\frac{1}{\mathcal{A}}\sum_{\mathbf{G}} V(\mathbf{k}'-\mathbf{k}+\mathbf{G}), \tag{2.65}$$

where the relation $\sum_{\mathbf{R}_A} e^{i\mathbf{k}\cdot\mathbf{R}_A}=N\sum_{\mathbf{G}}\delta_{\mathbf{k},\mathbf{G}}$ was used and $\mathcal{A}$ is the area of the N unit cells of graphene.

[33] We use the convention from [18] for a finite system of area $\mathcal{A}$: $f(\mathbf{r})=\frac{1}{\mathcal{A}}\sum_{\mathbf{q}} e^{i\mathbf{q}\cdot\mathbf{r}}f(\mathbf{q})$ with the inverse $f(\mathbf{q})=\int_{\mathcal{A}}\mathrm{d}\mathbf{r}e^{-i\mathbf{q}\cdot\mathbf{r}}f(\mathbf{r})$.

Collecting all the terms the matrix element for a single impurity with a slowly varying potential for graphene is:

$$\langle\psi_{\mathbf{k}'}|V(\mathbf{r})|\psi_{\mathbf{k}}\rangle = \frac{1}{\mathcal{A}}\left[\alpha\alpha'^{*}+\beta\beta'^{*}+s_0\Big(\alpha'^{*}\beta\Upsilon(\mathbf{k}')+\alpha\beta'^{*}\Upsilon^{*}(\mathbf{k})\Big)\right]\sum_{\mathbf{G}}V(\mathbf{k}'-\mathbf{k}+\mathbf{G})$$
$$\equiv g(\mathbf{k},\mathbf{k}')\frac{1}{\mathcal{A}}\sum_{\mathbf{G}}V(\mathbf{k}'-\mathbf{k}+\mathbf{G}), \qquad (2.66)$$

where we have introduced $g = g(\mathbf{k},\mathbf{k}')$. Note that we chose the argument in the Υ function in g, so that $\langle\psi_{\mathbf{k}'}|V(\mathbf{r})|\psi_{\mathbf{k}}\rangle = \langle\psi_{\mathbf{k}}|V(\mathbf{r})|\psi_{\mathbf{k}'}\rangle^{*}$ is (formally[34]) fulfilled remembering the $\mathbf{k}$ dependence of α and β from eq.(2.25). For plane wave states the matrix element is just the Fourier transform (times $\frac{1}{\mathcal{A}}$), so the g function is the factor carrying the information from the Bloch states. In [91, 92] g is found to be $g = \alpha\alpha'^{*}+\beta\beta'^{*}$, which is the essential part of g in the case of s_0 being zero.

Nanotubes and backscattering in metallic nanotubes

For a nanotube the same calculation as above can be carried out, e.g. by using the Bloch states $|\kappa,\mathfrak{m}\rangle$ eq.(2.33) for the primitive unit cell. The result is:

$$\langle\kappa',\mathfrak{m}'|V(\mathbf{r})|\kappa,\mathfrak{m}\rangle = \Big[\alpha\alpha'^{*}+\beta\beta'^{*}+s_0\Big(\alpha'^{*}\beta\Upsilon(\kappa',\mathfrak{m}')+\alpha\beta'^{*}\Upsilon^{*}(\kappa,\mathfrak{m})\Big)\Big]$$
$$\times\frac{1}{\mathfrak{n}\mathfrak{L}}\sum_{u,\tilde{u}\in\mathbb{Z}}V(\kappa'-\kappa+2\pi u,\mathfrak{m}'-\mathfrak{m}+\tilde{u}\mathfrak{n})$$
$$\equiv g(\kappa\mathfrak{m},\kappa'\mathfrak{m}')\frac{1}{\mathfrak{n}\mathfrak{L}}\sum_{u,\tilde{u}\in\mathbb{Z}}V(\kappa'-\kappa+2\pi u,\mathfrak{m}'-\mathfrak{m}+\tilde{u}\mathfrak{n}), \quad (2.67)$$

where we have Fourier transformed in the coordinates[35] l,p to κ and $\mathfrak{m}$.

General metallic tube: Instead of using the primitive unit cell and the matrix element (2.67) we use the translational unit cell. By using the (larger) translational unit cell and k,n_c instead of the primitive unit cell and κ,$\mathfrak{m}$ in this calculation we obtain a matrix element and a g factor, which is (generally) not *explicitly* periodic with the reciprocal lattice vectors, since the Bloch functions are not explicitly periodic functions. Therefore we have to make the matrix element and g factors periodic by hand by repeating the values from the FBZ (see also the comment on page 26).

We consider the impurity matrix element for a general metallic (n,m) nanotube by using the states $\psi^{\xi}_{k,n_c^{\varsigma}}$ eq.(2.58) near $\varepsilon_{\mathrm{F}} = 0$ from the expansion around the $\mathbf{K}_{\varsigma=\pm1}$ points. The wave vector $\mathbf{k}$ of graphene is again restricted by the periodic

[34] By another choice this is still true since as before $\mathbf{k}\sim\mathbf{k}'+\mathbf{G}$.

[35] Explicit: $V(l,p) = \frac{1}{\mathfrak{n}\mathfrak{L}}\sum_{\mathfrak{m}=0}^{\mathfrak{n}-1}\sum_{\kappa}V(\kappa,\mathfrak{m})e^{i\frac{2\pi\mathfrak{m}p}{\mathfrak{n}}+i\kappa l}$ and $V(\kappa,\mathfrak{m}) = \sum_{p,l}V(l,p)e^{-i\frac{2\pi\mathfrak{m}p}{\mathfrak{n}}-i\kappa l}$.

boundary condition to be the one dimensional wave vector k along the tube and n_c determined by ς: $n_c = n_c^{\varsigma=\pm 1}$. In this section we first calculate the general g factor for a metallic tube and then consider backscattering.

To obtain the g factor from the matrix element eq.(2.66) we use $\boldsymbol{\mathfrak{K}} = \mathfrak{K}_T \frac{\mathbf{T}}{|\mathbf{T}|}$ to find $\Upsilon(\mathbf{k}) = \frac{\sqrt{3}a}{2}\mathfrak{K}_T\left(\frac{i(m-n)-\varsigma\sqrt{3}(n+m)}{2\sqrt{n^2+m^2+mn}}\right)$ from eq.(2.52) and inserting eq.(2.58) we have after some algebra:

$$g(k, n_c^{\varsigma}, \xi; k', n_c^{\varsigma'}, \xi') = \frac{1}{2}\left(\xi\xi' f_{n,m,\varsigma,\varsigma'} + 1\right) - s_0 \frac{\sqrt{3}a(\xi'\mathfrak{K}'_T + \xi\mathfrak{K}_T)}{4}, \tag{2.68}$$

where we have introduced

$$f_{n,m,\varsigma,\varsigma'} = \delta_{\varsigma,\varsigma'} - \frac{n^2+m^2+4mn}{2(n^2+m^2+mn)}(1-\delta_{\varsigma,\varsigma'}) + i\frac{\sqrt{3}\varsigma(m^2-n^2)}{2(n^2+m^2+mn)}(1-\delta_{\varsigma,\varsigma'}). \tag{2.69}$$

Now we have the general form of the matrix element for the scattering process $(k, \xi, \varsigma) \to (k', \xi', \varsigma')$ by a single impurity.

We now consider backscattering, i.e. a scattering process where the velocity before and after the process are opposite: $\xi = -\xi'$ (from $\varepsilon^{\xi}_{\mathfrak{K}_T, n_c^{\varsigma}} = \xi\hbar v_0 \mathfrak{K}_T$ eq.(2.58)). If we naively used plane waves instead of Bloch functions we would get only the Fourier transformed as the matrix element. This would lead to the expectation of a large backscattering, since the band structure for metallic tubes (see e.g. figure 2.7) reveals a possible small momentum backscattering processes for a slightly shifted Fermi level. We shall now see that the situation for Bloch states are more complicated. Backscattering between Bloch states is in general possible for both $\varsigma = \varsigma'$ and $\varsigma = -\varsigma'$ as we will examine now.

Backscattering for $\varsigma = \varsigma'$: For $\varsigma = \varsigma'$ we have the initial and final state in the scattering process around the same $\mathbf{K}_\varsigma$ point, i.e. we have a small crystal momentum transfer in the backscattering process (see e.g. fig. 2.3). Furthermore $n_c^{\varsigma} = n_c^{\varsigma'}$ which means that $\mathfrak{m} = \mathfrak{m}'$, so there is no exchange of crystal angular momentum in the backscattering process. For $\varsigma = \varsigma'$ we have $f_{n,m,\varsigma,\varsigma'} = 1$ so eq.(2.68) simplifies to

$$g(k, n_c^{\varsigma}, \xi; k', n_c^{\varsigma}, -\xi) = s_0 \frac{\sqrt{3}a\xi(\mathfrak{K}'_T - \mathfrak{K}_T)}{4}. \tag{2.70}$$

This g factor only contains terms neglected in [91, 92] and we will now see that g is indeed small. To find the conductivity from the impurity scattering by the Fermi Golden rule (or first Born approximation), only the squared matrix element is needed (see [101]), so this is considered now. Since $\varsigma = \varsigma'$ we have $n_c^{\varsigma} = n_c^{\varsigma'}$ and therefore $\mathfrak{K}'_T - \mathfrak{K}_T = k' - k \in]-\frac{\pi}{|\mathbf{T}|}, \frac{\pi}{|\mathbf{T}|}]$, since both k and k' are near either $k = 0$, $k = \frac{2\pi}{3|\mathbf{T}|}$ or $k = -\frac{2\pi}{3|\mathbf{T}|}$. So the squared g factor is:

$$|g(k, n_c^{\varsigma}, \xi; k', n_c^{\varsigma}, -\xi)|^2 = s_0^2 \frac{3a^2(k'-k)^2}{16}. \tag{2.71}$$

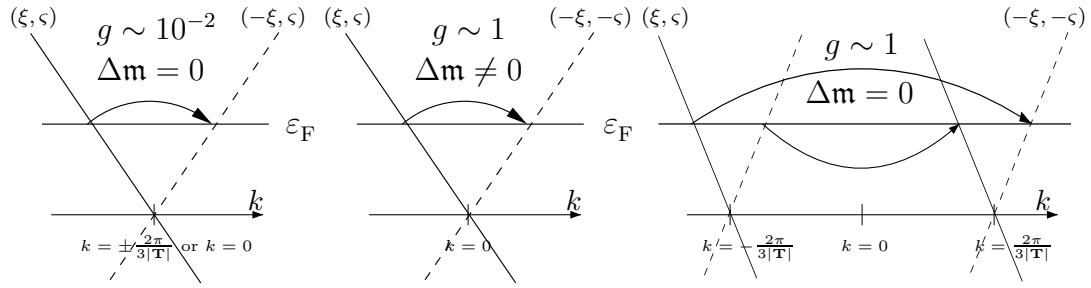

Figure 2.8: The three types of backscattering processes in any metallic nanotube with a slightly shifted Fermi level, which are all suppressed processes (see summery on p.43). Remember from section 2.2.4 that all metallic tubes have four crossings of the Fermi level ($\varepsilon_{\rm F}=0$) at either $\pm\frac{2\pi}{3|\mathbf{T}|}$ or doubly degenerated at $k=0$ and the (absolute value of the) velocity is the same v_0. (Left): Backscattering (for $\varsigma=\varsigma'$) with no crystal angular momentum ($\Delta\mathfrak{m}=0$) and a small wave vector $|k'-k|\sim\frac{2\varepsilon_{\rm F}}{\hbar v_0}$ exchange. This process is suppressed by $g\lesssim 10^{-4}$ from eq.(2.72). This is a scattering process around $k=0$, $k=\frac{2\pi}{3|\mathbf{T}|}$ or $k=-\frac{2\pi}{3|\mathbf{T}|}$, i.e. the whole FBZ is not showed. (Center): Scattering around $k=0$ (for $\varsigma=-\varsigma'$) between different crystal angular momentum states, which suppresses the backscattering even though $g\sim 1$ eq.(2.75). Typical example is an zigzag tube. (Right): Backscattering with a large wave vector transfer (for $\varsigma=-\varsigma'$) between states with the same crystal angular momentum and $g\sim 1$ from eq.(2.75). Note that the distance between the points $\pm\frac{2\pi}{3|\mathbf{T}|}$ are not to scale (i.e. $\frac{2\varepsilon_{\rm F}}{\hbar v_0}\ll\frac{4\pi}{3|\mathbf{T}|}$). An armchair tube is an typical example.

We now find the order of magnitude of $|g|^2$ in the phase space available for scattering, which is the phase space near the Fermi level due to Fermi functions in the collision integral. Therefore for wave vectors near a shifted Fermi level we have $(k'-k)^2\simeq\left(\frac{2\varepsilon_{\rm F}}{\hbar v_0}\right)^2=\frac{16\varepsilon_{\rm F}^2}{3a^2\gamma_0^2}$, so

$$\left|g\left(|k'-k|=\frac{2\varepsilon_{\rm F}}{\hbar v_0},\xi=-\xi',\varsigma=\varsigma'\right)\right|^2=s_0^2\left(\frac{\varepsilon_{\rm F}}{\gamma_0}\right)^2\lesssim 10^{-4}\tag{2.72}$$

by using $s_0\sim 0.1$, $\gamma_0=3$eV and doping of order $\varepsilon_{\rm F}\lesssim 0.3$eV. The Fourier transform on the other hand is large due to the small argument (i.e. small crystal momentum transfer and no crystal angular momentum transfer), but without specifying the potential we cannot say how large. In the plane wave approximation the matrix element is only the Fourier transform of the potential and therefore eq.(2.72) shows a strong suppression of backscattering of the plane wave result due to the Bloch functions factor g, when $\varsigma=\varsigma'$.

Backscattering for $\varsigma=-\varsigma'$: Backscattering ($\xi=-\xi'$) in the case $\varsigma=-\varsigma'$ is now examined. The $|g|^2=(\mathrm{Re}(g))^2+(\mathrm{Im}(g))^2$ factor is found from eq.(2.68) and the

definition eq.(2.69) to be:

$$\begin{aligned}\big(\mathrm{Re}(g)\big)^2 &= \left[\frac{1-\mathrm{Re}(f_{n,m,\varsigma,-\varsigma})}{2}+s_0\frac{\sqrt{3}\xi a(\mathfrak{K}'_T-\mathfrak{K}_T)}{4}\right]^2\\ &= \left[\frac{1}{2}\Bigg(1+\underbrace{\frac{n^2+m^2+4mn}{2(n^2+m^2+mn)}}_{\in[\frac{1}{2},1]\text{ for all }(n,m)}\Bigg)+s_0\frac{\sqrt{3}\xi a(\mathfrak{K}'_T-\mathfrak{K}_T)}{4}\right]^2\end{aligned} \tag{2.73}$$

and

$$\big(\mathrm{Im}(g)\big)^2=\frac{1}{4}\big(\mathrm{Im}(f_{n,m,\varsigma,-\varsigma})\big)^2=\frac{3}{16}\underbrace{\left(\frac{m^2-n^2}{n^2+m^2+nm}\right)^2}_{\in[0,1]\text{ for all }(n,m)}. \tag{2.74}$$

Note that the (n,m) dependent factor in $(\mathrm{Re}(g))^2$ is between $\frac{1}{2}$ (zigzag) and 1 (armchair) and the (n,m) dependent prefactor in $(\mathrm{Im}(g))^2$ between 0 (armchair) and 1 (zigzag) for all nanotubes. For energies near the Fermi level we have $\varepsilon_{\mathrm{F}}\simeq\xi\hbar v_0\mathfrak{K}_T$ and $\varepsilon_{\mathrm{F}}\simeq-\xi\hbar v_0\mathfrak{K}'_T$, so $a(\mathfrak{K}'_T-\mathfrak{K}_T)=-a\xi\frac{2\varepsilon_{\mathrm{F}}}{\hbar v_0}=-\xi\frac{4}{\sqrt{3}}\frac{\varepsilon_{\mathrm{F}}}{\gamma_0}$. Since $\frac{\varepsilon_{\mathrm{F}}}{\gamma_0}\lesssim 0.1$ and by the s_0 factor, the second term in the square brackets in the real part of $|g|^2$ (2.73) can be neglected for the relevant phase space and we have

$$|g_{\varepsilon\sim\varepsilon_{\mathrm{F}}}|^2\simeq\frac{1}{4}\left(1+\frac{n^2+m^2+4mn}{2(n^2+m^2+mn)}\right)^2+\frac{3}{16}\left(\frac{m^2-n^2}{n^2+m^2+mn}\right)^2\in\left[\frac{3}{4},1\right] \tag{2.75}$$

for all (n,m), i.e. $\frac{3}{4}$ for zigzag, 1 for armchair and in between for all chiral tubes. Therefore this kind of backscattering ($\varsigma=-\varsigma'$) does *not* have a suppressed g factor compared to the plane wave case.

Let us now consider the linear and angular crystal momentum exchange for a backscattering process with $\varsigma=-\varsigma'$. Here we have two cases: a small crystal momentum transfer $|k'-k|\simeq\frac{2\varepsilon_{\mathrm{F}}}{\hbar v_0}$ accompanied by an crystal angular momentum exchange $\Delta\mathfrak{m}\equiv\mathfrak{m}-\mathfrak{m}'\neq 0$ (figure 2.8(center)) and a large crystal momentum transfer of order $|k'-k|\sim\frac{2\pi}{3|\mathbf{T}|}$ (Umklapp) accompanied by no crystal angular momentum exchange $\Delta\mathfrak{m}=0$ (figure 2.8(right)).

For $\varsigma=-\varsigma'$ we have $n_c^{\varsigma}-n_c^{\varsigma'}=\varsigma\frac{m-n}{3}$ and therefore a crystal angular momentum exchange given by

$$\Delta\mathfrak{m}=\varsigma\frac{m-n}{3}\quad(\text{modulo }\mathfrak{n}), \tag{2.76}$$

since $\mathfrak{m}=n_c$ (modulo $\mathfrak{n}$).

To find the exchanged crystal (linear) momentum we have to consider the crossing of $\varepsilon_{\mathrm{F}}=0$ with the bands for k and k', which are $\mathbf{K}_{\varsigma}\cdot\frac{\mathbf{T}}{|\mathbf{T}|}$ and $\mathbf{K}_{\varsigma'}\cdot\frac{\mathbf{T}}{|\mathbf{T}|}$ (see eq.(2.57)) up to a reciprocal lattice vector $\frac{2\pi}{|\mathbf{T}|}s$ ($s\in\mathbb{Z}$), respectively. Therefore

the crossing points may be different, so we can get a large momentum transfer, but can also be the same giving a small momentum transfer. This is in contrast to the $\varsigma = \varsigma'$ case, where it was always the same crossing point leading to only the small momentum transfer process. Therefore (for $\varsigma = -\varsigma'$) $|k - k'|$ at the Fermi level is either $\frac{2\varepsilon_F}{\hbar v_0}$ as for $|\mathfrak{K}_T - \mathfrak{K}'_T|$ or substantially larger of order $\sim \frac{2\pi}{3|\mathbf{T}|}$. Note that the larger momentum transfer is an Umklapp process, since if e.g. $k \sim \frac{2\pi}{3|\mathbf{T}|}$ and $k' \sim -\frac{2\pi}{3|\mathbf{T}|}$ then $|k' - k| \sim \frac{4\pi}{3|\mathbf{T}|} = \frac{2\pi}{|\mathbf{T}|} - \frac{2\pi}{3|\mathbf{T}|}$, which is $-\frac{2\pi}{3|\mathbf{T}|}$ up to a reciprocal lattice vector.

A priori one can have four cases of backscattering for $\varsigma = -\varsigma'$: (1) $\Delta\mathfrak{m} = 0$ and $|k' - k|$ small, (2) $\Delta\mathfrak{m} \neq 0$ and $|k' - k|$ small, (3) $\Delta\mathfrak{m} = 0$ and $|k' - k|$ large and (4) $\Delta\mathfrak{m} \neq 0$ and $|k' - k|$ large. By calculating the crossing of the Fermi level (from eq.(2.57)) and $\Delta\mathfrak{m}$ (2.76) for all metallic tubes with $n < 100$ and $m < 100$ using *Mathematica*, we only find backscattering of type (2) (only around $k = 0$) and (3) as seen on figure 2.8(center) and 2.8(right), respectively. This can be shown by number theoretical arguments. Especially the absence of a backscattering with $\Delta\mathfrak{m} = 0$ and $|k' - k|$ small (type (1)) is interesting, since this would have a large Fourier transform leading to a large backscattering (since $g \sim 1$). So even though $g \sim 1$ for $\varsigma = -\varsigma'$ eq.(2.75) the backscattering is suppressed by either a crystal angular momentum transfer $\Delta\mathfrak{m} \neq 0$ or a large crystal momentum transfer $|k' - k| \sim \frac{2\pi}{3|\mathbf{T}|}$ in the Fourier transformed.

In summery, we have now found the matrix element for a single impurity with a slowly varying potential in eq.(2.67) valid for any nanotube. For all the metallic nanotubes we found three types of suppression of backscattering:

- $\underline{\varsigma = \varsigma'}$: $g \lesssim 10^{-4}$, $\Delta\mathfrak{m} = 0$, $|k' - k| \sim \frac{2\varepsilon_F}{\hbar v_0}$, i.e. a suppression from the g factor (figure 2.8(left)). Examples: (n, n), $(7, 4)$ or $(15, 6)$ around $k = \pm\frac{2\pi}{3|\mathbf{T}|}$.

- $\underline{\varsigma = -\varsigma'}$: $g \sim 1$, $\Delta\mathfrak{m} \neq 0$, $|k' - k| \sim \frac{2\varepsilon_F}{\hbar v_0}$, i.e. a suppression from the crystal angular momentum exchange (figure 2.8(center)). Examples: $(n, 0)$ $\Delta\mathfrak{m} = \pm\frac{n}{3}$, $(9, 30)$ $\Delta\mathfrak{m} = \pm 1$, $(9, 27)$ $\Delta\mathfrak{m} = \pm 3$, $(18, 12)$ $\Delta\mathfrak{m} = \pm 2$ or $(24, 12)$ $\Delta\mathfrak{m} = \pm 4$ around $k = 0$.

- $\underline{\varsigma = -\varsigma'}$: $g \sim 1$, $\Delta\mathfrak{m} = 0$, $|k' - k| \sim \frac{2\pi}{3|\mathbf{T}|}$, i.e. a suppression from the large crystal momentum exchange just as in the plane wave approximation (figure 2.8(right)). Examples: (n, n), $(7, 4)$, $(15, 6)$, or $(28, 25)$.

So we have found a suppression of backscattering in the tight binding scheme as also found by Ando et.al. [91, 92] (see also [108]) in the $\mathbf{k}\cdot\mathbf{p}$ scheme, even though the situations seen in figure 2.8(center/right) are not considered in those papers.

2.3.2 The Coulomb matrix element using Bloch states

To find the Coulomb drag between different tubes in a multiwall carbon nanotube it is essential to know the Coulomb interaction between the electrons

in the different tubes (see section 1.4). Therefore the Coulomb matrix element for electrons in different shells in a multiwall nanotube is now found using the tight binding states. The Coulomb interaction $V_{12}(|\mathbf{r}_1 - \mathbf{r}_2|)$ between electrons in different shells (with a separation of order 0.5nm) is slowly varying on the scale of the unit cell $a_{\text{C-C}}$ and therefore we can calculate the Coulomb matrix element in the same way as we did for the slowly varying impurity potential. We begin with a calculation of the Coulomb matrix element between electrons in two different nearby graphene layers in a graphite crystal using the Bloch states of the individual graphene layers eq.(2.12).

Coulomb interaction between different layers in Graphite

The Coulomb matrix element for two parallel graphene layers (labelled 1 and 2) using the Bloch states $\psi_{\mathbf{k}}(\mathbf{r})$ is:

$$\begin{aligned}\langle \mathbf{k}_1' \mathbf{k}_2' | V_{12}(|\mathbf{r}_1 - \mathbf{r}_2|) | \mathbf{k}_1 \mathbf{k}_2 \rangle &= \int \mathrm{d}\mathbf{r}_1 \int \mathrm{d}\mathbf{r}_2 \psi^*_{\mathbf{k}_1'}(\mathbf{r}_1) \psi^*_{\mathbf{k}_2'}(\mathbf{r}_2) V_{12}(|\mathbf{r}_1 - \mathbf{r}_2|) \psi_{\mathbf{k}_1}(\mathbf{r}_1) \psi_{\mathbf{k}_2}(\mathbf{r}_2) \\ &= \int \mathrm{d}\mathbf{r}_1 \psi^*_{\mathbf{k}_1'}(\mathbf{r}_1) \left[\int \mathrm{d}\mathbf{r}_2 \ \psi^*_{\mathbf{k}_2'}(\mathbf{r}_2) V_{12}(|\mathbf{r}_1 - \mathbf{r}_2|) \psi_{\mathbf{k}_2}(\mathbf{r}_2) \right] \psi_{\mathbf{k}_1}(\mathbf{r}_1). \end{aligned} \tag{2.77}$$

The square bracket can be found in the same way as the impurity potential matrix element in section 2.3.1 remembering that the Coulomb potential is a function of two coordinates, so

$$\begin{aligned}&\langle \mathbf{k}_1' \mathbf{k}_2' | V_{12}(|\mathbf{r}_1 - \mathbf{r}_2|) | \mathbf{k}_1 \mathbf{k}_2 \rangle \simeq \\ &\int \mathrm{d}\mathbf{r}_1 \ \psi^*_{\mathbf{k}_1'}(\mathbf{r}_1) \left[g_2(\mathbf{k}_2, \mathbf{k}_2') \frac{1}{N_2} \sum_{\mathbf{R}_A^{(2)}} V_{12}(|\mathbf{r}_1 - \mathbf{R}_A^{(2)}|) e^{i(\mathbf{k}_2 - \mathbf{k}_2') \cdot \mathbf{R}_A^{(2)}} \right] \psi_{\mathbf{k}_1}(\mathbf{r}_1) \\ &\simeq g_1(\mathbf{k}_1, \mathbf{k}_1') g_2(\mathbf{k}_2, \mathbf{k}_2') \left[\frac{1}{N_1 N_2} \sum_{\mathbf{R}_A^{(1)}, \mathbf{R}_A^{(2)}} V_{12}(|\mathbf{R}_A^{(1)} - \mathbf{R}_A^{(2)}|) e^{i(\mathbf{k}_2 - \mathbf{k}_2') \cdot \mathbf{R}_A^{(2)} + i(\mathbf{k}_1 - \mathbf{k}_1') \cdot \mathbf{R}_A^{(1)}} \right], \end{aligned} \tag{2.78}$$

by using the impurity potential result again at the last equality. The $g_i(\mathbf{k}_i, \mathbf{k}_i')$ function is the same as in eq.(2.66). The sum over the potential at different lattice sites can be found by inserting the Fourier transform $V_{12}(|\mathbf{R}_A^{(1)} - \mathbf{R}_A^{(2)}|) = \frac{1}{\mathcal{A}} \sum_{\mathbf{q}} V_{12}(\mathbf{q}) e^{i\mathbf{q} \cdot (\mathbf{R}_A^{(1)} - \mathbf{R}_A^{(2)})}$ and we get:

$$\begin{aligned}&\frac{1}{N_1 N_2} \sum_{\mathbf{R}_A^{(1)}, \mathbf{R}_A^{(2)}} V_{12}(|\mathbf{R}_A^{(1)} - \mathbf{R}_A^{(2)}|) e^{i(\mathbf{k}_2 - \mathbf{k}_2') \cdot \mathbf{R}_A^{(2)} + i(\mathbf{k}_1 - \mathbf{k}_1') \cdot \mathbf{R}_A^{(1)}} \\ &\qquad = \frac{1}{\mathcal{A}} \frac{1}{N_1 N_2} \sum_{\mathbf{q}} V_{12}(\mathbf{q}) \sum_{\mathbf{R}_A^{(1)}} e^{i(\mathbf{k}_1 - \mathbf{k}_1' + \mathbf{q}) \cdot \mathbf{R}_A^{(1)}} \sum_{\mathbf{R}_A^{(2)}} e^{i(\mathbf{k}_2 - \mathbf{k}_2' - \mathbf{q}) \cdot \mathbf{R}_A^{(2)}} \\ &\qquad = \frac{1}{\mathcal{A}} \sum_{\mathbf{G}_1, \mathbf{G}_2} V_{12}(\mathbf{k}_1' - \mathbf{k}_1 + \mathbf{G}_1) \delta_{\mathbf{k}_1 + \mathbf{k}_2, \mathbf{k}_1' + \mathbf{k}_2' + \mathbf{G}_1 + \mathbf{G}_2} \end{aligned} \tag{2.79}$$

where we used $\sum_{\mathbf{R}_A^{(i)}} e^{i\mathbf{k}_i\cdot\mathbf{R}_A^{(i)}} = N_i \sum_{\mathbf{G}_i} \delta_{\mathbf{k}_i,\mathbf{G}_i}$ in the second equality. Note that we get the crystal momentum conservation including the Umklapp processes ($\mathbf{G}_i \neq 0$), which are less important since the Fourier transform is decreasing. The Coulomb matrix element for graphene is therefore:

$$\langle \mathbf{k}_1'\mathbf{k}_2'|V_{12}(|\mathbf{r}_1-\mathbf{r}_2|)|\mathbf{k}_1\mathbf{k}_2\rangle = \\ g_1(\mathbf{k}_1,\mathbf{k}_1')g_2(\mathbf{k}_2,\mathbf{k}_2')\frac{1}{\mathcal{A}}\sum_{\mathbf{G}_1,\mathbf{G}_2} V_{12}(\mathbf{k}_1'-\mathbf{k}_1+\mathbf{G}_1)\delta_{\mathbf{k}_1+\mathbf{k}_2,\mathbf{k}_1'+\mathbf{k}_2'+\mathbf{G}_1+\mathbf{G}_2}, \quad (2.80)$$

where $g_i(\mathbf{k}_i,\mathbf{k}_i') = \alpha_i\alpha_i'^* + \beta_i\beta_i'^* + s_0\Big(\alpha_i'^*\beta_i\Upsilon(\mathbf{k}_i') + \alpha_i\beta_i'^*\Upsilon^*(\mathbf{k}_i)\Big)$. Therefore the Coulomb matrix element has one g_i factor for each layer times the plane wave result of the Fourier transform of the Coulomb potential between the layers.

Coulomb interaction between different tubes in a multiwall tube

To find the Coulomb matrix element between two different tubes in a multiwall carbon nanotube using the product states of $|\kappa\mathfrak{m}\rangle$ eq.(2.33) we can use the same approach as for the two graphene layers (eq.(2.77) and eq.(2.78)). The result is:

$$\langle \kappa_1'\mathfrak{m}_1'\kappa_2'\mathfrak{m}_2'|V_{12}(|\mathbf{r}_1-\mathbf{r}_2|)|\kappa_1\mathfrak{m}_1\kappa_2\mathfrak{m}_2\rangle = \frac{g_1(\kappa_1\mathfrak{m}_1,\kappa_1'\mathfrak{m}_1')g_2(\kappa_2\mathfrak{m}_2,\kappa_2'\mathfrak{m}_2')}{\mathfrak{n}_1\mathfrak{L}_1\mathfrak{n}_2\mathfrak{L}_2} \quad (2.81)$$
$$\times\left[\sum_{l_1,l_2}\sum_{p_1=0}^{\mathfrak{n}_1-1}\sum_{p_2=0}^{\mathfrak{n}_2-1} V_{12}(|\mathbf{R}_{l_1p_1}-\mathbf{R}_{l_2p_2}|)e^{i(\kappa_2-\kappa_2')l_2+i(\kappa_1-\kappa_1')l_1+i\frac{2\pi}{\mathfrak{n}_2}(\mathfrak{m}_2-\mathfrak{m}_2')p_2+i\frac{2\pi}{\mathfrak{n}_1}(\mathfrak{m}_1-\mathfrak{m}_1')p_1}\right],$$

where the l_i sum is from $-\mathfrak{L}_i/2$ to $\mathfrak{L}_i/2$ and $\mathbf{R}_{l_ip_i} = l_i\mathbf{H}_i + p_i\mathbf{C}_{\mathfrak{n}_i}$ for tube $i = 1,2$ (see also section 2.2.2 and footnote on p.25). A Fourier transformed can be introduced into this sum in order to obtain a result similar to eq.(2.80). When this is done one has to consider the question whether the two carbon nanotubes are commeasurable or not, i.e. if the combined lattices form a periodic lattice or not. This is done in appendix C.

Here we use the following approximation for the Coulomb matrix element between the two tubes (n_1,m_1) and (n_2,m_2) using the translational unit cells:

$$\langle k_1'n_{c_1}'k_2'n_{c_2}'|V_{12}(|\mathbf{r}_1-\mathbf{r}_2|)|k_1n_{c_1}k_2n_{c_2}\rangle = \\ g_1(k_1n_{c_1},k_1'n_{c_1}')g_2(k_2n_{c_2},k_2'n_{c_2}')\frac{1}{2\pi L}\sum_{G_1,G_2}\sum_{u_1,u_2\in\mathbb{Z}} V_{12}(k_1'-k_1+G_1,\overbrace{n_{c_1}'-n_{c_1}}^{(\text{modulo }\mathfrak{n}_1)}+\mathfrak{n}_1u_1) \\ \times\delta_{k_1+k_2,k_1'+k_2'+G_1+G_2}\delta_{\underbrace{n_{c_1}'-n_{c_1}}_{(\text{modulo }\mathfrak{n}_1)}+\mathfrak{n}_1u_1,\underbrace{n_{c_2}'-n_{c_2}}_{(\text{modulo }\mathfrak{n}_2)}+\mathfrak{n}_2u_2}, \quad (2.82)$$

where $\mathbf{k}_i$ is restricted to k_i, n_{c_i} by using the periodic boundary condition (2.29). The reciprocal lattice vectors long the tube are $G_i = \frac{2\pi}{|\mathbf{T}_i|} u_i$ ($u_i \in \mathbb{Z}$), L is the length of the tubes (assumed to be of equal length) and we calculate n_{c_i} modulo $\mathfrak{n}_i$ in order to label the states using the crystal angular momentum. Note that the crystal angular momentum conservation law can be modified for commensurable tubes (see appendix C), so we should consider each case carefully. Remember that the g-factors are not a priori periodic functions, but are made periodic by hand. Furthermore, the Fourier transform are used as:

$$V_{12}(k,m) = \int_0^{2\pi} \mathrm{d}\theta \int_{-\frac{L}{2}}^{\frac{L}{2}} \mathrm{d}z V(\theta, z) e^{-ikz - im\theta}. \tag{2.83}$$

Therefore the Coulomb matrix element we use are products of the g_i factors stemming from the Bloch states and a sum over the Fourier transformed Coulomb potential.

Chapter 3

Derivation of the transresistivity from coupled Boltzmann equations

In section 1.2 we saw the basic definition of the transresistivity ρ_{21} and the motivation to study ρ_{21} in order to obtain information about the Coulomb drag phenomenon. In this chapter, we derive a formula for the transresistivity ρ_{21} for a multiwall carbon nanotube in terms of the two singlewall tubes involved. In the experimental setup seen on figure 3.1 there is a voltmeter on the drag system (subsystem 2), which makes the current through the drag system vanish. This and two coupled Boltzmann equations derived shortly are the key ingredients in the derivation of the transresistivity ρ_{21}.

The derivation given here includes a general band structure with several bands crossing the Fermi level ε_{F} and a Coulomb matrix element of the form eq.(2.82), i.e. including the g_i factors from the Bloch states and not only a Fourier transform of the Coulomb interaction[1]. Previously, a transresistivity formula for several bands were stated in [114] for the case of two dimensional, planar geometry where the interaction matrix element were only used as a Fourier transformed interaction times some simple $\mathbf{k}$ independent of selections rules. The derivation given here is a generalization of the coupled Boltzmann approach given in [52] for one (general) band crossing the Fermi level. The transresistivity for a single quadratic band were first derived in [6] (see also section 1.5). The geometry considered here is two coaxial cylinders as for a multiwall tube (see figure 3.1), where the electric fields and currents densities are along the cylinder axis, i.e. E_i and J_i are scalers. Coulomb drag for the coaxial geometry has been considered in [110] for a quadratic model with continuous rotational symmetry, i.e the model in appendix A.

The transresistivity (or transconductivity) can also be derived from microscopic principles using the Kubo formula, which states that the retarded current-

[1]The g_i factors were neglected in our first approach to the problem of Coulomb drag in multiwall nanotubes, see appendix G.

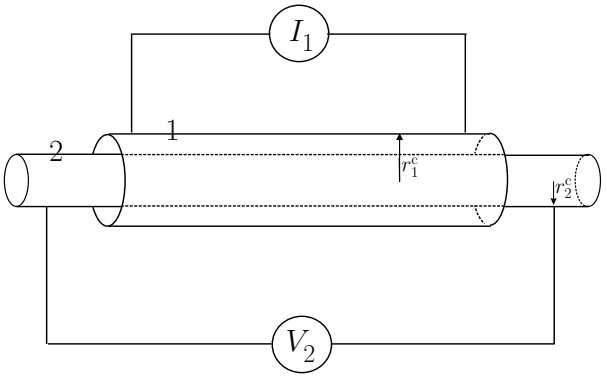

Figure 3.1: The geometry and labelling of a schematic setup to measure the Coulomb drag effect experimentally. A small bias on the outer cylinder gives a current I_1, which in turn induces a small voltage drop V_2 across the inner cylinder. From these quantities the transresistivity is found as $\rho_{21} = \frac{E_2}{J_1} = \frac{L_2 V_2}{2\pi r_1^c I_1}$.

current correlation function is proportional to the transconductivity [112]. This has some advantageous, e.g. one obtain a more general formula, which simplifies to the Boltzmann equation result in the DC, weak scattering limit. Furthermore it does not assume a voltmeter on one of the subsystems and therefore calculates the transresistivity in a symmetric setup, by doing perturbation theory using Feynman diagrams in the interaction Hamiltonian between the subsystems. In this sense the Kubo formula approach is more transparent that the Boltzmann approach. Note that in the DC limit the first order term is zero and the derived transresistivity is the second order term [112]. This derivation has not been generalized to include several bands.

Resistance and resistivity

For the sake of clarity the connection between resistance and resistivity in one, two and three dimensions are reviewed and a quasi one dimensional case is defined.

In three dimensions the current I is generally the integral of the current density $\mathbf{J}$ over the surface $\mathcal{S}$ which the current passes through:

$$I = \int_{\mathcal{S}} \mathbf{J} \cdot \mathrm{d}\mathbf{a}, \tag{3.1}$$

where d$\mathbf{a}$ is a surface element [119, p.213]. Only the homogeneous case is treated in this thesis and we therefore simplify to this case[2]. Therefore the current density in three dimensions (3D) is $J^{3\mathrm{D}} = \frac{I}{A}$ in the direction as seen on figure 3.2, where A is the cross section area. Furthermore, in all cases the voltage drop is $V = EL$, where L is the length of the system and E the magnitude of the static electric field along $\mathbf{J}$. Therefore, the connection between resistance R and resistivity ρ in 3D is:

$$R^{3\mathrm{D}} = \frac{V}{I} = \frac{L}{A}\frac{E}{J^{3\mathrm{D}}} \equiv \rho^{3\mathrm{D}}\frac{L}{A}, \tag{3.2}$$

[2]Variations in space can be included by introducing integrals over space such as in eq.(3.1).

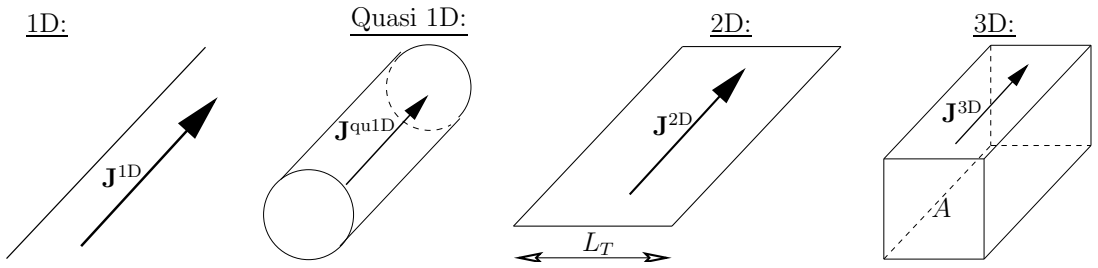

Figure 3.2: Direction of the current density in one, two, three and quasi one dimensional homogeneous systems.

where $\rho \equiv \frac{E}{J}$ is the definition of resistivity. Similarly in two (2D) and one (1D) dimensions the connection is:

$$J^{2D} = \frac{I}{L_T}, \qquad R^{2D} = \frac{V}{I} = \frac{L}{L_T}\frac{E}{J^{2D}} \equiv \rho^{2D}\frac{L}{L_T}, \tag{3.3}$$

$$J^{1D} = I \qquad R^{1D} = \frac{V}{I} = L\frac{E}{J^{1D}} \equiv \rho^{1D}L, \tag{3.4}$$

where L_T is the width of the two dimensional plane (see fig. 3.2).

For a small hollow cylinder (e.g. a singlewall carbon nanotube) we have a two dimensional surface, which is folded to a one dimensional wire in the sense that current only flows along the cylinder. This case is named quasi 1D (qu1D) since it is one dimensional, but has units as the two dimensional case:

$$J^{qu1D} = \frac{I}{2\pi r} \quad \text{and} \quad R^{qu1D} = \frac{V}{I} = \frac{L}{2\pi r}\frac{E}{J^{qu1D}} \equiv \rho^{qu1D}\frac{L}{2\pi r}. \tag{3.5}$$

This is the case we have chosen to use in the transresistivity calculation. Of course the value of the transresistance R_{21} is independent of the conventions used.

3.1 The Boltzmann equation approach

The approach used to derive the transresistivity ρ_{21} is the Boltzmann equation:

$$\frac{\partial f(t,\mathbf{r},\mathbf{p})}{\partial t} + \dot{\mathbf{r}} \cdot \frac{\partial f(t,\mathbf{r},\mathbf{p})}{\partial \mathbf{r}} + \dot{\mathbf{p}} \cdot \frac{\partial f(t,\mathbf{r},\mathbf{p})}{\partial \mathbf{p}} = \left(\frac{\partial f}{\partial t}\right)_{\text{coll}}, \tag{3.6}$$

where $f(t,\mathbf{r},\mathbf{p})$ is the distribution function at time t, position $\mathbf{r}$ and momentum $\mathbf{p}$. The dots above symbols denote time derivatives, e.g. $\dot{\mathbf{r}} = \frac{\mathrm{d}\mathbf{r}}{\mathrm{d}t}$. The Boltzmann equation is a continuity equation in $(\mathbf{r},\mathbf{p})$-space, where the right hand side is a functional[3] of f representing the collisions between the particles. The origin of the Boltzmann equation is semi-classical, since knowing the exact position $\mathbf{r}$ and

[3]It is not a derivative and the notation is purely historical [7].

momentum $\mathbf{p}$ is due to Heisenberg′s uncertainty principle not allowed in quantum mechanics. It is reasonable to use this semi-classical approach, since we are in the limit of small and constant external electric fields, i.e. the linear response limit [1, p.217]. The microscopic basic of the Boltzmann equation is the Fermi Liquid theory, where the particles in the Boltzmann equation are the free-particle-like excitations (quasi particles) [18].

In the coupled system there is one distribution function f_i $(i = 1, 2)$ for each subsystem and we consider a static and homogeneous situation, so the distributions are independent of t and $\mathbf{r}$ and their derivatives are zero in eq.(3.6). Instead of the momentum as a variable in f_i we use the one dimensional wave vector k along the cylinder, band index ν and spin σ, i.e. $f_i = f_i(k, \nu, \sigma)$. For a carbon nanotube the band index ν is a collection of indices, e.g. crystal angular momentum $\mathfrak{m}$ and parity Π for an armchair tube or by n_c and $\pm$ for a metallic tube, see chapter 2. Note that we used the translational unit cell in this description, but we could equally well have made a Boltzmann equation using the κ and $\mathfrak{m}$ indices from the helical and rotational symmetries and the primitive unit cell.

In each cylinder we work with a noninteracting electron gas in the periodic potential formed by the atoms to give single particle Bloch states $|k\nu\sigma\rangle$. These can be seen as the unperturbed states or the quasi particles in the Boltzmann equation. The only electron-electron interaction considered here is the one between electrons in different subsystems giving the drag effect. In the single subsystems impurity scattering is included to give finite conductivity for each single isolated cylinder. From now on the spin index σ is dropped, since the two spins have equal distribution functions.

3.2 Single subsystem properties

Before considering the coupled subsystems, let us focus on a single isolated subsystem and see the Boltzmann equation at work here.

The impurity scattering is considered in the relaxation time approximation [7, p.16][1, p.244] for the collision integral $\left(\frac{\partial f}{\partial t}\right)_{\text{coll}}$. Introducing a relaxation time $\tau_{k'\nu',k\nu}$ for impurity scattering from $|k\nu\rangle$ to $|k'\nu'\rangle$ the collision integral for a single subsystem is[4]:

$$\left(\frac{\partial f}{\partial t}\right)(k,\nu) = \sum_{\varepsilon_{k'\nu'}} \underbrace{-\frac{f(k,\nu) - f^0(\varepsilon_{k'\nu'})}{\tau_{k'\nu',k\nu}}}_{\text{Scattering from } |k\nu\rangle \text{ to } |k'\nu'\rangle} \equiv -\frac{f(k,\nu) - f^0(\varepsilon_{k\nu})}{\tau}, \tag{3.7}$$

where the sum is over all possible scattering processes and $f^0(\varepsilon)$ is the Fermi (equilibrium) distribution function, which is only dependent on the energy ε. The relaxation time τ introduced in the last equality depends a priori on k and

[4]Here the subsystem index i is dropped.

ν, but in the simple model used here we assume it to be independent of k and ν. Furthermore the form $-\frac{f(k,\nu)-f^0(\varepsilon_{k\nu})}{\tau}$ is a priori not even clear from the sum over the possible scattering processes[5]. However for semiconductors a constant τ works well [115].

Therefore the single subsystem one dimensional Boltzmann equation used is:

$$\dot{k}\frac{\partial f(k,\nu)}{\partial k} = -\frac{f(k,\nu)-f^0(\varepsilon_{k\nu})}{\tau} \tag{3.8}$$

and the time derivative of k is found from the semi-classical equation of motion [1, chap.12] in one dimension $\hbar\dot{k} = \tilde{e}E$, where $\tilde{e}$ is the charge of the current carrier (hole or electron). The electric field E is along the cylinder as the wave vector k. The Boltzmann equation (3.8) can be solved exactly by $f(k) = \int_0^\infty \mathrm{d}x e^{-x} f^0(\varepsilon(k - \frac{\tilde{e}\tau}{\hbar}Ex))$, which gives rise to nonlinear current as a function of electric field [116]. Instead of using this solution, we linearize the Boltzmann equation by introducing the deviation from equilibrium $\psi(k,\nu)$ through:

$$\begin{aligned} f(k,\nu) &\equiv f^0(\varepsilon_{k\nu}) + f^0(\varepsilon_{k\nu})(1-f^0(\varepsilon_{k\nu}))\psi(k,\nu) \\ &= f^0(\varepsilon_{k\nu}) - k_{\mathrm{B}}T\frac{\partial f^0(\varepsilon_{k\nu})}{\partial \varepsilon_{k\nu}}\psi(k,\nu). \end{aligned} \tag{3.9}$$

Substituting this form of f in the left hand side of the Boltzmann equation (3.8) and assuming that E and $\psi(k,\nu)$ are small, only the derivative of f^0 is kept to first order in E and ψ, i.e. we model the linear response limit. So the linearized Boltzmann equation simplifies to:

$$\frac{\tilde{e}E}{\hbar}\frac{\partial f^0(\varepsilon_{k\nu})}{\partial k} = -\frac{f(k,\nu)-f^0(\varepsilon_{k\nu})}{\tau}, \tag{3.10}$$

which makes the distribution function a simple linear function of the electric field E as opposed to the complicated nonlinear exact solution, i.e. for small E fields we have

$$\psi(k,\nu) = \frac{\tilde{e}\tau v_{k\nu}}{k_{\mathrm{B}}T}E, \tag{3.11}$$

where $v_{k\nu}$ is the mean velocity[6] given by $v_{k\nu} = \frac{1}{\hbar}\frac{\partial\varepsilon_{k\nu}}{\partial k}$. The linearized Boltzmann equation makes the current proportional to E as we shall se below.

We now consider the current density J along the cylinder and define the mobility μ_{Tr}, which is a single system property, that we will use later on. The

[5] If one were to make a better model, we should use the impurity collision integral: $\left(\frac{\partial f}{\partial t}\right)_{\mathrm{coll}}(k,\nu) = -\sum_{k',\nu'}(\Gamma_{k'\nu',k\nu}f_{k\nu}(1-f_{k'\nu'}) - \Gamma_{k\nu,k'\nu'}f_{k'\nu'}(1-f_{k\nu}))$, where $\Gamma_{k'\nu',k\nu}$ is the transition rate [18, chap.13][7].

[6] In the sense that $v_{k\nu}$ is the quantum mechanical mean value of the velocity operator in the Bloch state $|k\nu\rangle$, i.e. $v_{k\nu} = \langle k\nu|\hat{v}|k\nu\rangle$ [1, Appendix E].

current density for a (hollow) cylinder with radius r and length L is:

$$J = \sum_\sigma \frac{1}{2\pi r} \sum_\nu \frac{1}{L} \sum_{k\in \mathrm{FBZ}} \tilde{e} v_{k\nu} f(k,\nu) \qquad \text{(No current in equilibrium.)}$$

$$= \sum_\sigma \frac{1}{2\pi r} \sum_\nu \frac{1}{L} \sum_{k\in \mathrm{FBZ}} \tilde{e} v_{k\nu} (f(k,\nu) - f^0(\varepsilon_{k\nu})) \qquad \text{(Using eq.(3.10))}$$

$$= -\frac{\tilde{e}^2 E\tau}{\hbar} \sum_\sigma \frac{1}{2\pi r} \sum_\nu \frac{1}{L} \sum_{k\in \mathrm{FBZ}} v_{k\nu} \frac{\partial f^0(\varepsilon_{k\nu})}{\partial k} \tag{3.12}$$

$$\equiv \tilde{e} n \mu_{\mathrm{Tr}} E. \tag{3.13}$$

Here FBZ is the first Brillouin zone and n is taken to be a quasi 1D carrier density defined as the carrier number divided by the surface area of the cylinder $2\pi rL$, i.e. it has units as in 2D. In the last equation (3.13) the mobility μ_{Tr} was defined and eq.(3.12) shows that this definition makes sense, since here $J \propto E$. This definition of μ_{Tr} is only dependent on the band structure in this approximation. Note that this calculation of the current density has units as in the quasi one dimensional case[7].

3.3 Coupling of the two subsystems

3.3.1 The model of the coupled Boltzmann equations

The task is now to couple the two subsystems. This is done to lowest order in the interaction between the subsystems and in linear response to the external electric field E_1. We simply couple two single subsystem Boltzmann equation of the form of eq.(3.10) by a linearized collision integral $S_{\mathrm{L}}[\psi_1, \psi_2](k_2, \nu_2)$ between the electrons in the two subsystems. The coupled linearized Boltzmann equations are:

$$\frac{\tilde{e}_1 E_1}{\hbar} \frac{\partial f^0(\varepsilon_{k_1\nu_1})}{\partial k_1} = -\frac{f_1(k_1,\nu_1) - f^0(\varepsilon_{k_1\nu_1})}{\tau_1}, \tag{3.14}$$

$$\frac{\tilde{e}_2 E_2}{\hbar} \frac{\partial f^0(\varepsilon_{k_2\nu_2})}{\partial k_2} = -\frac{f_2(k_2,\nu_2) - f^0(\varepsilon_{k_2\nu_2})}{\tau_2} + S_{\mathrm{L}}[\psi_1, \psi_2 = 0](k_2, \nu_2), \tag{3.15}$$

where an index i ($i = 1, 2$) has been added to label the subsystem properties. The reasoning for this coupling is as follows: The induced field E_2 is due to the weak inter subsystem coupling much less than the external field E_1, i.e. $|E_1| \gg |E_2|$. So if there were no coupling, the deviations from equilibrium would

[7] The normalization factor for the sum over the bands ν is the length of the circumference $L_c = 2\pi r$ because the origin of the bands are a quantization of the wave vector in the circumferential direction in only a few quanta, i.e. $k_c = \frac{2\pi}{|\mathbf{C}|} n_c$ where $n_c \in \{0, 1, \ldots, \mathcal{N} - 1\}$ becomes the (dimensionfull part of the) band index ν, see section 2.2.2.

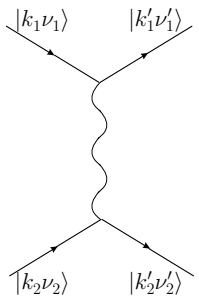

Figure 3.3: This is the basic scattering process for the interaction between the to subsystems, $i = 1, 2$. So the electrons in the single particle Bloch states for each system interact via the (screened) Coulomb interaction, which causes the Coulomb drag effect.

satisfy $|\psi_1| \gg |\psi_2|$, since eq.(3.10) gives $\psi_i \propto E_i$. But even for a small coupling this is still true, so the collision terms from the impurity scattering in the single subsystems are of order E_1 and E_2, respectively. As we shall see the linearized collision integral S_{L} has a product of the inter subsystem interaction and the sum of the deviation functions and is thereby to higher order in E_1 than the single subsystem collision term in eq.(3.14) but not in eq.(3.15), where there is no first order term in E_1 (only in E_2). Therefore the collision integral appears only in eq.(3.15). So the fact that these equations are not symmetric with respect to interchange of 1 and 2 reflect that the experimental setup is not symmetric (in the sense that a current is running in subsystem 1 but not in 2).

The full collision integral $S[\psi_1, \psi_2](k_2, \nu_2)$ is now given and linearized to $S_{\mathrm{L}}[\psi_1, \psi_2](k_2, \nu_2)$. The basic idea is that a particle in $|k_1\nu_1\rangle$ and a particle in $|k_2\nu_2\rangle$ interacts via the Coulomb interaction and are scattered to $|k_1'\nu_1'\rangle$ and $|k_2'\nu_2'\rangle$ as pictured on figure 3.3. This happens with a transition rate $w(1'2'; 12)$, i.e. scattering probability per unit time, where i is short for $k_i\nu_i$. The scattering rates are proportional to the occupation of the states i.e. the distribution functions f_i and to the availability of the states after the scattering event $1 - f_i'$. Both the scattering out and in of the states $|k_1\nu_1\rangle$ and $|k_2\nu_2\rangle$ contribute to the collision integral. These arguments lead to [7]

$$
\begin{aligned}
S[\psi_1, \psi_2](k_2, \nu_2) = &- \sum_{\sigma_1\sigma_1'\sigma_2'} \sum_{\nu_1\nu_1'\nu_2'} \sum_{k_1 \in \mathrm{FBZ}} \sum_{k_1' \in \mathrm{FBZ}} \sum_{k_2' \in \mathrm{FBZ}} \\
&\times \Bigg(\underbrace{w(1'2'; 12) f_1(k_1, \nu_1) f_2(k_2, \nu_2) \Big(1 - f_1(k_1', \nu_1')\Big) \Big(1 - f_2(k_2', \nu_2')\Big)}_{\text{Scattering out of } |k_1\nu_1\rangle|k_2\nu_2\rangle} \\
&- \underbrace{w(12; 1'2') f_1(k_1', \nu_1') f_2(k_2', \nu_2') \Big(1 - f_1(k_1, \nu_1)\Big) \Big(1 - f_2(k_2, \nu_2)\Big)}_{\text{Scattering into } |k_1\nu_1\rangle|k_2\nu_2\rangle} \Bigg). \quad (3.16)
\end{aligned}
$$

Note that the collision integral is a function of k_2 and ν_2 as it should be[8] and has dimension of $(\text{time})^{-1}$. This collision integral is not exact since it could contain higher order distribution functions such as $f_i^{(2)}(k_1, \nu_1, k_1', \nu_1')$ [7, p.4].

[8]It is also a function of σ_2, which is suppressed in the notation.

To get the linearized collision integral f_i in eq.(3.9) (now with subsystem indices) is substituted into the collision integral (3.16) and only terms up to first order in ψ_1 and ψ_2 are kept. The reasonable assumption $w(1'2';12) = w(12;1'2')$ is also made. To chancel terms in the long expression obtained by inserting (3.9) into (3.16) we use the H-theorem. It states (in the simple version used here) that in equilibrium the energy conserving scattering in and out of the states $|k_1\nu_1\rangle$,$|k_2\nu_2\rangle$ is the same:

$$f^0(\varepsilon_{k_1\nu_1})f^0(\varepsilon_{k_2\nu_2})\Big(1-f^0(\varepsilon_{k_1'\nu_1'})\Big)\Big(1-f^0(\varepsilon_{k_2'\nu_2'})\Big) = \\ f^0(\varepsilon_{k_1'\nu_1'})f^0(\varepsilon_{k_2'\nu_2'})\Big(1-f^0(\varepsilon_{k_1\nu_1})\Big)\Big(1-f^0(\varepsilon_{k_2\nu_2})\Big). \quad (3.17)$$

This expression can also be understood from the collision integral (3.16), since if eq.(3.17) was not true (and $w(12;1'2') = w(1'2';12)$) more particles would scatter, say, into $|k_1\nu_1\rangle|k_2\nu_2\rangle$ that out of the same state in *equilibrium* and one would not have equilibrium by definition. Eq.(3.17) can also be seen by straightforward calculation using energy conservation and the form for the Fermi function. So the linearized collision integral $S_{\rm L}[\psi_1,\psi_2](k_2,\nu_2)$ is:

$$S[\psi_1,\psi_2](k_2,\nu_2) \simeq S_{\rm L}[\psi_1,\psi_2](k_2,\nu_2) = \\ -\sum_{\sigma_1\sigma_1'\sigma_2'}\sum_{\nu_1\nu_1'\nu_2'}\sum_{k_1,k_1',k_2'\in{\rm FBZ}} w(1'2';12)f^0(\varepsilon_{k_1\nu_1})f^0(\varepsilon_{k_2\nu_2})\Big(1-f^0(\varepsilon_{k_1'\nu_1'})\Big)\Big(1-f^0(\varepsilon_{k_2'\nu_2'})\Big) \\ \times[\psi_1(k_1,\nu_1)+\psi_2(k_2,\nu_2)-\psi_1(k_1',\nu_1')-\psi_2(k_2',\nu_2')] \quad (3.18)$$

In the coupled Boltzmann equations ψ_2 is set to zero in $S_{\rm L}[\psi_1,\psi_2=0](k_2,\nu_2)$ in eq.(3.15), since these terms are much smaller than the ψ_1 terms, as noted earlier.

Already at this stage we note a measurable feature of our model: The coupling $S_{\rm L}$ between the subsystems and thereby ρ_{21} must go to zero for the temperature going to zero $T\to 0$, since for zero temperature (and assuming $w(1'2';12)$ to be energy conserving) we have $\varepsilon_{k_i'\nu_i'} \simeq \varepsilon_{k_i\nu_i}$ so $f^0(\varepsilon_{k_i\nu_i})\big(1-f^0(\varepsilon_{k_i\nu_i})\big) \simeq k_{\rm B}T\delta(\varepsilon_{\rm F}-\varepsilon_{k_i\nu_i}) \to 0$ for $T\to 0$.

We have now established the model, which we will use to find the transresistivity ρ_{21}.

3.3.2 The transition rate and the Coulomb interaction

The transition rate $w(1'2';12)$ depends on the electron-electron interaction, which is taken to be the screened Coulomb interaction V_{12}. Other interactions could be considered such as the phonon mediated electron-electron interaction [49]. The transition rate $w(1'2';12)$ is found by the help of the Fermi's golden rule [78, p.332][18, p.226], which is derived from first order time dependent perturbation

theory on a time independent potential:

$$w(1'2';12) = \frac{2\pi}{\hbar}|\langle k_1' k_2' \nu_1' \nu_2'|V_{12}(|\mathbf{r_1}-\mathbf{r_2}|)|k_1 k_2 \nu_1 \nu_2\rangle|^2 \times \delta(\varepsilon_{k_1\nu_1}+\varepsilon_{k_2\nu_2}-\varepsilon_{k_1'\nu_1'}-\varepsilon_{k_2'\nu_2'}), \quad (3.19)$$

where $|k_1 k_2 \nu_1 \nu_2\rangle$ is just the product state of $|k_1\nu_1\rangle$ and $|k_2\nu_2\rangle$. This stems from the way to derive a collision integral (by the help of Fermis golden rule) via a two-particle operator in second quantization [8, p.130], where the matrix elements are between product states. So we are not in contrast with the Pauli principle. Furthermore, there could be an exchange term [117, chap.1], which is not included, since the electrons are spatially separated and no tunnelling is allowed. In eq.(3.19) it was stated explicitly that the screened Coulomb interaction V_{12} is only a function of the distance between the electrons at $\mathbf{r}_1$ and $\mathbf{r}_2$. Therefore the assumption $w(1'2';12) = w(12;1'2')$ made earlier is fulfilled by this form for the transition rate. The transition rate $w(1'2';12)$ in eq.(3.19) also contains an implicit spin dependence $\delta_{\sigma_1,\sigma_1'}\delta_{\sigma_2,\sigma_2'}$, since the Coulomb interaction is spin independent.

The Coulomb matrix element between two tubes in a multiwall nanotube were discussed in detail in section 2.3.2 using the slow variation of $V_{12}(|\mathbf{r}_1-\mathbf{r}_2|)$ on the scale of the interatomic distance $a_{\text{C-C}}$. We found the Coulomb matrix element in eq.(2.82) for two general tubes in the tight binding model to be (without the spin dependence):

$$\langle k_1' n_{c_1}' k_2' n_{c_2}'|V_{12}(|\mathbf{r}_1-\mathbf{r}_2|)|k_1 n_{c_1} k_2 n_{c_2}\rangle = g_1(k_1 n_{c_1}, k_1' n_{c_1}') g_2(k_2 n_{c_2}, k_2' n_{c_2}') \frac{1}{2\pi L} \sum_{G_1 G_2} \sum_{u_1,u_2\in\mathbb{Z}} V_{12}(k_1'-k_1+G_1, \overbrace{n_{c_1}'-n_{c_1}}^{(\text{modulo } \mathfrak{n}_1)} + \mathfrak{n}_1 u_1) \times \delta_{k_1+k_2,k_1'+k_2'+G_1+G_2} \delta_{\underbrace{n_{c_1}'-n_{c_1}}_{(\text{modulo } \mathfrak{n}_1)}+\mathfrak{n}_1 u_1, \underbrace{n_{c_2}'-n_{c_2}'}_{(\text{modulo } \mathfrak{n}_2)}+\mathfrak{n}_2 u_2}, \quad (3.20)$$

where L is the length of the tubes (assumed to be the same $L_1 = L_2 \equiv L$), $G_i = \frac{2\pi}{a_i} m_i$ ($m_i \in \mathbb{Z}$) is a reciprocal lattice vector for subsystem $i = 1, 2$ and a_1,a_2 are the two lattice constants along the cylinders (which in nanotube notation is $a_i = |\mathbf{T}_i|$). In order to simplify the notation, we have introduced the ν_i index, where the crystal angular momentum is included (and possibly some parity). Therefore we write the matrix element as

$$\langle k_1' k_2' \nu_1' \nu_2'|V_{12}(|\mathbf{r_1}-\mathbf{r_2}|)|k_1 k_2 \nu_1 \nu_2\rangle = g_1(k_1\nu_1, k_1'\nu_1') g_2(k_2\nu_2, k_2'\nu_2') \times \frac{1}{2\pi L} \sum_{G_1 G_2} V_{12}(k_1'-k_1+G_1, \nu_1, \nu_1', \omega) \delta_{k_1+k_2,k_1'+k_2'+G_1+G_2} \mathcal{J}(\nu_1\nu_1', \nu_2\nu_2'), \quad (3.21)$$

where we have introduced the function $\mathcal{J}(\nu_1\nu_1', \nu_2\nu_2')$ to include the selection rules from the crystal angular momentum conservation and possibly some simple parity selection rule as in the case of armchair nanotubes as we shall see[9]. $\mathcal{J}$ also includes the u_i-sums, which in the following manipulations can be treated exactly as the G_i-sums, but the $u_i \neq 0$ processes are strongly suppressed by the Fourier transform and therefore without importance. The ν_1,ν_1' dependence in V_{12} is stated explicitly to remember the angular momentum dependence in the Fourier transformed.

Note that the Fourier transform in eq.(3.21) also depends on the transferred wave vector $k_1' - k_1$ and the transferred energy $\hbar\omega \equiv \varepsilon_{k_1'\nu_1'} - \varepsilon_{k_1\nu_1}$ in the basic scattering process seen on figure 3.3. The ω dependence in V_{12} is introduced by hand in the Boltzmann equation approach (as in [52]), since it physically describes the dynamical screening effects from other electrons. The Kubo formula derivation [112] justifies this procedure. In the Kubo formula derivation the interaction is resumed in the Random Phase approximation (RPA) and the result for the screened Coulomb interaction is the bare (ω independent) interaction divided by the (ω dependent) dielectric function.

Therefore by taking the square of the matrix element eq.(3.21) the transition rate (including the spin part) is:

$$\begin{aligned} w(1'2';12) &= w(k_1'\nu_1', k_2'\nu_2'; k_1\nu_1, k_2\nu_2, \omega) = \\ &\frac{2\pi}{\hbar}|g_1(k_1\nu_1, k_1'\nu_1')|^2|g_2(k_2\nu_2, k_2'\nu_2')|^2\frac{1}{(2\pi L)^2}\sum_{G_1G_2G_1'G_2'} V_{12}(k_1' - k_1 + G_1, \nu_1, \nu_1', \omega) \\ &\times V_{12}^*(k_1' - k_1 + G_1', \nu_1, \nu_1', \omega)\ \delta_{k_1+k_2, k_1'+k_2'+G_1+G_2}\ \delta_{G_1+G_2, G_1'+G_2'}\ \delta_{\sigma_1,\sigma_1'}\delta_{\sigma_2,\sigma_2'} \\ &\times |\mathcal{J}(\nu_1\nu_1', \nu_2\nu_2')|^2\ \delta(\varepsilon_{k_1\nu_1} + \varepsilon_{k_2\nu_2} - \varepsilon_{k_1+q\nu_1'} - \varepsilon_{k_2-q\nu_2'}). \quad (3.22) \end{aligned}$$

It should be noted that the $|\mathcal{J}|^2$ function is invariant under interchange of ν_i and ν_i' for both i separately and the product of the Fourier transforms are even in ω. If this is not the case, the derivation given below is not valid and the transresistivity expression becomes more complicated.

The expression for the transition rate eq.(3.22) includes a crystal momentum conservation law stemming from the Coulomb interaction. Furthermore it has the $\delta_{G_1+G_2,G_1'+G_2'}$ factor, which means that Umklapp scattering can only take place if the two subsystem lattices are commensurable in the sense that $a_1 = ca_2$ for some rational number c. This was previously found in [113].

3.3.3 Calculation of ρ_{21} from the Boltzmann equations

We now use the two coupled Boltzmann equations and the linearized collision integral with Fermis golden rule to find the final formula for the transresistivity

[9]Note that the parity selection rule is not a priori included in eq.(3.20), but is included by hand.

ρ_{21}. We begin by inserting eq.(3.22) into the linearized collision integral (3.18):

$$S_{\rm L}[\psi_1,\psi_2=0](k_2,\nu_2) = -\sum_{\sigma_1\sigma_1'\sigma_2'}\delta_{\sigma_1,\sigma_1'}\delta_{\sigma_2,\sigma_2'}\frac{1}{(2\pi)^2}\sum_{\nu_1\nu_1'\nu_2'}\frac{1}{L^2}\sum_{k_1,k_1',k_2'\in\mathrm{FBZ}}\sum_{G_1G_2,G_1'G_2'}\frac{2\pi}{\hbar}$$
$$\times\,\delta_{k_1+k_2,k_1'+k_2'+G_1+G_2}\delta_{G_1+G_2,G_1'+G_2'}\;|g_1(k_1\nu_1,k_1'\nu_1')|^2|g_2(k_2\nu_2,k_2'\nu_2')|^2|\mathcal{J}(\nu_1\nu_1',\nu_2\nu_2')|^2$$
$$\times\,V_{12}(k_1'-k_1+G_1,\nu_1,\nu_1',\omega)V_{12}^*(k_1'-k_1+G_1',\nu_1,\nu_1',\omega)\,[\psi_1(k_1,\nu_1)-\psi_1(k_1',\nu_1')]$$
$$\times f^0(\varepsilon_{k_1\nu_1})f^0(\varepsilon_{k_2\nu_2})\Big(1-f^0(\varepsilon_{k_1'\nu_1'})\Big)\Big(1-f^0(\varepsilon_{k_2'\nu_2'})\Big)\delta(\varepsilon_{k_1\nu_1}+\varepsilon_{k_2\nu_2}-\varepsilon_{k_1'\nu_1'}-\varepsilon_{k_2'\nu_2'}).$$

The spin sum over σ_1 and σ_1' gives a factor of 2 and the Kronecker delta function for the crystal wave vector conservation removes one of the k-sums, say $k_2' = k_1+k_2-k_1'-G_1-G_2$. Furthermore we have to chose G_2 so that $k_2'\in$FBZ, which removes the G_2-sum. Afterwards the variable change $G_2'\to G_2'-G_2$ in the G_2' sum is made and the new summation index is again called G_2'. The long cylinder limit ($L\to\infty$) is now taken so the wave vector sums become integrales[10]: $\frac{1}{L}\sum_k(\cdots)\to\int\frac{\mathrm{d}k}{2\pi}(\cdots)$. Note that the long cylinder limit is taken after the use of Fermi's golden rule.

After a change of variables in the wave vector integrals from k_1,k_1' to $k_1,q=k_1'-k_1$, the linearized collision integral is:

$$S_{\rm L}[\psi_1,\psi_2=0](k_2,\nu_2) = -\sum_{\sigma_2'}2\delta_{\sigma_2,\sigma_2'}\frac{1}{(2\pi)^2}\sum_{\nu_1\nu_1'\nu_2'}\int_{-\frac{\pi}{a_1}}^{\frac{\pi}{a_1}}\frac{\mathrm{d}q}{2\pi}\int_{-\frac{\pi}{a_1}}^{\frac{\pi}{a_1}}\frac{\mathrm{d}k_1}{2\pi}\sum_{G_1G_1'G_2'}\frac{2\pi}{\hbar}$$
$$\times\,\delta_{G_1,G_1'+G_2'}\;|g_1(k_1\nu_1,k_1+q\nu_1')|^2|g_2(k_2\nu_2,k_2-q-G_1\nu_2')|^2\;|\mathcal{J}(\nu_1\nu_1',\nu_2\nu_2')|^2$$
$$\times\,V_{12}(q+G_1,\nu_1,\nu_1',\omega)V_{12}^*(q+G_1',\nu_1,\nu_1',\omega)$$
$$\times\,f^0(\varepsilon_{k_1\nu_1})f^0(\varepsilon_{k_2\nu_2})\Big(1-f^0(\varepsilon_{k_1+q\nu_1'})\Big)\Big(1-f^0(\varepsilon_{k_2-q-G_1\nu_2'})\Big)$$
$$\times\,[\psi_1(k_1,\nu_1)-\psi_1(k_1+q,\nu_1')]\;\delta(\varepsilon_{k_1\nu_1}+\varepsilon_{k_2\nu_2}-\varepsilon_{k_1+q\nu_1'}-\varepsilon_{k_2-q-G_1\nu_2'}). \quad (3.23)$$

The change of variables uses that the integrand is periodic in q with period $\frac{2\pi}{a_1}$, so the integrals decouple as: $\int_{-\frac{\pi}{a_1}}^{\frac{\pi}{a_1}}\mathrm{d}k_1\int_{-\frac{\pi}{a_1}-k_1}^{\frac{\pi}{a_1}-k_1}\mathrm{d}q(\cdots)=\int_{-\frac{\pi}{a_1}}^{\frac{\pi}{a_1}}\mathrm{d}k_1\int_{-\frac{\pi}{a_1}}^{\frac{\pi}{a_1}}\mathrm{d}q(\cdots)$. To see the periodicity of the integrand we begin by noting that the energy for subsystem 1, ψ_1 (from eq.(3.14) and thereby eq.(3.11)) and g_1 (see section 2.3.2) are periodic by $\frac{2\pi}{a_1}$. The Fourier transforms, g_2 and the energy for subsystem 2 are not periodic, but by using the G_1-sum and G_1'-sum the integrand is periodic. In eq.(3.23) we have also used the periodicity of the subsystem 2 by e.g. $g_2(k_2\nu_2,k_2-q-G_1-G_2\nu_2')=g_2(k_2\nu_2,k_2-q-G_1\nu_2')$.

Now yet another variable change is made: $q\to q+G_1$ (again called q) and

[10]Since the spacing between neighboring k points goes to zero.

the collision integral is:

$$S_{\rm L}[\psi_1,\psi_2=0](k_2,\nu_2) = -\sum_{\sigma_2'} 2\delta_{\sigma_2,\sigma_2'} \frac{1}{(2\pi)^2} \sum_{\nu_1\nu_1'\nu_2'} \sum_{G_1G_1'G_2'} \int_{-\frac{\pi}{a_1}+G_1}^{\frac{\pi}{a_1}+G_1} \frac{\mathrm{d}q}{2\pi} \int_{-\frac{\pi}{a_1}}^{\frac{\pi}{a_1}} \frac{\mathrm{d}k_1}{2\pi}$$
$$\times \frac{2\pi}{\hbar}\delta_{G_1,G_1'+G_2'} \; |g_1(k_1\nu_1, k_1+q\nu_1')|^2 |g_2(k_2\nu_2, k_2-q\nu_2')|^2 \; |\mathcal{J}(\nu_1\nu_1', \nu_2\nu_2')|^2$$
$$\times V_{12}(q,\nu_1,\nu_1',\omega) V_{12}^*(q+G_1'-G_1,\nu_1,\nu_1',\omega)$$
$$\times f^0(\varepsilon_{k_1\nu_1}) f^0(\varepsilon_{k_2\nu_2}) \Big(1-f^0(\varepsilon_{k_1+q\nu_1'})\Big)\Big(1-f^0(\varepsilon_{k_2-q\nu_2'})\Big)$$
$$\times [\psi_1(k_1,\nu_1) - \psi_1(k_1+q,\nu_1')] \; \delta(\varepsilon_{k_1\nu_1}+\varepsilon_{k_2\nu_2}-\varepsilon_{k_1+q\nu_1'}-\varepsilon_{k_2-q\nu_2'}), \quad (3.24)$$

where the integrand is not periodic in q by G_1, so the q-integral is over all q (as in [113]). The two variable changes in eq.(3.23) and eq.(3.24) were not made in one go, since in eq.(3.23) we needed a reciprocal lattice vector in both Fourier transforms to have an integrand periodic by $\frac{2\pi}{a_1}$.

The condition that $J_2 = 0$ is now used and no further physical assumptions are made, except inversion symmetry in k space giving $\varepsilon_{k\nu} = \varepsilon_{-k\nu}$. So the rest of the derivation is purely mathematical manipulations. Using the second of the two coupled Boltzmann equations (3.15) the current density J_2 (in the long cylinder limit) is found to be:

$$J_2 = \sum_{\sigma_2} \frac{1}{2\pi r_2^c} \sum_{\nu_2} \int_{-\frac{\pi}{a_2}}^{\frac{\pi}{a_2}} \frac{\mathrm{d}k_2}{2\pi} \tilde{e}_2 v_{k_2\nu_2} f_2(k_2,\nu_2)$$
$$= \sum_{\sigma_2} \frac{1}{2\pi r_2^c} \sum_{\nu_2} \int_{-\frac{\pi}{a_2}}^{\frac{\pi}{a_2}} \frac{\mathrm{d}k_2}{2\pi} \tilde{e}_2 v_{k_2\nu_2} \tau_2 \left[-\frac{\tilde{e}_2 E_2}{\hbar} \frac{\partial f^0(\varepsilon_{k_2\nu_2})}{\partial k_2} + S_{\rm L}[\psi_1,0](k_2,\nu_2) \right]$$
$$= \tilde{e}_2 n_2 \mu_{\rm Tr}^{(2)} E_2 + \sum_{\sigma_2} \frac{1}{2\pi r_2^c} \sum_{\nu_2} \int_{-\frac{\pi}{a_2}}^{\frac{\pi}{a_2}} \frac{\mathrm{d}k_2}{2\pi} \tilde{e}_2 v_{k_2\nu_2} \tau_2 S_{\rm L}[\psi_1,0](k_2,\nu_2) = 0, \quad (3.25)$$

where the definition (3.13) of the single *isolated* subsystem mobility was used in the third equality. This is an important step on the way to get the transresistivity ρ_{21} since from the first of the two coupled Boltzmann equations (3.14) one obtains $J_1 = \tilde{e}_1 n_1 \mu_{\rm Tr}^{(1)} E_1$, so

$$\rho_{21} = \frac{E_2}{J_1} = \frac{E_2}{\tilde{e}_1 n_1 \mu_{\rm Tr}^{(1)} E_1} \quad (3.26)$$

and with the help of eq.(3.25) and $S_{\rm L} \propto E_1$ from eq.(3.24) we essentially have ρ_{21} in eq.(3.25). Now we work out the details.

The following equalities, which are straightforward to prove[11],

$$\delta(\varepsilon_{k_1\nu_1}+\varepsilon_{k_2\nu_2}-\varepsilon_{k_1+q\nu_1'}-\varepsilon_{k_2-q\nu_2'})=\hbar\int_{-\infty}^{\infty}\mathrm{d}\omega\Big[\delta(\varepsilon_{k_1\nu_1}-\varepsilon_{k_1+q\nu_1'}-\hbar\omega)\times\delta(\varepsilon_{k_2\nu_2}-\varepsilon_{k_2-q\nu_2'}+\hbar\omega)\Big], \quad (3.27)$$

$$f^0(\varepsilon)\big(1-f_1^0(\varepsilon')\big)=\big(f^0(\varepsilon')-f^0(\varepsilon)\big)n_{\mathrm{B}}(\varepsilon-\varepsilon'), \quad (3.28)$$

with $n_{\mathrm{B}}(\varepsilon)$ being the Bose function with chemical potential $\mu=0$ ($\beta=\frac{1}{k_{\mathrm{B}}T}$),

$$n_{\mathrm{B}}(x)=\frac{1}{e^{\beta x}-1}, \quad (3.29)$$

are inserted into the linearized collision integral (3.24). Also the deviation functions ψ_1, which are found from the first Boltzmann equation (3.14) to be $\psi_1(k_1,\nu_1)=\tilde{e}_1E_1v_{k_1\nu_1}\tau_1\beta$, are inserted into the linearized collision integral (3.24) and thereby eq.(3.25) becomes:

$$\begin{aligned}\tilde{e}_2n_2\mu_{\mathrm{Tr}}^{(2)}E_2=&\overbrace{4}^{\text{spin}}\frac{1}{(2\pi r_2^c)}\frac{1}{(2\pi)^2}\sum_{\nu_1\nu_1'\nu_2\nu_2'}\sum_{G_1G_1'G_2'}\int_{-\frac{\pi}{a_1}+G_1}^{\frac{\pi}{a_1}+G_1}\frac{\mathrm{d}q}{2\pi}\frac{2\pi}{\hbar}\hbar\int_{-\infty}^{\infty}\mathrm{d}\omega\ n_{\mathrm{B}}(-\hbar\omega)n_{\mathrm{B}}(\hbar\omega)\\
&\times V_{12}(q,\nu_1,\nu_1',\omega)V_{12}^*(q+G_1'-G_1,\nu_1,\nu_1',\omega)\ |\mathcal{J}(\nu_1\nu_1',\nu_2\nu_2')|^2\ \delta_{G_1,G_1'+G_2'}\\
\times&\Big[\int_{-\frac{\pi}{a_2}}^{\frac{\pi}{a_2}}\frac{\mathrm{d}k_2}{2\pi}\tilde{e}_2v_{k_2,\nu_2}\tau_2\big[f^0(\varepsilon_{k_2-q\nu_2'})-f^0(\varepsilon_{k_2\nu_2})\big]\ |g_2(k_2\nu_2,k_2-q\nu_2')|^2\\
&\times\delta(\varepsilon_{k_2\nu_2}-\varepsilon_{k_2-q\nu_2'}+\hbar\omega)\Big]\\
\times&\Big[\int_{-\frac{\pi}{a_1}}^{\frac{\pi}{a_1}}\frac{\mathrm{d}k_1}{2\pi}\tilde{e}_1E_1\beta\tau_1\big[v_{k_1\nu_1}-v_{k_1+q\nu_1'}\big]\ |g_1(k_1\nu_1,k_1+q\nu_1')|^2\\
&\times\big[f^0(\varepsilon_{k_1+q\nu_1'})-f^0(\varepsilon_{k_1\nu_1})\big]\delta(\varepsilon_{k_1\nu_1}-\varepsilon_{k_1+q\nu_1'}-\hbar\omega)\Big]. \quad (3.30)\end{aligned}$$

Notice that we now have a product of two integrals over k_1 and k_2, respectively, which are integrated over the transferred wave vector and energy. So the properties from the band structure $\varepsilon_{k\nu}$ for the two subsystems are separated into two factors, which are connected via the interaction[12].

[11]Note that a variable change has be made from the transferred energy $\omega=\frac{\varepsilon_{k_1+q\nu_1'}-\varepsilon_{k_1\nu_1}}{\hbar}$ to $-\omega$, which in turn again is called ω in eq.(3.27). This is done to follow the notation in [52], which we are generalizing.

[12]If we instead of using the Coulomb matrix element from the nanotubes used a Coulomb matrix element for general Bloch states we could still separate into factors belonging to different subsystems. The price of this would be to take the spatial integrals from the Coulomb matrix element outside the k-sums and including the Bloch states in the factors for the system. Afterwards one can Fourier transform to get a result as in [113, eq.(2)].

We will now rewrite the integral over k_2 in eq.(3.30) to make it look like the integral over k_1. First we divide it into two equal parts and thereafter the variable substitutions $k_2 \to -k_2$ and $k_2 \to k_2 - q$ are made in the first and second part[13], respectively:

$$\int_{-\frac{\pi}{a_2}}^{\frac{\pi}{a_2}} \frac{\mathrm{d}k_2}{2\pi} v_{k_2\nu_2} \tau_2 \big[f^0(\varepsilon_{k_2 - q\nu_2'}) - f^0(\varepsilon_{k_2\nu_2}) \big] |g_2(k_2\nu_2, k_2 - q\nu_2')|^2 \delta(\varepsilon_{k_2\nu_2} - \varepsilon_{k_2 - q\nu_2'} + \hbar\omega)$$

$$= \frac{1}{2} \Bigg[\int_{-\frac{\pi}{a_2}}^{\frac{\pi}{a_2}} \frac{\mathrm{d}k_2}{2\pi} v_{-k_2\nu_2} \tau_2 \big[f^0(\varepsilon_{-k_2 - q\nu_2'}) - f^0(\varepsilon_{-k_2\nu_2}) \big] |g_2(-k_2\nu_2, -k_2 - q\nu_2')|^2$$

$$\times \delta(\varepsilon_{-k_2\nu_2} - \varepsilon_{-k_2 - q\nu_2'} + \hbar\omega) \Bigg] + \frac{1}{2} \Bigg[\int_{-\frac{\pi}{a_2}}^{\frac{\pi}{a_2}} \frac{\mathrm{d}k_2}{2\pi} v_{k_2 + q\nu_2} \tau_2 \big[f^0(\varepsilon_{k_2\nu_2'}) - f^0(\varepsilon_{k_2 + q\nu_2}) \big]$$

$$\times |g_2(k_2 + q\nu_2, k_2\nu_2')|^2 \delta(\varepsilon_{k_2 + q\nu_2} - \varepsilon_{k_2\nu_2'} + \hbar\omega) \Bigg], \quad (3.31)$$

where we have used that the integrand is periodic in k_2 by $\frac{2\pi}{a_2}$ to change the integration limits in the second term. Inversion symmetry in k space[14] gives $\varepsilon_{-k\nu} = \varepsilon_{k\nu}$ and therefore $v_{-k\nu} = -v_{k\nu}$, since $v_{k\nu} = \frac{1}{\hbar}\frac{\partial \varepsilon_{k\nu}}{\partial k}$. Note that if we had used the primitive unit cell of the nanotubes and thereby κ instead of k, we could not have done this, i.e. $\varepsilon_{\kappa\mathrm{m}} \neq \varepsilon_{-\kappa\mathrm{m}}$. Furthermore from the explicit form[15] of g_2 it can be seen that $g_2(-k_2\nu_2, -k_2 - q\nu_2') = g_2^*(k_2\nu_2, k_2 + q\nu_2')$ and $g_2(k_2\nu_2, k_2'\nu_2') = g_2^*(k_2'\nu_2, k_2\nu_2')$. Therefore the integral over k_2 is:

$$\frac{1}{2} \Bigg[- \int_{-\frac{\pi}{a_2}}^{\frac{\pi}{a_2}} \frac{\mathrm{d}k_2}{2\pi} v_{k_2\nu_2} \tau_2 \big[f^0(\varepsilon_{k_2 + q\nu_2'}) - f^0(\varepsilon_{k_2\nu_2}) \big] \ |g_2(k_2\nu_2, k_2 + q\nu_2')|^2$$

$$\times \delta(\varepsilon_{k_2\nu_2} - \varepsilon_{k_2 + q\nu_2'} + \hbar\omega) \Bigg] + \frac{1}{2} \Bigg[\int_{-\frac{\pi}{a_2}}^{\frac{\pi}{a_2}} \frac{\mathrm{d}k_2}{2\pi} v_{k_2 + q\nu_2} \tau_2 \big[f^0(\varepsilon_{k_2\nu_2'}) - f^0(\varepsilon_{k_2 + q\nu_2}) \big]$$

$$\times |g_2(k_2 + q\nu_2, k_2\nu_2')|^2 \ \delta(\varepsilon_{k_2\nu_2'} - \varepsilon_{k_2 + q\nu_2} - \hbar\omega) \Bigg]. \quad (3.32)$$

This expression has essentially three things to be changed before it will look like the k_1 integration in eq.(3.30): The sign of ω in the delta function in the first term should be opposite, the band indices in the second term should be interchanged and when this is done the two terms will need an opposite sign. Since $|\mathcal{J}(\nu_1\nu_1', \nu_2\nu_2')|^2$ is assumed to be invariant under interchange of ν_2 and ν_2' we can interchange these band indices in the second term in eq.(3.32), when this is inserted in eq.(3.30).

[13] The new variables are again called k_2.

[14] Real space does not have to be inversion symmetric for this to be true, only time-reversal symmetry for the unperturbed system is required [52, Note 20].

[15] That is, the explicit form, which is made periodic by hand.

To solve the two other problems in eq.(3.32) we need to look at the properties of the k_1 integration, when the variable substitution $\omega \to -\omega$ in eq.(3.30) is made. By variable substitution $k_1 \to -k_1 - q$ we can see that the k_1 integral gets a minus and an interchange in band indices ν_1 and ν_1'. By the assumed symmetry of $|\mathcal{J}(\nu_1\nu_1', \nu_2\nu_2')|^2$, we can interchange ν_1 and ν_1' so we only have a minus left from the k_1 integration caused by the variable substitution $\omega \to -\omega$. This makes the k_2 integral similar to the k_1 integral. To make this point explicit, the reformulation of eq.(3.30) is given (before the variable substitution $\omega \to -\omega$ and after $\nu_2 \leftrightarrow \nu_2'$):

$$\begin{aligned}
\tilde{e}_2 n_2 \mu_{\mathrm{Tr}}^{(2)} E_2 = {} & \frac{4}{(2\pi r_2^c)} \frac{1}{(2\pi)^2} \sum_{\nu_1\nu_1'\nu_2\nu_2'} \sum_{G_1 G_1' G_2'} \int_{-\frac{\pi}{a_1}+G_1}^{\frac{\pi}{a_1}+G_1} \frac{\mathrm{d}q}{2\pi} \frac{2\pi}{\hbar} \hbar \int_{-\infty}^{\infty} \mathrm{d}\omega \; n_{\mathrm{B}}(-\hbar\omega) n_{\mathrm{B}}(\hbar\omega) \\
& \times \tilde{e}_1 E_1 \beta V_{12}(q, \nu_1, \nu_1', \omega) V_{12}^*(q + G_1' - G_1, \nu_1, \nu_1', \omega) \; |\mathcal{J}(\nu_1\nu_1', \nu_2\nu_2')|^2 \; \delta_{G_1, G_1'+G_2'} \\
& \times \Bigg[\int_{-\frac{\pi}{a_1}}^{\frac{\pi}{a_1}} \frac{\mathrm{d}k_1}{2\pi} \left[f^0(\varepsilon_{k_1+q\nu_1'}) - f^0(\varepsilon_{k_1\nu_1}) \right] |g_1(k_1\nu_1, k_1 + q\nu_1')|^2 \\
& \qquad \times \left[v_{k_1\nu_1} - v_{k_1+q\nu_1'} \right] \tau_1 \delta(\varepsilon_{k_1\nu_1} - \varepsilon_{k_1+q\nu_1'} - \hbar\omega) \Bigg] \\
\times \frac{\tilde{e}_2}{2} \Bigg[& \int_{-\frac{\pi}{a_2}}^{\frac{\pi}{a_2}} \frac{\mathrm{d}k_2}{2\pi} \left[f^0(\varepsilon_{k_2\nu_2}) - f^0(\varepsilon_{k_2+q\nu_2'}) \right] \; |g_2(k_2\nu_2, k_2 + q\nu_2')|^2 \qquad (3.33) \\
& \times \left\{ v_{k_2\nu_2} \tau_2 \delta(\varepsilon_{k_2\nu_2} - \varepsilon_{k_2+q\nu_2'} + \hbar\omega) + v_{k_2+q\nu_2'} \tau_2 \delta(\varepsilon_{k_2\nu_2} - \varepsilon_{k_2+q\nu_2'} - \hbar\omega) \right\} \Bigg].
\end{aligned}$$

Here the above described substitution $\omega \to -\omega$ is made, but *only* in the first term in the curly brackets in the k_2 integral. Now the two integrals over k_1 and k_2 are of the same form. Furthermore we make the variable change G_1', G_1 to $G_1' - G_1$, G_1 in the sum over the reciprocal lattice vectors and since the integrant thereby becomes independent of G_1 the G_1 sum can be carried out: $\sum_{G_1} \int_{-\frac{\pi}{a_1}+G_1}^{\frac{\pi}{a_1}+G_1} \frac{\mathrm{d}q}{2\pi}(\cdots) = \int_{-\infty}^{\infty} \frac{\mathrm{d}q}{2\pi}(\cdots)$. Using eq.(3.26), (3.33) (in the reformulated version) and

$$n_{\mathrm{B}}(-\hbar\omega) n_{\mathrm{B}}(\hbar\omega) = -\frac{1}{4 \sinh^2\left(\frac{\hbar\omega}{2k_{\mathrm{B}}T}\right)} \qquad (3.34)$$

we therefore obtain the transresistivity ρ_{21} as[16]:

$$\rho_{21} = \frac{\hbar^2}{4\pi\tilde{e}_1\tilde{e}_2 n_1 n_2 k_{\mathrm{B}} T}\frac{1}{2\pi r_2^c}\sum_{G_1G_2}\delta_{G_1,G_2}\frac{1}{(2\pi)^2}\sum_{\nu_1\nu_1'\nu_2\nu_2'}|\mathcal{J}(\nu_1\nu_1',\nu_2\nu_2')|^2 \tag{3.35}$$
$$\times\int_{-\infty}^{\infty}\frac{\mathrm{d}q}{2\pi}\int_{-\infty}^{\infty}\mathrm{d}\omega\frac{V_{12}(q,\nu_1,\nu_1',\omega)V_{12}^*(q+G_1,\nu_1,\nu_1',\omega)}{\sinh^2\left(\frac{\hbar\omega}{2k_{\mathrm{B}}T}\right)}F^{(1)}_{\nu_1\nu_1'}(q,\omega)F^{(2)}_{\nu_2\nu_2'}(q,\omega),$$

where the F-functions are defined as

$$F^{(i)}_{\nu_i\nu_i'}(q,\omega) \equiv \frac{2\pi\tilde{e}_i}{\hbar\mu^{(i)}_{\mathrm{Tr}}}\int_{-\frac{\pi}{a_i}}^{\frac{\pi}{a_i}}\frac{\mathrm{d}k_i}{2\pi}\left[f^0(\varepsilon_{k_i\nu_i})-f^0(\varepsilon_{k_i+q\nu_i'})\right]|g_i(k_i\nu_i,k_i+q\nu_i')|^2$$
$$\times\,\tau_i\left[v_{k_i+q\nu_i'}-v_{k_i\nu_i}\right]\delta(\varepsilon_{k_i\nu_i}-\varepsilon_{k_i+q\nu_i'}-\hbar\omega). \tag{3.36}$$

$F^{(i)}_{\nu_i\nu_i'}(q,\omega)$ is up to some factors the same as the k_1 integral in eq.(3.30) and therefore has the same properties,

$$F^{(i)}_{\nu_i\nu_i'}(q,-\omega) = -F^{(i)}_{\nu_i'\nu_i}(q,\omega), \tag{3.37}$$
$$F^{(i)}_{\nu_i\nu_i'}(-q,\omega) = -F^{(i)}_{\nu_i\nu_i'}(q,\omega), \tag{3.38}$$

which are shown as before by variable substitutions[17] and using inversion symmetry in k space. Note the band index switch in eq.(3.37). Furthermore the product of the Fourier transforms are even in ω and q (by redefining the reciprocal lattice sum). Therefore the integrand of ρ_{21} is even in q and ω (when the sum over the band indices are taken inside the integrals[18]) and the *final* form for the transresistivity in the quasi one dimensional case is:

$$\rho_{21} = \frac{\hbar^2}{\pi\tilde{e}_1\tilde{e}_2 n_1 n_2 k_{\mathrm{B}} T}\frac{1}{2\pi r_2^c}\sum_{G_1G_2}\delta_{G_1,G_2}\frac{1}{(2\pi)^2}\sum_{\nu_1\nu_1'\nu_2\nu_2'}|\mathcal{J}(\nu_1\nu_1',\nu_2\nu_2')|^2 \tag{3.39}$$
$$\times\int_{0}^{\infty}\frac{\mathrm{d}q}{2\pi}\int_{0}^{\infty}\mathrm{d}\omega\frac{V_{12}(q,\nu_1,\nu_1',\omega)V_{12}^*(q+G_1,\nu_1,\nu_1',\omega)}{\sinh^2\left(\frac{\hbar\omega}{2k_{\mathrm{B}}T}\right)}F^{(1)}_{\nu_1\nu_1'}(q,\omega)F^{(2)}_{\nu_2\nu_2'}(q,\omega).$$

This result is the quasi one dimensional transresistivity for a multiwall carbon nanotube with more than one band found using the Coulomb matrix element from a tight binding model. The result is the natural combination of the transresistivity including the Bloch states from [113] and for more than one band [114].

[16]Where the summation indices over the reciprocal lattice vectors again are called G_1 and G_2.

[17]The substitutions are $k_i \to -k_i - q$ in eq.(3.37) and $k_i \to -k_i$ in eq.(3.38).

[18]Since a interchange of band indices are necessary for the integrand to be even.

The transresistivity formula can be understood intuitively as follows: The Coulomb drag is related to the interaction and thereby the dependence of V_{12} in ρ_{21}. The sinh function is from thermal factors and the F-functions gives the available (q, ω) phase space for scattering for the given band structure. The sums and integrals are there to get all the possible drag process (not forbidden by the selection rules $\mathcal{J}$).

Note that τ_i could a priori have been dependent on k_i and ν_i, which would have made the velocity differences into $\left[v_{k_i+q,\nu_i'}\tau_i(k_i+q,\nu_i') - v_{k_i,\nu_i}\tau_i(k_i,\nu_i)\right]$ in the F functions as in [52]. This could also have been included here by letting τ_i depend on k and ν in eq.(3.7) and assuming that $\tau_i(k_i,\nu_i)$ is even in k_i, but since we will use a constant τ_i all through this thesis, this was not included in the derivation of ρ_{21} for simplicity. The advantage of a constant τ_i is that we can move it outside the integration in the F function and since $\mu_{\mathrm{Tr}}^{(i)} \propto \tau_i$ in eq.(3.12) it cancels out, i.e. the transresistivity ρ_{21} is independent of the single subsystem property τ_i, when this is approximately a constant.

The geometry also introduces a simple difference between the transresistivity expressions in eq.(3.39) and in [52, 114]. These are extra factors of $\frac{1}{(2\pi r_2^c)}$ and $\frac{1}{(2\pi)^2}$ and the q integral being over one instead of two dimensions. The geometric factor $\frac{1}{2\pi r_2^c}$ (from eq.(3.25)) means that $\rho_{21} \neq \rho_{12}$, since $r_1^c \neq r_2^c$. This is not unphysical, since the transresistance R_{21} is (remembering that $L = L_1 = L_2$)

$$R_{21} = \rho_{21}\frac{L}{2\pi r_1^c}, \tag{3.40}$$

so $R_{21} = R_{12}$.

Furthermore the prefactor of R_{21} (found from eq.(3.40) and (3.39)) does not depend on the cylinder radii, since the densities n_1 and n_2 are proportional to $\frac{1}{2\pi r_i^c}$, i.e. $n_1 n_2 2\pi r_1^c 2\pi r_2^c$ is radius independent. So the transresistance only depends on the radii in the electron interaction. This also shows that if we had done an one dimensional calculation, where the current density (3.25) and the densities were without the factor $\frac{1}{2\pi r_i^c}$, *but* still had used the same potential, then the transresistance R_{21} is the same as it should be, since R_{21} should not depend on our conventions for current density and carrier density. The reason for the use of the conventions for the quasi 1D case will become clear, when the model for the screened Coulomb interaction is considered.

Note that the F-function in eq.(3.36) is a generalization of (q times) the imaginary part of the susceptibility $\mathrm{Im}\chi(q,\omega)$ when one quadratic band crossing the fermi surface is used [6].

3.3.4 Simplifying the F-functions further

The assumption of a constant τ_i and the one dimensional integration over wave vectors in the F-functions make it possible to give the F-functions in an even

simpler form. Rewriting the definition (3.36) of $F^{(i)}_{\nu_i\nu_i'}(q,\omega)$ gives:

$$F^{(i)}_{\nu_i\nu_i'}(q,\omega) = -\frac{2\pi\tilde{e}_i\tau_i}{\hbar^2\mu^{(i)}_{\rm Tr}}\int_{-\frac{\pi}{a_i}}^{\frac{\pi}{a_i}}\frac{{\rm d}k_i}{2\pi}\left[f^0(\varepsilon_{k_i\nu_i}) - f^0(\varepsilon_{k_i+q\nu_i'})\right]|g_i(k_i\nu_i, k_i+q\nu_i')|^2 \times \frac{\partial}{\partial k}(\varepsilon_{k_i\nu_i} - \varepsilon_{k_i+q\nu_i'} - \hbar\omega)\delta(\varepsilon_{k_i\nu_i} - \varepsilon_{k_i+q\nu_i'} - \hbar\omega), \quad (3.41)$$

since $\frac{\partial\omega}{\partial k} = 0$. Furthermore for an arbitrary function $h(x)$ with zeros x_0 and $h'(x_0) \neq 0$ one has the relation[19]:

$$\delta(h(x)) = \sum_{x_0}\delta(h'(x_0)(x-x_0)) = \sum_{x_0}\frac{\delta(x-x_0)}{|h'(x_0)|}. \quad (3.42)$$

This is now used to find the simple form of $F^{(i)}_{\nu_i\nu_i'}(q,\omega)$ as:

$$F^{(i)}_{\nu_i\nu_i'}(q,\omega) = -\frac{\tilde{e}_i\tau_i}{\hbar^2\mu^{(i)}_{\rm Tr}}\sum_{k_s}[f^0(\varepsilon_{k_s\nu_i}) - f^0(\varepsilon_{k_s+q\nu_i'})] \times |g_i(k_s\nu_i, k_s+q\nu_i')|^2\frac{\frac{\partial}{\partial k}(\varepsilon_{k_s\nu_i} - \varepsilon_{k_s+q\nu_i'} - \hbar\omega)}{|\frac{\partial}{\partial k}(\varepsilon_{k_s\nu_i} - \varepsilon_{k_s+q\nu_i'} - \hbar\omega)|} \quad (3.43)$$

i.e.

$$\boxed{F^{(i)}_{\nu_i\nu_i'}(q,\omega) = \quad (3.44)$$
$$-\frac{\tilde{e}_i\tau_i}{\hbar^2\mu^{(i)}_{\rm Tr}}\sum_{k_s}{\rm sign}(v_{k_s\nu_i} - v_{k_s+q\nu_i'})[f^0(\varepsilon_{k_s\nu_i}) - f^0(\varepsilon_{k_s+q\nu_i'})]\ |g_i(k_s\nu_i, k_s+q\nu_i')|^2}$$

where k_s are the zeros of $\varepsilon_{k\nu_i} - \varepsilon_{k+q\nu_i'} - \hbar\omega = 0$ in the FBZ of subsystem i and

$${\rm sign}(x) = \begin{cases} 1 & \text{for} \quad x > 0 \\ 0 & \text{for} \quad x = 0 \\ -1 & \text{for} \quad x < 0 \end{cases}. \quad (3.45)$$

This formula is also true if $\frac{\partial}{\partial k}(\varepsilon_{k_i\nu_i} - \varepsilon_{k_i+q\nu_i'} - \hbar\omega)\big|_{k_i=k_s} = 0$ because then $F^{(i)}_{\nu_i\nu_i'}(q,\omega)$ was originally zero in eq.(3.41). Eq.(3.44) will be used in the evaluation of $F^{(i)}_{\nu_i\nu_i'}(q,\omega)$ in the coming chapters.

[19] If $h'(x_0) = 0$ one has to expand to first non-vanishing order and use that instead.

Outlook

Now we have a formula for the transresistivity to be used in the problem of Coulomb drag in multiwall carbon nanotubes, but before we go on to this problem we consider more closely ρ_{21} for different simple band structures in the next chapter and we see how this effects the Coulomb drag.

Chapter 4

The Coulomb drag in two simple models in one dimension

The purpose of the present chapter is to compare the transresistivity ρ_{21} for the (piecewise) linear dispersion relation $\varepsilon_k = \alpha_{\mathsf{l}}|k|$ (l for linear) to the usual free electron dispersion relation $\varepsilon_k = \alpha_{\mathsf{qu}}k^2$ in one dimension for both an unscreened and a completely screened Coulomb interaction. This is relevant because metallic carbon nanotubes have approximately linear bands near the Fermi level and so far little work has been done on Coulomb drag with non-quadratic band structure. The specific physical situation under consideration is two parallel coupled one dimensional quantum wires as seen on figure 4.1. This could be realized by etching in a two dimensional electron gas in GaAs [38] or by having parallel carbon nanotubes, but there is, however, no experimental way to change between the two idealized models used in this chapter. Note that the geometry of the system only enters the calculation of the electron interaction and the parallel configuration is chosen for simplicity. So we can use the coaxial geometry just by using another interaction as we shall see in chapter 5.

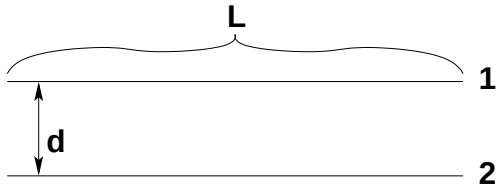

Figure 4.1: Two parallel quantum wires of length L and separation d, which is the geometry considered in this chapter. Note that the geometry of the system only enters in the electron interaction.

4.1 The transresistivity for one band in one dimension

The transresistivity formula (3.39) in one dimension with only a single band and no lattice simplifies to:

$$\rho_{21} = \frac{\hbar^2}{\pi \tilde{e}_1 \tilde{e}_2 n_1 n_2 k_{\mathrm{B}} T} \int_0^\infty \frac{\mathrm{d}q}{2\pi} \int_0^\infty \mathrm{d}\omega \; \frac{|W_{12}(q,\omega)|^2 F_1(q,\omega) F_2(q,\omega)}{\sinh^2\left(\frac{\hbar\omega}{2k_{\mathrm{B}}T}\right)}, \tag{4.1}$$

where n_i is the one dimensional carrier density and $W_{12}(q,\omega)$ is defined from the Coulomb matrix element as:

$$\langle k_1' k_2' | V_{12}(|\mathbf{r}_1 - \mathbf{r}_2|) | k_1 k_2 \rangle = \frac{1}{L} W_{12}(q,\omega) \delta_{k_1+k_2, k_1'+k_2'}, \tag{4.2}$$

i.e. we use $g = 1$ as for the plane wave states. The $F_i(q,\omega)$ function in the single band case is[1]:

$$F_i(q,\omega) = -\frac{\tilde{e}_i \tau_i}{\hbar^2 \mu_{\mathrm{Tr}}^{(i)}} \sum_{k_s} \mathrm{sign}(v_{k_s} - v_{k_s+q}) [f^0(\varepsilon_{k_s}) - f^0(\varepsilon_{k_s+q})], \tag{4.3}$$

where k_s is all the solutions of $\varepsilon_k - \varepsilon_{k+q} - \hbar\omega = 0$ (not only in the FBZ). Remember that $F_i(q,\omega)$ is odd in both q and ω (see eq.(3.37) and eq.(3.38)).

4.2 The quadratic band model

The transresistivity is found using the familiar free electron quadratic dispersion relation

$$\varepsilon_k = \alpha_{\mathsf{qu}} k^2 \tag{4.4}$$

in one dimension, where α_{qu} is a parameter (qu for quadratic) conventionally given in terms of an effective mass m^* as $\alpha_{\mathsf{qu}} = \frac{\hbar^2}{2m^*}$ [1, chap.2] to make it formally identical to the free electron case. This dispersion relation has a smooth velocity $v_k = \frac{2\alpha_{\mathsf{qu}}}{\hbar} k$ in contract to the linear model as we shall see (eq.(4.19)).

4.2.1 Single subsystem properties

The transresistivity ρ_{21} contains three single subsystem properties, which will be found: the carrier density n, the mobility μ_{Tr} and the chemical potential μ. We drop the subsystem indices $i = 1, 2$ in this section, since all properties are only for a single subsystem.

[1] Note that the subsystem index is now a lower index instead of a upper index on F for notational convenience.

The carrier density in the long wire limit[2] is:

$$n \equiv \frac{\langle N \rangle}{L} = \sum_\sigma \int_{-\infty}^{\infty} \frac{\mathrm{d}k}{2\pi} f^0(\varepsilon_k) = \sum_\sigma \int_{-\infty}^{\infty} \frac{\mathrm{d}k}{2\pi} \theta(\varepsilon_\mathrm{F} - \varepsilon_k) = \frac{2k_\mathrm{F}}{\pi}, \tag{4.5}$$

where we used temperature independence of n in the third equality and introduced the Fermi wave vector from the Fermi energy as $\varepsilon_\mathrm{F} = \varepsilon_{k_\mathrm{F}} = \alpha_{\mathsf{qu}} k_\mathrm{F}^2$.

The mobility μ_Tr is found by the Boltzmann equation as in section 3.2 and in the long wire and for one band, the current density J eq.(3.12) is:

$$J = -\frac{\tilde{e}^2 E\tau}{\hbar} \sum_\sigma \int_{-\infty}^{\infty} \frac{\mathrm{d}k}{2\pi} v_{k\nu} \frac{\partial f^0(\varepsilon_k)}{\partial k} = \frac{2\tilde{e}^2 E\tau}{\hbar} \int_{-\infty}^{\infty} \frac{\mathrm{d}k}{2\pi} \frac{2\alpha_{\mathsf{qu}}}{\hbar} f^0(\varepsilon_k) = \frac{2\tilde{e}^2 E\tau \alpha_{\mathsf{qu}} n}{\hbar^2},$$

by doing a partial integration (with vanishing boundary term) at the second equality and using $\sum_\sigma \int \frac{\mathrm{d}k}{2\pi} f^0(\varepsilon_k) = n$ in the last equality. By the definition $J = \tilde{e} n \mu_\mathrm{Tr} E$ the mobility is therefore:

$$\mu_\mathrm{Tr} = \frac{\tilde{e}\tau}{m^*} \qquad \text{with the effective mass} \qquad m^* = \frac{\hbar^2}{2\alpha_{\mathsf{qu}}}. \tag{4.6}$$

The chemical potential cannot be determined analytically in this model, so one can approximate it by the zero temperature chemical potential $\mu_{T\to 0} = \varepsilon_\mathrm{F}$ or do a Sommerfeld expansion[3] of μ as in [111]:

$$\mu \simeq \varepsilon_\mathrm{F} \left(1 - \frac{\pi^2}{6} (k_\mathrm{B}T)^2 \frac{\partial_\varepsilon g(\varepsilon_\mathrm{F})}{\varepsilon_\mathrm{F} g(\varepsilon_\mathrm{F})} \right) \tag{4.7}$$

where $g(\varepsilon_k)$ is the density of states, which for the quadratic band in the long wire limit is:

$$g(\varepsilon) \equiv \frac{1}{L} \sum_{k\sigma} \delta(\varepsilon - \varepsilon_k) = \frac{1}{\pi \sqrt{\alpha_{\mathsf{qu}} \varepsilon}}. \tag{4.8}$$

Therefore the chemical potential in the Sommerfeld approximation is:

$$\mu \simeq \varepsilon_\mathrm{F} \left(1 + \frac{\pi^2}{12} \left(\frac{T}{T_\mathrm{F}} \right)^2 \right) \qquad (T \ll T_\mathrm{F}). \tag{4.9}$$

This is a peculiar result since it *increases* instead of *decreases* as a function of temperature as one would expect because the classical limit $f^0(\varepsilon) \to e^{-(\varepsilon-\mu)/k_\mathrm{B}T}$ is decreasing, since using $n(T) = n(T=0) = \frac{2k_\mathrm{F}}{\pi}$ we have[4]:

$$\mu(T) = k_\mathrm{B}T \left[\ln\left(\frac{2}{\sqrt{\pi}} \right) + \frac{1}{2} \ln\left(\frac{T_\mathrm{F}}{T} \right) \right] \qquad \text{for} \quad T \gg T_\mathrm{F}. \tag{4.10}$$

The expected trend for the low temperature result will appear if one would include the higher order terms in the Sommerfeld expansion. Note that for a quadratic band this only happens in one dimension, since the density of states is constant and increasing in two and three dimensions, respectively.

[2]Since we integrate over k instead of summing: $\frac{1}{L}\sum_k \to \int \frac{\mathrm{d}k}{2\pi}$ when $L \to \infty$.

[3]This is basically a Taylor expansion of the chemical potential.

[4]Remembering the Gaussian integral $\int_{-\infty}^{\infty} \mathrm{d}x e^{-x^2} = \sqrt{\pi}$

4.2.2 The $F_i(q,\omega)$ function

The $F_i(q,\omega)$ function eq.(4.3) is now found. For quadratic dispersion relation there is only one zero of $\varepsilon_k - \varepsilon_{k+q} - \hbar\omega = 0$, which is

$$k_s = -\frac{1}{2}\Big(\frac{\hbar\omega}{\alpha_{\mathsf{qu}} q} + q\Big). \tag{4.11}$$

Therefore the sign of the velocity differences at k_s is:

$$\mathrm{sign}(v_{k_s} - v_{k_s+q}) = \mathrm{sign}\Big(-\frac{2\alpha_{\mathsf{qu}}}{\hbar} q\Big) = -\mathrm{sign}(q) = -1, \tag{4.12}$$

since $q > 0$ in the integrand eq.(4.1). Inserting the zero eq.(4.11), the mobility eq.(4.6) and eq.(4.12) in eq.(4.3) we have:

$$F_i(q,\omega) = +\frac{m_i^*}{\hbar^2}\left(f^0\left(\frac{(\hbar\omega)^2}{4\ \varepsilon_q} + \frac{\varepsilon_q}{4} + \frac{\hbar\omega}{2}\right) - f^0\left(\frac{(\hbar\omega)^2}{4\ \varepsilon_q} + \frac{\varepsilon_q}{4} - \frac{\hbar\omega}{2}\right)\right), \tag{4.13}$$

where $\varepsilon_q = \alpha_{\mathsf{qu}} q^2$.

The F function for zero and finite temperature is seen on figure 4.2. At zero temperature it is either zero or $-\frac{m^*}{\hbar^2}$, since the Fermi functions are step functions at $T = 0$. At higher temperatures the edges smear out due to the Fermi functions as seen on the figure. The transresistivity ρ_{21} in eq.(4.1) is obtained by integrating over the (positive) (q,ω)-plane and since both $W_{12}(q,\omega)$ and $\sinh^{-2}\left(\frac{\hbar\omega}{2k_{\mathrm{B}}T}\right)$ are decreasing as a function of q and ω, respectively, the most important points are for small q and ω. Therefore the important phase space available from the F function in the $\varepsilon_k = \alpha_{\mathsf{qu}} k^2$ model is around $(q,\omega) = (0,0)$ and $(q,\omega) = (2k_{\mathrm{F}}, 0)$, respectively. It is evident from the figure that there is more phase space around $q = 2k_{\mathrm{F}}$ (i.e. larger $F \neq 0$ area) than around $q = 0$, but the two decreasing factors ($W_{12}(q,\omega)$ and $\sinh^{-2}\left(\frac{\hbar\omega}{2k_{\mathrm{B}}T}\right)$) suppress the phase space around $q = 2k_{\mathrm{F}}$ more. So which one of the two points, that is the most important one in the drag is a competition between the available phase space (area of F) and the decreasing factors. So the main processes in the drag effect in the quadratic model in one dimension are the backscattering process $\pm k_{\mathrm{F}} \to \mp k_{\mathrm{F}}$, ($q = 2k_{\mathrm{F}}$) and forward scattering with very small q.

This is in sharp contrast to the two dimensional quadratic model, where the F function is also nonzero between $q = 0$ and $q = 2k_{\mathrm{F}}$ and is proportional to q, but otherwise has the same shape as figure 4.2 [52, 6], which increases the phase space around $q = 0$ substantially. Therefore the important processes in two dimensional Coulomb drag are all the particle-hole excitations around the Fermi surface (at low temperatures) and the backscattering $q = 2k_{\mathrm{F}}$ has no special importance[5]. In [6] the result of only the ω integration in the two dimensional case is shown and it has a peak around $1.4k_{\mathrm{F}}$, so if any, this is the main process.

[5]This contrast between a one and two dimensional system is general in the sense that

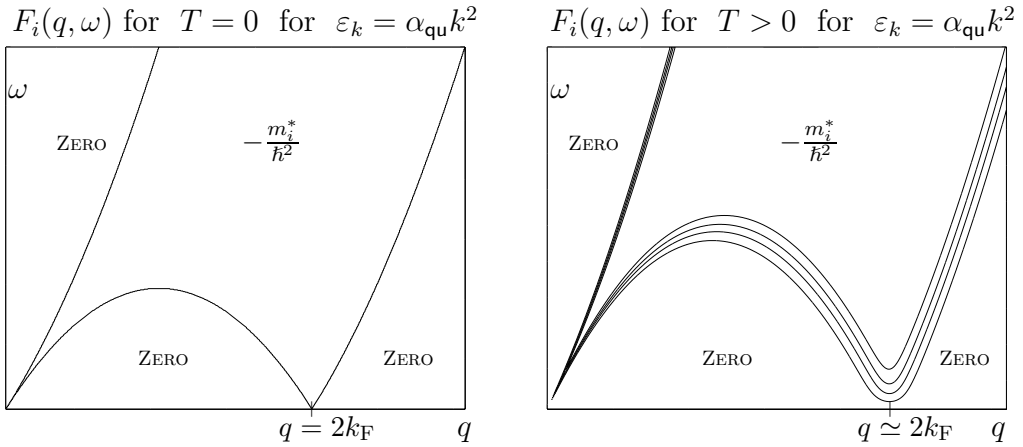

Figure 4.2: Contour plots of $F_i(q,\omega)$ in the quadratic model for $T=0$ and $T>0$. For $T>0$ the value $\frac{T}{T_{\mathrm{F}}} = 0.05$ and the approximation for the chemical potential $\mu \simeq \varepsilon_{\mathrm{F}}$ were used. If the Sommerfeld approximation is used the figure is not changed qualitatively for low temperatures ($T \ll T_{\mathrm{F}}$), but at higher temperatures the zero-temperature $2k_{\mathrm{F}}$ point is moved to higher q. Observe how the boundary gets broader at $T>0$ due to the Fermi functions.

4.2.3 The transresistivity ρ_{21}

The static limit of the potential, i.e. $W_{12}(q,\omega)$ independent of ω, and two equivalent subsystems are used. Therefore inserting $F_i(q,\omega)$ from eq.(4.13), n_i eq.(4.5) and $\tilde{e}_i = -e$ in the transresistivity eq.(4.1) we have:

$$\rho_{21} = \frac{\pi\hbar^4}{8\varepsilon_{\mathrm{F}} e^2 m^* k_{\mathrm{B}} T} \int_0^\infty \frac{\mathrm{d}q}{2\pi} |W_{12}(q)|^2 \int_0^\infty \mathrm{d}\omega \frac{F(q,\omega)^2}{\sinh^2\left(\frac{\hbar\omega}{2k_{\mathrm{B}}T}\right)} \tag{4.14}$$

$$= \frac{\pi m^*}{8\varepsilon_{\mathrm{F}} e^2 k_{\mathrm{B}} T} \int_0^\infty \frac{\mathrm{d}q}{2\pi} |W_{12}(q)|^2 \int_0^\infty \mathrm{d}\omega \frac{\left[f^0\left(\frac{(\hbar\omega)^2}{4\ \varepsilon_q} + \frac{\varepsilon_q}{4} + \frac{\hbar\omega}{2}\right) - f^0\left(\frac{(\hbar\omega)^2}{4\ \varepsilon_q} + \frac{\varepsilon_q}{4} - \frac{\hbar\omega}{2}\right)\right]^2}{\sinh^2\left(\frac{\hbar\omega}{2k_{\mathrm{B}}T}\right)}.$$

Introducing $T_\mu = \frac{\mu}{k_{\mathrm{B}}}$ and the dimensionless variables

$$\Omega = \frac{\hbar\omega}{2k_{\mathrm{B}}T}\ , \qquad Q = \frac{\sqrt{\alpha_{\mathsf{qu}}}q}{\sqrt{k_{\mathrm{B}}T}} \qquad \text{and} \qquad \tilde{f}^0(x) = \frac{1}{e^x+1}, \tag{4.15}$$

we get ρ_{21} in the new variables to be:

$$\rho_{21} = \frac{(m^*)^{\frac{3}{2}}\sqrt{k_{\mathrm{B}}T}}{4\sqrt{2}e^2\hbar\varepsilon_{\mathrm{F}}} \int_0^\infty \mathrm{d}Q \left|W_{12}\left(\sqrt{T/T_{\mathrm{F}}}k_{\mathrm{F}}Q\right)\right|^2$$
$$\times \int_0^\infty \mathrm{d}\Omega \frac{\left[\tilde{f}^0\left(\frac{\Omega^2}{Q^2} + \frac{Q^2}{4} + \Omega - \frac{T_\mu}{T}\right) - \tilde{f}^0\left(\frac{\Omega^2}{Q^2} + \frac{Q^2}{4} - \Omega - \frac{T_\mu}{T}\right)\right]^2}{\sinh^2(\Omega)}. \tag{4.16}$$

particle-hole excitations are heavily suppressed in one dimension due to lack of phase space for $\mathrm{Im}\chi(q,\omega)$ (which is F for the quadratic model)[17].

Note that if the densities are not identical, $n_1 \neq n_2$, then the transresistivity will be heavily suppressed, since the momentum conservation will be harder to fulfill near the Fermi surface.

To make sure that ρ_{21} in eq.(4.16) is finite it is necessary to consider the integrand. We are in a situation where both the denominator ($\sinh^2(\Omega)$) and numerator is zero at $\Omega = 0$, so we want to make sure that the $\Omega \to 0$ limit is finite. The integrand is clearly finite for all other values of Ω. The question of whether the integrand is finite for all Q values depends on the specific form of $W_{12}(q)$, but for a screened potential all $q \geq 0$ will give a finite $W_{12}(q)$ and for an unscreened potential the $q \to 0$ limit will diverge. Note that the integrand goes to zero for large Q and Ω, since $\sinh^{-2}(\Omega) \to 0$ for $\Omega \to \infty$ and assuming that $W_{12}(q) \to 0$ for $q \to \infty$. By using L`Hospitals rule[6] and the fact that $\lim_{x\to x_0}(g(x))^2 = (\lim_{x\to x_0} g(x))^2$ for $|\lim_{x\to x_0} g(x)| < \infty$ the limit $\Omega \to 0$ for the integrand is proportional to:

$$\lim_{\Omega\to 0} \frac{\left[\tilde{f}^0\left(\frac{\Omega^2}{Q^2}+\frac{Q^2}{4}+\Omega-\frac{T_\mu}{T}\right)-\tilde{f}^0\left(\frac{\Omega^2}{Q^2}+\frac{Q^2}{4}-\Omega-\frac{T_\mu}{T}\right)\right]^2}{\sinh^2(\Omega)} = \frac{1}{4\cosh^4\left(\frac{Q^2}{8}-\frac{T_\mu}{2T}\right)}.$$

So the integrand is finite for all Ω in the integration interval. The limit is a peak around the important scattering process $q = 2k_{\mathrm{F}}$ broadened by temperature. If the potential $W_{12}(q)$ fulfils the criteria

$$\int_0^\infty \mathrm{d}Q \left|W_{12}\left(\sqrt{T/T_{\mathrm{F}}}k_{\mathrm{F}}Q\right)\right|^2 F(Q,\Omega)^2 < \infty \quad \text{for all } \Omega \geq 0, \tag{4.17}$$

then the Q integration is finite. However the integration can be finite without eq.(4.17) being true.

We have now justified, *not* proven, that the integral eq.(4.16) is finite. In section 4.5 the transresistivity will be found numerically.

4.3 The linear band model

In this section we calculate the transresistivity in one dimension with the dispersion relation

$$\varepsilon_k = \alpha_{\mathrm{l}}|k|, \tag{4.18}$$

where $\frac{\alpha_{\mathrm{l}}}{\hbar}$ is the velocity and the wave vector is not restricted to the first Brillouin zone, but instead $k \in]-\infty, \infty[$ as for free electrons. This dispersion relation gives rise to a discontinuity at $k = 0$ for the velocity:

$$v_k = \frac{\alpha_{\mathrm{l}}}{\hbar}(2\theta(k)-1) = \begin{cases} -\frac{\alpha_{\mathrm{l}}}{\hbar} & \text{for } k < 0 \\ \frac{\alpha_{\mathrm{l}}}{\hbar} & \text{for } k > 0 \end{cases}, \tag{4.19}$$

[6]This says that $\lim_{x\to x_0}\frac{f(x)}{g(x)} = \lim_{x\to x_0}\frac{f'(x)}{g'(x)}$ for differentiable functions with nonzero derivative.

where $\theta(k)$ is the step function.

4.3.1 Single subsystem properties

The single subsystem properties n, $\mu_{\rm Tr}$ and μ are now found, again dropping the subsystem index $i = 1, 2$ for convenience.

The carrier density is found as in eq.(4.5) to be

$$n = \frac{2k_{\rm F}}{\pi}, \tag{4.20}$$

i.e. the same result expressed in terms of $k_{\rm F}$ is obtained in both models, but *not* in terms of $\varepsilon_{\rm F}$, since $\varepsilon_{\rm F}^{(\mathsf{lin})} = \alpha_{\mathsf{l}} k_{\rm F}^{(\mathsf{lin})}$ where as $\varepsilon_{\rm F}^{(\mathsf{qu})} = \alpha_{\mathsf{qu}} (k_{\rm F}^{(\mathsf{qu})})^2$.

The mobility is again found from the current density:

$$\begin{aligned} J &= -\frac{\tilde{e}^2 E\tau}{\hbar} \sum_\sigma \int_{-\infty}^{\infty} \frac{{\rm d}k}{2\pi} v_{k\nu} \frac{\partial f^0(\varepsilon_k)}{\partial k} \\ &= -\frac{2\tilde{e}^2 E\tau}{\hbar} \left[\int_{-\infty}^{0} \frac{{\rm d}k}{2\pi} \left(-\frac{\alpha_{\mathsf{l}}}{\hbar} \right) \frac{\partial f^0(\varepsilon_k)}{\partial k} + \int_0^{\infty} \frac{{\rm d}k}{2\pi} \frac{\alpha_{\mathsf{l}}}{\hbar} \frac{\partial f^0(\varepsilon_k)}{\partial k} \right] \\ &= \frac{2\tilde{e}^2 E\tau \alpha_{\mathsf{l}}}{\pi\hbar^2} \frac{1}{e^{-\mu/k_{\rm B}T} + 1}, \end{aligned} \tag{4.21}$$

where the velocity (4.19) and $f^0(\varepsilon_{k\to\pm\infty}) = 0$ were used. So using the expression $J = \tilde{e} n \mu_{\rm Tr} E$ and the carrier density eq.(4.20) the mobility is:

$$\mu_{\rm Tr} = \frac{\tilde{e}\tau}{m^*(T)} \qquad \text{with the effective mass} \quad m^*(T) = \frac{\hbar^2 k_{\rm F}}{\alpha_{\mathsf{l}}} (1 + e^{-\mu/k_{\rm B}T}). \tag{4.22}$$

This definition of a effective mass is not the same as the one used in most textbooks (such as in [5, p.210]), where the effective mass is proportional to the inverse curvature of the dispersion relation. The reason for the definition given here is to obtain the relation $\mu_{\rm Tr} = \frac{\tilde{e}\tau}{m^*}$. Note the relation $\varepsilon_k = \frac{\hbar^2 k_{\rm F}}{m^*(0)} |k|$ and the temperature dependence of the effective mass $m^*(T)$ in contrast to the temperature independent effective mass of a parabolic band, where the two definitions are the same (see section 4.2.1).

A particularly nice property of this model is that the chemical potential μ can be found exactly as follows[7]:

$$\begin{aligned} n(T) &= \sum_\sigma \int_{-\infty}^{\infty} \frac{{\rm d}k}{2\pi} \frac{1}{e^{(\alpha_{\mathsf{l}}|k| - \mu)/k_{\rm B}T} + 1} = \frac{2k_{\rm B}T}{\pi\alpha_{\mathsf{l}}} \int_{-\mu/k_{\rm B}T}^{\infty} dx \frac{1}{e^x + 1} \\ &= \frac{2k_{\rm B}T}{\pi\alpha_{\mathsf{l}}} \left(\frac{\mu}{k_{\rm B}T} + \ln(1 + e^{-\mu/k_{\rm B}T}) \right) \end{aligned} \tag{4.23}$$

[7] By use of the integral: $\int dx \frac{1}{e^x+1} = x - \ln(1 + e^x)$.

and using $n(T) = n(T = 0)$ and eq.(4.20) the exact chemical potential is:

$$\mu = k_{\mathrm{B}} T \ln(e^{T_{\mathrm{F}}/T} - 1) \simeq \begin{cases} \varepsilon_{\mathrm{F}} & \text{for} \quad T \ll T_{\mathrm{F}} \\ k_{\mathrm{B}} T \ln(\frac{T_{\mathrm{F}}}{T}) & \text{for} \quad T \gg T_{\mathrm{F}} \end{cases} . \tag{4.24}$$

Note that the low and high temperature limits are the same as in the quadratic model.

4.3.2 The $F_i(q, \omega)$ function

The first step to finding $F_i(q, \omega)$ for the linear dispersion relation is the sign of the velocity difference by using eq.(4.19):

$$\begin{aligned} \mathrm{sign}(v_k - v_{k+q}) &= \mathrm{sign}\left(\frac{2\alpha_{\mathrm{l}}}{\hbar}(\theta(k) - \theta(k+q))\right) = \mathrm{sign}\big(\theta(k) - \theta(k+q)\big) \\ &= -\theta(k+q)\theta(-k), \end{aligned} \tag{4.25}$$

which can be seen by analyzing the step functions for $q > 0$.

The zeros k_s of $\alpha_{\mathrm{l}}|k| - \alpha_{\mathrm{l}}|k+q| - \hbar\omega = 0$ can be found by dividing the solution into two cases depending of the sign of k. For $k > 0$ the $F_i(q, \omega)$ function is zero because $\mathrm{sign}(v_k - v_{k+q}) \propto \theta(-k)$ is zero in this case. If on the other hand $k < 0$ the $F_i(q, \omega)$ function is only non-zero if $\mathrm{sign}(v_k - v_{k+q}) \propto \theta(k+q) \neq 0$, i.e. if $k + q > 0$. In that case $|k+q| = k + q$ and $|k| = -k$, so

$$\alpha_{\mathrm{l}}|k| - \alpha_{\mathrm{l}}|k+q| - \hbar\omega = -\alpha_{\mathrm{l}}k - \alpha_{\mathrm{l}}(k+q) - \hbar\omega = 0, \tag{4.26}$$

which has the solution

$$k_s = -\frac{1}{2}\Big(\frac{\hbar\omega}{\alpha_{\mathrm{l}}} + q\Big). \tag{4.27}$$

Therefore $F_i(q, \omega)$ is obtained by inserting the mobility eq.(4.22), the sign difference of the velocities eq.(4.25) and the zero eq.(4.27) into eq.(4.3):

$$F_i(q,\omega) = +\frac{m_i^*(T)}{\hbar^2}\theta(-\hbar\omega + \alpha_{\mathrm{l}}q)\left[f^0\left(\frac{1}{2}|\hbar\omega + \alpha_{\mathrm{l}}q|\right) - f^0\left(\frac{1}{2}|\hbar\omega - \alpha_{\mathrm{l}}q|\right)\right], \tag{4.28}$$

where $\theta(\hbar\omega + \alpha q)$ is omitted, since $\omega \geq 0$ (and $q \geq 0$) in the integration.

Figure 4.3 shows that for $T = 0$ the $F_i(q, \omega)$ function is step-like and at $T > 0$ only two of the three edges are smeared out due to the Fermi functions in eq.(4.28). The line $\hbar\omega = \alpha q$ is a discontinuity for $F_i(q, \omega)$ even at $T > 0$ since it stems from the discontinuity in the dispersion relation. Therefore the important available phase space in the integral of ρ_{21} is only around $q = 2k_{\mathrm{F}}$ and no phase space is available around $q = 0$ at low temperatures[8] for the $\varepsilon_k = \alpha_{\mathrm{l}}|k|$ model.

[8] At high temperatures a large smearing by the Fermi functions can pick up some $q = 0$ phase space, but nothing compared to the quadratic model.

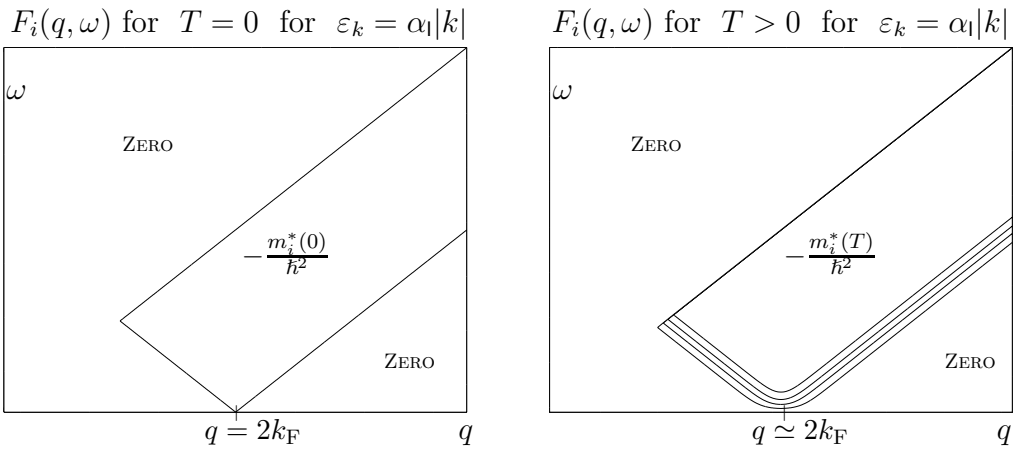

Figure 4.3: Contour plots of $F_i(q,\omega)$ for $T=0$ and $T>0$. For $T>0$ we use $T = 0.05T_\mathrm{F}$ and the exact chemical potential μ. If the approximation $\mu \simeq \varepsilon_\mathrm{F}$ is used the figure is not changed qualitatively at low temperatures.

This is in contrast to the quadratic model, where both $q=0$ and $q=2k_\mathrm{F}$ were important. So only backscattering around the Fermi level is the main process in the Coulomb drag in the linear model.

In other words, if the band structure is linearized around the Fermi level, the $\mathrm{sign}(v_k - v_{k+q})$ factor in the $F_i(q,\omega)$ function completely neglects the forward scattering process[9] around $q=0$.

4.3.3 The transresistivity ρ_{21}

The potential $W_{12}(q,\omega)$ is again used in the static limit, $W_{12}(q,\omega) = W_{12}(q)$ and the transresistivity eq.(4.1) in the linear model is found to be for equivalent subsystems:

$$\rho_{21} = \frac{(m^*(T))^2}{\pi\hbar^2 e^2 n^2 k_\mathrm{B} T}\int_0^\infty \frac{\mathrm{d}q}{2\pi}|W_{12}(q)|^2 \qquad (4.29)$$
$$\times \int_0^\infty \mathrm{d}\omega\ \theta(-\hbar\omega+\alpha_\mathrm{l} q)\frac{\left[f^0\left(\frac{1}{2}(\hbar\omega+\alpha_\mathrm{l} q)\right) - f^0\left(\frac{1}{2}(-\hbar\omega+\alpha_\mathrm{l} q)\right)\right]^2}{\sinh^2\left(\frac{\hbar\omega}{2k_\mathrm{B}T}\right)}$$
$$= \frac{(m^*(T))^2}{2\pi^2\hbar^2 e^2 n^2 k_\mathrm{B} T}\int_0^\infty \mathrm{d}\omega \int_{\frac{\hbar\omega}{\alpha_\mathrm{l}}}^\infty \mathrm{d}q|W_{12}(q)|^2\ \frac{\left[f^0\left(\frac{1}{2}(\hbar\omega+\alpha_\mathrm{l} q)\right) - f^0\left(\frac{1}{2}(-\hbar\omega+\alpha_\mathrm{l} q)\right)\right]^2}{\sinh^2\left(\frac{\hbar\omega}{2k_\mathrm{B}T}\right)},$$

[9]Some authors recently argued that the small momentum transfer process are the most important ones for one dimension [107].

which in terms of the dimensionless variable eq.(4.15) and $\mathcal{Q} = \frac{\alpha_{\parallel} q}{2k_{\mathrm{B}}T}$ is:

$$\rho_{21} = \frac{\hbar(1+e^{-\mu/k_{\mathrm{B}}T})^2 k_{\mathrm{B}}T}{2e^2\alpha_{\parallel}^3} \tag{4.30}$$
$$\times \int_0^\infty \mathrm{d}\Omega \int_\Omega^\infty \mathrm{d}\mathcal{Q} \left| W_{12}\left(2k_{\mathrm{F}}\frac{T}{T_{\mathrm{F}}}\mathcal{Q}\right)\right|^2 \frac{\left[\tilde{f}^0\big(\Omega+\mathcal{Q}-\frac{T_\mu}{T}\big) - \tilde{f}^0\big(-\Omega+\mathcal{Q}-\frac{T_\mu}{T}\big)\right]^2}{\sinh^2(\Omega)}.$$

As in the quadratic model we consider the $\Omega \to 0$ limit of the integrand, to make sure the integral is finite:

$$\lim_{\Omega\to 0} \frac{\left[\tilde{f}^0\big(\Omega+\mathcal{Q}-\frac{T_\mu}{T}\big) - \tilde{f}^0\big(-\Omega+\mathcal{Q}-\frac{T_\mu}{T}\big)\right]^2}{\sinh^2(\Omega)} = \frac{1}{4\cosh^4\left(\frac{\mathcal{Q}}{2}-\frac{T_\mu}{2T}\right)}, \tag{4.31}$$

which again peaks at the important backscattering process $q = 2k_{\mathrm{F}}$ broadened by temperature. The integration is finite if the potential $W_{12}(q)$ fulfils:

$$\int_\Omega^\infty \mathrm{d}\mathcal{Q} \left| W_{12}\left(2k_{\mathrm{F}}\frac{T}{T_{\mathrm{F}}}\mathcal{Q}\right)\right|^2 (F(\mathcal{Q},\Omega))^2 < \infty \quad \text{for all } \Omega \geq 0. \tag{4.32}$$

Again the opposite is not true, i.e. we can have a finite ρ_{21} without eq.(4.32) being fulfilled.

4.4 The Coulomb matrix element

The task is now to do the integrals of ρ_{21} in eq.(4.16) and eq.(4.30) numerically in the two models to compare the results. We will consider two completely opposite limits of a screened potential: An unscreened potential and a completely screened potential.

4.4.1 The unscreened Coulomb potential

We now investigate the simple unscreened Coulomb potential $V_{12}(|\mathbf{r}_1 - \mathbf{r}_2|) = \frac{e^2}{4\pi\varepsilon_0\varepsilon_r|\mathbf{r}_1-\mathbf{r}_2|}$ for two coupled quantum wires, where ε_r is some relative permittivity for the material (see figure 4.1). We have a static interaction, since $V_{12}(|\mathbf{r}_1 - \mathbf{r}_2|)$ is not time dependent as a screened potential could be. Note that this is the first and only time in the calculation of ρ_{21} that the geometry of the coupled quantum wires is taken into account.

To find the Coulomb matrix element we need the wave functions in the two models. In the quadratic model the wave functions are plane waves $\frac{1}{\sqrt{L}}e^{ikx}$ and in the linear $\varepsilon_k = \alpha_{\parallel}|k|$ model we also use plane waves for simplicity, even though

these are only approximations to the wave functions in this model. So in both models the Coulomb matrix element is:

$$\begin{aligned}\langle k_1' k_2'|V_{12}(|\mathbf{r}_1-\mathbf{r}_2|)|k_1 k_2\rangle &= \frac{1}{L^2}\int_{-L/2}^{L/2}\mathrm{d}x_1\int_{-L/2}^{L/2}\mathrm{d}x_2 e^{-ik_1'x_1-ik_2'x_2}V_{12}(|\mathbf{r}_1-\mathbf{r}_2|)e^{ik_1x_1+ik_2x_2}\\ &= \frac{1}{L^2}\int_{-L/2}^{L/2}\mathrm{d}x_1\int_{-L/2}^{L/2}\mathrm{d}x_2\; e^{-ik_1'x_1-ik_2'x_2+ik_1x_1+ik_2x_2}\frac{1}{L}\sum_q V_{12}(q)e^{iq(x_1-x_2)}\\ &= \frac{1}{L}V_{12}(k_1'-k_1)\delta_{k_1+k_2,k_1'+k_2'},\end{aligned} \tag{4.33}$$

where $V_{12}(q)$ is the one dimensional Fourier transformed potential, since $|\mathbf{r}_1-\mathbf{r}_2| = \sqrt{d^2+(x_1-x_2)^2}$, where x_i $(i=1,2)$ are the coordinates along the wires and d the wire separation. Therefore $W_{12}(q)$ from eq.(4.2) is identified as the Fourier transformed potential when plane waves are used, and it is:

$$\begin{aligned}W_{12}(q) &= \int_{-L/2}^{L/2}\mathrm{d}x\frac{e^2}{4\pi\varepsilon_0\varepsilon_r\sqrt{d^2+x^2}}\;e^{iqx}\\ &\simeq \frac{e^2}{4\pi\varepsilon_0\varepsilon_r}\int_{-\infty}^{\infty}\mathrm{d}x\frac{e^{iqx}}{\sqrt{d^2+x^2}} = \frac{e^2}{2\pi\varepsilon_0\varepsilon_r}\mathrm{K}_0(|q|d),\end{aligned} \tag{4.34}$$

where the long wire limit is used to do the integral analytically and $\mathrm{K}_0(|q|d)$ is the modified second order Bessel function as also found in [39, p.56]. Note that this potential is even in q, which is a special case of $V_{12}(-q) = V_{12}^*(q)$ from the real Coulomb potential $V_{12}(|\mathbf{r}|)$. Note also that the limits of $\mathrm{K}_0(|q|d)$ are $-\ln(|q|d/2)$ for $|qd| \ll 1$ and $\sqrt{\pi|q|d/2}e^{-|q|d}$ for $|qd| \gg 1$, so the potential is logarithmical divergent for $q \to 0$.

This potential does satisfy the integrability criteria eq.(4.32) and eq.(4.17) for $W_{12}(q)$ in the linear and quadratic model, since by partial integration we have (up to a constant factor):

$$\begin{aligned}&\int_0^\infty \mathrm{d}Q(\mathrm{K}_0(sQ))^2A(Q) =\\ &-\int_0^\infty \mathrm{d}Q\;\partial_Q A(Q)\int_0^Q \mathrm{d}x(\mathrm{K}_0(sx))^2 + \left[A(Q)\int_0^Q \mathrm{d}x(\mathrm{K}_0(sx))^2\right]_{Q=0}^{Q\to\infty}\end{aligned} \tag{4.35}$$

where $A(Q)$ is defined as $(F(Q,\Omega))^2$ and s is $k_\mathrm{F}\sqrt{\frac{T}{T_\mathrm{F}}}$ or $2k_\mathrm{F}\frac{T}{T_\mathrm{F}}$ in the quadratic and linear model, respectively. (Note that Q in eq.(4.35) is just a integration variable, so it can be both Q and $\mathcal{Q}$.) To justify that the integral eq.(4.35) is finite we note that $\lim_{Q\to\infty}A(Q) = 0$ and $\partial_Q A(Q) < \infty$ for all $Q \geq 0$ by use of the F functions squared. Furthermore

$$0 \leq \int_0^{x_0}\mathrm{d}x(\mathrm{K}_0(x))^2 < \int_0^\infty \mathrm{d}x(\mathrm{K}_0(x))^2 = \frac{\pi^2}{4} \qquad \text{for all} \qquad x_0 \geq 0, \tag{4.36}$$

so the integral is justified to be finite and we can do a numerical integration without worrying about trying to find a finite number for something infinite.

4.4.2 The completely screened Coulomb potential

The physical effect of screening is to limit the long-range Coulomb interaction due to electron-electron interaction [18]. In the extreme limit of completely screened electrons the interaction is a contact interaction: $V_{12}(|\mathbf{r}_1 - \mathbf{r}_2|) = U_0\delta(|\mathbf{r}_1 - \mathbf{r}_2|)$. This is of course an extreme limit and is never relevant in real Coulomb drag systems, since $\mathbf{r}_1 \neq \mathbf{r}_2$ is always true for separated subsystems. By again using plane waves for the wave functions in both the linear and quadratic model the Coulomb matrix element becomes $\langle k_1' k_2'|V_{12}(|\mathbf{r}_1 - \mathbf{r}_2|)|k_1 k_2\rangle = \frac{1}{L}U_0\delta_{k_1+k_2,k_1'+k_2'}$, so

$$W_{12}(q) = U_0 = \frac{e^2}{2\pi\varepsilon_0\varepsilon_r}\mathrm{K}_0(2k_\mathrm{F}d) = \text{const}, \tag{4.37}$$

where the constant U_0 was chosen to be the $q = 2k_\mathrm{F}$ value of the unscreened potential eq.(4.34), so that we have the same wire separation d dependence for the two potentials. However, the constant U_0 potential moves outside the integrals in ρ_{21}, so the value only changes the magnitude and not the T dependence of ρ_{21}. Even though this is a very simple featureless potential it does capture the essential mathematical difference between a screened and an unscreened Coulomb potential, which is that screening makes the divergence for small q disappear. Note that the constant potential does not satisfy eq.(4.17) and eq.(4.32), but the double integral in ρ_{21} is finite anyway, which can be seen by using a rewriting, which will be given in eq.(4.39).

4.5 Numerical evaluation of ρ_{21} and comparison of the linear and quadratic model

4.5.1 The transresistivity ρ_{21} at low temperatures

Before we do the integrals numerically we try to find a low temperature dependence of ρ_{21} analytically.

How the two dimensional method for $T \ll T_\mathrm{F}$ fails

In the two dimensional quadratic model one could successfully show $\rho_{21} \propto T^2$ for $T \ll T_\mathrm{F}$ by using $F_i(q,\omega)$ at zero temperature and maintain the $\sinh^2(\frac{\hbar\omega}{2k_\mathrm{B}T})$ factor in the integrand. If we do the same in the one dimensional $\varepsilon_k = \alpha_\mathrm{l}|k|$

model, the ω-integration can be done analytically as:

$$\begin{aligned}\rho_{21} &\propto \int_0^\infty \mathrm{d}q|W_{12}(q)|^2 \int_0^\infty \mathrm{d}\omega\ \theta(\alpha_{\mathsf{l}} q - \hbar\omega) \frac{\left[\theta(2\varepsilon_{\mathrm{F}} - \hbar\omega - \alpha_{\mathsf{l}} q) - \theta(2\varepsilon_{\mathrm{F}} + \hbar\omega - \alpha_{\mathsf{l}} q)\right]^2}{\sinh^2\left(\frac{\hbar\omega}{2k_{\mathrm{B}}T}\right)} \\ &= \int_0^\infty \mathrm{d}q|W_{12}(q)|^2 \int_{\frac{\alpha_{\mathsf{l}}}{\hbar}|q-2k_{\mathrm{F}}|}^{\frac{\alpha_{\mathsf{l}} q}{\hbar}} \mathrm{d}\omega\ \frac{1}{\sinh^2\left(\frac{\hbar\omega}{2k_{\mathrm{B}}T}\right)} \\ &= \frac{2k_{\mathrm{B}}T}{\hbar} \int_0^\infty \mathrm{d}q|W_{12}(q)|^2 \left[\coth\left(\frac{\alpha_{\mathsf{l}}}{2k_{\mathrm{B}}T}|q-2k_{\mathrm{F}}|\right) - \coth\left(\frac{\alpha_{\mathsf{l}}}{2k_{\mathrm{B}}T} q\right)\right], \quad (4.38)\end{aligned}$$

which is a divergent integral at $q = 2k_{\mathrm{F}}$ and $q = 0$, since[10] $\coth(x) \simeq \frac{1}{x}$ for $|x| \ll 1$. This approximation is therefore too crude and we cannot find a low temperature dependence for ρ_{21} in the same way as in the two dimensional case. The same thing also happens in the $\varepsilon_k = \alpha_{\mathsf{qu}} k^2$ model in one dimension as can be seen by the same analysis on eq.(4.14). Note that there is no way to make the integrals of ρ_{21} temperature independent in either the linear or quadratic model. So the method inspired by the two dimensional case does not work for neither the unscreened nor the completely screened potential.

Low temperature expansion for the completely screened potential

In both the linear and quadratic model we can used the rewriting

$$\frac{\left[\tilde{f}^0(\Omega + x) - \tilde{f}^0(-\Omega + x)\right]^2}{\sinh^2(\Omega)} = \frac{1}{\left(\cosh(x) + \cosh(\Omega)\right)^2}, \quad (4.39)$$

where x is $\mathcal{Q} - \frac{T_\mu}{T}$ in the linear model and $\frac{\Omega^2}{Q^2} + \frac{Q^2}{4} - \frac{T_\mu}{T}$ in the quadratic model. Therefore the transresistivity for the completely screened potential in the linear model $\varepsilon_k = \alpha_{\mathsf{l}}|k|$ is:

$$\begin{aligned}\rho_{21} &\propto (1 + e^{-\mu/k_{\mathrm{B}}T})^2 k_{\mathrm{B}}T \int_0^\infty \mathrm{d}\Omega \int_0^\infty \mathrm{d}\mathcal{Q} \frac{\theta(\mathcal{Q} - \Omega)}{\left(\cosh(\mathcal{Q} - \frac{T_\mu}{T}) + \cosh(\Omega)\right)^2} \\ &= (1 + e^{-\mu/k_{\mathrm{B}}T})^2 k_{\mathrm{B}}T \int_0^\infty \mathrm{d}\Omega \int_{-\frac{T_\mu}{T}}^\infty \mathrm{d}\widetilde{\mathcal{Q}} \frac{\theta(\widetilde{\mathcal{Q}} + \frac{T_\mu}{T} - \Omega)}{\left(\cosh(\widetilde{\mathcal{Q}}) + \cosh(\Omega)\right)^2}, \quad (4.40)\end{aligned}$$

where $\widetilde{\mathcal{Q}} = \mathcal{Q} - \frac{T_\mu}{T}$. For $T \to 0$ the integration limit is $-\infty$ and $e^{-\mu/k_{\mathrm{B}}T} \to 0$. Furthermore since the important part of the integral is for (numerically) small values of Ω and $\widetilde{\mathcal{Q}}$ we can set $\theta(\widetilde{\mathcal{Q}} + \frac{T_\mu}{T} - \Omega)$ equal to one, so the integral becomes independent of temperature and we therefore expect:

$$\rho_{21} \propto T \quad \text{for} \quad T \ll T_{\mathrm{F}} \quad (4.41)$$

[10] The definition $\coth(x) \equiv \frac{\cosh(x)}{\sinh(x)}$ is used.

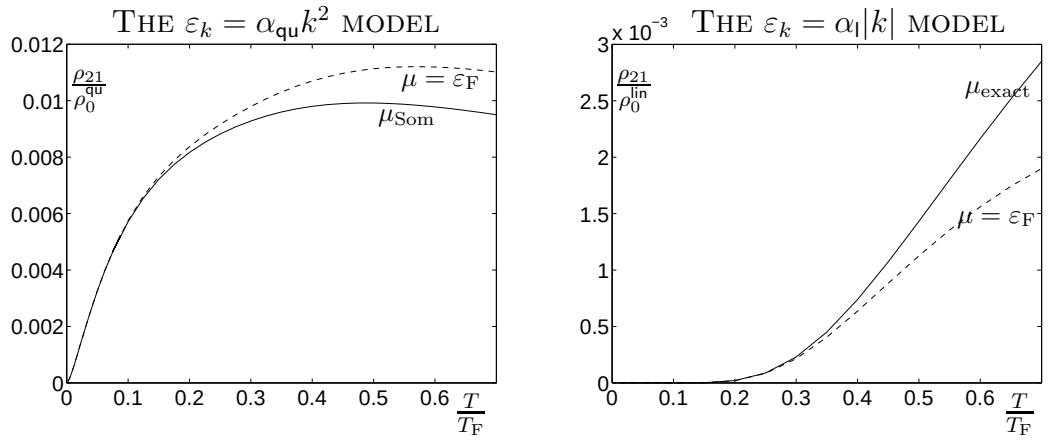

Figure 4.4: The transresistivity as a function of $\frac{T}{T_{\mathrm{F}}}$ for the linear and quadratic model in one dimension for the unscreened potential. The dashed lines are for the chemical potential in the low temperature approximation $\mu \simeq \varepsilon_{\mathrm{F}}$ and the full lines are for the exact eq.(4.24) and the Sommerfeld chemical potential eq.(4.9) in the two models, respectively. In both models we use the parameter $k_{\mathrm{F}} d = 4$, so the densities are the same in the two models.

in the linear model for the completely screened constant potential. Similarly it can be showed that $\rho_{21} \propto T$ for $T \ll T_{\mathrm{F}}$ for the quadratic model (see also [40]).

4.5.2 The numerical integration of ρ_{21}

We now have four different cases to investigate numerically: The linear and quadratic model for both the unscreened and the completely screened model. In any case a numerical integration over Q ($\mathcal{Q}$) and Ω for each temperature T is done to find the transresistivity as a function of temperature $\rho_{21}(T)$. The calculated integrals in the linear and quadratic model are eq.(4.16) and eq.(4.30) inserting the unscreened interaction $W_{12}(q)$ from eq.(4.34):

$$\rho_{21}^{\mathsf{lin}} = \rho_0^{\mathsf{lin}} \ (1 + e^{-\mu/k_{\mathrm{B}}T})^2 \frac{T}{T_{\mathrm{F}}} \tag{4.42}$$
$$\times \int_0^\infty \mathrm{d}\Omega \int_\Omega^\infty \mathrm{d}\mathcal{Q} \left| \mathrm{K}_0 \left(2k_{\mathrm{F}} d \frac{T}{T_{\mathrm{F}}} \mathcal{Q} \right) \right|^2 \frac{\left[\tilde{f}^0\big(\Omega + \mathcal{Q} - \frac{T_\mu}{T}\big) - \tilde{f}^0\big(-\Omega + \mathcal{Q} - \frac{T_\mu}{T}\big) \right]^2}{\sinh^2(\Omega)}$$

and

$$\rho_{21}^{\mathsf{qu}} = \rho_0^{\mathsf{qu}} \ \sqrt{\frac{T}{T_{\mathrm{F}}}} \int_0^\infty \mathrm{d}Q \left| \mathrm{K}_o \left(\sqrt{T/T_{\mathrm{F}}} k_{\mathrm{F}} d Q \right) \right|^2$$
$$\times \int_0^\infty \mathrm{d}\Omega \frac{\left[\tilde{f}^0 \left(\frac{\Omega^2}{Q^2} + \frac{Q^2}{4} + \Omega - \frac{T_\mu}{T} \right) - \tilde{f}^0 \left(\frac{\Omega^2}{Q^2} + \frac{Q^2}{4} - \Omega - \frac{T_\mu}{T} \right) \right]^2}{\sinh^2(\Omega)}, \tag{4.43}$$

where the temperature independent prefactors are:

$$\rho_0^{\mathsf{lin}} = \frac{\hbar e^2 \varepsilon_{\mathrm{F}}^{\mathsf{lin}}}{8\pi^2 \alpha_{\mathsf{l}}^3 (\varepsilon_0 \varepsilon_r)^2} \quad \text{and} \quad \rho_0^{\mathsf{qu}} = \frac{\hbar e^2}{64\pi^2 \alpha_{\mathsf{qu}}^{\frac{3}{2}} \sqrt{\varepsilon_{\mathrm{F}}^{\mathsf{qu}}} (\varepsilon_0 \varepsilon_r)^2}, \tag{4.44}$$

which both have dimension of resistivity in one dimension: Ω/m.

To obtain the case of the completely screened potential we just need to use eq.(4.37), i.e. move the Bessel functions with a constant argument outside the integrals in eq.(4.42) and eq.(4.43) to get the constant $(\mathrm{K}_0(2k_{\mathrm{F}}d))^2$ in front.

The only parameter we have to fix (apart from the prefactors) in order to do the numerical integration is $k_{\mathrm{F}}d$, which is chosen to be $k_{\mathrm{F}}d = 4$ as would be the case if for example $d = 40\mathrm{nm}$ and $k_{\mathrm{F}} = 10^8\mathrm{m}^{-1}$ as in [38]. Details on the method for the numerical integration in the program MATLAB can be found in appendix D.

4.5.3 Comparison of ρ_{21} in the linear and quadratic model

Equal Fermi Temperatures?

By choosing the same $k_{\mathrm{F}}d$ in the linear and quadratic model we have the same carrier density $n = \frac{2k_{\mathrm{F}}}{\pi}$ in the two models, if we assume the wire separation d to be the same. However, the Fermi temperature T_{F} can be different in the to models, since in the quadratic model and in the linear model we have $k_{\mathrm{B}}T_{\mathrm{F}}^{\mathsf{qu}} = \alpha_{\mathsf{qu}}k_{\mathrm{F}}^2$ and $k_{\mathrm{B}}T_{\mathrm{F}}^{\mathsf{lin}} = \alpha_{\mathsf{l}}k_{\mathrm{F}}$, respectively. Therefore a specific T/T_{F} point on the graphs cannot in general be compared as representing the same temperature. However, if we choose $\alpha_{\mathsf{l}} = k_{\mathrm{F}}\alpha_{\mathsf{qu}}$, then the two Fermi temperatures are the same, $T_{\mathrm{F}}^{\mathsf{qu}} = T_{\mathrm{F}}^{\mathsf{lin}}$, but this makes the Fermi velocities different: $v^{\mathsf{lin}} = \frac{1}{2}v_{k_{\mathrm{F}}}^{\mathsf{qu}}$. The Fermi velocities are proportional to the relaxation time τ in a simple Drude picture, which drops out of the transresistivity, when τ is taken to be independent of k (see chapter 3). So the different Fermi velocities should not affect the transresistivity. Therefore if we assume the two Fermi temperatures to be equal for the two models, we can think of T/T_{F} as the same temperature in both models, which makes it easier to compare the form of the graphs of the transresistivities. On the other hand the relative size of the transresistivity is dependent on the Fermi temperatures, since the ratio between the prefactors for equal densities are

$$\frac{\rho_0^{\mathsf{qu}}}{\rho_0^{\mathsf{lin}}} = \frac{1}{8}\left(\frac{T_{\mathrm{F}}^{\mathsf{lin}}}{T_{\mathrm{F}}^{\mathsf{qu}}}\right)^2, \tag{4.45}$$

i.e. dependent on the Fermi temperatures and is 1/8, when they are equal.

The role of the chemical potential

In figure 4.4 ρ_{21} for the unscreened potential is given for both the low temperature chemical potential, $\mu \simeq \varepsilon_{\mathrm{F}}$, and for the exact chemical potential and the Sommerfeld expansion of μ, respectively. The effect of changing the chemical potential μ

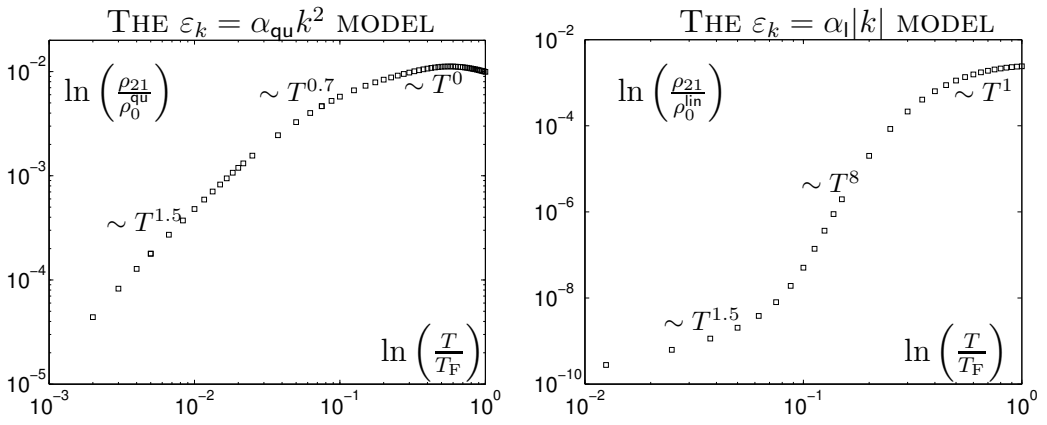

Figure 4.5: A double logarithmic plot of the transresistivity as a function of $\frac{T}{T_{\mathrm{F}}}$ for the linear and quadratic model in one dimension for the unscreened potential. In both models we use $k_{\mathrm{F}}d = 4$ and low temperature chemical potential $\mu = \varepsilon_{\mathrm{F}}$. We have fitted power laws, $\rho_{21} \propto T^n$, to different temperature intervals in both models and it seems like that both models have $\rho_{21} \propto T^{1.5}$ for low temperatures, but the $T^{1.5}$ regime is different in the two models. Each square on the figure represents a result of a numerical integration.

away from being the Fermi level is seen to be quite small in both the linear and quadratic model and as expected larger the larger the temperature. The effect on ρ_{21} of using the Sommerfeld expansion contra the exact chemical potential is opposite, i.e. it pulls ρ_{21} down and up wards, respectively. This is a direct consequence of the fact that the exact chemical potential eq.(4.24) is decreasing and the Sommerfeld expansion to first order eq.(4.9) is increasing. Due to the modest effect of changing the chemical potential away from ε_{F} we do not show a plot for the Sommerfeld and exact μ for the completely screened interaction.

Results of the unscreened potential

For the unscreened potential, the transresistivity is shown on figure 4.4 for the linear and quadratic model. It is evident that both transresistivities are increasing at first and go to zero at zero temperature. The ρ_{21} for the quadratic model seems to have a negative curvature over most of the interval $0 < T/T_{\mathrm{F}} < 0.7$, whereas ρ_{21} for the linear model has a positive curvature.

To obtain a better measure of comparison for the two models for an unscreened potential we consider a logarithmic plot of the transresistivities as seen in figure 4.5. Here we have fitted a power law dependence, $\rho_{21} \propto T^n$, to find the best n in each of the approximative linear intervals (in the log-plot). We see that both models show something like a $T^{1.5}$ dependence at low temperatures, but the crossover to another power law takes place at different T/T_{F} in the two models. The behavior after the $T^{1.5}$ regime is qualitatively different in the two models: $\rho_{21} \propto T^8$ and $\rho_{21} \propto T^{0.7}$, respectively. Furthermore the $\varepsilon_k = \alpha_{\mathsf{l}}|k|$ model has the $T^{1.5}$ behavior for substantially lower transresistivities than the quadratic model

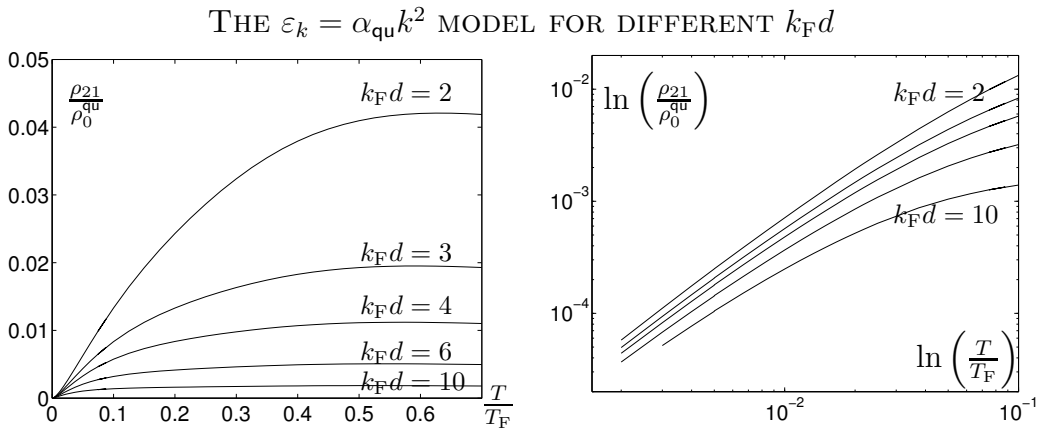

Figure 4.6: The transresistivity for the quadratic model for the unscreened potential for different values of $k_{\mathrm{F}}d$ from 2 (top curve) to 10 (bottom curve). It is seen that for this range of parameters the qualitative behavior of ρ_{21} is maintained. The same can be seen in the linear model as a numerical calculation shows (not given here). Note the fact that the longer apart the two wires are the smaller the induced current in the drag system.

(for $T_{\mathrm{F}}^{\mathsf{lin}} = T_{\mathrm{F}}^{\mathsf{qu}}$).

Similar conclusions can be obtained by considering other values of $k_{\mathrm{F}}d$ as seen in figure 4.6, since the form of the curves do not change drastically. Furthermore, we observe that when the wire separation becomes larger the transresistivity decreases, which can be understood by the intuitive assumption that the more separated the two subsystems are, the smaller the induced current should be.

Results of the completely screened potential

For the completely screened interaction (i.e. $W_{12}(q)$ constant) the transresistivities are seen in figure 4.7 for both the quadratic and linear model. Agreement between the expected power law $\rho_{21} \propto T$ from eq.(4.41) for low temperatures is found in both the linear and quadratic model. However, the quadratic model is linear until about $\frac{T}{T_{\mathrm{F}}} \sim 0.1$ whereas a substantial deviation from $\rho_{21} \propto T$ is first seen at about $\frac{T}{T_{\mathrm{F}}} \sim 3$ for the linear model (not shown).

Comparison of ρ_{21} for the two potentials

We now compare the unscreened and the completely screened potential. In both cases the F functions give the available phase space, but with a constant potential the integrand is not decreasing for q and thereby not limiting the phase space in that direction, i.e. all drag processes with different q but equal ω are equally probable. This is in contrast to the unscreened potential, which has a logarithmic divergence for $q \to 0$ and is decreasing with q. This logarithmic divergence gives the (small) phase space around $q = 0$ for the k^2 model a large weight and gives

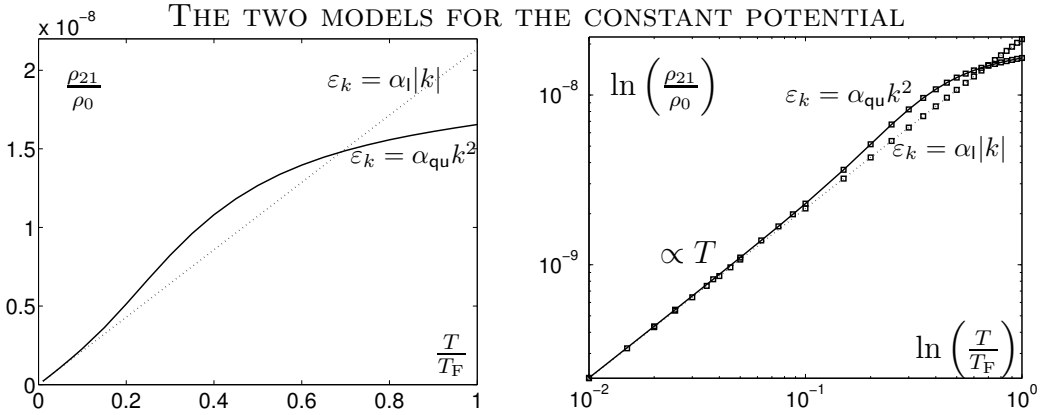

Figure 4.7: The transresistivity is shown for the linear (dotted) and quadratic (solid) model for the constant potential of eq.(4.37) for $k_{\mathrm{F}}d = 4$ and $\mu = \varepsilon_{\mathrm{F}}$ in a normal (left) and a logarithmic (right) plot. Here ρ_0 is ρ_0^{qu} and ρ_0^{lin}, respectively and the squares on the right figure are the calculated temperature points. Observe that both models are proportional to T for $T/T_{\mathrm{F}} \lesssim 0.1$ as found analytically in eq.(4.40).

rise to $\rho_{21} \propto T^{1.5}$ instead of $\rho_{21} \propto T$ for a screened potential[11].

In the linear model the decrease of $W_{12}(q)$ gives rise to higher powers of T than for the constant potential. As temperature increases the F functions smears out as Fermi functions and allows more and more lower q phase space. This phase space with lower q than $2k_{\mathrm{F}}$ gets enhanced by the non-constant and logarithmic divergent potential and gives the two power laws $\rho_{21} \propto T^{1.5}$ and $\rho_{21} \propto T^8$ with powers higher than one. For a constant potential the lower q phase space does not get enhanced more than the higher (than $2k_{\mathrm{F}}$) phase space and we therefore obtain the linear dependence.

Note, however, that in modelling a realistic system, e.g. two coupled quantum wires in GaAs, a good description of the screening is very important in the electron-electron interaction and will change the power laws for $T/T_{\mathrm{F}} \gtrsim 0.2$ substantially (see [51, 52]). So the unscreened and the completely screened potential are not sufficient descriptions at higher temperatures.

4.6 Concluding remarks on the simple models

We have now analyzed the difference between the Coulomb drag for a quadratic $\varepsilon_k = \alpha_{\mathsf{qu}}k^2$ and a piecewise linear $\varepsilon_k = \alpha_{\mathsf{l}}|k|$ dispersion relation in one dimension for an unscreened and a completely screened potential.

The F functions give the available phase space for electron scattering in the drag process and as found in sections 4.2.2 and 4.3.2 the two models reveals

[11]Note that in [40] it was showed that $\rho_{21} \propto T$ for another screened potential than the completely screened one used here.

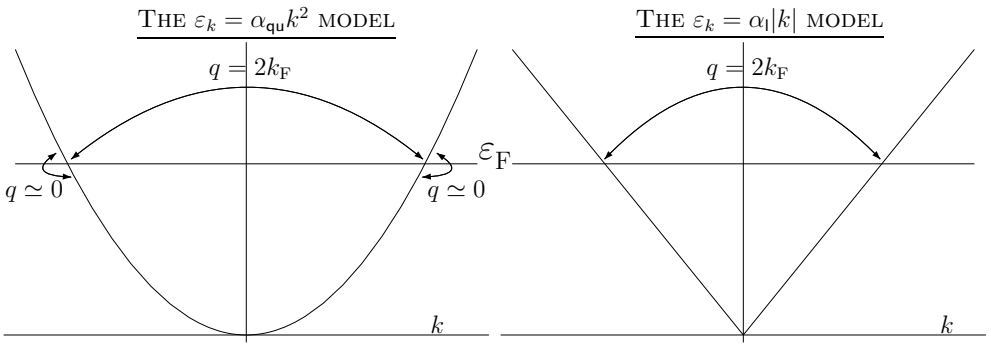

Figure 4.8: The different electron scattering processes mainely responsible for the Coulomb drag in the two models. In the quadratic model $\varepsilon_k \propto k^2$ the important processes are the small q forward scattering and the backscattering with $q \simeq 2k_{\mathrm{F}}$ in contrast to the linear model $\varepsilon_k \propto |k|$, where only the backscattering with $q \simeq 2k_{\mathrm{F}}$ is important due to the sign of the velocity difference in the F function in one dimension.

qualitatively different behavior. The quadratic model has two important processes: the small momentum transfer forward scattering process $q \simeq 0$ with small phase space and the backscattering process $q \simeq 2k_{\mathrm{F}}$ with larger phase space. The linear model, on the other hand, has only the backscattering $q \simeq 2k_{\mathrm{F}}$ process and completely neglects the forward scattering small q processes as illustrated on figure 4.8. This difference is due to the binary nature of the sign function of the velocity difference in F, which only appears in the one dimensional rewriting of the F function (see page 63). Therefore, any small velocity difference between the k points before and after the scattering process becomes magnified to $|\mathrm{sign}(v_k - v_{k+q})| = 1$, since it is not suppressed by the velocity difference $(v_k - v_{k+q})$ as in two dimensions.

The Coulomb interaction in the two opposite limits of the screening treats this difference in the dispersion relations very differently. It is therefore evident that a better model for the screening (in between the two extreme cases) is important and will be given for the nanotubes. For the two simple band structure models we see that for a constant potential $\rho_{21} \propto T$ for low temperatures, whereas for the logarithmic divergent potential we have $\rho_{21} \propto T^{1.5}$.

The general point is therefore, that by linearizing around the Fermi Level, as we have done in the case of the carbon nanotube band structure (see section 2.2.4), we completely neglect the forward scattering small momentum transfer processes. Furthermore, the screening should be included in the interaction.

Chapter 5

Coulomb drag in multiwall carbon nanotubes

In the previous chapters we have found many of the ingredients to calculate the Coulomb drag in a multiwall carbon nanotube within the Fermi Liquid picture such as the band structure, the Coulomb matrix elements and the transresistivity formula. In this chapter we find the Coulomb drag in a multiwall nanotube as a function of temperature T and Fermi level $\varepsilon_{\rm F}$ (i.e. a gate voltage), where both drive and drag subsystems are metallic tubes. We present numerical results in the case of drag between two armchair tubes.

5.1 Models of metallic nanotubes

From section 2.2.4 we know that the band structure as a function of k for all metallic nanotubes are either like an armchair tube with crossings at $\pm\frac{2\pi}{3|\mathbf{T}|}$ or like a zigzag tube with a double degenerate crossing at $k = 0$.

The model for armchair-like nanotubes

The armchair-like nanotubes are similar to the armchair nanotube in the sense that their band structures have two crossings of the Fermi level ($\varepsilon_{\rm F} = 0$) at $\pm\frac{2\pi}{3|\mathbf{T}|}$ with velocity $\pm v_0$. For higher (lower) energies the bands crossing the Fermi level for an armchair-like tube can be quite different from the armchair cosine bands eq.(2.43). Since the transport properties are only determined by the structure around the Fermi level, we will consider all these tubes as one class of tubes called armchair-like tubes. As the energy bands around the Fermi level we use the linear approximation around $\varepsilon_{\rm F} = 0$:

$$\varepsilon_k^{\Pi} = -\Pi\hbar v_0(|k| - k_0), \tag{5.1}$$

where $v_0 = \frac{\sqrt{3}}{2}\frac{\gamma_0 a}{\hbar}$ is the velocity near $\varepsilon_{\rm F} = 0$, $k_0 \equiv \frac{2\pi}{3|\mathbf{T}|}$ and $\Pi = \pm 1$ is only the parity index for (real) armchair tubes and just an index for the others. These

bands are made periodic by hand by repeating the FBZ=$]-\frac{\pi}{|\mathbf{T}|},\frac{\pi}{|\mathbf{T}|}]$ remembering that the FBZ is generally different for different armchair-like tubes. The two crosses at $\pm\frac{2\pi}{3|\mathbf{T}|}$ connected in this way have different n_c, but the same crystal angular momentum[1] and therefore we can label the bands by the same $\mathfrak{m}$.

The linearization is a good approximation as long as the Fermi level is not shifted too much $|\varepsilon_{\mathrm{F}}| \ll \gamma_0$, which is normally the case experimentally (see p.27). The linearization could also have been done around each ε_{F} used, but this is not done, since it would not preserve the particle-hole symmetry (from the graphene band structure) around $\varepsilon_{\mathrm{F}} = 0$ for each chosen ε_{F}.

The model for zigzag-like nanotubes

The second class of metallic tubes are the zigzag-like tubes defined as the tubes with a double degenerate crossing of $\varepsilon_{\mathrm{F}} = 0$ at $k = 0$ as for the zigzag tubes. Again a linearized band structure around the Fermi level is used for all the zigzag-like tubes:

$$\varepsilon^{\xi}_{k\mathfrak{m}} = \xi\hbar v_0 k, \tag{5.2}$$

where $\xi = \pm 1$ is an index. It is important to remember, that there are two bands for each ξ with different crystal angular momentum $\mathfrak{m}$. Furthermore, the FBZ is repeated periodically and again the FBZ is different for different zigzag-like tubes.

Neglecting small momentum forward scattering by linearization of $\varepsilon_{k\nu}$

By using a linearized model for the band structure around $\varepsilon_{\mathrm{F}} = 0$ for both the armchair-like and zigzag-like nanotube we only have two velocities $\pm v_0$ in the models. Since we have a factor of $\mathrm{sign}(v_{k_s\nu_i} - v_{k_s+q\nu'_i})$ in the F function eq.(3.44), we only have scattering with opposite velocities contributing to the Coulomb drag, i.e. *only backscattering are present in the linearized models* analogous to the $\varepsilon \propto |k|$ model considered in chapter 4. Therefore the g_i factors for backscattering in any metallic nanotube from section 2.3.1 can be used directly. If we should include the small q forward scattering processes, we should relax the strictly linear model to e.g. a cosine or a sine band as for the armchair and zigzag tubes in the tight binding model, respectively. However as in the quadratic model in chapter 4 the curvature of the bands will limit the available phase space (i.e. the F function) for small q forward scattering.

[1] Numerically it seem like the bands crossing the Fermi level for all armchair-like tubes have $\mathfrak{m} = 0$, which is found in several examples using the program in [87].

5.2 The screened Coulomb interaction

In section 2.3.2 we found the Coulomb matrix element in terms of the Fourier transformed Coulomb interaction, but did not specify the interaction further. Now we specify the interaction to include the effect of screening in the Coulomb interaction in a very simple way. The model of the screening presented here is better that the ones given in chapter 4, where only the unscreened and completely screened potential were considered. But the model is only strictly valid for a two dimensional (quasi one dimensional) cylinder, i.e. for large nanotubes where several bands are taken into account. We will however also use it to describe smaller tubes, since we are more interested in the effect of the band structure than the precise form of the screened interaction. The screened Coulomb interaction has a finite limit for $q \to 0$, which ensures the integral in the transresistivity to be finite. The calculation of the screening is done in the random phase approximation (RPA) and in the Thomas-Fermi approximation in appendix F.

5.2.1 The random phase approximation (RPA)

We now briefly consider the screening of the Coulomb potential in the random phase approximation, which simplifies to the Thomas-Fermi result in the limit of small q and $\omega \to 0$ (the static limit) as seen in appendix F.

The RPA for a single subsystem is obtained by a resummation of the most divergent Feynman diagrams in the self energy for an interacting electron gas [18, chap.12] (or from the equation of motion technique [126, sec.5.5]), which gives in general for a translational invariant subsystem a Dyson equation for the screened interaction $V(\mathbf{q},\omega)$ of the form:

$$V(\mathbf{q},\omega) = V^0(\mathbf{q}) + V^0(\mathbf{q})\chi(\mathbf{q},\omega)V(\mathbf{q},\omega), \tag{5.3}$$

where $V^0(\mathbf{q})$ is the bare Coulomb interaction and $\chi(\mathbf{q},\omega)$ the free polarizability (or Lindhard function):

$$\chi(\mathbf{q},\omega) = \frac{1}{\mathcal{V}} \sum_{\sigma\mathbf{k}} \frac{f^0(\varepsilon_{\mathbf{k}+\mathbf{q}}) - f^0(\varepsilon_{\mathbf{k}})}{\varepsilon_{\mathbf{k}+\mathbf{q}} - \varepsilon_{\mathbf{k}} - \hbar\omega + i\eta}, \tag{5.4}$$

where $\mathcal{V}$ is the normalization factor, η a positive infinitesimal [18] and the band indices were included in the wave vectors. So from eq.(5.3) we can get the screened interaction and the dielectric function $\varepsilon^{\mathrm{RPA}}(\mathbf{q},\omega)$ in the RPA as

$$V(\mathbf{q},\omega) = \frac{V^0(\mathbf{q})}{\varepsilon^{\mathrm{RPA}}(\mathbf{q},\omega)} \quad \text{where} \quad \varepsilon^{\mathrm{RPA}}(\mathbf{q},\omega) = 1 - V^0(\mathbf{q})\chi(\mathbf{q},\omega). \tag{5.5}$$

Now we consider the screened Coulomb interaction between electrons in the two subsystems in the RPA as in [112], i.e. we briefly generalize the above arguments to include two subsystems. By having two subsystems we have Coulomb

interaction both in the individual systems V_{ii} and between the systems V_{ij} $(i \neq j)$. Therefore we have four Dyson equations for the four screened interactions V_{ij}, but to find V_{12} it is sufficiently to consider only two [112, fig.2]:

$$V_{12}(\mathbf{q},\omega) = V^0_{12}(\mathbf{q}) + V^0_{12}(\mathbf{q})\chi_2(\mathbf{q},\omega)V_{22}(\mathbf{q},\omega) + V^0_{11}(\mathbf{q})\chi_1(\mathbf{q},\omega)V_{12}(\mathbf{q},\omega), \quad (5.6)$$
$$V_{22}(\mathbf{q},\omega) = V^0_{22}(\mathbf{q}) + V^0_{22}(\mathbf{q})\chi_2(\mathbf{q},\omega)V_{22}(\mathbf{q},\omega) + V^0_{21}(\mathbf{q})\chi_1(\mathbf{q},\omega)V_{12}(\mathbf{q},\omega), \quad (5.7)$$

where there is one polarizability function χ_i for each subsystem. Solving these two equations with two unknowns (V_{12} and V_{22}) we find:

$$V_{12}(\mathbf{q},\omega) = \frac{V^0_{12}(\mathbf{q})}{\varepsilon^{\mathrm{RPA}}(\mathbf{q},\omega)} \quad \text{where} \quad (5.8)$$
$$\varepsilon^{\mathrm{RPA}}(\mathbf{q},\omega) = \big(1 - V^0_{11}(\mathbf{q})\chi_1(\mathbf{q},\omega)\big)\big(1 - V^0_{22}(\mathbf{q})\chi_2(\mathbf{q},\omega)\big) - (V^0_{12}(\mathbf{q}))^2\chi_1(\mathbf{q},\omega)\chi_2(\mathbf{q},\omega), \quad (5.9)$$

using that $V^0_{21}(\mathbf{q}) = V^0_{12}(\mathbf{q})$. The introduced dielectric function should in principle have the indices 12, but since this is the only dielectric function we consider, they are neglected.

The system of two concentric cylinders are now considered. The bare interaction[2] was found in the Thomas-Fermi approximation eq.(F.28) by setting $q_{\mathrm{TF}} = 0$:

$$V^0_{ii}(r^c_i, r^c_i, q, \Delta\mathfrak{m}) = \frac{e^2}{\kappa}\mathrm{K}_{\Delta\mathfrak{m}}(qr^c_i)\mathrm{I}_{\Delta\mathfrak{m}}(qr^c_i) \quad \text{for } i = 1, 2, \quad (5.10)$$
$$V^0_{12}(r^c_1, r^c_2, q, \Delta\mathfrak{m}) = V^0_{21}(r^c_2, r^c_1, q, \Delta\mathfrak{m}) = \frac{e^2}{\kappa}\mathrm{K}_{\Delta\mathfrak{m}}(qr^c_1)\mathrm{I}_{\Delta\mathfrak{m}}(qr^c_2), \quad r^c_2 < r^c_1. \quad (5.11)$$

This is independent of the Thomas-Fermi approximation, since it is equivalent to solving the Poisson equation (eq.(F.6)) for a point charge in cylindrical coordinates using the Greens function technique for differential equations.

The calculation of the polarizability on the other hand requires specification of the band structure. In [118] the tight binding bands near the Fermi level $\varepsilon^{\Pi}_k = -\Pi\gamma_0\left(1 - 2\cos\left(\frac{ka}{2}\right)\right)$ for an armchair tube and $\varepsilon^{\pm}_k = \pm 2\gamma_0 \sin\left(\frac{\sqrt{3}ka}{4}\right)$ for a zigzag tube were used to find the polarizabilities for a Fermi level at $\varepsilon_{\mathrm{F}} = 0$ and $T = 0$. The result for the zigzag and armchair tubes are the same in the limit of small q and ω and found to be [118, eq.(13) and eq.(21)]:

$$\chi(q,\omega) = \frac{1}{2\pi}\frac{8\gamma_0(qa)^2}{a\pi\sqrt{3}\left(\frac{4}{3}(\hbar\omega)^2 - (\gamma_0 qa)^2\right)}, \quad (5.12)$$

remembering that $a = \sqrt{3}a_{\text{c-c}}$. In [118] the inter band excitations were neglected, so the polarizability is simply the sum of the two polarizabilities of the two bands,

[2]Note that $\kappa = \epsilon_r\epsilon_0$ is used instead of ϵ_0, i.e. the linear medium of e.g. a substrate is included in the bare interaction. We use $\epsilon_r = 1.4$ as in [120] (see also p.124).

i.e. $\chi = \chi^{\Pi=1} + \chi^{\Pi=-1}$. To do a better calculation of the screening including the inter band excitations we should solve a 2×2 problem for each subsystem equivalent to the Dyson equations (5.6) and (5.7), where the indices now are subband indices instead of subsystem indices. This should then be generalized to two subsystems as above. Note that the normalization factor $\frac{1}{2\pi}$ in eq.(5.12) was not present in [118], but included here to use the same normalization as done previously in the k and band index sums.

We can now find the (dynamically) screened Coulomb interaction from eq.(5.8) in the RPA. We use the static limit $\omega \to 0$, i.e.

$$\chi(q,0) = \frac{1}{2\pi}\frac{-8\gamma_0(qa)^2}{a\pi\sqrt{3}(\gamma_0 qa)^2} = -\frac{2}{\pi^2\hbar v_0} \equiv -\frac{\kappa}{e^2}\mathfrak{s}, \tag{5.13}$$

so the interaction used in all metallic nanotubes is explicitly:

$$V_{12}(r_1^c, r_2^c, q, \Delta\mathfrak{m}) = \frac{V_{12}^0(r_1^c, r_2^c, q, \Delta\mathfrak{m})}{\varepsilon^{\mathrm{RPA}}(q, \Delta\mathfrak{m}, 0)}, \qquad \text{where} \tag{5.14}$$

$$\begin{aligned}\varepsilon^{\mathrm{RPA}}(q, \Delta\mathfrak{m}, 0) = &\left[1 + \mathfrak{s}\mathrm{K}_{\Delta\mathfrak{m}}(qr_1^c)\mathrm{I}_{\Delta\mathfrak{m}}(qr_1^c)\right]\left[1 + \mathfrak{s}\mathrm{K}_{\Delta\mathfrak{m}}(qr_2^c)\mathrm{I}_{\Delta\mathfrak{m}}(qr_2^c)\right] \\ &- \mathfrak{s}^2\left[\mathrm{K}_{\Delta\mathfrak{m}}(qr_1^c)\mathrm{I}_{\Delta\mathfrak{m}}(qr_2^c)\right]^2.\end{aligned} \tag{5.15}$$

The limits of the screened interaction for $q \to 0$ for different $\Delta\mathfrak{m}$ are now considered and found to be finite for all q (as it should be). For $\Delta\mathfrak{m} = 0$ we have $V_{12}^0(r_1^c, r_2^c, q, 0) \to \infty$ for $q \to 0$, but the screened Coulomb interaction is finite for all q, since the small q limit is

$$\lim_{q\to 0^+} V_{12}(r_1^c, r_2^c, q, 0) = \frac{e^2}{\kappa}\frac{1}{\mathfrak{s}\left(2 + \mathfrak{s}\ln\left(\frac{r_1^c}{r_2^c}\right)\right)}, \tag{5.16}$$

found by using the small x expansions of $\mathrm{K}_0(x)$ and $\mathrm{I}_0(x)$ [123, p.138-139]. For $\Delta\mathfrak{m} \geq 1$ the bare interaction V_{12}^0 is not divergent:

$$\lim_{q\to 0} V_{12}^0(r_1^c, r_2^c, q, \Delta\mathfrak{m}) = \frac{e^2}{\kappa}\frac{1}{2\Delta\mathfrak{m}}\left(\frac{r_2^c}{r_1^c}\right)^{\Delta\mathfrak{m}} \quad \text{for} \quad \Delta\mathfrak{m} \geq 1, \tag{5.17}$$

hence neither the screened interaction. Note that the interaction decreases as a function of $\Delta\mathfrak{m}$.

5.3 Coulomb drag in multiwall armchair-like nanotubes

We now consider the problem of Coulomb drag between two armchair-like nanotubes. This problem falls into two parts: Firstly drag between two real armchair tubes, e.g. a (5,5) tube in a (10,10) tube, where we can use a parity selection rule, and secondly, drag between two armchair-like tubes without a parity selection rule.

5.3.1 Properties of single armchair-like nanotubes

The single subsystem properties entering the transresistivity are now found. The density of free electrons n for the armchair-like band structure eq.(5.1) (in the long tube limit) is (dropping the subsystem index i):

$$n = \frac{1}{2\pi r^c} \sum_{\sigma\nu} \int_{-\frac{\pi}{|\mathbf{T}|}}^{\frac{\pi}{|\mathbf{T}|}} \frac{\mathrm{d}k}{2\pi} f^0(\varepsilon_{k\nu}) = \frac{2\varepsilon_{\mathrm{F}} + \hbar v_0 \frac{\pi}{|\mathbf{T}|}}{\pi^2 r^c \hbar v_0}, \tag{5.18}$$

where the temperature independence of the density were used and the ν sum was simply a sum over $\Pi = \pm 1$. Furthermore, we use the chemical potential in the low temperature approximation $\mu \simeq \varepsilon_{\mathrm{F}}$, since this works well as we found for the simple models in chapter 4.

The transport mobility μ_{Tr} is the only single subsystem property entering the transresistivity, which we have not found yet. The current density for a single subsystem in the Boltzmann framework eq.(3.12) is found by dividing the FBZ into intervals, where the velocity is differentiable as in eq.(4.21):

$$J = -\frac{e^2 E\tau}{\hbar} \sum_{\sigma} \frac{1}{2\pi r^c} \sum_{\nu} \int_{-\frac{\pi}{|\mathbf{T}|}}^{\frac{\pi}{|\mathbf{T}|}} \frac{\mathrm{d}k}{2\pi} v_{k\nu} \frac{\partial f^0(\varepsilon_{k\nu})}{\partial k} = \frac{2e^2 E\tau v_0}{\hbar \pi^2 r^c}, \tag{5.19}$$

where the ν sum is over $\Pi = \pm 1$. Therefore the mobility is found by the definition eq.(3.13) to be:

$$\mu_{\mathrm{Tr}} = \frac{J}{(-e)nE} = \frac{2(-e)\tau v_0^2}{2\varepsilon_{\mathrm{F}} + \hbar v_0 \frac{\pi}{|\mathbf{T}|}} \tag{5.20}$$

for armchair-like tubes.

5.3.2 The F functions for armchair-like tubes

The $F^{(i)}_{\nu_i\nu_i'}(q,\omega)$ functions eq.(3.44):

$$F^{(i)}_{\nu_i\nu_i'}(q,\omega) = \\ -\frac{\tilde{e}_i\tau_i}{\hbar^2\mu^{(i)}_{\mathrm{Tr}}} \sum_{k_s} \mathrm{sign}(v_{k_s\nu_i} - v_{k_s+q\nu_i'})[f^0(\varepsilon_{k_s\nu_i}) - f^0(\varepsilon_{k_s+q\nu_i'})] \; |g_i(k_s\nu_i, k_s+q\nu_i')|^2 \tag{5.21}$$

are now found for the two armchair-like bands $\Pi = \pm 1$ in eq.(5.1) and we therefore have to find the four F functions: F_{++}, F_{--}, F_{+-} and F_{-+}. Note that in contrast to the two simple models (chapter 4), we have periodic bands and therefore have either two or none solutions of $\varepsilon^{\Pi}_{k_s} = \varepsilon^{\Pi'}_{k_s+q} + \hbar\omega$ in the FBZ for all combinations of Π' and Π. The prefactor is the same for all four F functions:

$$C^{(i)}_F \equiv \frac{\tilde{e}_i\tau_i}{\hbar^2\mu^{(i)}_{\mathrm{Tr}}} = \frac{2\varepsilon_{\mathrm{F}} + \hbar v_0 \frac{\pi}{|\mathbf{T}_i|}}{2(\hbar v_0)^2}, \tag{5.22}$$

GRAPHICAL SOLUTION OF $\varepsilon_k^{\Pi=-1} = \varepsilon_{k+q}^{\Pi=-1} + \hbar\omega$

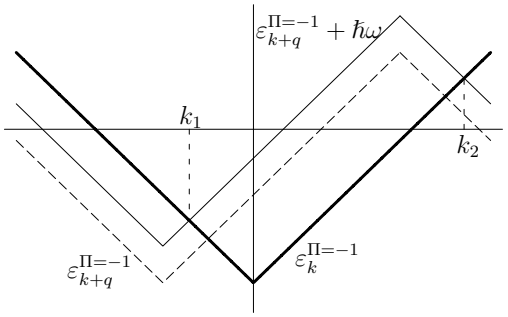

Figure 5.1: Illustration of a possible way to solve the equation $\varepsilon_k^{\Pi} = \varepsilon_{k+q}^{\Pi'} + \hbar\omega$ for the case of $\Pi = \Pi' = -1$. The energies $\varepsilon_k^{\Pi=-1}$ (thick line), $\varepsilon_{k+q}^{\Pi=-1}$ (dashed line) and $\varepsilon_{k+q}^{\Pi=-1} + \hbar\omega$ (normal line) are showed. Two solutions k_1 and k_2 are seen to exist for $\hbar v_0 q > \hbar\omega$, which gives the step function $\theta(v_0 q - \omega)$ in the F_{--} function.

where we used electrons $\tilde{e}_i = -e$ and the mobility eq.(5.20).

Let us begin by calculating the $F_{--}(q,\omega)$ function in detail. We need to find the solutions $k \in \text{FBZ}$ of $\varepsilon_k^{\Pi=-1} = \varepsilon_{k+q}^{\Pi=-1} + \hbar\omega$ for $0 < q < \frac{\pi}{|\mathbf{T}_i|}$ remembering that the $F^{(i)}$ function is periodic in q by $\frac{2\pi}{|\mathbf{T}_i|}$ and odd in q eq.(3.38). The solution can be found in the same way as in section 4.3.2, i.e. by dividing the piecewise linear dispersion relation into linear pieces. Here we simply solve the equation $\varepsilon_k^{\Pi=-1} = \varepsilon_{k+q}^{\Pi=-1} + \hbar\omega$ graphically as seen on figure 5.1, which is an equivalent approach. For $\Pi' = \Pi = -1$ the solutions k_1 and k_2 are found to be:

$$-\hbar v_0(k_1 + k_0) = \hbar v_0(k_1 + q - k_0) + \hbar\omega \;\Leftrightarrow\; k_1 = -\frac{1}{2}\left(q + \frac{\omega}{v_0}\right), \quad (5.23)$$

$$\hbar v_0(k_2 - k_0) = -\hbar v_0\Big(k_2 + q - \frac{2\pi}{|\mathbf{T}_i|} + k_0\Big) + \hbar\omega \;\Leftrightarrow\; k_2 = \frac{1}{2}\left(\frac{2\pi}{|\mathbf{T}_i|} - q + \frac{\omega}{v_0}\right).$$

These solutions only exist if $\varepsilon_{k+q}^{\Pi=-1} + \hbar\omega$ is not above $\varepsilon_k^{\Pi=-1}$ for all k, which means that $\hbar v_0 q > \hbar\omega$ and the step function $\theta(v_0 q - \omega)$ should be included in the F_{--} function. This step function also appears from the sign-function of the velocity difference, when one solves the equation $\varepsilon_k^{\Pi=-1} = \varepsilon_{k+q}^{\Pi=-1} + \hbar\omega$ in piecewise linear intervals. When the two solutions exist the sign difference is:

$$\text{sign}(v_{k_1\Pi=-1} - v_{k_1+q\Pi=-1}) = \text{sign}(-v_0 - v_0) = -1, \quad (5.24)$$

$$\text{sign}(v_{k_2\Pi=-1} - v_{k_2+q\Pi=-1}) = \text{sign}(+v_0 + v_0) = +1. \quad (5.25)$$

Furthermore, the energies of the solutions k_1 and k_2 are:

$$\varepsilon_{k_1}^{\Pi=-1} = -\hbar v_0(k_1 + k_0) = \frac{\hbar}{2}(\omega + v_0 q) - \hbar v_0 k_0 \equiv \varepsilon_1, \quad (5.26)$$

$$\varepsilon_{k_2}^{\Pi=-1} = \hbar v_0(k_2 - k_0) = \frac{\hbar}{2}(\omega - v_0 q + v_0 k_0) \equiv \varepsilon_2, \quad (5.27)$$

$$\varepsilon_{k_1+q}^{\Pi=-1} = \hbar v_0(k_1 + q - k_0) = \frac{\hbar}{2}(v_0 q - \omega) - \hbar v_0 k_0 = -\varepsilon_2 - \frac{1}{2}\hbar v_0 k_0, \quad (5.28)$$

$$\varepsilon_{k_2+q}^{\Pi=-1} = -\hbar v_0(k_2 + q - \frac{2\pi}{|\mathbf{T}_i|} + k_0) = -\frac{\hbar}{2}(v_0 q + \omega) + \frac{1}{2}\hbar v_0 k_0 = -\varepsilon_1 - \frac{1}{2}\hbar v_0 k_0,$$

which are used in the Fermi functions.

Now we only need the g_i factor to know F_{--}. For a (real) armchair nanotube we can insert eq.(2.38) (with $n_c = n$) and eq.(2.44) into eq.(2.66) to obtain the non-linearized g_i factor:

$$g_i(k,\Pi,k',\Pi') = \frac{1}{2}(\Pi'\Pi+1) + \frac{s_0}{2}\left[\Pi'\Big(1-2\cos\Big(\frac{ka}{2}\Big)\Big) + \Pi\Big(1-2\cos\Big(\frac{k'a}{2}\Big)\Big)\right], \quad (5.29)$$

so

$$g_i(k,\Pi,k+q,\Pi) = 1 + s_0\Pi\left[1-\cos\left(\frac{ka}{2}\right)-\cos\left(\frac{(k+q)a}{2}\right)\right]. \quad (5.30)$$

Since $s_0 \sim 10^{-1}$ the k and q dependence do not change the value away from 1 by more then ~ 0.2. The form eq.(5.30) is of course only true for real armchair tubes, but as we derived in section 2.3.1 (from p. 39) the g factor for backscattering between different crosses (fig.2.8(right)) is $\frac{3}{4} < g \leq 1$ eq.(2.75) for all armchair-like tubes and therefore we use $g \simeq 1$ in F_{--} to model all the armchair-like tubes.

Inserting into eq.(5.21) the F_{--} function is:

$$F^{(i)}_{--}(q,\omega) = -C^{(i)}_F\theta(-\omega+v_0q) \quad (5.31)$$
$$\times\left[-\left(f^0(\varepsilon_1)-f^0\Big(-\varepsilon_2-\frac{1}{2}k_0\hbar v_0\Big)\right)+\left(f^0(\varepsilon_2)-f^0\Big(-\varepsilon_1-\frac{1}{2}k_0\hbar v_0\Big)\right)\right],$$

where ε_1 and ε_2 are found in eq.(5.26) and eq.(5.27), respectively.

In the same way we find F_{++} to be:

$$F^{(i)}_{++}(q,\omega) = -C^{(i)}_F\theta(-\omega+v_0q) \quad (5.32)$$
$$\times\left[-\left(f^0(\tilde{\varepsilon}_1)-f^0\Big(-\tilde{\varepsilon}_2+\frac{1}{2}\hbar v_0k_0\Big)\right)+\left(f^0(\tilde{\varepsilon}_2)-f^0\Big(-\tilde{\varepsilon}_1+\frac{1}{2}\hbar v_0k_0\Big)\right)\right],$$

where $\tilde{\varepsilon}_1 = \frac{\hbar}{2}(\omega+v_0q) - \frac{1}{2}\hbar v_0k_0$ and $\tilde{\varepsilon}_2 = \frac{\hbar}{2}(\omega-v_0q) + \hbar v_0k_0$. Again we have used $g \simeq 1$ for the same reason as above. Therefore the two F functions F_{++} and F_{--} for *intra band scattering* $\Pi \to \Pi$ are now known and can be seen on figure 5.2. The F functions gives the available phase space for scattering and the $\sinh\left(\frac{\hbar\omega}{2k_BT}\right)^{-2}$ and Fourier transformed interaction in ρ_{21} are decreasing as a function of q and ω, respectively, suppressing the phase space away from the origin. Therefore figure 5.2 shows that the most important intra band scattering processes at low temperatures[3] are:

[3]Remembering that the lower the temperature T the more the factor $\sinh\left(\frac{\hbar\omega}{2k_BT}\right)^{-2}$ suppresses the phase space for larger ω.

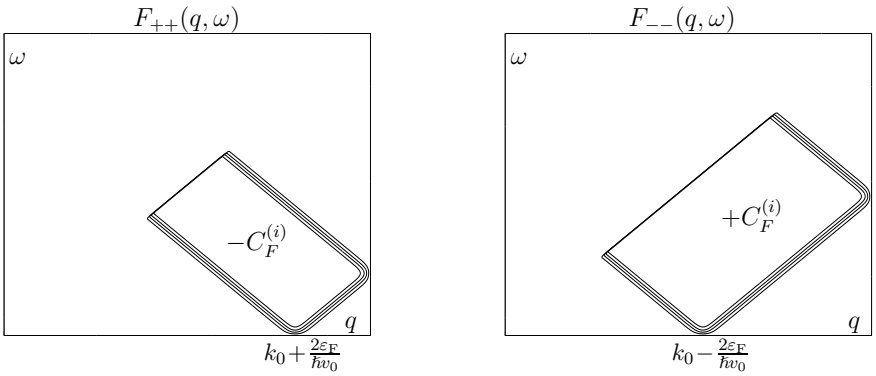

Figure 5.2: The F functions for the intra band scattering for $q \in [0, \frac{\pi}{|\mathbf{T}|}]$ and $\varepsilon_F > 0$. The values of $F_{\Pi\Pi}$ are found to be $\pm C_F^{(i)}$, respectively. To get $F_{\Pi\Pi}$ for all q we can use that F is odd in q to get $q \in$FBZ and thereafter repeat the FBZ periodically as a function of q. Note the smearing by the Fermi functions due to the temperature on some edges and the sharp edge at $\omega = v_0 q$ from the step function $\theta(-\omega + v_0 q)$. The temperature $T = 0.1 T_F$ were used.

- For $\Pi = +1$: $q = k_0 + \frac{2\varepsilon_F}{\hbar v_0}$, i.e. the Umklapp process $k' \to k$ for $k' = -k_0 + \frac{\varepsilon_F}{\hbar v_0}$ and $k = k_0 - \frac{\varepsilon_F}{\hbar v_0}$ in the FBZ, so $q = k' - k + \frac{2\pi}{|\mathbf{T}|} = k_0 + \frac{2\varepsilon_F}{\hbar v_0}$ (or equivalently $k' = k_0 - \frac{\varepsilon_F}{\hbar v_0}$ and $k = -k_0 + \frac{\varepsilon_F}{\hbar v_0}$ so $q = k' - k - \frac{2\pi}{|\mathbf{T}|} = -\big(k_0 + \frac{2\varepsilon_F}{\hbar v_0}\big)$).
- For $\Pi = -1$: $q = k_0 - \frac{2\varepsilon_F}{\hbar v_0}$, i.e. the Umklapp process $k' \to k$ for $k' = -k_0 - \frac{\varepsilon_F}{\hbar v_0}$ and $k = k_0 + \frac{\varepsilon_F}{\hbar v_0}$ so $q = k' - k + \frac{2\pi}{|\mathbf{T}|} = k_0 - \frac{2\varepsilon_F}{\hbar v_0}$ (or equivalently $k' = k_0 + \frac{\varepsilon_F}{\hbar v_0}$ and $k = -k_0 - \frac{\varepsilon_F}{\hbar v_0}$ so $q = k' - k - \frac{2\pi}{|\mathbf{T}|} = -\big(k_0 - \frac{2\varepsilon_F}{\hbar v_0}\big)$).

These scattering processes are seen on figure 5.4.

The F functions F_{-+} and F_{+-} for *inter band scattering* $\Pi \to -\Pi$ are now considered. The g_i factor for armchair tubes eq.(5.29) for $\Pi = -\Pi$ is:

$$\begin{aligned} g_i(k, \Pi, k+q, -\Pi) &= s_0 \Pi \left[\cos\left(\frac{ka}{2}\right) - \cos\left(\frac{(k+q)a}{2}\right) \right] \\ &\simeq s_0 \Pi \sin\left(\frac{ka}{2}\right) aq, \end{aligned} \tag{5.33}$$

where we expanded to first order in q around zero. This is a good approximation, since the inter band backscattering around the Fermi level has a small q. Using $k = \pm\frac{2\pi}{3a}$ in eq.(5.33) we exactly get the result from eq.(2.70) as we should. Again we will like to model all armchair-like tubes and we therefore use the g factor from eq.(2.71)

$$|g_i(k, \Pi, k+q, -\Pi)|^2 = s_0^2 \frac{3(qa)^2}{16} \tag{5.34}$$

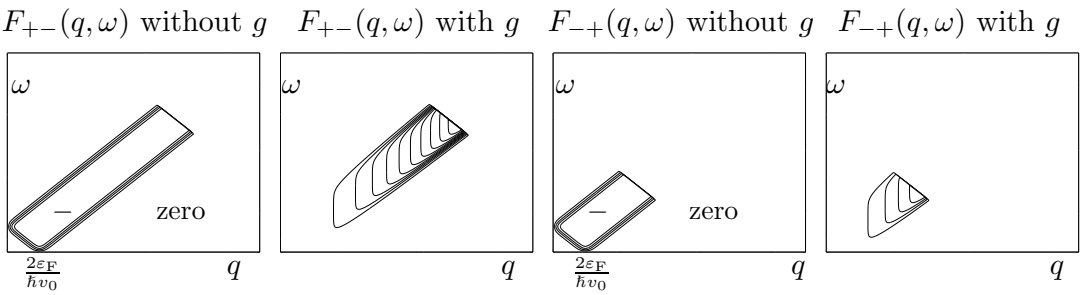

Figure 5.3: Contour plots of the F functions for inter band scattering with and without the g factors for $q \in [0, \frac{\pi}{|\mathbf{T}|}]$ and $\varepsilon_F > 0$. For low temperatures and $g = 1$ the processes with $q = \frac{2\varepsilon_F}{\hbar v_0}$ (i.e. $k' \to k$ for $k' = \pm\big(k_0 + \frac{\varepsilon_F}{\hbar v_0}\big)$ and $k = \pm\big(k_0 - \frac{\varepsilon_F}{\hbar v_0}\big)$ or $k' = \pm\big(-k_0 + \frac{\varepsilon_F}{\hbar v_0}\big)$ and $k = \pm\big(-k_0 - \frac{\varepsilon_F}{\hbar v_0}\big)$) are seen to be important, *but* due to $|g|^2 \propto s_0^2(aq^2) \sim 10^{-4}$ this is strongly suppressed as seen on the contour plots including the g factors. The signs indicate the signs of the F functions.

in the inter band F functions, since this exactly describes the small q inter band backscattering without crystal angular momentum transfer. Note that by linearization of the band structure only backscattering is considered and therefore the g factors for backscattering is used in both the inter and intra band F functions.

The equation $\varepsilon_k^{\Pi} = \varepsilon_{k+q}^{-\Pi} + \hbar\omega$ for $0 < q < \frac{\pi}{|\mathbf{T}_i|}$ can again be solve graphically or by dividing the dispersion relations into piecewise linear intervals as above. This leads to

$$F_{+-}^{(i)}(q,\omega) = -C_F^{(i)} s_0^2 \frac{3(qa)^2}{16} \theta(\omega - v_0 q + v_0 k_0)\theta(-\omega - v_0 q + 2v_0 k_0) \times \Big[-\big(f^0(\varepsilon_1') - f^0(-\varepsilon_2')\big) + \big(f^0(\varepsilon_2') - f^0(-\varepsilon_1')\big)\Big] \quad (5.35)$$

and

$$F_{-+}^{(i)}(q,\omega) = -C_F^{(i)} s_0^2 \frac{3(qa)^2}{16} \theta(-\omega - v_0 q + v_0 k_0) \times \Big[-\big(f^0(\varepsilon_1') - f^0(-\varepsilon_2')\big) + \big(f^0(\varepsilon_2') - f^0(-\varepsilon_1')\big)\Big] \quad (5.36)$$

where $\varepsilon_1' = \frac{\hbar}{2}(\omega + v_0 q)$ and $\varepsilon_2' = \frac{\hbar}{2}(\omega - v_0 q)$. Here the two inter band F functions have the same Fermi functions but are cut off by different lines (i.e. different step functions) in the (q,ω) plane. Figure 5.3 shows the inter band F functions with and without the g factors, i.e. for the phase space for inter band scattering (see figure 5.4(left)).

The factors $s_0^2 \sim 10^{-2}$ and $(aq)^2$ in F_{+-} and F_{-+} suppress the inter band processes substantially compared to using plane wave states in the Coulomb matrix

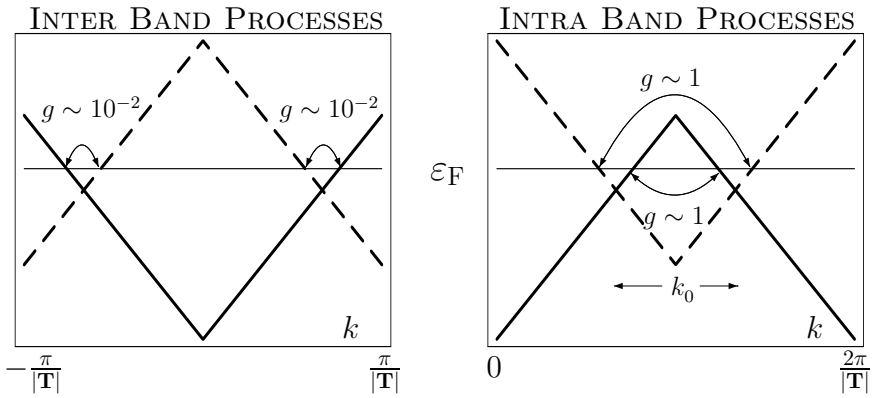

Figure 5.4: The main backscattering processes contributing to the drag and the suppression of the small momentum $q = \frac{2\varepsilon_{\mathrm{F}}}{\hbar v_0}$ inter band scattering due to the g factor. Note that the intra band processes (on the right) are seen in the interval from zero to $\frac{2\pi}{|\mathbf{T}|}$, since we have Umklapp processes. Note that an extremely high Fermi level $\varepsilon_{\mathrm{F}} = 1\mathrm{eV}$ is used in this figure for illustrative reasons.

element ($g = 1$), which were our first approach to the problem, see appendix G. The reason for the large difference between using plane wave states and the Bloch states in the matrix element is the fact of the two atomic unit cell, which gives a two component tight binding state leading to a g factor of the "dot-product" form

$$(\alpha'^*, \beta'^*) \cdot \begin{pmatrix} \alpha \\ \beta \end{pmatrix} \tag{5.37}$$

to zeroth order in s_0. A priori α and β depend on k, but to linear order they are independent of k. This is a good approximation, since $\gamma_0 \gg \varepsilon_{\mathrm{F}}$. If we had only one atom in the unit cell, this would not have been the case, but on the other hand we would not have obtained two bands near ε_{F}, which could lead to the believe of a small q inter band backscattering.

Thus, by analyzing the F functions including the g factors it seem like the most important processes in the Coulomb drag are the intra band backscattering processes as seen on figure 5.4.

5.3.3 Particle-hole symmetry

Particle-hole symmetry means that there are as many electrons as holes in the conductor. Or to be more precise: For each occupied k state (at $T = 0$) with energy ε_k and velocity v_k there exists one and only one empty state k' with the same velocity $v_{k'} = v_k$ and the opposite energy with respect to the Fermi level: $\varepsilon_{\mathrm{F}} - \varepsilon_{k'} = -(\varepsilon_{\mathrm{F}} - \varepsilon_k)$. So in this way there is a one to one correspondence between the particles (i.e. the filled states) and holes (i.e. the empty states). An example of particle-hole symmetry is a half filled cosine band. The graphene

band structure has particle-hole symmetry for $\varepsilon_{\mathrm{F}} = 0$, since it is symmetric around $\varepsilon_{\mathrm{F}} = 0$. The symmetry is pasted on in the wrapping procedure to the nanotube band structure and preserved in the linear approximation of the bands.

Let us now consider the Coulomb drag between two subsystems, where one of the subsystems, say subsystem 1, has particle-hole symmetry. One can chose to use either holes $\tilde{e}_1 = +e$ or electrons $\tilde{e}_1 = -e$ in the calculation of ρ_{21} eq.(3.39) and the same result would be obtained except for the prefactor $\tilde{e}_1$, which has different signs. Therefore the Coulomb drag (i.e. ρ_{21}) is zero, if one (or both) of the systems have particle-hole symmetry. Explicitly the F functions disappear at $\varepsilon_{\mathrm{F}} = 0$, which can be seen by using $f^0_{-\mu}(\varepsilon) = 1 - f^0_{\mu}(-\varepsilon)$ after doing the sum over the band indices. This has been used to show that one can have a sign change in ρ_{21} (for the cosine band), if one of the subsystems goes from an electron-like to a hole-like subsystem though the particle-hole symmetry [113].

The absence of Coulomb drag for a particle-hole symmetric system can also be understood intuitive in the following way: The drag effect is based on the momentum transfer from one system to the other. If there are as many electrons as holes in the drag system, the drive system will transfer an equal amount of momentum to the electrons and holes in the drag system. Since the electrons and holes have opposite electric charges no voltage will arise.

5.3.4 Selection rules for armchair-like tubes

Bands near the Fermi level have the same crystal angular momentum for the armchair-like tubes and therefore we have no selection rule from crystal angular momentum conservation, so we shall use $\Delta\mathfrak{m} = 0$ in the Fourier transformed interaction. Furthermore, we can safely neglect the Umklapp process in the crystal angular momentum conservation law (if the tubes are commensurable), since the Fourier transform suppresses them.

The parity selection rule for (real) armchair nanotubes

There is however a parity selection rule for (real) armchair nanotubes, which we will now derive. It stems from the specific symmetry of the lattice for a (n, n) tube as described on page 30 (see figure 2.5), where the eigenstates $\psi^{\Pi}_k(\theta, r, z)$ for the bands crossing ε_{F} were found to be parity eigenstates in the angular coordinate (eq.(2.46)): $\mathcal{P}_\theta\Big(\psi^{\Pi}_k(\theta, r, z)\Big) \equiv \psi^{\Pi}_k(-\theta, r, z) = \Pi\psi^{\Pi}_k(\theta, r, z)$.

We now consider the matrix element $\langle k'_1 k'_2 \Pi'_1 \Pi'_2 | V_{12}(|\mathbf{r_1} - \mathbf{r_2}|) | k_1 k_2 \Pi_1 \Pi_2 \rangle$, where the only assumption needed to have a parity selection rule is that the electron-electron interaction $V_{12}(|\mathbf{r_1} - \mathbf{r_2}|)$ only depends on the distance $|\mathbf{r_1} - \mathbf{r_2}|$ between the electrons. This distance in cylinder coordinates (θ_i, r_i, z_i) $(i = 1, 2)$

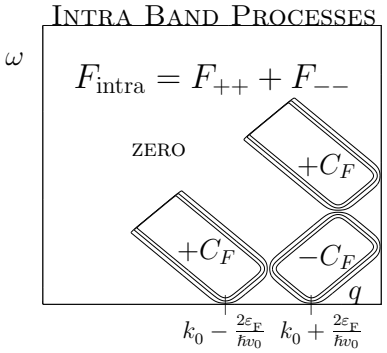

Figure 5.5: The F_{intra} function giving the phase space for intra band scattering in (real) armchair tubes. By comparing with figure 5.2 we note that there is an area of phase space, where $F_{+-}+F_{-+}$ cancels out. (Remember that F_{intra} is odd in q and should be repeated periodically as a function of q.)

is:

$$|\mathbf{r_1} - \mathbf{r_2}| = \sqrt{\big(r_1\cos(\theta_1) - r_2\cos(\theta_2)\big)^2 + \big(r_1\sin(\theta_1) - r_2\sin(\theta_2)\big)^2 + (z_1 - z_2)^2}$$
$$= \sqrt{(r_1 - r_2)^2 + 4r_1r_2\sin^2\left(\frac{\theta_1 - \theta_2}{2}\right) + (z_1 - z_2)^2}, \tag{5.38}$$

which is seen to be even in $\theta_1 - \theta_2$ and in $z_1 - z_2$. So $V_{12}(|\mathbf{r_1} - \mathbf{r_2}|)$ is even in $\theta_1 - \theta_2$ and $z_1 - z_2$. The matrix element is explicitly:

$$\langle k_1' k_2' \Pi_1' \Pi_2' | V_{12}(|\mathbf{r_1} - \mathbf{r_2}|) | k_1 k_2 \Pi_1 \Pi_2 \rangle =$$
$$\int_0^\infty \mathrm{d}r_1 r_1 \int_0^\infty \mathrm{d}r_2 r_2 \int_{-\infty}^\infty \mathrm{d}z_1 \int_{-\infty}^\infty \mathrm{d}z_2 \int_{-\pi}^\pi \mathrm{d}\theta_1 \int_{-\pi}^\pi \mathrm{d}\theta_2 \; \psi_{k_1'}^{\Pi_1'*}(\theta_1, r_1, z_1)\psi_{k_2'}^{\Pi_2'*}(\theta_2, r_2, z_2)$$
$$\times V_{12}(|\mathbf{r_1} - \mathbf{r_2}|) \; \psi_{k_1}^{\Pi_1}(\theta_1, r_1, z_1)\psi_{k_2}^{\Pi_2}(\theta_2, r_2, z_2). \tag{5.39}$$

By changing the integration variables from θ_1, θ_2 to $-\theta_1, -\theta_2$ and using that the Bloch states are parity eigenstates and that $V_{12}(|\mathbf{r_1} - \mathbf{r_2}|)$ is even in this variable change by eq.(5.38) it is seen that $\Pi_1\Pi_2\Pi_1'\Pi_2' = 1$ for the matrix element not to be zero. Equivalently $\Pi_1\Pi_2 = \Pi_1'\Pi_2'$ since $\Pi = \pm 1$, so *the product of the parity has to be conserved in the scattering process.* This is the parity selection rule.

An equivalent derivation is to inserted $\big(\mathcal{P}_{\theta_1}\mathcal{P}_{\theta_2}\big)^{-1}\big(\mathcal{P}_{\theta_1}\mathcal{P}_{\theta_2}\big) = 1$ in the matrix element:

$$\langle k_1' k_2' \Pi_1' \Pi_2' | V_{12}(|\mathbf{r_1} - \mathbf{r_2}|) | k_1 k_2 \Pi_1 \Pi_2 \rangle =$$
$$\langle k_1' k_2' \Pi_1' \Pi_2' | \big(\mathcal{P}_{\theta_1}\mathcal{P}_{\theta_2}\big)^{-1}\big(\mathcal{P}_{\theta_1}\mathcal{P}_{\theta_2}\big) V_{12}(|\mathbf{r_1} - \mathbf{r_2}|) \big(\mathcal{P}_{\theta_1}\mathcal{P}_{\theta_2}\big)^{-1}\big(\mathcal{P}_{\theta_1}\mathcal{P}_{\theta_2}\big) | k_1 k_2 \Pi_1 \Pi_2 \rangle$$
$$= \Pi_1\Pi_2\Pi_1'\Pi_2' \langle k_1' k_2' \Pi_1' \Pi_2' | V_{12}(|\mathbf{r_1} - \mathbf{r_2}|) | k_1 k_2 \Pi_1 \Pi_2 \rangle, \tag{5.40}$$

i.e.

$$\langle k_1' k_2' \Pi_1' \Pi_2' | V_{12}(|\mathbf{r_1} - \mathbf{r_2}|) | k_1 k_2 \Pi_1 \Pi_2 \rangle \propto \delta_{\Pi_1\Pi_2, \Pi_1'\Pi_2'}. \tag{5.41}$$

This selection rule for drag between (real) armchair nanotubes reduces the num-

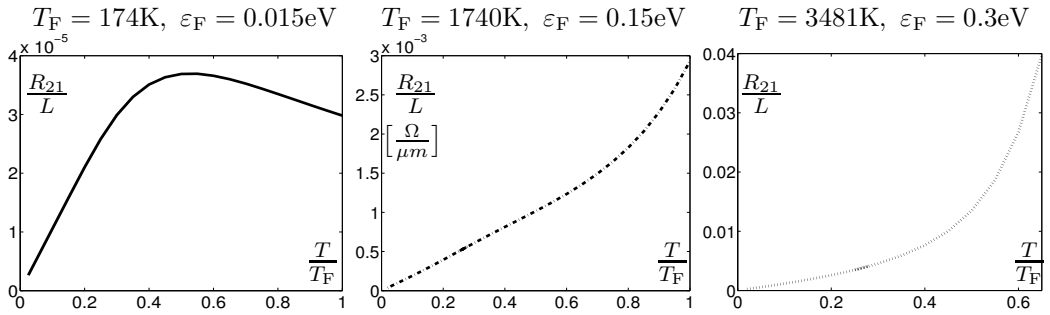

Figure 5.6: The transresistance per length $\frac{R_{21}}{L}$ (in units of Ω/μm) from a numerical integration of eq.(5.43) for a $(5,5)$ in a $(10,10)$ tube as a function of the temperature T in units of the Fermi Temperature T_F. Curves for three different Fermi levels ε_F are seen: $\varepsilon_F = 0.015$eV (Left, full line), $\varepsilon_F = 0.15$eV (Middle, dashed-dotted line) and $\varepsilon_F = 0.3$eV (Right, dotted line). Note the difference in magnitude between the transresistances R_{21} and the very large (real) temperatures for the middle and right curves (since T_F is large).

ber of non-zero matrix elements by half[4]. Note that for armchair nanotubes laying parallel to each other (i.e. not coaxial) the parity selection rule is not found, since the distance is no longer even in $\theta_1 - \theta_2$.

Let us now carry out the sum over the band indices in the transresistivity eq.(3.39) for the parity selection rule. For all (real) armchair nanotubes we have $|\mathbf{T}| = a$ so $F^{(i)}_{\Pi_i\Pi'_i}(q,\omega) = F_{\Pi_i\Pi'_i}(q,\omega)$, i.e. the F functions are independent of the subsystem i. Since the Fourier transforms are parity independent, we have (suppressing the q,ω dependence in the notation):

$$\sum_{\Pi_1\Pi_2\Pi'_1\Pi'_2} F_{\Pi_1\Pi'_1}F_{\Pi_2\Pi'_2}\delta_{\Pi_1\Pi_2,\Pi'_1\Pi'_2} = \\ \left(F_{++}+F_{--}\right)^2 + \left(F_{+-}+F_{+-}\right)^2 = (F_{\text{intra}})^2 + (F_{\text{inter}})^2 \quad (5.42)$$

introducing the inter and intra band scattering F functions. The $(F_{\text{inter}}(q,\omega))^2$ function contains the strongly suppressing factors $s_0^4 \sim 10^{-4}$ and q^4, which makes $F_{\text{intra}}(q,\omega)$ the most important term in the transresistivity. $F_{\text{intra}}(q,\omega)$ is plotted in figure 5.5.

5.3.5 Transresistivity for armchair tubes: numerical results

We now consider the Coulomb drag between a $(5,5)$ armchair tube and a $(10,10)$ armchair tube (seen in figure 1.2(a)) and find the transresistivity ρ_{21} by numerical integration. Two armchair tubes are commensurable and therefore the sum over

[4]In our original approach to drag in multiwall armchair nanotubes (appendix G) this was the *only* symmetry property from the Bloch states we use in the calculation of the matrix element, which did not suppress the small q inter band backscattering.

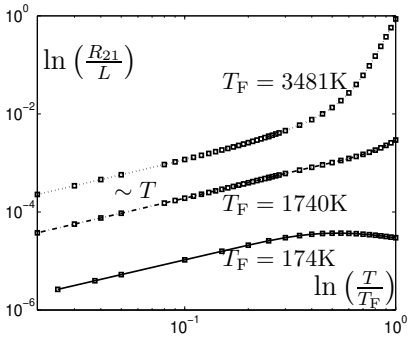

Figure 5.7: A logarithmic plot of the transresistances (per length) for three different Fermi levels ε_F. From a fit for small temperatures with a function of the form $R_{21} \propto T^n$ we find $n = 1$ independent of ε_F, i.e. the transresistance is linear with temperature for low temperatures. Each square is the result of a numerical integration.

G_1 can give some contribution to ρ_{21} in eq.(3.39), but they are suppressed by the Fourier transform $V_{12}^*(q+G_1)$ and therefore neglected in the numerical integration. Note however that this does not mean, that we neglect Umklapp scattering, since in the derivation of ρ_{21} we have included a sum over G_1 into the q-integral (see p.61) and introduced $q = k_1' - k_1 + G_1$ (see p.57). Using the F-functions from eq.(5.42) and the interaction eq.(5.14) ρ_{21} simplifies to:

$$\rho_{21} = \frac{\hbar^2}{\pi e^2 n_1 n_2 k_B T} \frac{1}{2\pi r_2^c} \times \int_0^\infty \frac{dq}{2\pi} \int_0^\infty d\omega \frac{|V_{12}(r_1^c, r_2^c, q, \Delta\mathfrak{m} = 0)|^2}{\sinh^2\left(\frac{\hbar\omega}{2k_B T}\right)} \left((F_{\text{intra}}(q,\omega))^2 + (F_{\text{inter}}(q,\omega))^2 \right), \tag{5.43}$$

where we now have calculated all the ingredients. We proceed the calculation of these integrals by numerical integration as in chapter 4 remembering to repeat the F function periodically as a function of q. The details of the numerical integration technique are found in appendix D[5].

In all of the figures, we give the transresistance per length $\frac{R_{21}}{L}$ (i.e. the 1D transresistivity) eq.(3.40), since this is the natural quantity to measure. The magnitude of the transresistance per length is seen to be of order $\text{m}\Omega/\mu\text{m}$, which is suppressed by about a factor of 10^6 compared to our previous result with $g = 1$ for the inter band backscattering processes (see appendix G).

In a Coulomb drag experiment the Fermi level ε_F is controlled by a gate voltage V_g, which is approximately proportional to ε_F. For a multiwall tube the gate is likely to have a larger effect on the Fermi level on the outer tubes than on the inner ones (i.e. position dependent). Therefore, in general we have a Fermi level for each tube, but in the calculations we will use the same Fermi level in both tubes and therefore neglect this small effect.

[5]We introduce the new dimensionless variables $x = \frac{\hbar v_0 q}{\varepsilon_F}$ and $y = \frac{\hbar\omega}{\varepsilon_F}$ and the prefactors from V_{12}, the F functions, the ρ_{21} formula it self and the variable change is: $\rho_0 = \frac{\pi r_1^c e^2 \varepsilon_F}{16\kappa^2\hbar^2 v_0^3} \frac{T_F}{T}$, which has the dimension of Ohm as it should in quasi 1D.

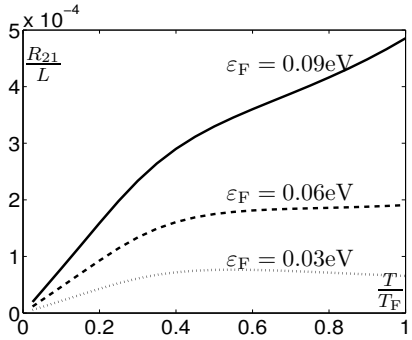

Figure 5.8: $\frac{R_{21}}{L}$ as a function of $\frac{T}{T_{\rm F}}$ for three different values of the Fermi energy. We see the crossover for higher $T/T_{\rm F}$ from the transresistance going down for $\varepsilon_{\rm F} = 0.03$eV to being (approximately) constant at $\varepsilon_{\rm F} = 0.06$eV and finally going up for $\varepsilon_{\rm F} = 0.09$eV.

The transresistance as a function of temperature

In figure 5.6 and 5.8 we calculated the transresistance as a function of temperature in units of $T_{\rm F}$ for different values of the Fermi level. We find a linear dependence, $R_{21} \propto T$, for $T \lesssim 0.4T_{\rm F}$ for all the Fermi levels considered, which is also found in the logarithmic plot on figure 5.7. Note that R_{21} goes to zero for $T \to 0$, as predicted in section 3.3.1 (p.54). Furthermore, we can numerically evaluate the two sperate terms $\rho_{21}^{(\rm inter)}$ (from the $F_{\rm inter}$ function) and $\rho_{21}^{(\rm intra)}$ in eq.(5.43) and we find that the shape of the curves and the magnitude is entirely due to the intra band F function, i.e. due to the intra band processes with a wave vector transfer of order $q \sim k_0$. This is exactly as we expected from the very small g factors eq.(5.34) for inter band backscattering.

We now try to understand the linear dependence $R_{21} \propto T$ along the same lines as for the completely screened potential (p.78). We should only consider the intra band backscattering processes, so for very low temperatures only the processes around $q = k_0 \pm \frac{2\varepsilon_{\rm F}}{\hbar v_0}$ are present (see figure 5.5). Therefore the Fourier transform can approximately be consider as a constant around each of these points, which can be taken outside the integrals. Since $F_{\rm intra}$ has four terms each of the form used in the numerator in eq.(4.39), we can use the rewriting (without the square) of $\frac{F_{\rm intra}}{\sinh(\frac{\hbar\omega}{2k_{\rm B}T})}$ in eq.(4.39). The explicit from of $F_{\rm intra}$ shows the four terms:

$$\begin{aligned} F_{\rm intra}(q,\omega) = F_{--}(q,\omega) + F_{++}(q,\omega) = -C_F^{(i)}\theta(-\omega + v_0 q) \qquad (5.44) \\ \times \Big[-f^0(\varepsilon_1) + f^0\Big(-\varepsilon_2 - \frac{1}{2}k_0\hbar v_0\Big) + f^0(\varepsilon_2) - f^0\Big(-\varepsilon_1 - \frac{1}{2}k_0\hbar v_0\Big) \\ - f^0\Big(\varepsilon_1 + \frac{1}{2}k_0\hbar v_0\Big) + f^0(-\varepsilon_2) + f^0\Big(\varepsilon_2 + \frac{1}{2}k_0\hbar v_0\Big) - f^0(-\varepsilon_1)\Big], \end{aligned}$$

where ε_1 and ε_2 are defined in eq.(5.26) and eq.(5.27), respectively. So by using the same arguments as for the case of a constant potential (p.78) we can conclude, that $R_{21} \propto T$ for $T \ll T_{\rm F}$ in the case of drag between two armchair nanotubes. This is the same conclusion as found in [40] for a single quadratic band in 1D

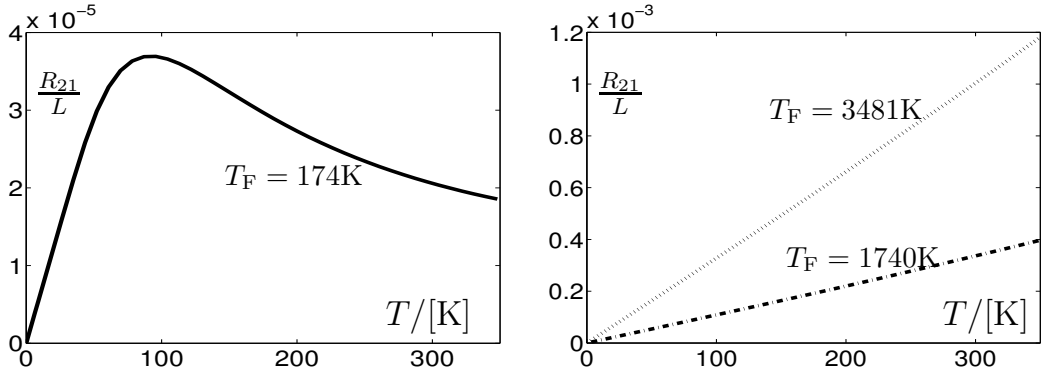

Figure 5.9: The transresistance per length (Ω/μm) as a function of the temperature T from zero to 350K for different $\varepsilon_{\rm F}$. We see that the slope around room temperature can change from positive to negative as a function of the Fermi level $\varepsilon_{\rm F}$, i.e. a gate voltage.

and in the two simple models in chapter 4 for the completely screened potential. So by measuring the transresistance of a double wall armchair nanotube as a function of temperature (for low temperatures) we can not see any difference in the power law $R_{21} \propto T$ between the simple free particle dispersion relation and the tight binding band structure (with linearized bands). The reason is, that in both models the drag stems from a large momentum transfer backscattering process: $q = 2k_{\rm F}$ for the quadratic (screened) model (or the $\varepsilon \propto |k|$ model) and $q = k_0 \pm \frac{2\varepsilon_{\rm F}}{\hbar v_0}$ for armchair tubes.

For temperatures above $\sim 0.4T_{\rm F}$ we see two different behaviors: For $\varepsilon_{\rm F} \lesssim 0.06$eV ($T_{\rm F} \sim 700$K) the transresistance falls of after the linear piece in contrast to the temperature dependence for $\varepsilon_{\rm F} \gtrsim 0.06$eV, where it increases beyond the linear power law after the linear piece. We see that the increase (decrease) is more pronounced the larger (smaller) the Fermi level $\varepsilon_{\rm F}$ is. The crossover is seen on figure 5.8 to be smooth. Note however that the temperature is very large for e.g. $T_{\rm F} = 1740$K (figure 5.6(middle)) in the regime of increase beyond the linear power law. The transresistance as a function of temperature T from zero to 350K is seen on figure 5.9, where we observe that the slope of R_{21} around room temperature can change sign by varying $\varepsilon_{\rm F}$.

For low Fermi levels we are close to the particle-hole symmetry, where R_{21} is zero. Then the temperature is raised the Fermi level will be smeared out, which brings the system closer to the particle-hole symmetry again, which in turn makes the transresistance drop.

The transresistance as a function of gate voltage

In figure 5.10(left) we have the transresistance as a function of the Fermi level for two different temperatures: $T = 300K$ and $T = 150K$. The Fermi level is in

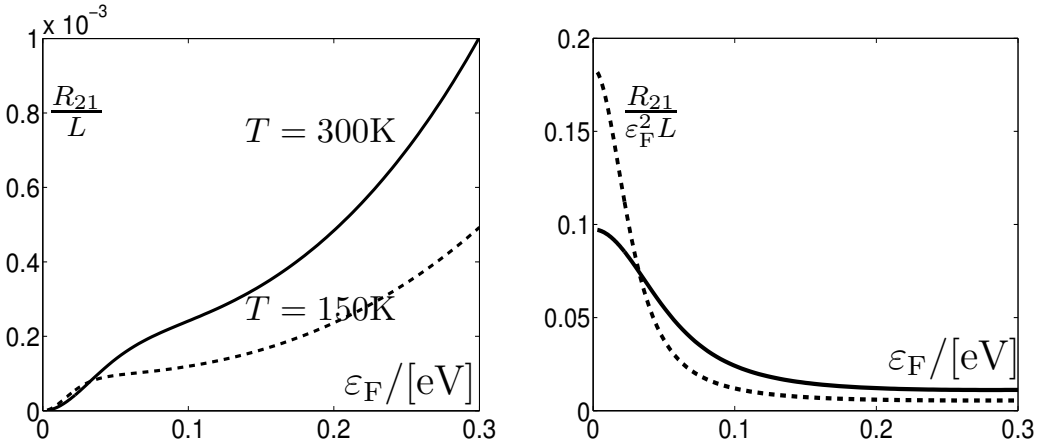

Figure 5.10: (Left): The transresistance per length $\frac{R_{21}}{L}$ (in Ω/μm) as a function of the Fermi level $\varepsilon_{\rm F}$ (in eV) (e.g. a gate voltage) for $T = 150K$ (dotted) and $T = 300K$ (full line). (Right): The transresistance per length over the Fermi energy squared $\frac{R_{21}}{(\varepsilon_{\rm F})^2 L}$ (in $\Omega/(\mu\text{m}(\text{eV})^2)$) as a function of $\varepsilon_{\rm F}$. Note that R_{21} is even in the Fermi level $\varepsilon_{\rm F}$, so a dip can be observed then going trough the particle-hole symmetry at $\varepsilon_{\rm F} = 0$.

the interval $|\varepsilon_{\rm F}| < 0.3$eV, which is realistic by changing a gate voltage or from doping (see p.27). We note that R_{21} goes to zero as it should for $\varepsilon_{\rm F} = 0$.

The transresistance is symmetric around $\varepsilon_{\rm F} = 0$ due to the particle-hole symmetry, which will introduce a dip as a function of the gate voltage at $\varepsilon_{\rm F} = 0$. This prediction only depends on the particle-hole symmetry and not on the details of the model. Since all nanotubes have particle-hole symmetry this is a feature to be found in any drag experiment for a multiwall carbon nanotube. The dip might be somewhat destroyed if the tunnelling between the tubes is to large.

In figure 5.11 there is a logarithmic plot of $\frac{R_{21}}{L}$ and in figure 5.10(right) we have $\frac{R_{21}}{L(\varepsilon_{\rm F})^2}$ as a function of $\varepsilon_{\rm F}$. These show that $R_{21} \propto \varepsilon_{\rm F}^2$ in to separate intervals: For very small Fermi levels $\varepsilon_{\rm F} \lesssim 10^{-2}$eV and for larger Fermi energies above $\varepsilon_{\rm F} \sim 0.15$eV. In between we have an increase slower that a square power law. The screened interaction is independent of $\varepsilon_{\rm F}$ and the $\varepsilon_{\rm F}$ dependence in the density n cancels with the $\varepsilon_{\rm F}$ dependence in the transport mobility $\mu_{\rm Tr}$, so we only have a $\varepsilon_{\rm F}$ dependence in the $F_{\rm intra}$ function left in the transresistivity formula eq.(5.43). Therefore we can justify $R_{21} \propto \varepsilon_{\rm F}^2$ for $\varepsilon_{\rm F} \lesssim 10^{-2}$eV by expanding the $F_{\rm intra}$ function to first order in $\varepsilon_{\rm F}$. The explicit form of $F_{\rm intra}$ in eq.(5.44) can be divided into four terms, each consisting of two terms with arguments of opposite signs. One of the terms is (including the chemical potential ($\mu \simeq \varepsilon_{\rm F}$) in the argument):

$$f^0(\varepsilon_2-\varepsilon_{\rm F})+f^0(-\varepsilon_2-\varepsilon_{\rm F}) = f^0(\varepsilon_2-\varepsilon_{\rm F})+1-f^0(\varepsilon_2+\varepsilon_{\rm F}) \simeq 1-2\varepsilon_{\rm F}\frac{\partial f^0}{\partial \varepsilon}\Big|_{\varepsilon_{\rm F}=0}, \quad (5.45)$$

where we have expanded to first order in $\varepsilon_{\rm F}$ and used $f^0(-\varepsilon_2-\varepsilon_{\rm F}) = 1 - f^0(\varepsilon_2 + \varepsilon_{\rm F})$.

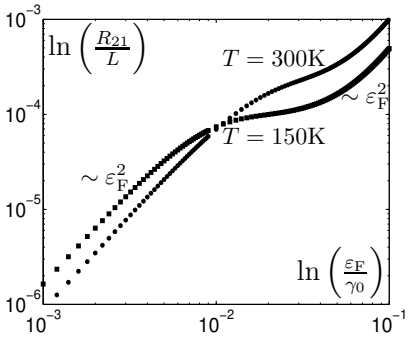

Figure 5.11: Logarithmic plot of $\frac{R_{21}}{L}$ as a function of the Fermi level, where each square ($T = 150$K) or circle ($T = 300$K) is the result for a numerical integration. We observe that the transresistance is quadratic in ε_F for very small Fermi levels and for larger Fermi levels. In between we have a small transition region.

Adding the four terms in F_{intra} the constants cancels out and we have $(F_{\text{intra}})^2 \propto \varepsilon_F^2$, which gives $R_{21} \propto \varepsilon_F^2$ for low Fermi energies.

5.3.6 Coulomb drag in armchair-like nanotubes

For armchair-like tubes (excluding the armchair tubes) we have no parity selection rule and in general $|\mathbf{T}_1| \neq |\mathbf{T}_2|$, so the $F^{(i)}$ functions are periodic in q over different periods $\frac{2\pi}{|\mathbf{T}_i|}$ and in particular the $k_0^{(i)} = \frac{2\pi}{3|\mathbf{T}_i|}$ is different for the two subsystems. So without the parity selection rule the sum over the bands give:

$$\begin{aligned}\sum_{\Pi_1\Pi_2\Pi_1'\Pi_2'} F^{(2)}_{\Pi_1\Pi_1'} F^{(2)}_{\Pi_2\Pi_2'} &= \left(\sum_{\Pi_1\Pi_1'} F^{(1)}_{\Pi_1\Pi_1'}\right)\left(\sum_{\Pi_2\Pi_2'} F^{(2)}_{\Pi_2\Pi_2'}\right) \\ &= F^{(1)}_{++}F^{(2)}_{++} + F^{(1)}_{++}F^{(2)}_{--} + F^{(1)}_{--}F^{(2)}_{++} + F^{(1)}_{--}F^{(2)}_{--} + \\ &\quad F^{(1)}_{++}F^{(2)}_{+-} + F^{(1)}_{++}F^{(2)}_{-+} + F^{(1)}_{--}F^{(2)}_{+-} + F^{(1)}_{--}F^{(2)}_{-+} + \\ &\quad F^{(1)}_{+-}F^{(2)}_{++} + F^{(1)}_{+-}F^{(2)}_{--} + F^{(1)}_{-+}F^{(2)}_{++} + F^{(1)}_{-+}F^{(2)}_{--} + \\ &\quad F^{(1)}_{+-}F^{(2)}_{+-} + F^{(1)}_{+-}F^{(2)}_{-+} + F^{(1)}_{-+}F^{(2)}_{+-} + F^{(1)}_{-+}F^{(2)}_{-+}, \end{aligned} \tag{5.46}$$

where the first four terms have no suppressing g factor (zeroth order in s_0), the next eight terms have $|g|^2 \sim (s_0 aq)^2$ and the last four terms have $|g|^4 \sim (s_0 aq)^4$. Note that it was the terms of order s_0^2, which was forbidden by parity in (real) armchair tubes. So if we neglect higher order in s_0 we have:

$$\sum_{\Pi_1\Pi_2\Pi_1'\Pi_2'} F^{(2)}_{\Pi_1\Pi_1'} F^{(2)}_{\Pi_2\Pi_2'} \simeq F^{(1)}_{++}F^{(2)}_{++} + F^{(1)}_{--}F^{(2)}_{--} + F^{(1)}_{++}F^{(2)}_{--} + F^{(1)}_{--}F^{(2)}_{++} + \mathcal{O}(s_0^2),$$

which is F_{intra} in the case of $|\mathbf{T}_1| = |\mathbf{T}_2|$. If on the other hand $|\mathbf{T}_1| \neq |\mathbf{T}_2|$ we will have $k_0^{(1)} \neq k_0^{(2)}$, so the $F^{(1)}_{++}F^{(2)}_{--}$ and $F^{(1)}_{--}F^{(2)}_{++}$ are not the same. The product of the $F^{(i)}$ functions are suppressed for the different positions of the $k_0^{(i)}$, since this makes the $F^{(i)}$ functions nonzero in different areas (see figure 5.2). Physically we can see that the drag must be strongly suppressed compared to drag between

two (real) armchair tubes, since the intra band backscattering processes around the Fermi level in each subsystem has a momentum transfer $\pm\big(k_0^{(i)} \pm \frac{2\varepsilon_{\rm F}}{\hbar v_0}\big)$, which is different in the two subsystems, so we can not conserve momentum with one of these backscattering processes in each subsystem for $|\mathbf{T}_1| \neq |\mathbf{T}_2|$. Therefore the transresistivity will have a peak around one as a function of $\frac{|\mathbf{T}_1|}{|\mathbf{T}_2|}$. This is analogue to the situation of different densities for two coupled two dimensional electrons gasses considered in [52].

5.4 Comments on Coulomb drag in other types of nanotubes

In this section, we comment on the possibility of Coulomb drag between other types of nanotubes than armchair tubes.

Experimentally we could have one or several tubes in between the drive and drag system in the Coulomb drag setup. The role of one of these tubes depends on, if it is semiconducting or metallic. A metallic tube could screen out the interaction between the electrons in the drive and drag systems and thereby destroy the effect. A semiconducting tube would probably not have a large effect.

Coulomb drag in zigzag-like nanotubes

For the zigzag-like tubes we can calculate the single subsystem properties and the $F_{\xi\mathfrak{m},\xi'\mathfrak{m}'}$ functions in the same way as for the armchair-like tubes from the linear bands in eq.(5.2).

The $F_{\xi\mathfrak{m},-\xi\mathfrak{m}'}$ function will have a form similar to the $F_{\Pi,-\Pi}$ function found in figure 5.3, but the g factor will depend on the value of the crystal angular momentum transfer $\Delta\mathfrak{m}$ (see section 2.3.1). This F function reflects the backscattering $\xi \to -\xi$ with a wave vector transfer of $q \simeq \frac{2\varepsilon_{\rm F}}{\hbar v_0}$, which both can have $\Delta\mathfrak{m} = 0$ and $\Delta\mathfrak{m} \neq 0$ for which the g factors are: $|g(\Delta\mathfrak{m} = 0)|^2 \propto (s_0 a q)^2$ and $g(\Delta\mathfrak{m} \neq 0) \sim 1$ (see figure 2.8). So we have two backscattering processes with $q \simeq \frac{2\varepsilon_{\rm F}}{\hbar v_0}$:

- The $\Delta\mathfrak{m} = 0$ process strongly suppressed by the g factor $|g(\Delta\mathfrak{m} = 0)|^2 \propto (s_0 a q)^2$.
- The $\Delta\mathfrak{m} \neq 0$ process with $g \sim 1$, but with a suppression in the interaction $V_{12}(r_1^c, r_2^c, q, \Delta\mathfrak{m})$, which is smaller the larger the $\Delta\mathfrak{m}$.

The suppression of $\Delta\mathfrak{m} \neq 0$ from $V_{12}(r_1^c, r_2^c, q, \Delta\mathfrak{m})$ is not as strong as the one for $\Delta\mathfrak{m} = 0$ from the g factor. However for the $\Delta\mathfrak{m} \neq 0$ backscattering process we have to conserve the crystal angular momentum, which is *not* in general possible for two different zigzag-like tubes, but only in special cases. When using the crystal angular momentum conservation we have to remember to take

incommensurability and commensurability into account (see appendix C and the crystal angular momentum conservation law for commensurable tubes eq.(C.9)).

Consider e.g. the drag between to real metallic zigzag tubes: a $(n,0)$ in a $(n',0)$ tube, which are commensurable. Here we have $\Delta\mathfrak{m} = \pm\frac{n}{3}$ and $\Delta\mathfrak{m} = \pm\frac{n'}{3}$ between the bands in the two tubes, respectively (see eq.(2.76)). Since the two tubes have different radii we have $n \neq n'$, so the crystal angular momentum can not be conserved directly (i.e. only in Umklapp processes[6]). So for two (real) metallic zigzag tubes the $\Delta\mathfrak{m} \neq 0$ process is forbidden by crystal angular momentum conservation and the $\Delta\mathfrak{m} = 0$ process is suppressed by the g factor. There are, however, other examples where one can have crystal angular momentum conservation, so the $q = \frac{2\varepsilon_{\mathrm{F}}}{\hbar v_0}$ and $\Delta\mathfrak{m} \neq 0$ backscattering process can be important in these cases. Such an example is a $(12,15)$ tube in a $(15,18)$ tube, which are commensurable (in the angular direction) and the crystal momentum exchange is $|\Delta\mathfrak{m}| = 1$. Note furthermore that this process is not suppressed if $|\mathbf{T}_1| \neq |\mathbf{T}_2|$, since $q = \frac{2\varepsilon_{\mathrm{F}}}{\hbar v_0}$ in independent of $|\mathbf{T}_i|$.

The other type of F function is $F_{\xi\mathfrak{m},\xi\mathfrak{m}'}$, which will have finite area (near $\omega = 0$) around $q = \frac{\pi}{|\mathbf{T}_i|} - \frac{2\varepsilon_{\mathrm{F}}}{\hbar v_0}$ (for $q \in [0, \frac{\pi}{|\mathbf{T}_i|}]$). This backscattering process will generally be suppressed by the large wave vector transfer $q = \frac{\pi}{|\mathbf{T}_i|} - \frac{2\varepsilon_{\mathrm{F}}}{\hbar v_0}$ in the Fourier transformed interaction and again we can have both $\Delta\mathfrak{m} = 0$ and $\Delta\mathfrak{m} \neq 0$ processes. However in this case we have $\xi = \xi'$ so for both $\Delta\mathfrak{m} = 0$ and $\Delta\mathfrak{m} \neq 0$ we have $g \sim 1$ as can be seen from eq.(2.68)[7]. These large momentum transfer backscattering processes could become important, if a crystal angular momentum transfer is not possible as in the case of two (real) metallic zigzag nanotubes. Note that for the $q = \frac{\pi}{|\mathbf{T}_i|} - \frac{2\varepsilon_{\mathrm{F}}}{\hbar v_0}$ process it is important (as for the armchair-like tubes) to have $|\mathbf{T}_1| = |\mathbf{T}_2|$ in order to have a possible momentum conservation around the Fermi level. So again we would observe a peak for R_{21} around one as a function of $\frac{|\mathbf{T}_1|}{|\mathbf{T}_2|}$.

If we are in a situation, where both the $q = \frac{2\varepsilon_{\mathrm{F}}}{\hbar v_0}$ processes are absent, then we should consider making a model without linearized bands in order not to neglect the small momentum forward scattering process $q \sim 0$, which might become important. This could be done by using the cosine and sine bands found in the tight binding model for armchair and zigzag tubes, respectively. These processes are again possible for both $\Delta\mathfrak{m} = 0$ and $\Delta\mathfrak{m} \neq 0$ (both have $g \sim 1$), since we have degenerate bands separated by different $\mathfrak{m}$ in the zigzag-like case. The $\Delta\mathfrak{m} = 0$ forward scattering process will dominate of the two forward scattering processes.

Coulomb drag between an armchair-like and a zigzag-like tube

We have so far considered drag between two armchair-like tubes and two zigzag-like tubes, but what if we have a zigzag-like and an armchair-like tube?

[6] These are however strongly suppressed by the interaction.

[7] Remember that $\varsigma = \varsigma'$ gives $\Delta\mathfrak{m} = 0$ and $\varsigma = -\varsigma'$ gives $\Delta\mathfrak{m} \neq 0$.

First of all we can have no angular momentum transfer in the armchair-like tube for scattering in the bands near the Fermi level and therefore the $\Delta\mathfrak{m} \neq 0$ process in the zigzag-like tube is excluded by angular momentum conservation. Therefore all the $q = \frac{2\varepsilon_{\mathrm{F}}}{\hbar\omega}$ processes are suppressed. The other backscattering processes around the Fermi level with transferred wave vector $q = k_0^{(i)} \pm \frac{2\varepsilon_{\mathrm{F}}}{\hbar\omega}$ (armchair-like) and $q = \frac{\pi}{|\mathbf{T}_i|} - \frac{2\varepsilon_{\mathrm{F}}}{\hbar\omega}$ (zigzag-like) are suppressed, because they are not in general of compatible magnitude — only in rare cases. So in the linearized models it is not likely to find any Coulomb drag between a zigzag-like and an armchair-like tube. If we include the small $q \sim 0$ forward scattering processes by using nonlinear bands, we could obtain the possibility of some Coulomb drag, but the phase space (i.e. the F functions) are small around the $q \sim 0$ in such models, since the bands near $\varepsilon_{\mathrm{F}} = 0$ are to a very good approximation linear.

Coulomb drag in semiconducting nanotubes

If we shift the Fermi level into the conduction (or valence) band of a semiconducting tube, it becomes conducting. In such a situation the drag processes are within a single band (i.e. $\Delta\mathfrak{m} = 0$) similar to a quadratic band for small tubes, where there are few bands with large separation. Here both the small q forward scattering and the large q backscattering processes will contribute to the drag. We can calculate the g factors in the same way as for the metallic tubes and for intra band scattering it is close to one. However, the magnitude of the backscattering momentum transfer around the Fermi level has to be approximately the same in the two tubes in order to have momentum conservation. If we deal with larger tubes more bands can come into play and thereby more scattering possibilities appear than captured in the single band quadratic model (see [108] for a discussion on scattering in larger multiwall nanotubes). This is also the case of larger metallic tubes. Coulomb drag in the quadratic model with more bands (with different angular momentum along the tube) for tubes of semiconducting material were considered in [110].

Coulomb drag between a semiconduction and a metallic tube

Coulomb drag between a semiconducting and a metallic tube is also a possibility and leads to many different scenarios. Again the wave vector transfer for backscattering processes near the Fermi surface have to be of the same order to have any significant effect. A crystal angular momentum exchange can take place, but it depends on the tubes involved. A small semiconducting tube only has the $\Delta\mathfrak{m} = 0$ process, so this also as to be fulfilled in the metallic tube. However the suppressing g factor of order s_0 can only be to second order in this setup.

5.5 Conclusion and extensions of the model

We have considered the Coulomb drag in a multiwall carbon nanotube with emphasis on the drag between armchair tubes. We classified all metallic nanotubes in two types: The armchair-like and zigzag-like tubes and modelled them by linear bands crossing the Fermi level $\varepsilon_{\mathrm{F}} = 0$ at $k = \pm\frac{2\pi}{3|\mathbf{T}_i|}$ and $k = 0$, respectively. By using linear bands we neglected the small q forward scattering processes a priori in the models. The screened interaction were used in a simple quasi 1D random phase approximation.

We found the F function for the armchair-like tubes and on the basis of the strongly suppressing g factors we excluded the small wave vector inter band backscattering processes. Therefore the main process (at low temperature compared to T_{F}) in the Coulomb drag in armchair-like tubes are the backscattering processes with $q \simeq k_0 \pm \frac{2\varepsilon_{\mathrm{F}}}{\hbar v_0}$ and $\Delta\mathfrak{m} = 0$ (see figure 5.4). This led to a linear dependence of the transresistance R_{21} as a function of temperature. The order of magnitude of the transresistance per length is $\mathrm{m}\Omega/\mu\mathrm{m}$. The same temperature dependence is found for the (screened) quadratic model (and the $\varepsilon \propto |k|$ model). The similarity is found because the main process in both models is the large q backscattering process, i.e. the details of the band structure do not have any effect on the temperature dependence of R_{21}.

In contrast to this, the Fermi level dependence of R_{21} is strongly dependent on the band structure. In particular the particle-hole symmetry introduces a dip at $\varepsilon_{\mathrm{F}} = 0$, which can be found experimentally by varying a gate voltage. This dip should exist for all tubes, since all tubes have particle-hole symmetry. However if the tunnelling between the tubes are too large this dip might not be seen. For armchair tubes we found $R_{21} \propto \varepsilon_{\mathrm{F}}^2$ for $\varepsilon_{\mathrm{F}} \lesssim 10^{-2}$ and above $\varepsilon_{\mathrm{F}} = 0.15\mathrm{eV}$. For armchair-like tubes we expect a suppression of the drag away from $\frac{|\mathbf{T}_1|}{|\mathbf{T}_2|} = 1$, since the scattering around the Fermi level will have different wave vector transfers in the two tubes.

Coulomb drag between zigzag-like metallic tubes were found to depend critically on the crystal angular momentum selection rule: In some tubes crystal angular momentum conservation could only be fulfilled for $\Delta\mathfrak{m} = 0$ (with a suppressing $g \sim s_0 aq$ factor), where as for others we could have $\Delta\mathfrak{m} \neq 0$ leading to a larger transresistivity.

Note that the coaxial geometry only entered in the calculation of the Coulomb interaction and in the parity selection rule. Therefore most of the considerations can also be used in the case of Coulomb drag between parallel nanotubes.

Possible extension of the model

We have found a benchmark result on the basis of Fermi liquid theory. An interesting extension (or rather a different project) could be to make a theory for Coulomb drag in a multiwall nanotube using Luttinger liquid theory approach, to

investigate whether electrons in multiwall nanotubes behave as Fermi or Luttinger liquids.

Within the present model we could do a more detailed calculation of drag in other kinds of tubes that armchair, to see if our expectations are correct. Furthermore, a model with nonlinear bands could be used to find the quantitative error introduced neglecting the small momentum transfer forward scattering process. The model of the screening of the Coulomb interaction could also be refined and one could consider the role of phonon mediated drag, which were found to be important in the case of two dimensional systems (see section 1.5). Furthermore, carbon nanotubes are often observed to be in the ballistic regime and therefore one could also consider the Coulomb drag between ballistic tubes including the band structure. This could be consider e.g. by removing the impurity scattering terms in the coupled Boltzmann equations or within the Landauer-Büttiker picture.

Another extension could be to include tunnelling between tubes in the model. A transresistance formula including this contribution could be found by placing some tunnelling centers in the tube (e.g. at the impurities or at dislocations) and then performing an average over these centers in the same way as one can make impurity average Greens functions, see [18, chap.10]. These Greens functions could then be included in a Kubo formula derivation of ρ_{21}. Note that in the experiment, the tunnelling effect and the drag effect will give different signs of the transresistivity.

Furthermore, our calculation of ρ_{21} could be used directly to evaluate the electronic part of the mechanical friction between two carbon nanotubes in a GHz oscillation, where an inner tube is mechanically oscillating in and out of an outer tube (with GHz frequency). The contribution from the Van der Waals forces are found in [127] (see also the experiment in [31]).

Summery

In this thesis, we have considered the idea of Coulomb drag between concentric nanotubes in a multiwall carbon nanotube with an emphasis on drag between metallic nanotubes. To study the Coulomb drag we calculated the transresistivity ρ_{21}.

The electrons in the nanotubes are described by single particle Bloch states. The two atomic unit cell of graphene gave rise to a two component tight binding state, which in turn gave four crossings of the Fermi level ε_{F} as a function of the one dimensional wave vector k in all metallic tubes. By using the slow variation of the Coulomb interaction between electrons in different tubes, we calculated the Coulomb matrix element between tight binding Bloch states. The result was a sum over the Fourier transformed interaction times a so-called g factor for each tube. These g factors are roughly the dot product of the two components in the Bloch states and the g factors were found to suppress some of the backscattering processes substantially. Furthermore, the Bloch states can be labelled by the crystal angular momentum $\mathfrak{m}$ (stemming from the discrete rotational symmetry) and we have classified the metallic tubes to be either armchair-like with bands crossing $\varepsilon_{\mathrm{F}} = 0$ at $k = \pm\frac{2\pi}{3|\mathbf{T}|}$ or zigzag-like with doubly degenerate bands crossing the Fermi level ($\varepsilon_{\mathrm{F}} = 0$) at $k = 0$.

We have used two coupled diffusive Boltzmann equations to derive a formula for the transresistivity ρ_{21}, i.e. a semiclassical transport theory. This calculation was performed in the regime of linear response to the external electric field and furthermore, the g factors from the Coulomb matrix element were included. Therefore we provide a benchmark result for Coulomb drag in multiwall nanotubes within the Fermi liquid theory, which could be compared to a similar theory within the Luttinger liquid picture. The comparison to the experimental results would then gain inside to the question, if multiwall carbon nanotubes are Luttinger liquids or Fermi liquids.

Furthermore, we considered the Coulomb drag in one dimension for two simple dispersion relations: $\varepsilon \propto k^2$ and $\varepsilon \propto |k|$ ($k \in \mathbb{R}$). This gave some inside into the phenomenon of Coulomb drag and to which scattering processes are responsible for the effect. Here we found, that the small momentum transfer was neglected by using a (piecewise) linear dispersion relation, which was clear from the explicit form of the F functions in the drag formula for one dimension. However, for a screened interaction, we found a linear temperature dependence (for low temperatures) in both models stemming from the backscattering process with momentum transfer of order $2k_{\mathrm{F}}$. This understanding were used to analyze the drag in multiwall tubes.

To model the Coulomb drag between metallic nanotubes we linearized the bands around $\varepsilon_{\mathrm{F}} = 0$ in order to preserve the particle-hole symmetry present for all nanotubes. This linearization neglected the small momentum transfer forward scattering processes and made it possible to use the g factors found earlier for

backscattering processes in all metallic tubes directly. Numerical results of the transresistance per length as a function of temperature and Fermi level (e.g. a gate voltage) were presented for the Coulomb drag between two armchair tubes: A $(5,5)$ in a $(10,10)$ tube. Here we found a linear temperature dependence for low temperatures (compared to the the Fermi temperature).

For all the armchair-like nanotubes we only have scattering around the Fermi level without crystal angular momentum exchange. Furthermore, the inter band backscattering processes (with small wave vector transfer $q \simeq \frac{2\varepsilon_{\mathrm{F}}}{\hbar v_0}$) were found to be strongly suppressed by a factor of order 10^{-8} in the Coulomb drag. Therefore the important scattering process in the Coulomb drag between armchair tubes were found to be the intra band backscattering process with wave vector transfer $q \simeq \frac{2\pi}{3|\mathbf{T}_i|} \pm \frac{2\varepsilon_{\mathrm{F}}}{\hbar v_0}$. For the $(5,5)$ tube in the $(10,10)$ tube the order of magnitude of the transresistance per length were found to be $\mathrm{m}\Omega/\mu\mathrm{m}$. For other armchair-like tubes we expect the magnitude to become smaller as we move away from the $\frac{|\mathbf{T}_1|}{|\mathbf{T}_2|} = 1$ case, since momentum conservation becomes harder to fulfill near the Fermi level for the $q \simeq \frac{2\pi}{3|\mathbf{T}_i|} \pm \frac{2\varepsilon_{\mathrm{F}}}{\hbar v_0}$ scattering.

For Coulomb drag between zigzag-like tubes the scattering with no crystal angular momentum exchange is again suppressed by the g factor. This is in contrast to backscattering with finite angular momentum exchange, which have $g \sim 1$. However, we have to conserve the crystal angular momentum in the scattering process, which is not possible for e.g. two (real) zigzag tubes, but possible for other zigzag-like tubes. Therefore the Coulomb drag between zigzag-like tubes depends critically on the possibility of scattering between bands with different crystal angular momentum.

The particle-hole symmetry present for all nanotubes will create a dip in ρ_{21} as a function of ε_{F} around $\varepsilon_{\mathrm{F}} = 0$, which could be found experimentally by varying a gate voltage. In the numerical calculation, we found the transresistance to begin quadratic in ε_{F} for very small ε_{F}, then a less increase is found in a small interval, after which ρ_{21} again appeared quadratic.

In an actual experiment, we can have many different scenarios, and I am looking forward to seeing the experimental curves appearing.

Appendix A
Band structure of a cylinder in the free electron model

To gain some insight into the application of periodic boundary conditions we consider a free two dimensional electron gas (2DEG) folded into a cylinder.

The dispersion relation for the 2DEG of size $A = L_x \times L_y$ is

$$\varepsilon_{\mathbf{k}} = \frac{\hbar^2}{2m^*}(k_x^2 + k_y^2), \tag{A.1}$$

where m^* is some effective mass and $k_i = \frac{2\pi}{L_i} m_i$ is the wave vector ($m_i \in \mathbb{Z}$ and $i = x, y$). In the free electron model we conventionally have periodic boundary conditions [1, chap.2], since L_i are assumed large. The large L_i makes k_i (almost) continuous. The single electron (non-normalized) wave function in a 2DEG is a plane wave $e^{ik_x x + ik_y y}$.

When one of the dimensions becomes smaller, say L_y, one normally consider it to be a particle in a box in that direction [109, chap.4], but if we wrap the plan to a tube it is physically reasonable to maintain the periodic boundary condition. Then L_y is small the spacing $\frac{2\pi}{L_y}$ between the possible k_y becomes large and if k_y is written in terms of the radius of the cylinder $r = \frac{L_y}{2\pi}$ we have $k_y = \frac{2\pi}{L_y} m_y = \frac{m_y}{r}$. This splits the two dimensional band structure up into one dimensional subbands labelled by $m_y \equiv m$:

$$\varepsilon_{k,m} = \frac{\hbar^2}{2m^*}\left(k^2 + \left(\frac{m}{r}\right)^2\right), \tag{A.2}$$

where $k \equiv k_x$ is still (almost) continuous, i.e. $\varepsilon_{k,m}$ are parabolas as a function of k with minimum at $\frac{\hbar^2 m^2}{2m^* r^2}$ determined by m. The emergence of one dimensional subbands from a two dimensional band structure can be seen as a cutting of the two dimensional (almost continuous) $\mathbf{k}$ space into lines. The same picture is used for nanotubes in figure 2.3. The wave function becomes $e^{ikx + im\theta}$, where $\theta = \frac{y}{r}$ is the angle in cylindrical coordinates. This is an eigenfunction for the angular momentum operator along the tube $\widehat{L}_x = -i\hbar\frac{\partial}{\partial\theta}$ with eigenvalue $\hbar m$, which is clear since the tube has continuous rotation symmetry. So the states and energies are labelled by angular and linear momentum quantum numbers m and k. The same band structure would have been obtained by making any other direction small (also combinations of x and y) by a rotation of the coordinate system. Note that the same energies and states can be obtained directly from the Schrödinger equation for a cylinder disregarding the radial direction.

Coulomb drag in such a model has been investigated in [110].

Appendix B
Tight-binding chain with different unit cells

In this appendix we describe a one dimensional atomic chain with equal spacing a between equivalent atoms with a single (usable) atomic orbital in the tight-binding approximation. We want to consider the difference between the description of the band structure for the chain with the smallest possible unit cell (i.e. the primitive unit cell) with one atom and a larger unit cell with two atoms. In principle the same difference arises when describing the nanotubes band structure in terms of the translational unit cell and the helical unit cell.

The one atomic unit cell

For the primitive unit cell with one atom a general lattice vector is $R = na$, where $n \in \mathbb{Z}$. The Wannier decomposition of the energy eigenstate is:

$$\psi_k(x) = \frac{1}{\sqrt{N}} \sum_{n\in\mathbb{Z}} e^{ikan} \Psi(x - na), \tag{B.1}$$

where $\Psi(x)$ are Wannier functions approximated by the atomic orbital and N the number of atoms in the chain ($N \gg 1$). The wave vector k is found from the periodic boundary condition $\psi_k(x) = \psi_k(x + Na) = e^{ikNa}\psi_k(x)$ to be $k = \frac{2\pi m}{Na}$, where the integer m is restricted so that $-\pi < ka \leq \pi$. The eigenstate eq.(B.1) is a solution to the Schrödinger equation $H\psi_k(x) = \varepsilon_k \psi_k(x)$ and the eigen energy in the nearest neighbour approximation is therefore found to be

$$\varepsilon_k = \frac{\langle\psi_k|H|\psi_k\rangle}{\langle\psi_k|\psi_k\rangle} = \frac{\varepsilon_0 - \gamma_0 2\cos(ka)}{1 + s_0 2\cos(ka)} \simeq -2\gamma_0 \cos(ka) \quad \text{for} \quad -\frac{\pi}{a} < k \leq \frac{\pi}{a}, \tag{B.2}$$

where $\gamma_0 > 0$ is the magnitude of the hopping matrix element $\langle\Psi(x-na)|H|\Psi(x-(n\pm1)a)\rangle$, ε_0 the energy of the atomic orbital (chosen to be zero) and the overlap s_0 between neighboring orbitals were neglected ($s_0 \simeq 0$).

The reciprocal lattice is spanned by $b = \frac{2\pi}{a}$ by the definition $ab = 2\pi$ and we see that the explicit form of the energy eq.(B.2) is periodic with $\frac{2\pi}{a}$ and the explicit form of the Bloch function eq.(B.1) fulfills the Bloch theorem $\psi_{k+G}(x) = \psi_k(x)$ for any $G = nb$ for $n \in \mathbb{Z}$.

The two atomic unit cell

Consider the same chain with two atoms in the unit cell, so the lattice vectors are of the form $R = n\tilde{a}$, where $\tilde{a} \equiv 2a$. The Wannier decomposition for two atoms in the unit cell is therefore:

$$\varphi_k(x) = \frac{1}{\sqrt{N_u}} \sum_{n\in\mathbb{Z}} e^{ik\tilde{a}n} \big(\alpha\Psi(x - n\tilde{a}) + \beta\Psi(x - n\tilde{a} - a)\big), \tag{B.3}$$

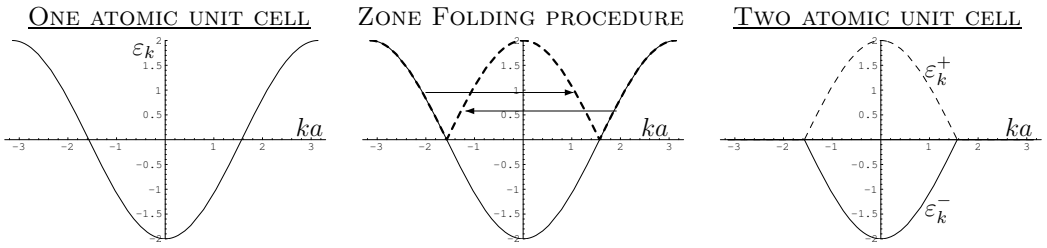

Figure B.1: (Left): The single tight-binding band found be using the primitive unit cell with one atom. Here the FBZ is $]-\frac{\pi}{a},\frac{\pi}{a}]$. (Center): The zone folding procedure, where the single band from the primitive unit cell is pushed into the smaller FBZ of the two atomic unit cell to obtain two bands. (Right): The two bands from the two atomic unit cell in the smaller FBZ $]-\frac{\pi}{2a},\frac{\pi}{2a}]$.

where $N_u = \frac{N}{2}$ is the number of unit cells and the k dependent parameters α and β are determent from the Schrödinger equation in the same way as in section 2.2.1 for graphene, i.e. be diagonalizing the 2×2 Hamiltonian matrix. The two eigenstates are[8]:

$$\begin{pmatrix} \alpha \\ \beta \end{pmatrix}_{\mp} = \frac{1}{\sqrt{2}} \begin{pmatrix} \pm e^{-ika} \\ 1 \end{pmatrix}, \tag{B.4}$$

i.e.

$$\varphi_k^{\pm}(x) = \frac{1}{\sqrt{N}} \sum_{n\in\mathbb{Z}} e^{ik\tilde{a}n} \big(\mp e^{-ika} \Psi(x-n\tilde{a}) + \Psi(x-n\tilde{a}-a) \big), \tag{B.5}$$

and the two eigen energies are

$$\varepsilon_k^{\pm} = \pm 2\gamma_0 \cos\left(\frac{k\tilde{a}}{2}\right) \quad \text{where} \quad -\frac{\pi}{\tilde{a}} < k \leq \frac{\pi}{\tilde{a}}. \tag{B.6}$$

The reciprocal lattice is spanned by $\tilde{b} = \frac{2\pi}{\tilde{a}}$ by the definition $\tilde{a}\tilde{b} = 2\pi$, i.e. half the length of the reciprocal lattice vector from the one atomic (primitive) unit cell. By using the explicit expressions for the energy eq.(B.6) and the Bloch wavefunction eq.(B.3) it seems like that a shift of k by $\tilde{b} = \frac{2\pi}{\tilde{a}}$ do not leave these invariant. This is because we need to repeat the energy and the Bloch wave from the interval $-\pi < k\tilde{a} \leq \pi$ to the other intervals of length $\frac{2\pi}{\tilde{a}}$ to make them into periodic functions by hand[9].

Comparison of the two different unit cells

The physics of the atomic chain should of course not depend on which unit cell is used. We therefore show now, that the states and energy band for the primitive

[8]Then diagonalizing the 2×2 matrix a factor of $\text{sign}(\cos(ka))$ appears in α, which is one since $-\pi < k\tilde{a} \leq \pi$.

[9]Note that the velocity (i.e. the derivative of the energy) is discontinuous at the zone boundary.

unit cell can be pushed from the FBZ $]-\frac{\pi}{a},\frac{\pi}{a}]$ into the smaller FBZ $]-\frac{\pi}{2a},\frac{\pi}{2a}]$ of the two atomic unit cell to give the same states and energies as found by using a two atomic unit cell from the beginning. This is seen on figure B.1.

We begin by rewriting $\psi_k(x)$ into $\varphi_k(x)$. The sum over n in eq.(B.1) is split into two sums by writing $R = na = n\tilde{a} + ja$, where $n \in \mathbb{Z}$ and $j \in \{0, 1\}$, so we get:

$$\begin{aligned}\psi_k(x) &= \frac{1}{\sqrt{N}} \sum_{n\in\mathbb{Z}} e^{ikan} \Psi(x - na) \\ &= \frac{1}{\sqrt{N}} \sum_{n\in\mathbb{Z}} e^{ik\tilde{a}n} \big(\Psi(x - n\tilde{a}) + e^{ika} \Psi(x - n\tilde{a} - a)\big), \end{aligned} \tag{B.7}$$

which is the eigenstate $\varphi_k^-(x)$ eq.(B.5) (up to a complex phase factor) for the ε_k^- band in figure B.1. To obtain the upper band (ε_k^+) we move the single $\cos(ka)$ band into the smaller FBZ by the substitutions $k \to k \pm \frac{\pi}{\tilde{a}}$ for the part outside $]-\frac{\pi}{2a},\frac{\pi}{2a}]$ as seen in the figure. This substitution in the wave function eq.(B.7) produces $\varphi_k^+(x)$ in eq.(B.5) (up to a complex phase factor).

We have thereby seen that the two ways of choosing the unit cell are equivalent. This is a general statement even though we have only shown it explicitly in this very simple case.

Appendix C
Commensurability and incommensurability effects in the Coulomb interaction between the tubes

In this appendix, we will shortly consider the difference between commensurable and incommensurable tubes in a double wall nanotube, which inters in the calculation of the Coulomb matrix element eq.(2.81), therefore we consider

$$\frac{1}{\mathfrak{n}_1\mathfrak{L}_1\mathfrak{n}_2\mathfrak{L}_2}\sum_{l_1,l_2}\sum_{p_1=0}^{\mathfrak{n}_1-1}\sum_{p_2=0}^{\mathfrak{n}_2-1}V_{12}(|\mathbf{R}_{l_1p_1}-\mathbf{R}_{l_2p_2}|)e^{i(\kappa_2-\kappa_2')l_2+i(\kappa_1-\kappa_1')l_1+i\frac{2\pi}{\mathfrak{n}_2}(\mathfrak{m}_2-\mathfrak{m}_2')p_2+i\frac{2\pi}{\mathfrak{n}_1}(\mathfrak{m}_1-\mathfrak{m}_1')p_1}, \tag{C.1}$$

where the l_i sum is from $-\mathfrak{L}_i/2$ to $\mathfrak{L}_i/2$, $(i=1,2)$.

The Coulomb interaction $V_{12}(|\mathbf{R}_{l_1p_1}-\mathbf{R}_{l_2p_2}|)$ is in general a function of the difference between the coordinates of the electrons, which makes it possible to Fourier transform as if $\mathbf{R}_{l_1p_1}-\mathbf{R}_{l_2p_2}$ is one coordinate to obtain a nice result in terms of the Fourier transform as for the graphene layers eq.(2.79). The same rewriting can *not* by used to simplify eq.(C.1), because it is not a priori clear if the Coulomb interaction is a function of l_1-l_2 and p_1-p_2, since

$$\mathbf{R}_{l_1p_1}-\mathbf{R}_{l_2p_2}=l_1\mathbf{H}_1+p_1\mathbf{C}_{\mathfrak{n}_1}-l_2\mathbf{H}_2-p_2\mathbf{C}_{\mathfrak{n}_2} \tag{C.2}$$

is not a priori a function of l_1-l_2 and p_1-p_2. It is here the commensurability or incommensurability of the two tubes inters, i.e. if the two tubes as a combined system proposes a periodic lattice or not.

The definition of commensurability for two tubes is: Tube 1 and 2 are commensurable if and only if there exist two rational numbers $c_H, c_C \in \mathbb{Q}$ such that

$$\mathbf{H}_1=c_H\mathbf{H}_2 \qquad \text{and} \qquad \mathbf{C}_{\mathfrak{n}_1}=c_C\mathbf{C}_{\mathfrak{n}_2}. \tag{C.3}$$

If this is not true the tubes are incommensurable. Note that $\mathbf{H}_i$ and $\mathbf{C}_{\mathfrak{n}_i}$ $(i=1,2)$ found from eq.(2.6) and eq.(2.7) are *not* calculated in the same coordinate system in the sense that $\mathbf{a}_1$ and $\mathbf{a}_2$ are in different directions for the two tubes due to the conformal mapping (wrapping) on the tube. Therefore one has to find $\mathbf{H}_1$, $\mathbf{H}_2$, $\mathbf{C}_{\mathfrak{n}_1}$ and $\mathbf{C}_{\mathfrak{n}_2}$ in the same coordinate system to determine if two tubes are commensurable or not from definition (C.3).

We now rewrite eq.(C.1) for the case of commensurable and incommensurable nanotubes by inserting Fourier transforms in the helical coordinates.

Commensurable nanotubes

Assuming that the tubes are commensurable we have

$$\mathbf{R}_{l_1p_1}-\mathbf{R}_{l_2p_2}=(c_Hl_1-l_2)\mathbf{H}_2+(c_Cp_1-p_2)\mathbf{C}_{\mathfrak{n}_2}, \tag{C.4}$$

so we can Fourier transform as

$$V_{12}(|\mathbf{R}_{l_1p_1}-\mathbf{R}_{l_2p_2}|)=\frac{1}{\mathfrak{n}_2\mathfrak{L}_2}\sum_{\tilde{\kappa}_2}\sum_{\tilde{\mathfrak{m}}_2=0}^{\mathfrak{n}_2-1}V_{12}(\tilde{\kappa}_2,\tilde{\mathfrak{m}}_2)e^{i\tilde{\kappa}_2(c_Hl_1-l_2)+i\frac{2\pi}{\mathfrak{n}_2}\tilde{\mathfrak{m}}_2(c_Cp_1-p_2)}, \quad \text{(C.5)}$$

where the $\tilde{\kappa}_2$ sum is over $\tilde{\kappa}_2=\frac{2\pi}{\mathfrak{L}_2}q$, $q\in\mathbb{Z}$ and the Fourier transform is

$$V_{12}(\tilde{\kappa}_2,\tilde{\mathfrak{m}}_2)=\sum_{l_2=-\mathfrak{L}_2/2}^{\mathfrak{L}_2/2}\sum_{p_2=0}^{\mathfrak{n}_2-1}V_{12}(|\mathbf{R}_{l_2p_2}|)e^{-i\tilde{\kappa}_2l_2-i\frac{2\pi}{\mathfrak{n}_2}\tilde{\mathfrak{m}}_2p_2}. \quad \text{(C.6)}$$

So by inserting eq.(C.5) into eq.(C.1) we get:

$$\begin{aligned}
&\frac{1}{\mathfrak{n}_1\mathfrak{L}_1\mathfrak{n}_2\mathfrak{L}_2}\sum_{l_1,l_2}\sum_{p_1=0}^{\mathfrak{n}_1-1}\sum_{p_2=0}^{\mathfrak{n}_2-1}V_{12}(|\mathbf{R}_{l_1p_1}-\mathbf{R}_{l_2p_2}|)e^{i(\kappa_2-\kappa_2')l_2+i(\kappa_1-\kappa_1')l_1+i\frac{2\pi}{\mathfrak{n}_2}(\mathfrak{m}_2-\mathfrak{m}_2')p_2+i\frac{2\pi}{\mathfrak{n}_1}(\mathfrak{m}_1-\mathfrak{m}_1')p_1}\\
&=\frac{1}{\mathfrak{n}_1\mathfrak{L}_1\mathfrak{n}_2^2\mathfrak{L}_2^2}\sum_{\tilde{\kappa}_2,\tilde{\mathfrak{m}}_2}V_{12}(\tilde{\kappa}_2,\tilde{\mathfrak{m}}_2)\sum_{l_1}e^{i(c_H\tilde{\kappa}_2+\kappa_1-\kappa_1')l_1}\sum_{l_2}e^{i(-\tilde{\kappa}_2+\kappa_2-\kappa_2')l_2}\\
&\qquad\times\sum_{p_1=0}^{\mathfrak{n}_1-1}e^{i\frac{2\pi}{\mathfrak{n}_1}(\frac{c_C\tilde{\mathfrak{m}}_2\mathfrak{n}_1}{\mathfrak{n}_2}+\mathfrak{m}_1-\mathfrak{m}_1')p_1}\sum_{p_2=0}^{\mathfrak{n}_2-1}e^{i\frac{2\pi}{\mathfrak{n}_2}(-\tilde{\mathfrak{m}}_2+\mathfrak{m}_2-\mathfrak{m}_2')p_2}\\
&=\frac{1}{\mathfrak{n}_2\mathfrak{L}_2}\sum_{u_1,\tilde{u}_1,u_2,\tilde{u}_2\in\mathbb{Z}}V_{12}(\kappa_2-\kappa_2'+2\pi u_2,\mathfrak{m}_2-\mathfrak{m}_2'+\mathfrak{n}_2\tilde{u}_2)\\
&\qquad\times\delta_{\kappa_1'+c_H\kappa_2',\kappa_1+c_H\kappa_2+2\pi(c_Hu_2-u_1)}\delta_{\mathfrak{m}_1'+c_C\mathfrak{m}_2'\mathfrak{n}_1,\mathfrak{m}_1+c_C\mathfrak{m}_2\mathfrak{n}_1+\mathfrak{n}_1\mathfrak{n}_2(c_C\tilde{u}_2-\tilde{u}_1)}, \quad \text{(C.7)}
\end{aligned}$$

where we used $\sum_{l_i}e^{i\kappa_il_i}=\sum_{u_i\in\mathbb{Z}}\delta_{\kappa_i,2\pi u_i}$ and $\sum_{p_i}e^{i\frac{2\pi\mathfrak{m}_i}{\mathfrak{n}_i}p_i}=\sum_{\tilde{u}_i\in\mathbb{Z}}\delta_{\mathfrak{m}_i,\mathfrak{n}_i\tilde{u}_i}$ in the last equality. So we see that the κ quantum number stemming from the helical symmetry and the crystal angular momentum $\mathfrak{m}$ are conserved as

$$\kappa_1'+c_H\kappa_2'=\kappa_1+c_H\kappa_2+2\pi(c_Hu_2-u_1), \quad \text{(C.8)}$$

$$\mathfrak{m}_1'+c_C\mathfrak{m}_2'\mathfrak{n}_1=\mathfrak{m}_1+c_C\mathfrak{m}_2\mathfrak{n}_1+\mathfrak{n}_1\mathfrak{n}_2(c_C\tilde{u}_2-\tilde{u}_1) \quad \text{(C.9)}$$

in the Coulomb interaction between Bloch states in the to commensurable tubes, where $u_i\neq 0$ and/or $\tilde{u}_i\neq 0$ are the Umklapp process. The analogue to the normal crystal momentum conservation in eq.(2.79) is clear.

Incommensurable nanotubes

For incommensurable nanotubes we have to Fourier transform each coordinate as:

$$\begin{aligned}
&V_{12}(|\mathbf{R}_{l_1p_1}-\mathbf{R}_{l_2p_2}|)=V_{12}(\mathbf{R}_{l_1p_1},\mathbf{R}_{l_2p_2})\\
&\quad=\frac{1}{\mathfrak{n}_1\mathfrak{L}_1\mathfrak{n}_2\mathfrak{L}_2}\sum_{\tilde{\kappa}_1,\tilde{\kappa}_2}\sum_{\tilde{\mathfrak{m}}_1,\tilde{\mathfrak{m}}_2}V_{12}(\tilde{\kappa}_1,\tilde{\mathfrak{m}}_1,\tilde{\kappa}_2,\tilde{\mathfrak{m}}_2)e^{i\tilde{\kappa}_1l_1+i\tilde{\kappa}_2l_2+i\frac{2\pi}{\mathfrak{n}_1}\tilde{\mathfrak{m}}_1p_1+i\frac{2\pi}{\mathfrak{n}_2}\tilde{\mathfrak{m}}_2p_2}, \quad \text{(C.10)}
\end{aligned}$$

which is inserted into eq.(C.1) to give:

$$\frac{1}{\mathfrak{n}_1\mathfrak{L}_1\mathfrak{n}_2\mathfrak{L}_2}\sum_{u_1,\tilde{u}_1,u_2,\tilde{u}_2\in\mathbb{Z}} V_{12}(\kappa_1-\kappa_1'+2\pi u_1,\mathfrak{m}_1-\mathfrak{m}_1'+\mathfrak{n}_1\tilde{u}_1,\kappa_2-\kappa_2'+2\pi u_2,\mathfrak{m}_2-\mathfrak{m}_2'+\mathfrak{n}_2\tilde{u}_2),$$

where there is no conservation laws a priori. If we assume commensurability at this point, this Fourier transform simplifies to eq.(C.7).

It is also possible to have two nanotubes, where one but not the other of the commensurability conditions (C.3) are fulfilled. In such a case we can find one of the conservation laws by Fourier transforming.

Note that we could also have introduced the commensurability using the translational unit cell, i.e. $\exists\ c_T \in \mathbb{Q}$ so $\mathbf{T}_1 = c_T\mathbf{T}_2$.

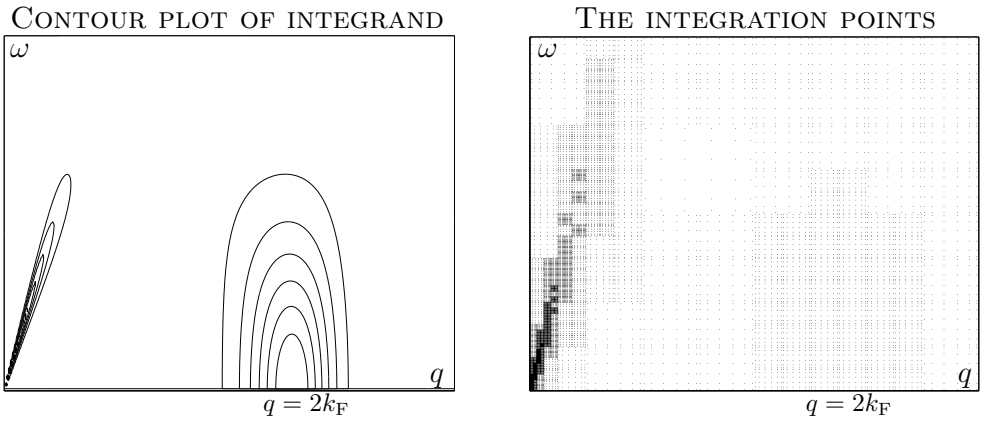

Figure D.1: The integrand of ρ_{21} for the quadratic $\varepsilon_k \propto k^2$ model with a constant potential $W_{12}(q)$ from chapter 4. (Left): A contour plot of the integrand. (Right): The grid used in the numerical integration. Here $\frac{T}{T_F} = 0.2$ is used.

Appendix D
Details on the numerical integration technique

In this appendix, we will shortly describe some details on the numerical integration used to find ρ_{21} for a specific temperature T, Fermi energy ε_F and so on.

The integral to find ρ_{21} is a double integral of q and ω over a square domain, which in the numerical calculation of course always is finite. So even if we in principle have to integrate to infinity we cut of the upper limit(s) of the integral(s). The upper limit in the numerical integration is chosen, so the value of the integral does not change (significantly), when the limit is raised.

The lower limits of the integrals are always zero, so the boundary of the integration domain is the set $\{(q,\omega) \in \mathbb{R}^2 | q = 0 \ \vee \omega = 0\}$. On the line $\omega = 0$ we have the problem of $\sinh^2(\frac{\hbar\omega}{2k_B T}) = 0$ and $F(q,\omega) = 0$, where the ratio has a finite limit value, but a numerical evaluation of the ratio *on* the line $\omega = 0$ does not make sense. The integrand on the $q = 0$ boundary depends on the potential used: finite for the screened potential (chapter **??**) and infinite for the unscreened potential (chapter 4). Therefore we can never explicitly use the $\omega = 0$ boundary and sometimes not the $q = 0$ boundary in the calculation of the integral.

This limits the choice of the numerical integration routine to someone, in which the boundary is not evaluated explicitly in the integration. Such a method is not available as a standard routine in the program MATLAB and the used routine can be found in appendix E. The method of the numerical integration is chosen to be either the midpoint rule or the three point Gauss quadrature rule (see e.g. [128, chap.4]), which both avoid use of the boundary explicitly.

The integrands of ρ_{21} are in no way slowly varying due to the Fermi functions, so one has to be very careful to chose a fine enough grid for the numerical inte-

gration around the points of fast variation. This is done in the program in the following way: First the integral is calculated in the square domain given. Then this domain is divided into four smaller domains and the integral is calculated on each of these smaller domains. If the sum of the four integrals on the smaller domains are within a specified tolerance of the calculated integral on the larger domain, then the calculation ends. If not, each of the smaller domains are divided again and the same procedure is repeated on each of the smaller domains. An example of this procedure is seen on figure D.1. In this example we focus on the integration of ρ_{21} in the quadratic model from eq.(4.43) with constant potential for $\frac{T}{T_{\mathrm{F}}} = 0.2$. The contour plot of the integrant shows that the integration should be carefully done near the origo and near $q = 2k_{\mathrm{F}}$. Compare to the F function for the quadratic model on figure 4.2. On the right of figure D.1 we see how fine a grid is used in the integration. Here each dot represents an calculated domain, i.e. where the dot-density is large, so is the calculated points. In the specific case we see the grid to be very find around $q = 0$ and fine around $q = 2k_{\mathrm{F}}$.

Appendix E
The code for the numerical integration routine

Comments on the routine

QUAD22(f,x,dx,y,dy) determines the integral of the function $f(x, y)$ over the rectangular domain $x < x' < x + dx$ and $y < y' < y + dy$. If x, dx etc are vectors or matrices of the same size indicating integration over several rectangular domains then so is the result.
QUAD22(f,x,dx,y,dy,tol,n) specifies the error tolerance for the integral and the number of quadrature points n in both dimensions. The midpoint rule is used when n is an integer whereas a 3 point Gauss quadrature rule is used when n is the string 'gauss3'. If the tolerance is not met with n points on the domain $[x, d + dx] \times [y, y + dy]$ QUAD22 splits the domain into four subdomains and calls itself on those subdomains.
QUAD22 is vectorized which means that it does not call itself four times (one for each subdomain) but instead it turns x, dx, y and dy into vectors and calls itself once for all four subdomains. This avoids a lot of recursive calls so that MATLAB can concentrate on adding numbers. QUAD22(f,x,dx,y,dy,tol,n,p1,p2,p3,...) specifies additional arguments to f(x,y,p1,p2,p3).

Examples on integrations in MATLAB:

- f = inline('sin(x).*sin(y)','x','y')
  I = quad22(f,0,pi,0,pi,1e-6)
  The result should be 4.
- f = inline('log(z)','z','dummy')
  I=quad22(f,0,1,0,1,1e-4,4)
  The analytical integral of the natural logarithm $\log(x)$ is $x \log(x) - x$ so result for definite integral from 0 to 1 should be -1.
- Use of the program to make plots like figure D.1.
  f = inline('log(k)*log(w)','w','k','a')
  [I,x,y] = quad22(f,0,1,0,1,1e-4,[],20);
  plot(x,y,'.','markersize',1)

The routine

```
function[I,X,Y]=quad22(f,x,dx,y,dy,tol,n,varargin)

if exist('tol') =1|isempty(tol) tol=1e-4; end
```

```
if exist('n') =1|isempty(n) n='gauss3'; end

% Perform quadrature
[i,I,X,Y]=midquad(f,x,dx,y,dy,n,varargin:);

% Determine which domains meet tolerance
ok=(abs(i-I)<tol);

% Refine those domains where tolerance is not met
if any( ok(:))
x=[x( ok); x( ok)+dx( ok)/2; x( ok); x( ok)+dx( ok)/2];
y=[y( ok); y( ok); y( ok)+dy( ok)/2; y( ok)+dy( ok)/2];
dx=[dx( ok)/2; dx( ok)/2; dx( ok)/2; dx( ok)/2];
dy=[dy( ok)/2; dy( ok)/2; dy( ok)/2; dy( ok)/2];

% draw a dot to indicate that we enter a new recursion level
disp('.')

% simple version: don't pick up any quadrature points
if nargout <= 1
I = sum(I(ok))+sum(quad22(f,x,dx,y,dy,tol,n,varargin:));

% Fancy version: collect all quadrature points used for I
else
[I2,X2,Y2] = quad22(f,x,dx,y,dy,tol,n,varargin:);
I = sum(I(ok)) + sum(I2);
X = X(ok,:);
Y = Y(ok,:);
X = [X(:); X2(:)];
Y = [Y(:); Y2(:)];
end
end


function [I,I2,x2,y2] = midquad(f,x,dx,y,dy,n,varargin)
% MIDQUAD quadrature by the midpoint rule.
% [I,I2] = MIDQUAD(f,x1,x2,y1,y2,n) determines the integral of f(x,y) over
% the domain x1 < x < x2 and y1 < y < y2 using n and 2n quadrature points
% in the midpoint rule. The idea is to estimate the error on I as |I - I2|.
% [I3,I6] = MIDQUAD(f,x1,x2,y1,y2,'gauss3') employs a 3 vs. 6 point Gauss
% quadrature rule in stead.
% [I,I2,x,y] = MIDQUAD(...) returns also the positions of the quadrature points
% used which it may be instructive to look at.
```

```
% Quadratre points for line integral
if strcmp(n,'gauss3')
    n = 3;
    % quadrature point positions in interval [−1, 1]
    z=[-0.77459666924148337 0.00000000000000000 0.77459666924148337];
    w=[ 0.55555555555555555 0.88888888888888888 0.55555555555555555];
    z2=[-0.93246951420315202 -0.66120938646626451 -0.23861918608319690 0.23861918608319690
    0.66120938646626451 0.93246951420315202];
    w2=[0.17132449237917034 0.36076157304813860 0.46791393457269104 0.46791393457269104
    0.36076157304813860 0.17132449237917034];
    % we prefer the interval [0,1] so variable changes are made:
    z=(z+1)/2;
    z2=(z2+1)/2;
    w=w/2;
    w2=w2/2;
else
    % midpoint rule quadrature points and weights in interval [0, 1]
    dz = 1/n;
    z = dz/2:dz:1;
    w = repmat(dz,1,n);
    z2 = dz/4:dz/2:1;
    w2 = repmat(dz/2,1,2*n);
end

% make quadrature grid for area integral
z=repmat(z,n,1);
w = w'*w;
z2=repmat(z2,2*n,1);
w2 = w2'*w2;

% number of intervals that that we are integrating
N = length(x(:));

% make quadrature points in x, y space
x2=repmat(x(:),1,4*n*n)+repmat(dx(:),1,4*n*n).*repmat(z2(:)',N,1);
x=repmat(x(:),1,n*n)+repmat(dx(:),1,n*n).*repmat(z(:)',N,1);

% traverse quadrature grid the other way for y:
z=z';
z2 = z2';
y2=repmat(y(:),1,4*n*n)+repmat(dy(:),1,4*n*n).*repmat(z2(:)',N,1);
y=repmat(y(:),1,n*n) + repmat(dy(:),1,n*n).*repmat(z(:)',N,1);
```

```
% evaluate integrand
f2 = feval(f,x2,y2,varargin:);
f=feval(f,x,y,varargin:);

% evaluate integral
I=sum(f.*repmat(w(:)',N,1),2).*dx(:).*dy(:);
I2 = sum(f2.*repmat(w2(:)',N,1),2).*dx(:).*dy(:);
```

I will like to thank Laurits Højgaard Olesen for extensive help with the above code.

Appendix F
The Thomas-Fermi approximation to screening

In this appendix, we consider the Fourier transform of the static screened Coulomb interaction in the Thomas-Fermi approximation following Ref.[6] and generalize there approach for two parallel planes to the case of coaxial cylinders. The result for a different band structure was previously stated (not derived) in [110]. This approach is only valid for large cylinders, i.e. where the quantization in the circumferential direction is close to being continuous.

The simple mental physical picture of screening is that a charged (test) particle is added to a gas of free charged particles and held rigidly at a position $\mathbf{r}_0$. If the free charges and the test particle have opposite charges, the free charges will be attracted to the test particle and thereby reducing (or *screening*) its field especially at large distances (or equivalent small wave vectors). Thereby the name. In any case (as the calculation will show) the other free charges generally changes the particle-particle interaction due to screening process. So screening is a many-body effect.

The semiclassical idea used here is to find the electrical potential $\phi_{\mathbf{r}_0}(\theta, r, z)$ at a point (θ, r, z) stemming from a test charge at $\mathbf{r}_0$ surrounded by some other free charges. Multiplying the obtained electrical potential ϕ with the charge at (θ, r, z) gives the interaction between the test charge and the charge at this point.

The stating point is the Poisson‘s equation (in SI-units),

$$-\nabla^2 \phi_{\mathbf{r}_0}(\theta, r, z) = \frac{\rho(\theta, r, z)}{\kappa}, \tag{F.1}$$

where $\rho(\theta, r, z)$ is the free charge density for all the charges including the test charge, $\kappa = \epsilon_r \epsilon_0$, ϵ_0 is the permittivity of free space and ϵ_r is the dielectric constant (or relative permittivity) of the medium [119]. Here we have taken the medium (i.e. the non-free charges) into account as a linear medium by the factor ϵ_r, which is about 1.4 for carbon nanotubes [120].

We now divide the charge density $\rho(\theta, r, z)$ into a part from the test charge ρ_{test} and a part from the other free charges ρ_{ind}. ρ_{ind} is the induced charge density from the test charge at $\mathbf{r}_0$. Equivalently the potential ϕ is divide into two parts,

$$\phi_{\mathbf{r}_0}(\theta, r, z) = \phi_{\text{test}}(\theta, r, z) + \phi_{\text{ind}}(\theta, r, z) \tag{F.2}$$

each satisfying there own Poisson‘s equation.

In the Thomas-Fermi approximation it is required that the full potential $\phi_{\mathbf{r}_0}(\theta, r, z)$ varies slowly on the scale of many lattice spacings, which makes it possible to include the potential $\phi_{\mathbf{r}_0}(\theta, r, z)$ in the energy for a single particle with charge $\tilde{e}$ by the simple substitution $\varepsilon_{k\nu} \to \varepsilon_{k\nu} + \tilde{e}\phi_{\mathbf{r}_0}(\theta, r, z)$ [1, p.341][18, p.220]. This can be used for the quantum numbers k and ν varying almost continuously as for cylinders with a not to strong circumferential quantization. By

using $\varepsilon_{k\nu} \to \varepsilon_{k\nu} + \tilde{e}\phi_{\mathbf{r}_0}(\theta, r, z)$ we know the charge density before and after the addition of the test particle, since it is simply proportional to the distribution functions. Furthermore in the static case considered here the Fermi functions are the distribution functions. This gives the induced charge density for electrons as:

$$\rho_{\text{ind}}(\theta, r, z) = \frac{(-e)}{2\pi r^c} \sum_{\sigma\nu} \int_{-\frac{\pi}{a}}^{\frac{\pi}{a}} \frac{\mathrm{d}k}{2\pi} \Big[f^0(\varepsilon_{k\nu} - e\phi_{\mathbf{r}_0}(\theta, r, z)) - f^0(\varepsilon_{k\nu}) \Big] \delta(r - r^c), \quad \text{(F.3)}$$

which is the basic equation of the (nonlinear) Thomas-Fermi approximation [1, p.341]. Here we restrict the electrons to on the cylinder with radius r^c by including a delta function in the radial direction[10]. This is completely analogue to the restriction made in the Thomas-Fermi screening calculation for a two dimensional electron gas [121]. Assuming that $\phi_{\mathbf{r}_0}(\theta, r, z)$ is small we linearize to first order in ϕ:

$$\begin{aligned} \rho_{\text{ind}}(\theta, r, z) &\simeq (-e) \frac{1}{2\pi r^c} \sum_{\sigma\nu} \int_{-\frac{\pi}{a}}^{\frac{\pi}{a}} \frac{\mathrm{d}k}{2\pi} (-e) \left(- \frac{\partial f^0(\varepsilon_{k\nu})}{\partial \mu} \right) \phi_{\mathbf{r}_0}(\theta, r, z) \delta(r - r^c) \\ &= -e^2 \frac{\partial n}{\partial \mu} \phi_{\mathbf{r}_0}(\theta, r, z) \delta(r - r^c) \equiv -2\kappa q_{\text{TF}}^{(r^c)} \phi_{\mathbf{r}_0}(\theta, r, z) \delta(r - r^c) \quad \text{(F.4)} \end{aligned}$$

where n is the free electron density, the Thomas-Fermi screening vector $q_{\text{TF}}^{(r^c)}$ was defined and it was used that $\frac{\partial f^0(\varepsilon_{k\nu})}{\partial \varepsilon_{k\nu}} = -\frac{\partial f^0(\varepsilon_{k\nu})}{\partial \mu}$. The factor of two in front of $q_{\text{TF}}^{(r^c)}$ is nothing but a convention.

The test charge at $\mathbf{r}_0 = (\theta_0, r_0, z_0)$ has the density

$$\rho_{\text{test}}(\theta, r, z) = (-e) \frac{\delta(r - r_0)}{r} \delta(\theta - \theta_0) \delta(z - z_0), \quad \text{(F.5)}$$

since by integration over space the charge of an electron $-e$ is obtained.

Now we have the setup to look at the system consisting of two coaxial cylinders (such as a multiwall carbon nanotube) as seen on figure 3.1. We restrict the electrons to be on either the inner or the outer cylinder. Further the coordinate system is chosen such that $\theta_0 = z_0 = 0$. This gives us the Poisson‘s equation

$$\begin{aligned} \nabla^2 \phi_{\mathbf{r}_0}(\theta, r, z) &= -\frac{1}{\kappa} \Big(\rho_{\text{test}} + \rho_{\text{ind},r_1^c} + \rho_{\text{ind},r_2^c} \Big) \quad \text{(F.6)} \\ &= \frac{e}{\kappa} \frac{\delta(r - r_0)}{r} \delta(\theta) \delta(z) + 2q_{\text{TF}}^{(r_1^c)} \phi_{\mathbf{r}_0}(\theta, r, z) \delta(r - r_1^c) + 2q_{\text{TF}}^{(r_2^c)} \phi_{\mathbf{r}_0}(\theta, r, z) \delta(r - r_2^c) \end{aligned}$$

by the use of (F.5) and (F.4) for each of the cylinders. The Laplacian operator ∇^2 in cylindrical coordinates is

$$\nabla^2 = \frac{1}{r} \frac{\partial}{\partial r} + \frac{\partial^2}{\partial r^2} + \frac{1}{r^2} \frac{\partial^2}{\partial \theta^2} + \frac{\partial^2}{\partial z^2}. \quad \text{(F.7)}$$

[10] An alternative approach could be to use some radial wave function with finite width such as in [6, Appendix].

The Poisson's equation (F.6) is now Fourier transformed[11] in the angle θ and in the z coordinate. We cannot Fourier transform in the radius r, since we do not have a symmetry in this direction because of the two shells. The Fourier transformation gives:

$$\left[\frac{1}{r}\frac{\partial}{\partial r}+\frac{\partial^2}{\partial r^2}-\left(\frac{m^2}{r^2}+q^2\right)\right]\phi_{\mathbf{r}_0}(r,m,q)= \\ \frac{e}{\kappa}\frac{\delta(r-r_0)}{r}+2q_{\mathrm{TF}}^{(r_1^c)}\phi_{\mathbf{r}_0}(r,m,q)\delta(r-r_1^c)+2q_{\mathrm{TF}}^{(r_2^c)}\phi_{\mathbf{r}_0}(r,m,q)\delta(r-r_2^c), \quad \text{(F.8)}$$

where for finite cylinder length L

$$\phi_{\mathbf{r}_0}(r,m,q)=\int_0^{2\pi}\mathrm{d}\theta\int_0^L\mathrm{d}z\ e^{-iqz-im\theta}\ \phi_{\mathbf{r}_0}(\theta,r,z). \quad \text{(F.9)}$$

Note that physically q and m are the transferred wave vector and angular momentum, respectively.

To find the Fourier transformed potential we have to solve the second order inhomogeneous differential equation (F.8) in r. To do this we use the Greens function method for ordinary differential equations[12]. Here it is a custom to introduce the linear operator $L(r,m,q)$ and the right hand side of eq.(F.8) as:

$$L(r,m,q)\equiv\frac{1}{r}\frac{\partial}{\partial r}+\frac{\partial^2}{\partial r^2}-\left(\frac{m^2}{r^2}+q^2\right), \quad \text{(F.10)}$$

$$h(r,r_0)\equiv\frac{e}{\kappa}\frac{\delta(r-r_0)}{r}+2q_{\mathrm{TF}}^{(r_1^c)}\phi_{\mathbf{r}_0}(r,m,q)\delta(r-r_1^c)+2q_{\mathrm{TF}}^{(r_2^c)}\phi_{\mathbf{r}_0}(r,m,q)\delta(r-r_2^c),$$

and the Greens function $G(r,\tilde{r})$, which solves the homogeneous version[13] of eq. (F.8):

$$L(r,m,q)G(r,\tilde{r})=\frac{\delta(r-\tilde{r})}{r}, \quad \text{(F.11)}$$

where $\tilde{r}$ is an arbitrarily radius for mathematical use only. If we know the Greens function we can find the potential by:

$$\phi_{\mathbf{r}_0}(r,m,q)=\int_0^\infty\mathrm{d}\tilde{r}\ \tilde{r}G(r,\tilde{r})h(\tilde{r},r_0), \quad \text{(F.12)}$$

which can be seen by use of $L(r,m,q)$ on both sides and use of the defining equation for the Greens function (F.11). Note that we have en extra factor of $\tilde{r}$

[11] The convention used for the angular Fourier transform is for an arbitrary function g: $g(\theta)=\frac{1}{2\pi}\sum_{m\in\mathbb{Z}}g(m)e^{im\theta}$ where $g(m)=\int_0^{2\pi}\mathrm{d}\theta g(\theta)e^{-im\theta}$. The same convention is used for the Fourier transform in the z direction replacing 2π by the cylinder length L [18, Appendix A].

[12] For a good introduction to the subject see [122].

[13] This equation is of cause only homogeneous for $r\neq\tilde{r}$.

in the integral in eq.(F.12), since when we change from cartesian coordinates to cylindrical the Jacobian matrix is r.

The Greens function is now found in order to get the potential. Since $\phi_{\mathbf{r}_0}(\theta, r, z)$ is real the Fourier transformed obeys $\phi_{\mathbf{r}_0}(r, m, -q) = \phi^*_{\mathbf{r}_0}(r, m, q)$. Therefore it is sufficient to take $q > 0$ in the following. Introducing $\xi \equiv qr$ ($\tilde{\xi} \equiv q\tilde{r}$) in eq.(F.11) and multiplying both sides of it by r^2 it is:

$$\left[\xi\frac{\partial}{\partial\xi} + \xi^2\frac{\partial^2}{\partial\xi^2} - \left(m^2 + \xi^2\right)\right] G\left(\frac{\xi}{q}, \frac{\tilde{\xi}}{q}\right) = \tilde{\xi}\delta(\xi - \tilde{\xi}). \tag{F.13}$$

For $\xi \neq \tilde{\xi}$ this is the Bessel's modified differential equation [123, p.138], where the general solution is a linear combination of the modified Bessel's functions of the first kind $\mathrm{I}_m(\xi)$ and of the second kind $\mathrm{K}_m(\xi)$ both of order m. To solve (F.13) we take the constants of this linear combination and make them functions of $\tilde{\xi}$, so[14]

$$G(\xi, \tilde{\xi}) = A(\tilde{\xi})\mathrm{I}_m(\xi) + B(\tilde{\xi})\mathrm{K}_m(\xi), \tag{F.14}$$

where $A(\tilde{\xi})$ and $B(\tilde{\xi})$ are these functions determent by the boundary conditions. The boundary conditions for the potential are by physical grounds found to be:

$$\phi_{\mathbf{r}_0}(r, q, m) \to 0 \quad \text{for} \quad r \to \infty, \tag{F.15}$$

$$|\phi_{\mathbf{r}_0}(r, q, m)| < \infty \quad \text{for} \quad r \to 0. \tag{F.16}$$

If $G(r, \tilde{r})$ obeys the same boundary conditions, then so will the potential. This can be seen from eq.(F.12) if we assume the integral to be finite for all r. The same boundary conditions for the potential and the Greens functions is therefore used. The limits of the modified Bessel's functions are:

$$|\mathrm{I}_m(x)| < \infty \quad \text{and} \quad \mathrm{K}_m(x) \to \infty \qquad \text{for} \qquad x \to 0, \tag{F.17}$$

$$\mathrm{I}_m(x) \to \infty \quad \text{and} \quad \mathrm{K}_m(x) \to 0 \qquad \text{for} \qquad x \to \infty \tag{F.18}$$

and by the help of these limits and boundary conditions for G we have an educated guess for the Greens function:

$$\text{(Guess)} \qquad G(r, \tilde{r}) = \begin{cases} A\mathrm{I}_m(qr)\mathrm{K}_m(q\tilde{r}) & \text{for } r \leqslant \tilde{r} \\ B\mathrm{I}_m(q\tilde{r})\mathrm{K}_m(qr) & \text{for } r > \tilde{r} \end{cases}, \tag{F.19}$$

where A and B now are constants.

To show that this is the solution and to find A and B we have to do three things. First of all we note that for $r \neq \tilde{r}$ the guess (F.19) fulfills eq.(F.11), since both Bessel's functions satisfies Bessel's modified differential equation. Secondly we require $G(r, \tilde{r})$ to be continues at $r = \tilde{r}$, since $\tilde{r}$ was just a arbitrary radius. This gives $A = B$. Thirdly the derivative of $G(r, \tilde{r})$ with respect to r

[14]The factor of $\frac{1}{q}$ is dropped in the notation in the arguments of G.

at $\tilde{r}$, $\frac{\partial G(r,\tilde{r})}{\partial r}\Big|_{r=\tilde{r}}$, has to have the same discontinuity as obtained by integrating eq.(F.11). This will give the constant A. By integrating the right hand side of eq.(F.11) for any interval around $\tilde{r}$ (again using the mesh $\mathrm{d}r\ r$) 1 is obtained. The left hand side integrated around $\tilde{r}$ is:

$$\lim_{\varepsilon\to 0^+}\int_{\tilde{r}-\varepsilon}^{\tilde{r}+\varepsilon}\mathrm{d}r\ r\left[\frac{1}{r}\frac{\partial}{\partial r}+\frac{\partial^2}{\partial r^2}-\left(\frac{m^2}{r^2}+q^2\right)\right]G(r,\tilde{r})=$$
$$\lim_{\varepsilon\to 0^+}\int_{\tilde{r}-\varepsilon}^{\tilde{r}+\varepsilon}\mathrm{d}r\ r\frac{\partial^2 G(r,\tilde{r})}{\partial r^2}=\tilde{r}\lim_{\varepsilon\to 0^+}\left[\frac{\partial G(r,\tilde{r})}{\partial r}\Big|_{r=\tilde{r}+\varepsilon}-\frac{\partial G(r,\tilde{r})}{\partial r}\Big|_{r=\tilde{r}-\varepsilon}\right]=1, \quad \text{(F.20)}$$

where the continuity of $G(r,\tilde{r})$ at $r=\tilde{r}$ was used in the first equality and a partial integration was done in the second equality. This can be compared to the result obtained from the guessed Greens function (F.19):

$$\lim_{\varepsilon\to 0^+}\left[\frac{\partial G(r,\tilde{r})}{\partial r}\Big|_{r=\tilde{r}+\varepsilon}-\frac{\partial G(r,\tilde{r})}{\partial r}\Big|_{r=\tilde{r}-\varepsilon}\right]=$$
$$Aq\left(\mathrm{I}_m(q\tilde{r})\frac{\partial \mathrm{K}_m(x)}{\partial x}\Big|_{x=q\tilde{r}}-\mathrm{K}_m(q\tilde{r})\frac{\partial \mathrm{I}_m(x)}{\partial x}\Big|_{x=q\tilde{r}}\right)=-A\frac{1}{\tilde{r}}, \quad \text{(F.21)}$$

where the last equality stems from connections between the Bessel functions. By comparison of eq.(F.20) and eq.(F.21) we have that $A=-1$ and therefore our guessed Greens function (F.19) is the right one[15]:

$$G(r,\tilde{r})=\begin{cases}-\mathrm{K}_m(q\tilde{r})\mathrm{I}_m(qr) & \text{for } r\leqslant\tilde{r}\\ -\mathrm{I}_m(q\tilde{r})\mathrm{K}_m(qr) & \text{for } r>\tilde{r}\end{cases}. \quad \text{(F.22)}$$

Now it is straight forward to get the Fourier transformed potential from a test charge for a general radius r:

$$\phi_{\mathbf{r}_0}(r,m,q)=\int_0^\infty \mathrm{d}\tilde{r}\ \tilde{r}G(r,\tilde{r})h(\tilde{r},r_0) \quad \text{(F.23)}$$
$$=\frac{e}{\kappa}G(r,r_0)+2q_{\mathrm{TF}}^{(r_1^c)}r_1^c\phi_{\mathbf{r}_0}(r_1^c,m,q)G(r,r_1^c)+2q_{\mathrm{TF}}^{(r_2^c)}r_2^c\phi_{\mathbf{r}_0}(r_2^c,m,q)G(r,r_2^c),$$

which is a expressed in terms of the potential at the two cylinders. To find these two potential values we can insert $r=r_1^c$ and $r=r_2^c$ in eq.(F.23) and thereby get two equations with two unknowns, which is easily solved to give:

$$\begin{pmatrix}\phi_{\mathbf{r}_0}(r_2^c,m,q)\\ \phi_{\mathbf{r}_0}(r_1^c,m,q)\end{pmatrix}=$$
$$\frac{-e}{\kappa\Delta}\begin{pmatrix}-1+2q_{\mathrm{TF}}^{(r_1^c)}r_1^cG(r_1^c,r_1^c) & -2q_{\mathrm{TF}}^{(r_1^c)}r_1^cG(r_2^c,r_1^c)\\ -2q_{\mathrm{TF}}^{(r_2^c)}r_2^cG(r_1^c,r_2^c) & -1+2q_{\mathrm{TF}}^{(r_2^c)}r_2^cG(r_2^c,r_2^c)\end{pmatrix}\begin{pmatrix}G(r_2^c,r_0)\\ G(r_1^c,r_0)\end{pmatrix} \quad \text{(F.24)}$$

[15]The Greens function stated here has an opposite (but right) sign of the Greens function stated in [110].

where

$$\Delta = \Big[-1 + 2q_{\mathrm{TF}}^{(r_1^c)} r_1^c G(r_1^c, r_1^c) \Big] \times \Big[-1 + 2q_{\mathrm{TF}}^{(r_2^c)} r_2^c G(r_2^c, r_2^c) \Big] - 4q_{\mathrm{TF}}^{(r_1^c)} q_{\mathrm{TF}}^{(r_2^c)} r_1^c r_2^c G(r_1^c, r_2^c) G(r_2^c, r_1^c). \quad \text{(F.25)}$$

This could now be inserted into eq.(F.23) and the potential at a general radius would be obtained. Since we do only need a potential energy for electron-electron interaction on the two different cylinders, we choose the radius to be one of the cylinders and the test charge to be on the other one. In this way we get the potential from one electron on one of the cylinders felt by another electron on the other cylinder. Therefore we chose $r_0 = r_1^c$ and $r = r_2^c$:

$$\phi_{r_1^c}(r_2^c, m, q) = \frac{(-e)}{\kappa \Delta} \mathrm{I}_m(q r_2^c) \mathrm{K}_m(q r_1^c). \quad \text{(F.26)}$$

Note that the same result is obtained by choosing $r_0 = r_2^c$ and $r = r_1^c$ as it should be, since the electron-electron interaction should not dependent on which electron we imagine to be a test charge. To get the potential energy $V_{12}(r_1^c, r_2^c, q, m)$ we just need to multiply $\phi_{r_1^c}(r_2^c, m, q)$ by $(-e)$.

By setting $q_{\mathrm{TF}}^{(r_i^c)} = 0$ we can identify the unscreened potential[16] $V_{12}^0(r_1^c, r_2^c, q, m)$ and the dielectric function in the static limit as $\Delta = \varepsilon^{\mathrm{TF}}(q)$. The Fourier transform of the screened Coulomb interaction $V_{12}(r_1^c, r_2^c, q, m)$ is therefore:

$$V_{12}(r_1^c, r_2^c, q, m) = \frac{V_{12}^0(r_1^c, r_2^c, q, m)}{\varepsilon^{\mathrm{TF}}(q)}, \quad \text{(F.27)}$$

$$V_{12}^0(r_1^c, r_2^c, q, m) = \frac{e^2}{\kappa} \mathrm{K}_m(q r_1^c) \mathrm{I}_m(q r_2^c), \quad \text{(F.28)}$$

$$\varepsilon^{\mathrm{TF}}(q) = \big[1 + 2q_{\mathrm{TF}}^{(r_1^c)} r_1^c \mathrm{K}_m(q r_1^c) \mathrm{I}_m(q r_1^c)\big] \big[1 + 2q_{\mathrm{TF}}^{(r_2^c)} r_2^c \mathrm{K}_m(q r_2^c) \mathrm{I}_m(q r_2^c)\big] - 4q_{\mathrm{TF}}^{(r_1^c)} q_{\mathrm{TF}}^{(r_2^c)} r_1^c r_2^c \big[\mathrm{K}_m(q r_1^c) \mathrm{I}_m(q r_2^c)\big]^2. \quad \text{(F.29)}$$

Remembering from eq.(F.4) that the Thomas-Fermi screening vector is:

$$2q_{\mathrm{TF}}^{(r_i^c)} = \frac{e^2}{\kappa} \frac{\partial n_i}{\partial \mu}. \quad \text{(F.30)}$$

For the armchair-like and zigzag-like tubes the Thomas-Fermi vector is the same using the approximation $\mu \simeq \varepsilon_{\mathrm{F}}$ and the densities eq.(5.18) and eq.(**??**):

$$2q_{\mathrm{TF}}^{(r_i^c)} = \frac{e^2}{\kappa} \frac{\partial n}{\partial \varepsilon_{\mathrm{F}}} = \frac{e^2}{\kappa} \frac{2}{\pi^2 r_i^c \hbar v_0}, \quad \text{(F.31)}$$

[16] This potential was previously found in [124] and [125] with different prefactors of 4π, since the calculation was done using Gaussian units.

so the dimensionless quantity $2q_{\rm TF}^{(r_1^c)}r_1^c = 2q_{\rm TF}^{(r_2^c)}r_2^c \equiv \mathfrak{s}$ is tube independent in our model.

We consider the static limit $\omega \to 0$ and show that the RPA interaction simplifies to the Thomas-Fermi interaction. For small q and $\omega \to 0$ the polarizability eq.(5.12) for both zigzag and armchair tubes is:

$$\chi(q,0) = \frac{1}{2\pi}\frac{-8\gamma_0(qa)^2}{a\pi\sqrt{3}(\gamma_0 qa)^2} = -\frac{2}{\pi^2\hbar v_0} = -\frac{\kappa}{e^2}2q_{\rm TF}^{(r_i^c)}r_i^c \tag{F.32}$$

independent of $i = 1, 2$. Therefore $\varepsilon^{\rm RPA}(\mathbf{q}, 0) = \varepsilon^{\rm TF}(\mathbf{q})$ for small q from eq.(5.9) and eq.(F.29), so the screened interactions are the same in the static small q limits as it should be.

Appendix G
Conference contribution to HCIS13

This article is accepted for publication in *Semiconductor Science and Technology* in 2004 in a special conference proceedings issue from the "International Conference on Nonequilibrium Carrier Dynamics in Semiconductors" (HCIS13).

It is basically a summery of my talk given at HCIS13 on the 31. of July 2003 in Modena, Italy.

Note that the thesis contains the g-factors from the band structure in the Coulomb matrix element, which were not included in this article. Figure G.1 is the one mentioned but not given in the article.

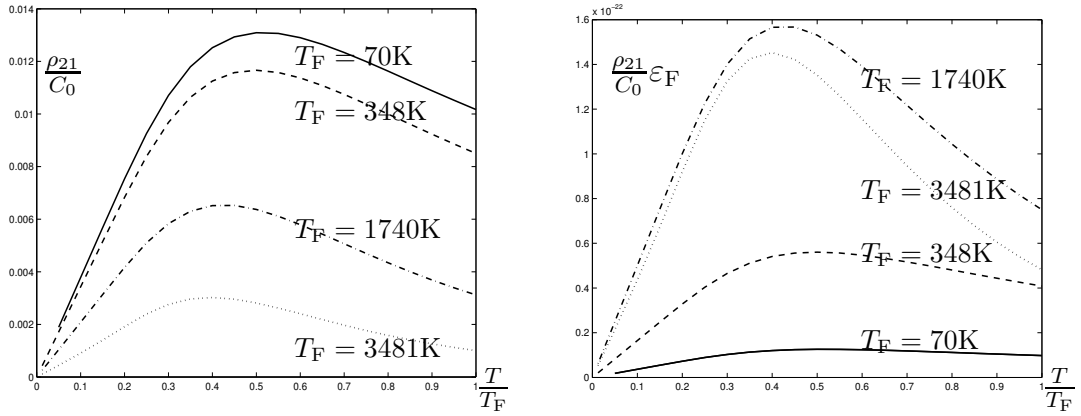

Figure G.1: ρ_{21} as a function of $\frac{T}{T_F}$ for different ε_F values: $\varepsilon_F = 0.3$eV (3481K) (dotted), $\varepsilon_F = 0.15$eV (1740K) (dashed-dotted), $\varepsilon_F = 0.03$eV (348K) (dashed) and $\varepsilon_F = 0.006$eV (70K) (full line). It is seen that ρ_{21} has a peak as a function of temperature for all the chosen ε_F. The value of $\frac{T}{T_F}$ at the peak is roughly the same, even though it might have a slight tendency to decrease as a function of ε_F. Since T_F is not the same for the different graphs this conclusion is not true as a function of temperature. C_0 and C_ρ (in figure 2 in the article) is connected by: $C_0 = c_\rho \varepsilon_F$.

CE: KR

INSTITUTE OF PHYSICS PUBLISHING SEMICONDUCTOR SCIENCE AND TECHNOLOGY

Semicond. Sci. Technol. **19** (2004) 1–3 PII: S0268-1242(04)72025-8

Coulomb drag in multiwall armchair carbon nanotubes

Anders Mathias Lunde[1,2] **and Antti-Pekka Jauho**[2]

[1] Niels Bohr Institute, Ørsted Laboratory, University of Copenhagen, DK-2100 Copenhagen, Denmark

[2] Mikroelektronik Centret, Technical University of Denmark, Ørsteds Plads, Bldg 345 East, DK-2800 Kgs. Lyngby, Denmark

E-mail: aml@mic.dtu.dk

Received
Published DD MMM 2003
Online at stacks.iop.org/SST/19/1 (DOI: 10.1088/0268-1242/19/0/000)

Abstract

We calculate the transresistivity ρ_{21} between two concentric armchair nanotubes in a diffusive multiwall carbon nanotube as a function of temperature T and Fermi level ε_F. We approximate the tight-binding band structure by two crossing bands with a linear dispersion near the Fermi surface. The cylindrical geometry of the nanotubes and the different parities of the Bloch states are accounted for in the evaluation of the effective Coulomb interaction between charges in the concentric nanotubes. We find a broad peak in ρ_{21} as a function of temperature at roughly $T \sim 0.4T_F$. Further, we predict a peak in ρ_{21} as a function of ε_F, which can be studied experimentally by changing a gate voltage or by doping.

The phenomenon of Coulomb drag [1] concerns momentum exchange between two spatially separated subsystems with independent contacts. Thus, a current J_1 through one subsystem induces a current J_2, or an electric field E_2, in the other subsystem due to the Coulomb interaction between the mobile charges. A convenient object to study both experimentally and theoretically is the transresistivity, defined as $\rho_{21} = E_2/J_1$. Following the initial experiments by Gramila *et al* [2], Coulomb drag has been investigated intensively for parallel bulk 2D systems (for a recent review, see [3]) and has recently been extended to the mesoscopic regime [4].

Here we consider two coaxial armchair carbon nanotubes (a multiwall carbon nanotube) with independent contacts on an inner and an outer nanotube. This configuration is a challenging but not an impossible technological achievement [5, 6]. It is further assumed that there is no tunnelling between the different tubes, labelled by 1 (outer) and 2 (inner). We work within the Fermi liquid picture, and generalize the formalism developed to study Coulomb drag in coupled quantum wells [7–9] to a multi-subband system.

To derive the transresistivity ρ_{21} coupled linearized Boltzmann equations in the limit of weak intertube interaction and small external electric field E_1 on the outer nanotube can be used [8]. This approach uses the Fermi Golden rule to model the Coulomb scattering process between the electrons in the two nanotubes. Alternatively, the Kubo formula can be used [10]. Neglecting Umklapp processes one arrives at

$$\rho_{21} = \frac{\hbar^2}{8\pi^4 r_2^c e^2 n_1 n_2 k_B T} \sum_{\nu_1\nu_1'\nu_2\nu_2'} \int_0^{\frac{\pi}{a}} \frac{dq}{2\pi} \int_0^{\infty} d\omega \times \frac{|V_{12}(q,\omega,\nu_1\nu_2,\nu_1'\nu_2')|^2}{\sinh^2\left(\frac{\hbar\omega}{2k_BT}\right)} F^{(1)}_{\nu_1\nu_1'}(q,\omega) F^{(2)}_{\nu_2\nu_2'}(q,\omega), \quad (1)$$

where ν_i (ν_i') are the band indices before (after) the scattering, $V_{12}(q,\omega,\nu_1\nu_2,\nu_1'\nu_2')$ the Coulomb matrix element (apart from a normalization factor $1/2\pi L$), $a = 0.249$ nm the lattice spacing, r_i^c the tube radius, n_i the conduction electron density, $\hbar q$ the momentum transfer, $\hbar\omega$ the energy transfer and

$$F^{(i)}_{\nu_i\nu_i'}(q,\omega) \equiv \frac{2\pi(-e)}{\hbar\mu^{(i)}_{Tr}} \int_{-\frac{\pi}{a}}^{\frac{\pi}{a}} \frac{dk_i}{2\pi} \left[f^0\left(\varepsilon_{k_i\nu_i}\right) - f^0\left(\varepsilon_{k_i+q\nu_i'}\right)\right] \times \tau_i \left[v_{k_i+q\nu_i'} - v_{k_i\nu_i}\right] \delta\left(\varepsilon_{k_i\nu_i} - \varepsilon_{k_i+q\nu_i'} - \hbar\omega\right), \quad (2)$$

where $v_{k\nu} = \frac{1}{\hbar}\frac{\partial\varepsilon_{k\nu}}{\partial k}$ is the band velocity, $f^0(\varepsilon)$ the Fermi function, τ_i the single tube relaxation-time from single tube impurity scattering and $\mu^{(i)}_{Tr}$ is the single tube mobility defined through $J = (-e)n\mu_{Tr}E$ for an isolated tube. (The F functions are generalizations of the imaginary part of the susceptibility.) Note that the transresistance is $R_{21} = \rho_{21}\frac{L}{2\pi r_1^c}$, where L is the length of the tubes (assuming that $L_1 = L_2 \equiv L$).

An armchair nanotube has a discrete translational symmetry, discrete rotational symmetry and a mirror plane along the tube axis, which gives rise to single-particle Bloch

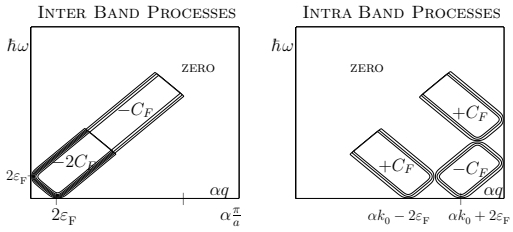

Figure 1. Contour plot of $F_{\text{inter}}(q,\omega)$ and $F_{\text{intra}}(q,\omega)$. The broadening is due to Fermi functions at finite temperature (here $T/T_F = 0.1$).

states labelled by a (crystal) wave vector k along the tube, (crystal) angular momentum m and a parity $\Pi = \pm 1$ in the angle θ in cylindrical coordinates (θ, r, z), respectively [11]. The two bands near ε_F for an armchair nanotube both have $m = 0$, so effectively the band index for these two bands are only $\nu = \Pi = \pm 1$. In a tight-binding calculation the bands near ε_F are of the form [11]: $\varepsilon_{k\Pi} = \Pi\gamma_0\big(1-2\cos\big(\frac{ka}{2}\big)\big)$, where $\gamma_0 = 3$ eV is an overlap integral and $\varepsilon_F = 0$ for a non-doped and non-gated tube. We take ε_F as a parameter, which can vary between ± 0.3 eV. Furthermore we linearize the bands around $\varepsilon_F = 0$, so we use $\varepsilon_{k\Pi} \simeq \Pi\alpha(|k| - k_0)$ in all calculations, where $\alpha = \frac{\sqrt{3}}{2}\gamma_0 a$ and $k_0 = \frac{2\pi}{3a}$.

We next address the calculation of the Coulomb matrix element $V_{12}(q,\omega,\nu_1\nu_2,\nu_1'\nu_2')$ needed in (1). One needs the parity eigenstates and the screened Coulomb interaction, which depends only on the distance $|\mathbf{r_1} - \mathbf{r_2}|$, so it is even in $\theta_1 - \theta_2$. This fact reduces the number of possibly non-zero matrix elements by a factor of 2, since by using the variable change $\theta_i \to -\theta_i$ $(i = 1, 2)$ in the matrix element one can show: $\langle k_1'k_2'\nu_1'\nu_2'|V_{12}(|\mathbf{r_1} - \mathbf{r_2}|)|k_1k_2\nu_1\nu_2\rangle = \nu_1'\nu_1\nu_2'\nu_2\langle k_1'k_2'\nu_1'\nu_2'|V_{12}(|\mathbf{r_1} - \mathbf{r_2}|)|k_1k_2\nu_1\nu_2\rangle$, i.e. the product of the parities is conserved in the collision. This is the only symmetry property of the Bloch states we use and, for simplicity, we take the single-particle states to be plane waves $\frac{1}{\sqrt{2\pi L}}\,\mathrm{e}^{im\theta+ikz}$, even though these are not parity eigenstates. Thus we find

$$\begin{aligned}&\langle k_1'k_2'\nu_1'\nu_2'|V_{12}(|\mathbf{r_1} - \mathbf{r_2}|)|k_1k_2\nu_1\nu_2\rangle\\ &= \frac{1}{2\pi L}\delta_{\nu_1\nu_2,\nu_1'\nu_2'}\delta_{k_1+k_2,k_1'+k_2'}\delta_{m_1+m_2,m_1'+m_2'}\\ &\quad\times V_{12}\big(q = k_1' - k_1, m = m_1' - m_1 = 0, r_1^c, r_2^c\big),\end{aligned} \tag{3}$$

where $V_{12}(q, m, r_1^c, r_2^c)$ is the Fourier transform of the screened Coulomb interaction. Screening is treated in the Thomas–Fermi approximation, where we take into account the cylindrical geometry of the tubes. One finds

$$V_{12}\big(q, m, r_1^c, r_2^c\big) = \frac{e^2}{\epsilon_r\epsilon_0}\frac{K_m\big(qr_1^c\big)I_m\big(qr_2^c\big)}{\varepsilon^{\text{TF}}(q)} \tag{4}$$

where the dielectric function is $\varepsilon^{\text{TF}}(q) = \big[1 + 2q_{\text{TF}}^{(r_1^c)}r_1^cK_m\big(qr_1^c\big)I_m\big(qr_1^c\big)\big]\big[1+2q_{\text{TF}}^{(r_2^c)}r_2^cK_m\big(qr_2^c\big)I_m\big(qr_2^c\big)\big] - 4q_{\text{TF}}^{(r_1^c)}q_{\text{TF}}^{(r_2^c)}r_1^cr_2^c\big[K_m\big(qr_1^c\big)I_m\big(qr_2^c\big)\big]^2$ with $q_{\text{TF}}^{(r_i^c)} = \frac{e^2}{2\epsilon_r\epsilon_0}\frac{\mathrm{d}n_i}{\mathrm{d}\varepsilon_F} = \frac{e^2}{\epsilon_r\epsilon_0\pi^2r_i^c\alpha}\cdot I_m$ and K_m are modified mth order Bessel functions of the first and second kind, respectively.

The $F^{(i)}_{\nu_i\nu_i'}$ functions (2) are independent of the subsystem, basically because the two energy bands near ε_F are radius independent in armchair nanotubes. Recalling (3), the sum over the band indices in (1) thus gives a factor $(F_{+-} + F_{-+})^2 + (F_{++} + F_{--})^2 \equiv (F_{\text{inter}})^2 + (F_{\text{intra}})^2$ in the integrand of ρ_{21}. The F-functions for inter and intra band scatterings, respectively, are shown in figure 1. Since the integrand of ρ_{21} has two decreasing functions, V_{12} and $\sinh^{-2}\big(\frac{\hbar\omega}{2k_BT}\big)$ as a function of q and ω, respectively, the inter band processes are by far the most important. From (2) we explicitly find

$$\begin{aligned}F_{\text{inter}}(q,\omega) &= C_F\{\Theta(-\hbar\omega - \alpha q + \alpha k_0)\\ &\quad + \Theta(\hbar\omega - \alpha q + \alpha k_0)\Theta(-\hbar\omega - \alpha q + 2\alpha k_0)\}\\ &\quad\times[f^0(\varepsilon_1) - f^0(-\varepsilon_2) - f^0(\varepsilon_2) + f^0(-\varepsilon_1)],\end{aligned} \tag{5}$$

where $\varepsilon_1 = \frac{1}{2}(\hbar\omega+\alpha q)$, $\varepsilon_2 = \frac{1}{2}(\hbar\omega-\alpha q)$ and $C_F = \frac{2\varepsilon_F+\alpha\pi/a}{2\alpha^2}$. A similar expression is obtained for F_{intra}. At $\varepsilon_F = 0$ both the inter and intra band contributions are zero, which is seen by using $f^0_{-\mu}(\varepsilon) = 1 - f^0_\mu(-\varepsilon)$($\mu$ being the chemical potential used in the approximation $\mu \simeq \varepsilon_F$), i.e. $\rho_{21}|_{\varepsilon_F=0} = 0$. Physically this is due to particle–hole symmetry.

Including all these considerations ρ_{21} in (1) yields

$$\begin{aligned}\rho_{21} &= C\int_0^{\frac{\pi}{a}}\mathrm{d}q\int_0^\infty\mathrm{d}\omega\frac{\big|V_{12}\big(q,0,r_1^c,r_2^c\big)\big|^2}{\sinh^2\big(\frac{\hbar\omega}{2k_BT}\big)}\\ &\quad\times[F_{\text{inter}}(q,\omega)^2 + F_{\text{intra}}(q,\omega)^2],\end{aligned} \tag{6}$$

where $C = \frac{\hbar^2}{16\pi^5r_2^2n_1n_2k_BT}$.

Figure 2 shows our numerical results for the transresistivity ρ_{21} as a function of Fermi level ε_F and temperature T.

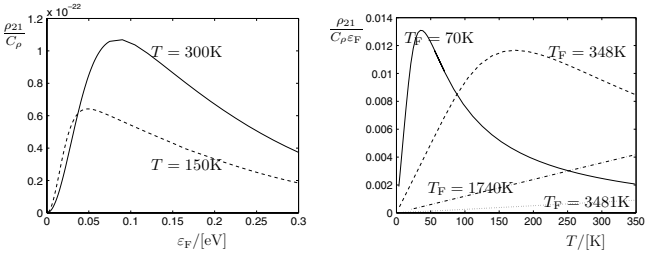

Figure 2. Transresistivity ρ_{21} as a function of the Fermi level ε_F (left) and as a function of the temperature (right) for a (5,5) tube in a (10,10) tube. The constant is $C_\rho = \frac{\hbar e^2r_1^c}{24\sqrt{3}\pi(\epsilon_r\epsilon_0)^2\gamma_0^2a^3}$ and for a 1 μm long tube system the transresistance at the peak for $T = 300$ K is $R_{21} = 1.4\,\text{k}\Omega$.

The interplay between the F functions (figure 1) and the matrix element shows that the most important process in the drag is the small q backscattering inter band process with energies around ε_F, e.g. the process with scattering between $k_0 \pm \frac{\varepsilon_F}{\alpha}$ in both tubes. The higher the Fermi level the larger the transferred wave vector q and thereby the smaller the Coulomb interaction (4), which makes ρ_{21} go down at high ε_F. On the other hand, at $\varepsilon_F = 0$ we have particle–hole symmetry (where ρ_{21} is zero) and a finite ε_F leads to a finite ρ_{21}. Thus ρ_{21} must have a peak as a function of ε_F, as also revealed by the numerical calculation showed in figure 2.

As a function of temperature, our calculations show a peak for small Fermi temperatures T_F, which is broader the larger T_F. A plot as a function of T/T_F (not shown) reveals that all $\rho_{21}(T_F)$ have a peak at $T/T_F \sim 0.4$. ρ_{21} decays at higher temperatures since the temperature smearing of the Fermi level causes the situation to be closer to the particle–hole situation at $\varepsilon_F = 0$ than at low temperature.

We expect other metallic nanotubes (e.g. zigzag) to show similar behaviour since these will have two linear bands crossing the Fermi level for a non-gated nanotube at the same point, so a similar situation is obtained.

In summary, we have investigated the Coulomb drag effect in coaxial armchair carbon nanotubes, where the important process for the drag is inter band backscattering with small transferred crystal wave vector. We found a peak in the transresistivity as a function of Fermi level (gate voltage) and temperature. For free (i.e. $\varepsilon_F = 0$) armchair nanotubes the drag vanishes due to the particle–hole symmetry.

Acknowledgment

We thank T Vuković and M Brandbyge for helpful comments on the nanotube band structure, L H Olesen for help on the numerical integration routines and P Hakonen, P Bøggild and J Nygård for discussions on the experimental realization.

References

[1] Pogrebinskii M B 1977 *Fiz. Tekh. Poluprovodn.* **11** 637
Pogrebinskii M B 1977 *Sov. Phys. Semicond.* **11** 372
Price P J 1983 *Physica* B and C **117** 750
[2] Gramila T J, Eisenstein J P, MacDonald A H, Pfeiffer L N and West K W 1991 *Phys. Rev. Lett.* **66** 1216
[3] Rojo A G 1999 *J. Phys.: Condens. Matter* **11** R31
[4] Narozhny B N and Aleiner I L 2000 *Phys. Rev. Lett.* **84** 5383
Mortensen N A, Flensberg K and Jauho A-P 2001 *Phys. Rev. Lett.* **86** 1841
[5] Hakonen P, Nygård J and Bøgglid P Private communication
[6] Collins P G, Arnold M S and Avouris P 2001 *Science* **292** 706
[7] Jauho A-P and Smith H 1993 *Phys. Rev.* B **47** 4420
[8] Flensberg K and B Y-K Hu 1995 *Phys. Rev.* B **52** 14796
[9] Alkauskas A *et al* 2002 *Phys. Rev.* B **66** 201304(R)
[10] Flensberg K, B Y-K Hu, Jauho A-P and Kinaret J 1995 *Phys. Rev.* B **52** 14761
[11] Vuković T, Milošević I and Damnjanović M 2002 *Phys. Rev.* B **65** 045418
Damnjanović M, Vuković T and Milošević I 2000 *Solid state Commun.* **116** 265
Damnjanović M, Milošević I, Vuković T and Sredanović R 1999 *Phys. Rev.* B **60** 2728

Appendix H
Poster contribution to DFS 2003

This poster was presented at The Danish Physical Society annual meeting on the 12. of June 2003, Nyborg, Denmark.

It represents some early results of my work.

Coulomb Drag in Multiwall Carbon Nanotubes

Anders Mathias Lunde[†,‡,*] and Antti-Pekka Jauho[‡]

[†] *Niels Bohr Institute, Ørsted Laboratory, University of Copenhagen, DK-2100 Copenhagen, Denmark*

[‡] *Mikroelektronik Centret, Technical University of Denmark, Ørsteds Plads, Bldg. 345 east, DK-2800 Kgs. Lyngby, Denmark*

*Email:lunan@fys.ku.dk

The Basic Task

If a current I_1 is sent though an outer nanotube in a multiwall carbon nanotube and one measures the voltage V_2 independently on an inner nanotube, what is then obtained? This is the basic task, i.e. to find the transresistivity $\rho_{21} = \frac{E_2}{J_1}$ as a function of temperature, when the inner and outer nanotubes are armchair nanotubes.

The Microscopic Picture

How does the voltage in the inner nanotube V_2 appear, when tunneling between the different nanotubes is neglected? The electrons carrying the current I_1 transfer momentum $q = k_1' - k_1$ along the tube to the electrons in the other nanotubes via there **electron-electron screened Coulomb interaction**, which makes a *drag* current in the inner nanotube. This in terms builds up a voltage V_2. Thereby the name **Coulomb drag**[1]. Furthermore the electrons scatter between different energy bands denoted by ν. The two energy bands near the Fermi surface for an armchair carbon nanotube have zero angular momentum along the tube and different **parity** for the z-component for the wave function, i.e. $\nu = \pm 1$ is parity.

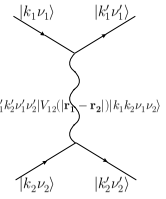

Basic assumptions

- The **Fermi liquid** picture is used.
- **Armchair Carbon nanotubes** are used, which gives simple selection rules and radius independent energy bands.
- The energy bands are approximated by **linear energy bands**.

The transresistivity model

In the limit of weak intertube interaction and small external electric field E_1 on the outer nanotube one gets the following **coupled linearized Boltzmann equations** for the non-equilibrium distribution functions $f_i(k_i, \nu_i)$ $(i = 1, 2)$:

$$\frac{(-e)E_1}{\hbar}\frac{\partial f^0(\varepsilon_{k_1,\nu_1})}{\partial k_1} = -\frac{f_1(k_1,\nu_1) - f^0(\varepsilon_{k_1,\nu_1})}{\tau_1}$$
$$\frac{(-e)E_2}{\hbar}\frac{\partial f^0(\varepsilon_{k_2,\nu_2})}{\partial k_2} = -\frac{f_2(k_2,\nu_2) - f^0(\varepsilon_{k_2,\nu_2})}{\tau_2} + S[f_1, f_2 = f^0](k_2,\nu_2)$$

where $f^0(\varepsilon)$ is the Fermi function and $S[f_1, f_2 = f^0]$ is the **linearized collision integral**,

$$S[f_1, f_2 = f^0](k_2,\nu_2) \propto \sum_{\nu_1,\nu_1',\nu_2'} \int_{-\frac{\pi}{a}}^{\frac{\pi}{a}} \mathrm{d}k_1 \mathrm{d}k_1' \mathrm{d}k_2' \quad |\langle k_1'k_2'\nu_1'\nu_2'|V_{12}(|\mathbf{r}_1 - \mathbf{r}_2|)|k_1k_2\nu_1\nu_2\rangle|^2$$
$$\times f^0(\varepsilon_{k_1,\nu_1}) f^0(\varepsilon_{k_2,\nu_2})(1 - f^0(\varepsilon_{k_1',\nu_1'}))(1 - f^0(\varepsilon_{k_2',\nu_2'}))$$
$$\times [\psi_{k_1,\nu_1} - \psi_{k_1',\nu_1'}]\delta(\varepsilon_{k_1,\nu_1} + \varepsilon_{k_2,\nu_2} - \varepsilon_{k_1',\nu_1'} - \varepsilon_{k_1',\nu_1'})$$

where the deviation from equilibrium $\psi(k,\nu)$ was defined though $f(k,\nu) - f^0(\varepsilon_{k,\nu}) \equiv f^0(\varepsilon_{k,\nu})(1 - f^0(\varepsilon_{k,\nu}))\psi(k,\nu)$. From this the transresistivity ρ_{21} can be derived by using that $J_2 = 0$ when the voltage is measured on an inner nanotube [1,2]. Alternatively the Kubo formula can be used[3].

Coulomb Drag setup in carbon nanotubes

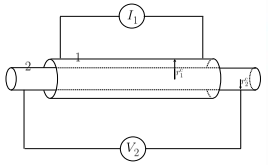

How to measure Coulomb drag.

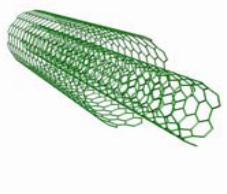

Two coaxial armchair nanotubes.

$$\boxed{E_2 = \rho_{21} J_1}$$

The transresistivity ρ_{21} as a function of temperature

This is the transresistivity ρ_{21} (blue line) for a (5,5) armchair nanotube in a (10,10) nanotube as a function of temperature, where the Fermi level is raised to $0.1\gamma_0$ by doping or a gate voltage. The *inter* band contribution to ρ_{21} is the red dots and the *intra* band contribution is the green line. So clearly the inter band processes are by far the most important. These are all preliminary results for the numerical integration. Here $C_0 = \frac{\hbar^2 e^2 (4\varepsilon_F + \sqrt{3}\gamma_0 a)^2}{72\sqrt{3}\pi^3 n_1 n_2 e^2 (r_1^c r_2^c)^2 (\gamma_0 a)^2}$.

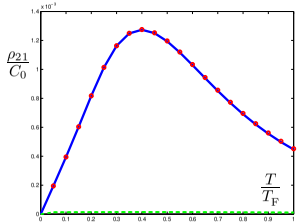

The F-functions

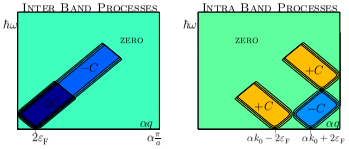

Since the integrand of ρ_{21} has two decreasing functions ($V_{12}(q)$ and $\sinh^{-2}(\frac{\hbar\omega}{2k_BT})$) the inter band processes are seen to be the most important. At $\varepsilon_F = 0$ both the inter and intra band contributions are zero so $\rho_{21}|_{\varepsilon_F=0} = 0$. Here $k_0 = \frac{2\pi}{3a}$, $C = \frac{4\varepsilon_F + \sqrt{3}\gamma_0\pi}{3\gamma_0^2 a^2}$ and α is the slope of the energy bands near the Fermi surface.

Energy Bands for an Armchair Carbon Nanotube

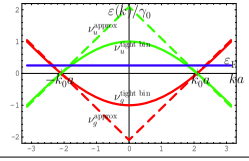

The full lines are **tight binding energy bands**[4] and the dashed lines are the linear approximations used here. The Fermi level ε_F is at zero, but can be raised/lowered by e.g. a gate voltage as seen here. Both bands have **zero angular momentum** along the tube, but **different parity** in the z-component of the eigenstates (red ν_g is even and green ν_u is odd). γ_0 is the overlap integral for the carbon atoms on the nanotube and is of order 3eV.

The Transresistivity Formula

Neglecting Umklapp processes the transresistivity ρ_{21} for armchair nanotubes simplifies to:

$$\rho_{21} = \frac{\hbar^2}{16\pi^5 n_1 n_2 e^2 (r_1^c r_2^c)^2 k_B T} \int_0^{\frac{\pi}{a}} \mathrm{d}q \int_0^{\infty} \mathrm{d}\omega \frac{|V_{12}(q, m=0, r_1^c, r_2^c)|^2}{\sinh^2\left(\frac{\hbar\omega}{2k_BT}\right)}$$
$$\times \Big[\underbrace{(F_{\nu_u\nu_u}(q,\omega) + F_{\nu_g\nu_g}(q,\omega))^2}_{\text{Intra band processes}} + \underbrace{(F_{\nu_g\nu_u}(q,\omega) + F_{\nu_u\nu_g}(q,\omega))^2}_{\text{Inter band processes}} \Big]$$

where $V_{12}(q, m, r_1^c, r_2^c)$ is the Fourier transformed screened Coulomb potential along the cylinder and in the angle and $\hbar\omega$ and $\hbar q$ is the transferred energy and crystal-momentum in the drag process. Furthermore the F**-function** is found to be:

$$F_{\nu\nu'}(q,\omega) = -\frac{4\varepsilon_F + \sqrt{3}\gamma_0\pi}{3\gamma_0^2 a^2} \sum_{k_s \in [-\frac{\pi}{a}, \frac{\pi}{a}]} \mathrm{Sign}\left[v_\nu(k_s) - v_{\nu'}(k_s + q)\right] \left\{ f^0(\varepsilon_{k_s\nu}) - f^0(\varepsilon_{k_s + q\nu'}) \right\}$$

where k_s is the solution of $\varepsilon_{k_s,\nu} - \varepsilon_{k_s+q\nu'} - \hbar\omega = 0$ and $v_\nu(k)$ is the velocity. The F-function is a generalization of the imaginary part of the susceptibility.

The electron-electron interaction

The electron-electron matrix element is :

$$\langle k_1'k_2'\nu_1'\nu_2'|V_{12}(|\mathbf{r_1} - \mathbf{r_2}|)|k_1k_2\nu_1\nu_2\rangle =$$
$$(2\pi)^2\delta(k_1 + k_2 - k_1' - k_2')\delta_{\nu_1\nu_2,\nu_1'\nu_2'} V_{12}(q = k_1' - k_1, m = 0, r_1^c, r_2^c),$$

where parity is conserved in the sense that $\nu_1 \times \nu_2 = \nu_1' \times \nu_2'$. The screened Coulomb interaction V_{12} in the **static limit** is obtained from Poisson equation using the **Thomas-Fermi approximation** and one finds:

$$V_{12}(q, m, r_1^c, r_2^c) = \frac{\frac{e^2}{\epsilon_r\epsilon_0} K_m(qr_1^c) I_m(qr_2^c)}{\varepsilon^{\mathrm{TF}}(q)}$$
$$\varepsilon^{\mathrm{TF}}(q) = \left[1 + 2q_{\mathrm{TF}}^{(r_1^c)} r_1^c K_m(qr_1^c) I_m(qr_1^c)\right]\left[1 + 2q_{\mathrm{TF}}^{(r_2^c)} r_2^c K_m(qr_2^c) I_m(qr_2^c)\right]$$
$$- 4q_{\mathrm{TF}}^{(r_1^c)} q_{\mathrm{TF}}^{(r_2^c)} r_1^c r_2^c \left[K_m(qr_1^c) I_m(qr_2^c)\right]^2$$

where the Thomas-Fermi screening vector is $q_{\mathrm{TF}}^{(r_i^c)} = \frac{e^2}{\epsilon_r\epsilon_0}\frac{\mathrm{d}n_i}{\mathrm{d}\varepsilon_F} = \frac{4e^2}{\epsilon_r\epsilon_0\pi^2 r_i^c\sqrt{3}\gamma_0 a}$ and I_m and K_m are modified m^{th} order Bessel functions of the first and second kind, respectively.

Conclusions

- For an armchair multiwall carbon nanotube with $\varepsilon_F = 0$ the F-functions cancel and thereby $\rho_{21} = 0$.
- A gate voltage or doping makes $\varepsilon_F \neq 0$ and gives a finite drag $\rho_{21} \neq 0$, which is mainly due to inter band processes.
- Coulomb drag is in general a good method to obtain information about the e-e interaction, since in contrast to other transport measurements ρ_{21} depends on $V_{12}(|\mathbf{r_1} - \mathbf{r_2}|)$.

References

[1] A-P Jauho and H. Smith,Phys. Rev. B **47**, 4420 (1993).

[2]K. Flensberg and B. Y-K Hu, Phys. Rev. B **52**, 14796 (1995).

[3]K. Flensberg, B. Y-K Hu, A-P Jauho and J. Kinaret, Phys. Rev. B. **52**, 14761 (1995).

[4]R. Saito, M. Fujita, G. Dresselhaus and M.S. Dresselhaus, Phys. Rev. B **46**, 1804 (1992).

Bibliography

[1] N.W. Ashcroft and N.D. Mermin,*Solid State Physics*, College ed., Harcourt College Publishers (1976).

[2] P. W. Anderson, *More is different*, Science **177**, 393 (1972).

[3] M. B. Pogrebinskii, Fiz. Tekh. Poluprovodn. **11** 637 (1977) [Sov. Phys. Semicond. **11** 372 (1977)];

[4] P. J. Price, *Hot electron effects in heterolayers*, Physica **B** and **C 117**, 750 (1983).

[5] Charles Kittel, *Introduction to Solid State Physics*, 7.ed., John Wiley & Sons (1996).

[6] Antti-Pekka Jauho and Henrik Smith,*Coulomb drag between two-dimensional electron systems*,Phys. Rev. B **47**, 4420 (1993).

[7] Henrik Smith and H. Højgaard Jensen, *Transport Phenomena*, Clarendon Press, Oxford, (1989).

[8] C. P. Enz, *A course on Many-body theory Applied to Solid-state Physics*, First Edition, Lecture notes in Physics vol.11, World Scientific (1992).

[9] H. W. Kroto, J. R. Heath, S. C. Obrien, R. F. Curl and R. E. Smalley C_{60}*–Buckminsterfullerene*, Nature **318**, 162 (1985).

[10] S. Iijima, *Helical microtubules of graphitic carbon*, Nature **354**, 56 (1991).

[11] K. Jiang, Q. Li and S. Fan, *Spinning continuous carbon nanotube yarns*, Nature **419**, 801 (2002).

[12] R. Krupke, F. Hennrich, H. v. Löhneysen and M. M. Kappes, *Separation of Metallic from Semiconducting Single-Walled Carbon Nanotubes*, Science **301**, 344 (2003).

[13] M. Bockrath, D. H. Cobden, J. Lu, A. G. Rinzler, R. E. Smalley, L. Balents and P. L. McEuen, *Luttinger-liquid behaviour in carbon nanotubes*, Nature **397**, 598 (1997).

[14] H. Ishii, H. Kataura, H. Shiozawa, H. Yoshioka, H. Otsubo, Y. Takayama, T. Miyahara, S. Suzuki, Y. Achiba, M. Nakatake, T. Narimura, M. Higashiguchi, K. Shimada, H. Namatame and M. Taniguchi, *Direct observation of Tomonaga-Luttinger-liquid state in carbon nanotubes at low temperatures*, Nature **426**, 540 (2003).

[15] R. Egger and A. O. Gogolin, *Effective Low-Energy Theory for Correlated Carbon Nanotubes*, Phys. Rev. Lett. **79**, 5082 (1997) and *Correlated transport and non-Fermi-liquid behavior in single-wall carbon nanotubes*, Eur. Phys. J. B. **3**, 281 (1998).

[16] C. Kane, L. Balents and M. P. A. Fisher, *Coulomb Interactions and Mesoscopic Effects in Carbon Nanotubes*, Phys. Rev. Lett. **79**, 5086 (1997).

[17] J. Voit, *A brief introduction to Luttinger Liquids*, condmat/0005114 (2000) (Proceedings of the International Winterschool on Electronic Properties of Novel Materials 2000, Kirchberg).

[18] Henrik Bruus and Karsten Flensberg, *Quantum field theory in condensed matter physics*, Lecture notes, Niels Bohr Institute (2001) (see e.g. www.fys.ku.dk/flensberg).

[19] J. Voit, *One-dimensional Fermi liquids*, Rep. Prog. Phys. **58**, 977 (1995).

[20] R. Egger, A. Bachtold, M.S. Fuhrer, M. Bockrath, D.H. Cobden and P.L. McEuen, *Luttinger liquid behavior in metallic carbon nanotubes*, condmat/0008008 (2000).

[21] R. Tarkiainen, M. Ahlskog, J. Penttilä, L. Roschier, P. Hakonen, M. Paalanen and E. Sonin, *Multiwalled carbon nanotubes: Luttinger versus Fermi liquid*, Phys. Rev. B **64**, 195412 (2001).

[22] N. Kang, L. Lu, W. J. Kong, J. S. Hu, W. Yi, Y. P. Wang, D. L. Zhang, Z. W. Pan and S. S. Xie, *Observation of a temperature dependence of the thermoelectric power in multiwall carbon nanotubes*, Phys. Rev. B **67**, 033404 (2003).

[23] V. Krstić, S. Blumentritt, J. Muster, S. Roth and A. Rubio, *Role of disorder on transport in boron-doped multiwalled carbon nanotubes*, Phys. Rev. B **67**, 041401(R) (2003).

[24] R. Egger , *Luttinger Liquid Behavior in Multiwall Carbon Nanotubes*, Phys. Rev. Lett. **83**, 5547 (1999).

[25] J. Cumings, P. G. Collins and A. Zettl, *Peeling and sharpening multiwall nanotubes*, Nature **406**, 586 (2000).

[26] P. G. Collins, M. S. Arnold, and P. Avouris, *Engineering carbon nanotubes and nanotube circuits using electrical breakdown*, Science **292**, 706 (2001).

[27] S. Dohn, *Investigation of mechano-electrical properties of multi-walled carbon nanotubes*, Master thesis, Micro- and Nanotechnology Research center (2003).

[28] Ajit Kumar Dutta, *Electrical conductivity of single crystals of graphite*, Phys. Rev. **90**, 187 (1953);
R. L. Powell and G. E. Childs, *American institute of physics handbook* **4**, 142 (1972). (see also: www.phy.mtu.edu/∼jaszczak/graphprop.html)

[29] A. Bachtold, C. Strunk, J.-P. Salvetat, J.-M. Bonard, L. Forró, T. Nussbaumer, C. Schönenberger, *Aharonov-Bohm oscillations in carbon nanotubes*, Nature **397**, 673 (1999).

[30] S. Frank, P. Poncharal, Z.L. Wang and W. A de Heer, *Carbon nanotube quantum conductors*, Science **280**, 1744 (1998).

[31] J. Cumings and A. Zettl, *Low-friction nanoscale linear bearing realized from multiwall carbon nanotubes*, Science **289**, 602 (2000).

[32] M.Fuhrer, J.Nygård, L.Shih, M.Forero, Young-Gui Yoon, M.S.C. Mazzoni, H. Joon Choi, J. Ihm, S. G. Louie, A. Zettl and P. L. McEuen, *Crossed Nanotube Junctions*, Science **288**, 494 (2000).

[33] Jesper Nygård, *Experiments on mesoscopic electron transport in carbon nanotubes*, Ph.D. Thesis, Faculty of Science, University of Copenhagen, Second edition, ISBN 87-988165-0-0 (2000).

[34] Andrei Komnik and Reinhold Egger, *Nonequilibrium transport for crossed Luttinger liquids* Phys. Rev. Lett. **80**, 2881 (1998) and *Transport and Coulomb drag for two interacting carbon nanotubes*, Eur. Phys. J. B **19**, 271 (2000).

[35] B. Gao, A. Komnik, R. Egger, D.C. Glattli and A. Bachtold, *Evidence for Luttinger liquid behavior in crossed metallic single-wall nanotubes*, condmat/0311645 (2003).

[36] K. Flensberg, *Coulomb drag of Luttinger liquids and quantum-Hall edges*, Phys. Rev. Lett. **81**, 184 (1998).

[37] S. Das and S. Rao, *Transport through multiply connected quantum wires*, condmat/0310713 (2003).

[38] P. Debray, V. Gurevich, R. Klesse and R.S. Newrock, *Coulomb drag between ballistic one-dimensional electron systems*, Semiconductor science and technology **17**, R21 (2002).

[39] Niels Asger Mortensen, *Mesoscopic Coulomb Drag*, Ph.D. thesis, MIC (2001).

[40] B. Y.-K. Hu and K. Flensberg, *Nonlinear Coulomb Frictional Drag in Coupled Quantum Wells and Wires*, Hot Carriers in Semicondoctors, eds. K. Hess et al., 421, Plenum Press (1996).

[41] Anders Hansson and Sven Stafström, *Intershell conductance in multiwall carbon nanotubes*, Phys. Rev. B **67**, 075406 (2003).

[42] S. Sanvito, Young-Kyun Kwon, D. Tománek, and C. J. Lambert, *Fractional quantum conductance in carbon nanotubes*, Phys. Rev. Lett. **84**, 1974 (2000).

[43] H. J. Choi, J. Ihm, Y.-G. Yoon and S. G. Louie, *Possible explanation for the conductance of a single quantum unit in metallic carbon nanotubes*, Phys. Rev. B **60**, 14009 (1999).

[44] S. Roche, F. Triozon, A. Rubio, and D. Mayou, *Conduction mechanisms and magnetotransport in multiwalled carbon nanotubes*, Phys. Rev. B **64**, 121401 (2001).

[45] S. Roche, F. Triozon, A. Rubio, and D. Mayou, *Electronic conduction in multi-walled carbon nanotubes: role of intershell coupling and incommensurability*, Phys. Lett. A **285**, 94 (2001).

[46] J.-C. Charlier and J.-P. Michenaud, *Energetics of multilayered carbon tubules*, Phys. Rev. Lett. **70**, 1858 (1993).

[47] A. G. Rojo, *Electron-drag effects in coupled electron systems*, J. Phys.: Condens. Matter **11**, R31 (1999).

[48] T. J. Gramila, J. P. Eisenstein, A. H. MacDonald, L. N. Pfeiffer, and K. W. West, *Mutual friction between parallel two-dimensional electron systems*, Phys. Rev. Lett **66**, 1216 (1991).

[49] Martin Chr. Bønsager, Karsten Flensberg, Ben Yu-Kuang Hu and A.H. Macdonald, *Frictional drag between quantum wells mediated by phonon exchange*, Phys. Rev. B **57**, 7085 (1997).

[50] T. J. Gramila, J. P. Eisenstein, A. H. MacDonald, L. N. Pfeiffer and K. W. West, *Evidence for virtual-phonon exchange in semiconductor heterostructures*, Phys. Rev. B **47**, 12957 (1993).

[51] Karsten Flensberg and Ben Yu-Kuang Hu, *Coulomb Drag as a Probe of Coupled Plasmon Modes in Parallel Quantum Wells*, Phys. Rev. Lett. **73**, 3572 (1994).

[52] Karsten Flensberg and Ben Yu-Kuang Hu, *Plasmon enhancement of Coulomb drag in double-quantum-well systems*, Phys. Rev. B **52**, 14796 (1995).

[53] N. P. R. Hill, J. T. Nicholls, E. H. Linfield, M. Pepper, D. A. Ritchie, G. A. C. Jones, B. Yu-Kuang Hu and K. Flensberg, *Correlation Effects on the Coupled Plasmon Modes of a Double Quantum Well*, Phys. Rev. Lett. **78**, 2204 (1997).

[54] L. V. Butov, A. L. Ivanov, A. Imamoglu, P. B. Littlewood, A. A. Shashkin, V. T. Dolgopolov, K. L. Campman and A. C. Gossard, *Stimulated Scattering of Indirect Excitons in Coupled Quantum Wells: Signature of a Degenerate Bose-Gas of Excitons*, Phys. Rev. Lett. **86**, 5608 (2001).

[55] L. V. Butov, *Degenerate excition gases in cupled quantum-well systems*, invited talk at *13th International Conference on Nonequilibrium Carrier Dynamics in Semiconductors* in Modena, Itali (2003).

[56] B. N. Narozhny and I. L. Aleiner, *Mesoscopic fluctuations of the coulomb drag*, Phys. Rev. Lett. **84**, 5383 (2000).

[57] N. A. Mortensen, K. Flensberg and A.-P. Jauho, *Coulomb drag in coherent mesoscopic systems*, Phys. Rev. Lett. **86**, 1841 (2001).

[58] R. Saito, G. Dresselhaus and M. S. Dresselhaus, *Physical Properties of Carbon Nanotubes*, 3.ed., Imperial College press (1998).

[59] H. Ajiki and T. Ando, *Electronic states of carbon nanotubes*, J. Phys. Soc. Jpn. **62**, 1255 (1993).

[60] N. Hamada, S.-I. Sawada, and A. Oshiyama, *New one-dimensional conductors: Graphitic microtubules*, Phys. Rev. Lett. **68**, 1579 (1992).

[61] J. W. Mintmire and C. T. White, *Electronic and structural properties of carbon nanotubes*, Carbon **33**, 893 (1995).

[62] C. T. White, D. H. Robertson and J. W. Mintmire, *Helical and rotational symmetries of nanoscale graphitic tubules*, Phys. Rev. B **47**, 5485 (1993).

[63] M.S. Dresselhaus, G. Dresselhaus and R. Saito, *Carbon fibers based on C_{60} and their symmetry*, Phys. Rev. B **45**, 6234 (1992).

[64] Riichiro Saito, Mitsutaka Fujita, G. Dresselhaus and M.S. Dresselhaus, *Electronic structure of the graphene tubules based on C_{60}*, Phys. Rev. B **46**, 1804 (1992).

[65] P. R. Wallace, *The Band Theory of Graphite*, Phys. Rev. **71**, 622 (1947).

[66] S. Reich, J. Maultzsch, C. Thomsen and P. Ordejón, *Tight-binding description of graphene*, Phys. Rev. B **66**, 035412 (2002).

[67] T. Vuković, I. Milošević and M. Damnjanović, *Carbon nanotubes band assignation, topology, Bloch states, and selection rules*, Phys. Rev. B **65**, 045418 (2002).

[68] G. S. Painter and D. E. Ellis, *Electronic Band Structure and Optical Properties of Graphite from a Variational Approach*, Phys. Rev. B **1**, 4747 (1970).

[69] S. D. M. Brown, P. Corio, A. Marucci, M. S. Dresselhaus and G. Dresselhaus, *Second-order resonant Raman spectra of single-walled carbon nanotubes*, Phys. Rev. B **61**, 7734 (2000).

[70] J. W. G. Wilder, L. C. Venema, A. G. Rinzler, R. E. Smalley and C. Dekker, *Electronic structure of atomically resolved carbon nanotubes*, Nature **391**, 59 (1998).

[71] T. W. Odom, J.-L. Huang, P. Kim and C. M. Lieber, *Atomic structure and electronic properties of single-walled carbon nanotubes*, Nature **391**, 62 (1998).

[72] Young-Kyun Kwon and D. Tománek, *Electronic and structural properties of multiwall carbon nanotubes*, Phys. Rev. B **58**, 16001 (1998) and ref. therein.

[73] A. Kleiner and S. Eggert, *Curvature, hybridization, and STM images of carbon nanotubes*, Phys. Rev. B **64**, 113402 (2001) and ref. therein.

[74] R. Saito, M. Fujita, G. Dresselhaus, and M. S Dresselhaus, *Electronic structure of chiral graphene tubules*, Appl. Phys. Lett. **60**, 2204 (1992).

[75] M. Damnjanović, I. Milošević, T. Vuković and R. Sredanović, *Full symmetry, optical activity, and potentials of single-wall and multiwall nanotubes*, Phys. Rev. B **60**, 2728 (1999).

[76] M. Damnjanović, T. Vuković and I. Milošević, *Modified group projectors: tight-binding method*, J. Phys. A: Math. gen **33**, 6561 (2000).

[77] I. Milošević, T. Vuković, S. Dmitrović and M. Damnjanović, *Polarized optical absorption in carbon nanotubes: A symmetry-based approach*, Phys. Rev. B **67**, 165418 (2003).

[78] J.J. Sakurai, *Modern Quantum mechanics*, Revised Edition, Addison-Wesley (1994).

[79] M. Krüger, M. R. Buitelaar, T. Nussbaumer, and C. Schönenberger and L. Forró, *Electrochemical carbon nanotube field-effect transistor*, Appl. Phys. Lett. **78**, 1291 (2001).

[80] C. Schönenberger, M. Buitelaar, M. Krüger, I. Widmer, T. Nussbaumer and M. Iqbal, *Doping state of multi-wall carbon nanotubes wires and quantum dots*, Proceedings Moriond 2001, cond-mat/0106501 (2001).

[81] C. Zhou, J. Kong and H. Dai, *Intrinsic Electrical Properties of Individual Single-Walled Carbon Nanotubes with Small Band Gaps*, Phys. Rev. Lett. **84**, 5604 (2000).

[82] R. S. Lee, H. J. Kim, J. E. Fischer, J. Lefebvre, M. Radosavljević, J. Hone, and A. T. Johnson , *Transport properties of a potassium-doped single-wall carbon nanotube rope*, Phys. Rev. B **61**, 4526 (2000).

[83] A. Javey, H. Kim, M. Brink, Q. Wang, A. Ural, J. Guo, P. Mcintyre, P. Mceuen, M. Lundstrom and H. Dai, *High-κ dielectrics for advanced carbon-nanotube transistors and logic gates*, Nature Materials **1**, 241 (2002).

[84] C. Zhou, J. Kong, E. Yenilmez, and H. Dai, *Modulated Chemical Doping of Individual Carbon Nanotubes*, Science **290**, 1552 (2000).

[85] M. Damnjanović, T. Vuković and I. Milošević, *Fermi level quantum numbers and the secondary gap of conducting carbon nanotubes*, Solid state Comm. **116**, 265 (2000).

[86] P. Delaney, H. J. Choi, J. Ihm, S. G. Louie and M. L. Cohen, *Broken symmetry and pseudogaps in ropes of carbon nanotubes*, Nature **391**, 466 (1998).

[87] M. Brandbyge, *Atomic and Electronic Structure of Carbon nanotubes*, (1999) see http://library.wolfram.com/infocenter/MathSource/384/
(A *Mathematica* program, which can generate the band structure for any carbon nanotube).

[88] G. Bastard, *Wave mechanics applied to semiconductor heterostructures*, Monographies De Physique, Wiley and Sons, Incorporated (1996).

[89] D. P. DiVincenzo and E. J. Mele, *Self-consistent effective-mass theory for intralayer screening in graphite intercalation compounds*, Phys. Rev. B **29**, 1685 (1984).

[90] C. L. Kane and E. J. Mele, *Size, Shape, and Low Energy Electronic Structure of Carbon Nanotubes*, Phys. Rev. Lett. **78**, 1932 (1997).

[91] T. Ando and T. Nakanishi, *Impurity scattering in carbon nanotubes- Absence of Back scattering*, J. Phys. Soc. Jpn. **67**, 1704 (1998).

[92] T. Ando, T. Nakanishi and R. Saito, *Berry's phase and absence of back scattering in carbon nanotubes*, J. Phys. Soc. Jpn. **67**, 2857 (1998).

[93] P. L. McEuen, M. Bockrath, D. H. Cobden, Y.-G. Yoon and S. G. Louie, *Disorder, Pseudospins, and Backscattering in Carbon Nanotubes*, Phys. Rev. Lett. **83**, 5098 (1999).

[94] Supriyo Datta, *Electronic transport in mesoscopic systems*, Cambridge studies in semiconductor physics and microelectronic engineering, Cambridge University Press, (1995).

[95] C. T. White and T. N. Todorov, *Carbon nanotubes as long ballistic conductors*, Nature **393**, 240 (1998).

[96] J. Kong, E. Yenilmez, T. W. Tombler, W. Kim, H. Dai, R. B. Laughlin, Lei Liu, C. S. Jayanthi and S. Y. Wu, *Quantum Interference and Ballistic Transmission in Nanotube Electron Waveguides*, Phys. Rev. Lett. **87**, 106801 (2001).

[97] A. Bachtold, M. S. Fuhrer, S. Plyasunov, M. Forero, E. H. Anderson, A. Zettl, and P. L. McEuen, *Scanned Probe Microscopy of Electronic Transport in Carbon Nanotubes*, Phys. Rev. Lett. **84**, 6082 (2000).

[98] W. Liang, M. Bockrath, D. Bozovic, J. H. Hafner, M. Tinkham and H. Park, *Fabry-Perot interference in a nanotube electron waveguide*, Nature **411**, 665 (2001).

[99] R. Martel, T. Schmidt, H. R. Shea, T. Hertel and Ph. Avouris, *Single- and multi-wall carbon nanotube field-effect transistors*, Appl. Phys. Lett. **73**, 2447 (1998).

[100] Petr Král and Moshe Shapiro, *Nanotube Electron Drag in Flowing Liquids*, Phys. Rev. Lett. **86**, 131 (2001).

[101] T. Seri and T. Ando, *Boltzmann Conductivity of a Carbon Nanotube in Magnetic Fields*, J. Phys. Soc. Jpn. **66**, 169 (1997).

[102] A. Javey, J. Guo, M. Paulsson, Q. Wang, D. Mann, M. Lundstrom, H. Dai, *High-Field, Quasi-Ballistic Transport in Short Carbon Nanotubes*, cond-mat/0309242 (2003).

[103] G. Y. Slepyan, S. A. Maksimenko, B. A. Lakhtakia, O. M. Yevtushenko and A. V. Gusakov, *Electronic and electromagnetic properties of nanotubes*, Phys. Rev. B **57**, 9485 (2003).

[104] Z. Yao, C. L. Kane, and C. Dekker, *High-Field Electrical Transport in Single-Wall Carbon Nanotubes*, Phys. Rev. Lett. **84**, 2941 (2000).

[105] V. W. Scarola and G. D. Mahan, *Phonon drag effect in single-walled carbon nanotubes*, Phys. Rev. B **66**, 205405 (2002).

[106] J. Vavro, M. C. Llaguno, J. E. Fischer, S. Ramesh, R. K. Saini, L.M. Ericson,V. A. Davis, R. H. Hauge, M. Pasquali and R. E. Smalley, *Thermoelectric Power of p-Doped Single-Wall Carbon Nanotubes and the Role of Phonon Drag*, Phys. Rev. Lett. **90**, 065503 (2003).

[107] M. Pustilnik, E. G. Mishchenko, L. I. Glazman and A. V. Andreev, *Coulomb Drag by Small Momentum Transfer between Quantum Wires*, Phys. Rev. Lett. **91**, 126805 (2003).

[108] R. Klesse, *Electron scattering in multiwall carbon nanotubes*, Phys. Rev. B **66**, 085409 (2002).

[109] Richard L. Liboff, *Introductory Quantum Mechanics*, Third edition, Addison Wesley (1998).

[110] G. Qin, *Coulomb drag in coupled 2D-2D and 2D-1D cylindrical quantum wells*, J. Phys. Condens. Matter **7**, 9785-9798 (1995).

[111] Henrik Smith, *Solid state physics notes*, Lecture notes, Niels Bohr Institute (2001).

[112] Karsten Flensberg, Ben Yu-Kuang Hu, Antti-Pekka Jauho and Jari M. Kinaret, *Linear-response theory of the Coulomb drag in coupled electron systems*, Phys. Rev. B **52**, 14761 (1995).

[113] Audrius Alkauskas, Karsten Flensberg, Ben Yu-Kuang Hu and Antti-Pekka Jauho, *Sign reversal of drag in bilayer systems with in-plane periodic potential modulation*, Phys. Rev. B **66**, 201304(R) (2002).

[114] Ben Yu-Kuang Hu, *Optical-phonon-induced frictinal drag in coupled two-dimensional electron gases*, Phys. Rev. B **57**, 12345 (1998).

[115] B. K. Ridley, *Quantum processes in Semiconductors*, Third edition, Oxford science publications (1993).

[116] Antti-Pekka Jauho, *Superlattices and Bloch oscillations*, Lecture note, MIC, DTU, (2002).

[117] Hartmut Haug and Antti-Pekka Jauho, *Quantum Kinetics in transport and optics of semiconductors*, First Edition (corrected printing), Springer (1998).

[118] William Que, *Luttinger parameter g for metallic carbon nanotubes and related systems*, Phys. Rev. B **66**, 193405 (2002).

[119] David J. Griffiths, *Introduction to electrodynamics*, Third edition, Prentice Hall, upper saddle River, New Jersey (1999).

[120] R. Egger and A. O. Gogolin , *Correlated transport and non-Fermi-liquid behavior in single-wall carbon nanotubes*, Eur. Phys. J. B **3**, 281 (1998).

[121] T. Ando, A. B. Fowler and F. Stern, *Electronic properties of two-dimensional systems*, Rev. Mod. Phys. **54**, 437 (1982).

[122] G. F. Roach, *Green's functions – Introductory theory with applications*, Van Nostrand Reinhold Company, London (1970).

[123] Murray R. Spiegel, *Mathematical handbook of formulas and tables*, 36th Printing 1997, McGraw-Hill (1968).

[124] P. Longe and S. M. Bose, *Collective excitations in metallic graphene tubules*, Phys. Rev. B **48**, 18239 (1993).

[125] M. F. Lin and Kenneth W.-K. Shung, *Elementary excitations in cylindrical tubules*, Phys. Rev. B **47**, 6617 (1993).

[126] G. D. Mahan, *Many-particle physics*,second edition, Plenum Press (1990).

[127] S. B. Legoas, V. R. Coluci, S. F. Braga, P. Z. Coura, S. O. Dantas and D. S. Galvao , *Molecular-Dynamics Simulations of Carbon Nanotubes as Gigahertz Oscillators*, Phys. Rev. lett. **90**, 055504 (2003).

[128] W. H. Press, S. A. Teukolsky, W. T. Vetterling and B. P. Flannery, *Numerical Recipes – in* FORTRAN *77*, Second ed., Cambridge university press (1992).